Roger Wolf

# The Higgs Boson Discovery at the Large Hadron Collider



### **Springer Tracts in Modern Physics**

### Volume 264

### **Honorary Editor**

G. Höhler, Karlsruhe, Germany

### Series editors

Yan Chen, Shanghai, China Atsushi Fujimori, Tokyo, Japan Johann H. Kühn, Karlsruhe, Germany Thomas Müller, Karlsruhe, Germany Frank Steiner, Ulm, Germany William C. Stwalley, Storrs, CT, USA Joachim E. Trümper, Garching, Germany Peter Wölfle, Karlsruhe, Germany Ulrike Woggon, Berlin, Germany

### **Springer Tracts in Modern Physics**

Springer Tracts in Modern Physics provides comprehensive and critical reviews of topics of current interest in physics. The following fields are emphasized: Elementary Particle Physics, Condensed Matter Physics, Light Matter Interaction, Atomic and Molecular Physics, Complex Systems, Fundamental Astrophysics.

Suitable reviews of other fields can also be accepted. The editors encourage prospective authors to correspond with them in advance of submitting a manuscript. For reviews of topics belonging to the above mentioned fields, they should address the responsible editor as listed below.

Special offer: For all clients with a print standing order we offer free access to the electronic volumes of the Series published in the current year.

### **Elementary Particle Physics**

Johann H. Kühn Institut für Theoretische Teilchenphysik Karlsruhe Institut für Technologie KIT Postfach 69 80 76049 Karlsruhe, Germany Email: johann.kuehn@KIT.edu www-ttp.physik.uni-karlsruhe.de/~jk

Thomas Müller Institut für Experimentelle Kernphysik Karlsruhe Institut für Technologie KIT Postfach 69 80 76049 Karlsruhe, Germany Email: thomas.muller@KIT.edu

www-ekp.physik.uni-karlsruhe.de

### **Complex Systems**

Frank Steiner
Institut für Theoretische Physik
Universität Ulm
Albert-Einstein-Allee 11
89069 Ulm, Germany
Email: frank.steiner@uni-ulm.de

**Fundamental Astrophysics** 

Joachim E. Trümper

Max-Planck-Institut für Extraterrestrische Physik

www.physik.uni-ulm.de/theo/qc/group.html

Postfach 13 12

85741 Garching, Germany Email: jtrumper@mpe.mpg.de www.mpe-garching.mpg.de/index.html

### Solid State and Optical Physics

Ulrike Woggon Institut für Optik und Atomare Physik Technische Universität Berlin Straße des 17. Juni 135 10623 Berlin, Germany Email: ulrike.woggon@tu-berlin.de www.ioap.tu-berlin.de

### **Condensed Matter Physics**

Yan Chen
Fudan University
Department of Physics
2250 Songhu Road
Shanghai, China 400438
Email: yanchen99@fudan.edu.cn
www.physics.fudan.edu.cn/tps/branch/cqc/en/people/
faculty/

Atsushi Fujimori

Editor for The Pacific Rim

Department of Physics

University of Tokyo

7-3-1 Hongo, Bunkyo-ku

Tokyo 113-0033, Japan

Email: fujimori@phys.s.u-tokyo.ac.jp

http://wyvern.phys.s.u-tokyo.ac.jp/welcome\_en.html

Peter Wölfle
Institut für Theorie der Kondensierten Materie
Karlsruhe Institut für Technologie KIT
Postfach 69 80
76049 Karlsruhe, Germany
Email: peter.woelfle@KIT.edu
www-tkm.physik.uni-karlsruhe.de

### Atomic, Molecular and Optical Physics

William C. Stwalley
University of Connecticut
Department of Physics
2152 Hillside Road, U-3046
Storrs, CT 06269-3046, USA
Email: w.stwalley@uconn.edu
www-phys.uconn.edu/faculty/stwalley.html

. .

# The Higgs Boson Discovery at the Large Hadron Collider



Roger Wolf Karlsruhe Institute of Technology KIT Karlsruhe Germany

ISSN 0081-3869 ISSN 1615-0430 (electronic)
Springer Tracts in Modern Physics
ISBN 978-3-319-18511-8 ISBN 978-3-319-18512-5 (eBook)
DOI 10.1007/978-3-319-18512-5

Library of Congress Control Number: 2015937527

14.80.Bn, 12.15.-y, 11.15.Ex

Springer Cham Heidelberg New York Dordrecht London

© Springer International Publishing Switzerland 2015

This work is subject to copyright. All rights are reserved by the Publisher, whether the whole or part of the material is concerned, specifically the rights of translation, reprinting, reuse of illustrations, recitation, broadcasting, reproduction on microfilms or in any other physical way, and transmission or information storage and retrieval, electronic adaptation, computer software, or by similar or dissimilar methodology now known or hereafter developed.

The use of general descriptive names, registered names, trademarks, service marks, etc. in this publication does not imply, even in the absence of a specific statement, that such names are exempt from the relevant protective laws and regulations and therefore free for general use.

The publisher, the authors and the editors are safe to assume that the advice and information in this book are believed to be true and accurate at the date of publication. Neither the publisher nor the authors or the editors give a warranty, express or implied, with respect to the material contained herein or for any errors or omissions that may have been made.

Printed on acid-free paper

Springer International Publishing AG Switzerland is part of Springer Science+Business Media (www.springer.com)

### Acknowledgments

I have written this document in the context of my habilitation at the Karlsruhe Institut für Technologie (KIT). It is partially based on the lecture "Teilchenphysk II -Higgsphysik" that I have given during the summer term 2014. I am grateful to Prof. Dr. Thomas Müller and Prof. Dr. Günter Quast for their support and for giving me the opportunity to proceed with my habilitation at the Institut für Experimentelle Kernphysik (EKP). Many thanks to Prof. Dr. Thomas Müller for making the contact with Springer, initiating that this document could be published as part of the "Springer Tracts in Modern Physics" and to the publisher for the professional partnership throughout the creation time of the document. I am grateful to the *Deutsche* Forschungsgemeinschaft (DFG) and the Massachusetts Institute of Technology (MIT) (especially to Prof. Dr. Markus Klute), for the exciting and unforgettable time I could have at CERN during the years of the Higgs boson discovery 2011 and 2012. Many thanks to Dr. Andrew Gilbert and Dr. Joram Berger for many valuable comments on the script and to the students of my working group at EKP for their proofreading. I am indebted to the Baden-Württemberg Stiftung for the financial support of my research group by the "Elite Program for Postdocs" from 2014 on.

### **Contents**

1	Intr	oduction		1			
	1.1	The Standard Model of Particle Physics					
	1.2	The Problem of Massive Particles in the Standard Model					
	1.3	3 Synopsis and Guideline to the Book					
	Refe			12			
2	The Higgs Boson in the Standard Model of Particle Physics 1						
	2.1	The Pri	nciple of Gauge Symmetries	15			
		2.1.1 l	Extension to Non-Abelian Gauge Symmetries	18			
	2.2	The Ele	ctroweak Gauge Theory	23			
		2.2.1 I	Extension to a Theory of Electroweak				
		]	Interactions	25			
	2.3	Electrov	weak Symmetry Breaking and the Higgs Boson	32			
		2.3.1	The Goldstone Model	32			
		2.3.2	Extension to a Gauge Theory	34			
	2.4	·					
		of Particle Physics		36			
		2.4.1	Custodial Symmetry	40			
			Giving Masses to Fermions	43			
			Summary and Conclusions	47			
	Refe	References					
3	Hig	gs Boson	Searches Before the Advent of the Large				
			ider	53			
	3.1	Constraints Within the Theory		53			
			The Unitarity Bound	55			
			The Goldstone Potential at Higher Orders	57			
	3.2						
		Measurements					
			Electroweak Precision Observables	60 60			
			Statistical Model	62			

viii Contents

			Results of the Likelihood Analysis	65
	3.3	Direct	Searches at the Large Electron Positron Collider	68
		3.3.1	Statistical Framework	69
		3.3.2	Direct Search Results	74
	3.4		Searches at the Tevatron Proton	
		Anti-F	Proton Collider	76
	Refe	erences		78
4	Disc	overy (	of the Higgs Boson at the Large Hadron Collider	81
	4.1	Setting	g up the Scene for Discovery	81
		4.1.1	The Large Hadron Collider	81
		4.1.2	Main Experiments and Event Reconstruction	83
		4.1.3	First Measurements of Known Standard Model	
			Processes	89
	4.2	The E	ve of the Hunt for the Higgs Boson	92
		4.2.1	Decay Channels and Production Modes	92
		4.2.2	First Searches and Statistical Methods	96
	4.3	The D	Discovery of a New Particle in the Bosonic	
			Channels	99
		4.3.1	The Signal in the $H \rightarrow \gamma \gamma$ Decay Channel	102
		4.3.2	The Signal in the $H \rightarrow ZZ$ Decay Channel	108
		4.3.3	Evidence of the Signal in the $H \rightarrow WW$	
			Decay Channel	114
		4.3.4	Conclusions on the Bosonic Decay Channels	120
	4.4		of the New Particle in the Fermionic	
			Channels	122
		4.4.1	The Coupling to Leptons	123
		4.4.2	The Coupling to Quarks	135
		4.4.3	Conclusions on the Coupling to Fermions	146
	Refe		· · · · · · · · · · · · · · · · · · ·	148
_	D	4	of the New Doublele	151
5	_		of the New Particle	151 151
	5.1		and Decay Width of the New Particle	131
		5.1.1	Canonical Estimate of the Mass and Decay	151
		5 1 2	Width	151
		5.1.2	Decay Width Estimate from the Off-Shell	1.55
	<i>-</i> -	<b>a</b> :	Cross Section	155
	5.2		and CP Symmetry	161
		5.2.1	Groundwork for Spin and CP Analyses	161
		5.2.2	Estimate of Spin and CP in the $H \rightarrow ZZ$	
			Decay Channel	164

Contents ix

	5.3 Co	ng Structure
	5.3	Prerequisite Studies
	5.3	Statistical Model
	5.3	Test of the Coupling Structure 1'
	Reference	
6	Conclusi	
	Reference	

## Chapter 1 Introduction

### 1.1 The Standard Model of Particle Physics

The theory to describe all fundamental constituents of matter and their interactions is the Standard Model of Particle Physics (SM) [1–3]. It is a Lorentz covariant quantum field theory and as such a multi-particle theory, with operators for particle creation and destruction. It is capable not only of explaining the dynamics of elementary particles but also transitions from one particle into another, particle decays, particle annihilation or the production of new particles out of the quantum vacuum, which corresponds to the energy ground state of the theory. In quantum mechanics particles are categorized into bosons (with integer spin) and fermions (with half integer spin). In multi-particle environments both groups of particles have a distinct behavior: while bosons share the same phasespace, which allows for a description of their dynamics in a single, space-symmetric wave function, fermions always occupy a unique element in a multi-particle phasespace, which can never be shared with any other fermion at the same time. This fact is expressed by the exclusion principle of Wolfgang Pauli [4]. Fermions, in contrast to bosons, are described by wave functions which are anti-symmetric in their space coordinates. The behavior of multi-particle systems made of fermions or bosons follows the Fermi or Bose-Einstein statistics, which hold for all fundamental, non-divisible particles that we know so far, as well as for more complex composite objects that still need to be treated on a quantum mechanical basis, like atoms or molecules. Nowadays, the particle physics experiments have the ability to analyze structures at distances as small as  $10^{-19}$  cm, corresponding to a sub-per mill of the size of the proton. To our understanding, all matter that we know is made up of *quarks* and *leptons*, which both are fermions, with spin 1/2. Both kinds of particles have been found to lack further structure (i.e. they are not made up of even more fundamental particles), to be non-divisible and point-like up to the current level of accuracy. To our current knowledge we can assign four fundamental forces to govern all interactions between them which are mediated by the exchange of bosonic particles: gravitation, the electromagnetic, weak and strong force. Each of these forces will be briefly discussed in the following paragraphs. Unless one last

1

2 1 Introduction

missing non-trivial fundamental symmetry is found, a symmetry between fermions and bosons, called *supersymmetry* [5–8], it seems that nature chose fermions with spin  $^{1}/_{2}$  to represent the fundamental constituents of matter and bosons with spin 1 as force mediating particles, with the only exception of the still undiscovered, *graviton*, which is expected to have spin 2.

### The Electromagnetic Force

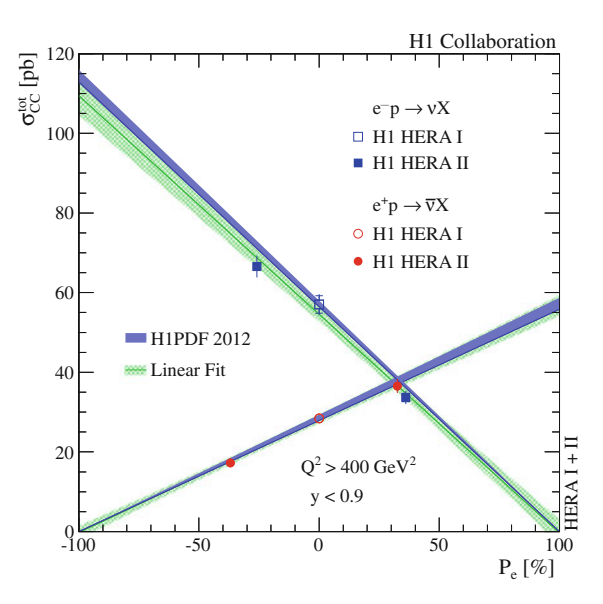
In the SM, the electromagnetic force is mediated by the *photon*. It has been explored for more than 200 years and has been utilized in our daily life in the form of electric devices like radio or television. It has thus become one of the best understood fundamental interactions in nature. Like gravitation, which will be discussed below, it is a force of infinite range with a potential that is proportional to the inverse of the distance between the interacting sources. It can be understood on the basis of classical field theory [9]. Quantum field theoretical aspects only come into play on scales where quantum effects cannot be neglected any more, e.g. at distances of atomic radii. The electromagnetic force can be repelling or attractive, depending on the electric charges it couples to. These can be positive or negative, but always with the exact same quantized absolute value, which is clear from the fact that, while nature is full of electrons and protons, the universe as a whole is charge neutral. The quantization of charge is in fact the first hint to the underlying quantum nature of our universe already at macroscopic scales. The Maxwell theory of electrodynamics has furthermore been a precedent case, where two phenomena in nature, which at first sight appeared to be independent, electricity and magnetism, could be explained as originating from the same common fundamental force, that could be described by a single theory [10].

### The Weak Force

In the SM, the weak force is mediated by the massive W and Z bosons. It is not experienced in daily life, which is a tribute to its very short range that further more a priori requires a quantum mechanical treatment. According to its coupling strength, the weak force is of the same order of magnitude as the electromagnetic force. Its eponymous weakness traces back to the fact that the mediating particles carry a non-vanishing mass, more than 80 times larger than the mass of the hydrogen atom(!) and quite large when compared the scale of elementary particles. This leads to a strong damping at large distances and thus to observable effects that can only be understood in the paradigm of quantum mechanics. The weak and electromagnetic forces are another example of two forces, though apparently independent on first sight, that could be described in a unified electroweak theory, this time on the quantum level. One can see this entanglement already from the fact that the mediating particles of the weak force, the  $W^+$  and  $W^-$  boson, carry electric charge, so that they themselves are subject to the electromagnetic force.

The weak force has the remarkable peculiarity that the *W* bosons only couple to left-handed fermions (and right-handed anti-fermions), thus distinguishing between different helicity states of matter. In the realm of high energy physics this fact has

Fig. 1.1 Cross section of inclusive charged current  $e^{-}p$  ( $e^{+}p$ ) scattering as a function of the polarization of the electron (positron), as measured by the H1 experiment at the hadron electron collider, HERA, in Hamburg [11]. The exchanged gauge boson  $W^-$  ( $W^+$ ) in these reactions only couples to left-handed electrons (right-handed positrons). For the opposite polarization the extrapolation of the cross section matches zero in both cases



been most intuitively shown by a measurement at the hadron electron collider HERA in Hamburg, as shown in Fig. 1.1 [11]. On the y-axis of this figure the inclusive cross section for the  $e^-p \to \nu X$  ( $e^+p \to \bar{\nu} X$ ) process at HERA is shown as a function of the polarization of the corresponding lepton. The measured cross section is compared with a simple linear extrapolation and a more accurate prediction of the SM. The plot shows how the coupling of the  $W^-$  ( $W^+$ ) to a right- (left-)handed  $e^{-}$  ( $e^{+}$ ) goes to zero. As a consequence the weak force is the only force, that we know so far, that is not covariant under the discrete parity operation P, where the space vector  $\mathbf{x}$  is turned into  $-\mathbf{x}$ . This transformation is equivalent to a change from a left-handed into a right-handed coordinate system. It means that the way we describe the weak force is sensitive to the choice of the coordinate system. This phenomenon has first been discovered by the Chinese-American physicist Chien-Shiung Wu [12] and Richard L. Garwin and collaborators [13]. For many years, particle physicists believed that the combination of P with another discrete symmetry operation, the charge conjugation, C, where a particle is replaced by its anti-particle would lead to a good symmetry, also for the weak force. Since the W bosons couple to left-handed particles and to right-handed anti-particles this sounds like a reasonable assumption. It turns out that not even the combination of P and C, CP is a conserved symmetry operation for the weak force. This is a non-trivial and subtle finding in particle physics, with dramatic consequences on cosmological scales: if the CP operation was not violated, all matter in our universe, which we believe has been produced as matter and anti-matter to equal parts, would have annihilated and vanished seconds after its creation and our universe would be an empty and void place. This connection to cosmological scales turns out to be even more puzzling: it is known today that the amount of CP violation that has been

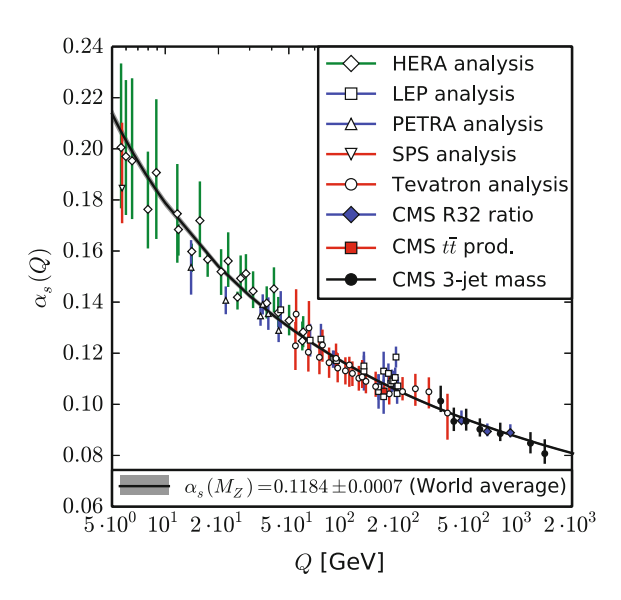
4 1 Introduction

observed in elementary particle reactions is not sufficient to explain the amount of matter in the universe. So there must be additional sources of *CP* violation that are not yet described in the SM.

### The Strong Force

In the SM, the strong force is mediated by eight gluons. It is perhaps the least intuitive force to us, with a range of not more than a few femtometers (fm), corresponding to the size of a proton. It couples to color charge, which is a strictly non-observable internal degree of freedom of quarks and gluons. The strong force has two particularly striking features: when probed at short distances between the interacting particles the strength of the strong coupling,  $\alpha_s$ , decreases, leading to a phenomenon called asymptotic freedom [14, 15]. This name refers to the fact that in the asymptotic limit, where the distance between the interacting particles goes to zero, strongly interacting particles can be considered as quasi free. This behavior has been confirmed by the measurements of many experiments, both past and present, which have probed  $\alpha_s$ at a range of different energy scales, which are related to different distances via the uncertainty relation of Werner Heisenberg. The measurements at the highest energy scales so far have been made by the CMS experiment [16]. A recent compilation of several measurements of  $\alpha_s$ , at different scales, Q, is shown in Fig. 1.2. On the other hand when going to smaller energy scales (corresponding to larger distances) the potential of the strong force increases linearly [17], resulting in the creation of new color neutral particles out of the quantum vacuum, if the energy stored in the potential field exceeds the threshold for their creation. This phenomenon is referred to as *confinement*. It guarantees the non-observability of the color charge.

Fig. 1.2 The coupling constant of the strong force  $\alpha_s$ , measured by different experiments and at different energy scales, Q [16]. According to the uncertainty relation of Werner Heisenberg larger energy scales correspond to smaller distances from the strongly interacting source that can be probed. The measurements demonstrate how the strong force gets weaker and weaker the closer the probe is made to the source of the force, a phenomenon referred to as asymptotic freedom in the literature



### Gravitation

Gravitation is the only force which can not yet be described in a consistent way together with all other interactions. In a quantum field theory, gravitation is mediated by the graviton, which is the only force mediating particle with spin 2. Gravitation is the most intuitive force to us from our daily life experience. It is however the most difficult to get hold of in the framework of a quantum field theory. At the same time it is by many orders of magnitude the weakest of all known forces, rendering it irrelevant to all processes which are within the experimental reach of particle physics nowadays and in the foreseeable future. As an illustration the strength of gravitation is an incredible 36(!) orders of magnitude weaker than the electromagnetic force. What gives its importance on macroscopic and especially cosmological scales is the fact that gravitation, which seems to couple to the (heavy) mass of matter, unlike the electromagnetic force, is always attractive and not shielded, in contrast to any of the other known forces. Since mass will be a major topic of this book it should be noted that the heavy mass that the graviton couples to does not necessarily have to be the same as the mass of inertia, that usually is placed as a parameter into equations of motion, be it in classical or quantum mechanical descriptions. Within the framework of a quantum field theory gravitation is described by the coupling to the graviton, as discussed above, while the mass of inertia can be described by the coupling to the Higgs boson field,  $\phi$ , with a non-vanishing vacuum expectation value, v, as will be discussed during the course of this book. Both masses have a relation to the macroscopic world, since any particle (irrespective of being a fundamental or composed object) will gain mass according to the  $\gamma$  factor of special relativity, depending on the frame of reference it is described in. Finally, there is the famous relation between energy and mass by Albert Einstein,  $E = mc^2$ , which gives another view on the subject of mass. Taking the example of a proton at the Large Hadron Collider (*LHC*) more than 99 % of its mass are made up of its binding energy. It is thus carried by gluons, which are in fact massless particles in the sense of inertia. In that sense the mass of the proton is fundamentally very different from the mass of the electron.

### The Power of Gauge Symmetries

All fundamental forces together lead to a rich and non-trivial phenomenology with a large variety of unique observations. The strength of the SM is to be capable of describing the whole plethora of these observations, not only qualitatively, but quantitatively and with outstanding precision (as will be discussed in Chap. 3). These phenomena range from lowest energies of a few electronvolt (eV)<sup>1</sup> up to energy scales of a few hundred giga-electronvolt (GeV), thus spanning 11 orders of magnitude. The SM obtains this predictive power by the application of *gauge symmetries*, which are a major ingredient in describing the structure of the interactions outlined above. The structure of the strong interaction results from an  $SU(3)_C$  symmetry in the

<sup>&</sup>lt;sup>1</sup>An electronvolt corresponds to the energy that an electron gains after traversing the difference of an electric potential of 1 V.

6 1 Introduction

color space, whose basis is often discussed in terms of red, green and blue. The structure of the electroweak force can be obtained from an  $SU(2)_L$  symmetry in the space of weak isospin (often discussed in terms of up- and down-type flavors) and a  $U(1)_Y$  symmetry, related to the electric charge. The application of gauge symmetries allows for the derivation of all predictions of the SM following the classical Lagrange formalism and the commutator relations of field quantization. The symmetries of the SM are the external  $Poincar\acute{e}$  symmetry of the space-time coordinates (implying Lorentz covariance, energy, momentum and angular momentum conservation) and the internal local gauge symmetries of  $SU(3)_C \times SU(2)_L \times U(1)_Y$ , leading to the observed structure of gauge interactions. Of these internal symmetries the  $SU(3)_C$  symmetry and the  $U(1)_Y$  symmetry are exact. But nature seems to distinguish the  $SU(2)_L$  symmetry, which as the only symmetry within the SM leads to a problem with massive particles.

### 1.2 The Problem of Massive Particles in the Standard Model

As will be discussed in detail in Chap. 2, local gauge symmetries naturally lead to the presence of *gauge bosons*, the exchange particles discussed in Sect. 1.1, in the theory. The symmetry strictly requires these gauge bosons to be massless, which is unproblematic for photons and gluons, but in drastic contrast to the known masses of  $m_Z = 91.1876 \pm 0.0021\,\text{GeV}$  for the Z and  $m_W = 80.385 \pm 0.015\,\text{GeV}$  for the W boson [18]. Even worse the maximally parity violating structure of the weak force also breaks local gauge invariance for all massive fermions, due to their coupling to the W boson. This leads to the apparent antagonism that, while the  $SU(2)_L \times U(1)_Y$  gauge symmetry does describe the coupling structure of the electroweak force, at the same time it seems to contradict the fact that the W and Z bosons, and (nearly) all fermions have a non-vanishing mass.

The proposed solution to this problem is the mechanism of *spontaneous symmetry* breaking, where the gauge symmetry is still intrinsic to the Lagrangian density of the theory, but not manifest in its energy ground state, which in the case of discussion is the quantum vacuum. The principle of spontaneous symmetry breaking is well known and can be demonstrated with a very simple classical example of a needle standing upright on its tip on a plane ground as illustrated in Fig. 1.3 (left). This system does obey rotational symmetry around an upright axis in a coordinate system with its origin in the tip of the needle. But it is unstable and will eventually fall into its energy ground state, ending up with the needle lying on the ground of the plane in some specific direction in  $\varphi$ . The equations of motion which describe the system still obey the rotational symmetry, but the ground state does not. The symmetry still implicitly shines through by the fact that the symmetry breaking ground state is degenerate in  $\varphi$ : the needle could have fallen in any direction in  $\varphi$  and there is nothing to distinguish one particular ground-state direction from any other. Furthermore if the coordinate system to describe the physical system were moved away from the tip of the needle the  $\varphi$  symmetry of the system would not be visible from the equations of motion any



Fig. 1.3 (Left) The example of a needle standing upright on its tip on a plane ground. Rotational symmetry is obeyed by the system, but the state, is unstable. In the energetic ground state the needle has fallen into some direction in  $\varphi$ . While the rotational symmetry is still present in the equations of motion it is spontaneously broken in the energy ground state and thus hidden. (Right) The same situation is shown for the electroweak symmetry: a new field  $\phi$  is introduced with a characteristic self-coupling, which leads to an energy potential that is rotationally symmetric in the complex plane of  $\phi$ . The energy ground state in the well of this potential breaks the symmetry. The shown form of the potential is the easiest way to achieve this symmetry breaking. It is often referred to as the Mexican hat potential

more—it would be hidden. In the case of the electroweak  $SU(2)_L \times U(1)_Y$  symmetry this idea has been introduced by *Peter Higgs, François Englert, Robert Brout* and others, independently between the years 1961 and 1964 [19–24]. It is since referred to as the Higgs mechanism. Since all fields, which had been known in the theory by that time are  $SU(2)_L \times U(1)_Y$  symmetric, it had to be realized by a new field,  $\phi$ , with a characteristic self interaction that leads to spontaneous symmetry breaking in the quantum vacuum. An illustration of the potential related to this self coupling is shown in Fig. 1.3 (right).

Thanks to the Higgs mechanism the electroweak gauge symmetry and its predictive power are preserved within the equations of motion. Instead, the energy ground state of the quantum vacuum becomes non-zero. The degeneracy of the energy ground state that has been discussed in the above example of the needle can also be seen in this case. In the four dimensions of the SM potential it introduces three additional degrees of freedom, which can be translated into longitudinal polarization degrees of freedom of the massive gauge bosons. A fourth degree of freedom (in the figure the radial excitation) is left and leads to the postulation of a new particle, the Higgs boson, which should have the quantum numbers of the vacuum. The Higgs boson constitutes a new state: it is neither a fermionic constituent of matter, like leptons and quarks, nor a force mediating particle, like a gauge boson. It is the only elementary particle in the SM with spin 0. The massive vector bosons and fermions acquire their masses via a coupling to the non-vanishing expectation value of the new Higgs field,  $\phi$ , in the quantum vacuum. Gauge invariance is guaranteed by additional non-trivial couplings to the physical Higgs boson field, which are predicted to be proportional to the mass of the fermions and proportional to the mass of the gauge bosons squared. In this formulation the mass of fundamental particles emerges dynamically from the interaction with the Higgs field,  $\phi$ , that is omnipresent in the quantum vacuum.

8 1 Introduction

It should be emphasized, and will be discussed in Chap. 2, that the exact way of the coupling of the fermions to the Higgs field,  $\phi$ , is an independent prediction, conceptually different from the way in which the gauge bosons acquire their mass. Since the Higgs boson, does have a self-coupling, originating from the Higgs potential, and as the characteristic quantity of the coupling is the mass, the Higgs boson itself also has a mass. In the SM, the mass of the Higgs boson is the only still unconstrained (or very weakly constrained) parameter, while all other parameters have been determined or significantly constrained by experiment.

The discovery of a Higgs boson-like particle at the *LHC* on 4 July 2012 [25–27], almost 50 years after this postulation, formed an epoch in the history of particle physics, which finally led to awarding the Nobel Prize in physics to *Peter Higgs* and François Englert in 2013. The new particle had been discovered independently with the two large multipurpose detectors ATLAS [28] and CMS [29], combining five main decay channels (into photons, Z bosons, W bosons,  $\tau$ -leptons and b-quarks) relevant for the low mass Higgs boson search program of the LHC. For each of the experiments the discovery was based on a dataset corresponding to less than half of the data collected by the end of the data taking period at center-of-mass energies of 7 and 8 TeV. In the meantime, it has been confirmed on the complete dataset of the LHC data taking period of the years 2011 and 2012 (also referred to as LHC run-1 data taking period in the following), and more information has been revealed about the mass, spin, CP properties and coupling structure of the new particle. These results have been provided by the collaborations of the two experiments on a very short time scale after the discovery. Their albeit non-compromised high scientific quality stands for a tremendous effort that has been made by both collaborations.

### 1.3 Synopsis and Guideline to the Book

In this book, the findings of the Higgs boson discovery, that has been made based on the data of the *LHC* run-1 data taking period, will be summarized and put into the context of the general understanding of electroweak symmetry breaking. In its discussion the book will be restricted to the electroweak sector of the SM. By its structure it is meant to serve three purposes: (i) it should be a text book for undergraduate students and people not yet familiar with the subject, to learn the essentials of electroweak symmetry breaking and Higgs boson physics, to be able to understand the main questions that had been raised and addressed during the discovery phase; (ii) it should be a compact and comprehensive reference for people who would like to look up one or the other detail of the topics that have been of concern during this time and therefore would like to concentrate on individual chapters or sections of the book; (iii) it should be a compendium for experts in the field, who should be able quickly to catch the essential information (in form of tables, figures and references) out of one single document.

The book will be opened with a summary of the electroweak sector of the SM in Chap. 2, in which the complete electroweak part of the Lagrangian density of the

SM will be unrolled on the level of gauge field theories. This approach requires hardly any prior knowledge of the concepts of quantum field theories and still allows to understand many of the main features of the SM. It is meant to motivate the introduction of gauge interactions via local gauge symmetries and will address the peculiarity in the choice of nature to have the  $W^-$  boson coupling only to lefthanded fermions, as well as the issues of local gauge symmetries with massive vector bosons and fermions. A strong emphasis will be put on the conceptional solution of the ostensible antagonism, that local gauge symmetries can describe the nature of electroweak interactions to an incredible precision, while the presence of massive vector bosons explicitly breaks these symmetries. As discussed above the solution to this problem is the phenomenon of spontaneous symmetry breaking, which will be discussed in detail. The main questions to be addressed in this chapter are: what is the role of symmetries in the SM? What is the role of mass? What makes a particle a Higgs boson? This chapter will largely rely on a lecture for undergraduate students by Prof. Dieter Gromes that I had the pleasure to attend as a student at the University of Heidelberg and from which I profited throughout my complete professional career up to these days. The section on custodial symmetry in the SM relies on a very compact set of lecture notes by Prof. Scott Willenbrock [30], which I took the freedom to adapt to the nomenclature used throughout this chapter, to comment and to simplify in a few cases to make it more digestible also for the unfamiliar reader. The text is aimed at being complete and with a minimal amount of loopholes or unexplained assumptions that the unfamiliar reader would have to accept. It contains detailed step by step calculations to improve clarity and to strip off any magic from the theoretical conclusions, following the philosophy of a great book by Prof. Peter Schmüser [31]. It is recommended for readers, who are new to the subject to do the exercise and to go through this chapter with a few blank sheets of paper and a pen to follow one or the other calculation. As usual, also here the rule holds: most effective learning is achieved by doing the calculations yourself at least once.

The first section of Chap. 3 is dedicated to a brief review of the constraints that could already be set on the mass of the Higgs boson by the pure requirement of the SM to be consistent (up to a given energy scale), without any further experimental input. These boundaries always have to be understood to be tied to the assumption of the SM being applicable and perturbative up to a given energy scale. Not finding a Higgs boson within the boundaries given by these theory constraints would only have indicated the non-applicability of the SM from a given energy scale on. This is true for the more fundamental unitarity bounds as well as for the boundaries due to the behavior of the SM at the level of higher-order contributions to the treelevel predictions. This section has been inspired by a review given by Dr. Abdelakh Djouadi [32] last updated in 2008. Especially after the discovery, which turned such estimates to some extent academic, it is not meant to reflect the state of the art of such kinds of constraints, which anyhow inherently rely on several assumptions and approximations. It is rather meant to give a feeling of the principles on which these constraints have been built upon. The chapter is then continued with a discussion of the first indirect constraints within the theory that could be derived from electroweak

10 1 Introduction

precision measurements at the Large Electron Positron Collider (*LEP*). These global parameter estimates still today stand out as one of the most remarkable tests of the SM. They allowed precise predications about the mass of the *top* quark and, with less precision, about the mass of the Higgs boson, before these particles had been discovered. Finding indeed both particles in the predicted mass ranges stated a great success of these parameter estimates. The chapter is then concluded by the direct searches for the SM Higgs boson at *LEP* [33–37] and at the *Tevatron* proton antiproton collider [38–40], which had been conducted before the advent of the *LHC*. While not successful, as we know, especially the direct searches at *LEP* laid out all statistical groundwork and tools that have been used (with some small modifications) up to today. The searches for the SM Higgs boson at *LEP* are therefore used to introduce most of the statistical concepts, with the concrete physics case at hand.

In the first section of Chap. 4 finally the last round of the hunt for the SM Higgs boson at the LHC is heralded. A few technical details on the accelerator and the experiments are given, the dramatic start up time and the path along the first measurements of known SM processes, like the production of Z bosons, W bosons, single top quarks and top quark pairs  $(t\bar{t})$  are outlined, each of which set a milestone in the understanding of the machine and the theory. The level of understanding of all these processes on the *LHC* run-1 dataset is remarkable. I think it is fair to say that this was unexpected and exceeded all hopes that people had by the time the LHC started operation. The section is then continued with a review of the state of the art of the theoretical inputs specific to the search for the SM Higgs boson, like cross sections and branching fractions in all relevant production modes and decay channels. To keep a good level of overview, numbers are mostly given for 8 TeV center-of-mass energy, corresponding to the most relevant dataset, which represents 80% of the collected data. The section concludes with a snapshot of the understanding in the search for the SM Higgs boson, shortly before the discovery announcement at the 4 July in 2012. The discovery is discussed in more detail in the following section of the chapter. I will give a small discussion of the event of the discovery itself, but refrain from a detailed description of the analyses that had been used to make the discovery. Instead I will give a detailed and comprehensive description of the individual final and published analyses that have contributed not only to the discovery but also to the further understanding of the observed new particle on the full LHC run-1 dataset along the whole period of data analyses from mid 2012 till the end of 2014. The final and best possible alignment and calibration of each of the sub-detectors of the large LHC experiments have been exploited for these final publications, all analyses that had contributed to the discovery had been completely revised and increased in complexity to maximize their expected sensitivity, and other analyses in more decay channels or inclusive production modes had been added to increase our understanding of the discovered particle. Where appropriate, a short note will be added in the discussion of the analyses which had already been part of the discovery to give an idea of the simplifications and shortcuts that had been made by that time.

There will be a natural split in the discussion of the individual analyses by bosonic and fermionic decay channels, which is given by history. While the discovery of the new particle was driven by the searches in the bosonic decay channels, the searches

in the fermionic decay channels had their second triumph with the report of the evidence that the observed particle indeed couples to fermions, between 2013 and 2014. This finding was a major ingredient and the main justification to call the new particle a Higgs boson as will be discussed throughout this and the following chapter. The reason why the analyses in the fermionic decay channels took a longer timespan to be conclusive, compared to the analyses in the bosonic decay channels traces back to the fact that the SM Higgs boson is much more difficult to dig out from the overwhelming number of events from other processes of the SM, which contaminate these decay channels, as will be discussed in more detail in the corresponding sections. Since I have much better insights and personal experience from my daily work within the Higgs physics working groups of the CMS collaboration, the discussion of the analyses and physics conclusions is restricted to this experiment. It should be mentioned that the ATLAS experiment being complementary to CMS in many aspects arrived at similar and compatible results. The complementarity of the two experiments will be discussed in more detail in this chapter. Where publicly available the results of the ATLAS collaboration will also be given and compared to the results as obtained by the CMS collaboration.

In Chap. 5 the analyses of the properties of the observed particle are discussed. This discussion includes the best possible determination of the mass, crosschecks on the decay width and its compatibility with being the SM Higgs boson. These will be followed by an analysis of the spin and CP properties and the coupling structure as derived from the combination of the analyzed data in all decay channels and production modes that have been discussed in Chap. 4. The results of these studies conclude into what we know about the observed particle today, based on the LHC run-1 dataset. They give a great example of how the expectations of an experiment can be outperformed by clever and extensive analysis methods, once high quality data become available. The discussions in this chapter explain the history of wording used in the community, talking of the discovery of a new particle at the beginning, the discovery of a new boson shortly after and the discovery of a Higgs boson in the end. All that we have learned about the Higgs boson based on the LHC run-1 dataset clearly supports the SM as a theory of particle physics. The experimental confirmation of the centerpiece of a theory to come 50 years(!) after its postulation is an unprecedented triumph. But the results of the LHC run-1 data taking period also have left a large amount of homework and points where we can improve with more data. We will do this again to challenge the SM in a sector, that has just became accessible to experimental verifications, while it remains one of the most exciting and least understood of the theory: the sector of electroweak symmetry breaking. Here the data that have been analyzed give great hope that future experiments, data taking periods and accelerators will give rise to even more fundamental findings and a much deeper understanding of the world of smallest structures. I will conclude the book with an outlook along these lines.

12 1 Introduction

### References

- 1. S. Glashow, Partial symmetries of weak interactions. Nucl. Phys. 22, 579-588 (1961)
- 2. S. Weinberg, A model of leptons. Phys. Rev. Lett. 19, 1264–1266 (1967)
- 3. A. Salam, Weak and electromagnetic interactions. Conf. Proc. C680519, 367–377 (1968)
- 4. W. Pauli, The connection between spin and statistics. Phys. Rev. 58, 716–722 (1940)
- 5. Y. Golfand, E. Likhtman, Extension of the algebra of Poincare group generators and violation of P invariance. JETP Lett. **13**, 323–326 (1971)
- J. Wess, B. Zumino, Supergauge transformations in four-dimensions. Nucl. Phys. B 70, 39–50 (1974)
- 7. P. Fayet, Supergauge invariant extension of the Higgs mechanism and a model for the electron and its neutrino. Nucl. Phys. B **90**, 104–124 (1975)
- 8. P. Fayet, Spontaneously broken supersymmetric theories of weak, electromagnetic and strong interactions. Phys. Lett. B **69**, 489 (1977)
- 9. L. Landau, E.M. Lifschitz, Klassische Feldtheorie (Akademie Verlag GmbH, Berlin, 1992)
- J. Maxwell, A dynamical theory of the electromagnetic field. R. Soc. Trans. 155, 459–512 (1865)
- 11. H1 Collaboration, Inclusive deep inelastic scattering at high  $Q^2$  with Longitudinally polarised lepton beams at HERA. JHEP 1209, 061 (2012). arXiv:1206.7007
- 12. C.S. Wu, E. Ambler, R.W. Hayward et al., Experimental test of parity conservation in beta decay. Phys. Rev. **105**, 1413–1415 (1957)
- R.L. Garwin, L.M. Lederman, M. Weinrich, Observations of the failure of conservation of parity and charge conjugation in meson decays: the magnetic moment of the free muon. Phys. Rev. 105, 1415–1417 (1957)
- D.J. Gross, F. Wilczek, Ultraviolet behavior of non-abelian gauge theories. Phys. Rev. Lett. 30, 1343–1346 (1973)
- D.J. Gross, Twenty five years of asymptotic freedom. Nucl. Phys. Proc. Suppl. 74, 426–446 (1999)
- 16. CMS Collaboration, Measurement of the ratio of the inclusive 3-jet cross section to the inclusive 2-jet cross section in pp collisions at  $\sqrt{s} = 7$  TeV and first determination of the strong coupling constant in the TeV range. Eur. Phys. J. C 73, 2604 (2013). arXiv:1304.7498
- H. Rothe, Lattice Gauge Theories, Lecture Notes in Physics (World Scientific, Singapore, 1992)
- Particle Data Group, Review of particle physics, Chin. Phys. C 38, 090001 (2014). doi:10. 1088/1674-1137/38/9/090001
- 19. P.W. Higgs, Broken symmetries, massless particles and gauge fields. Phys. Lett. 12, 132 (1964)
- P.W. Higgs, Broken symmetries and the masses of gauge bosons. Phys. Rev. Lett. 13, 508 (1964)
- P.W. Higgs, Spontaneous symmetry breakdown without massless bosons. Phys. Rev. 145, 1156 (1966)
- F. Englert, R. Brout, Broken symmetry and the mass of gauge vector mesons. Phys. Rev. Lett. 13, 321 (1964)
- G.S. Guralnik, C.R. Hagen, T.W.B. Kibble, Global conservation laws and massless particles. Phys. Rev. Lett. 13, 585 (1964)
- 24. T.W.B. Kibble, Symmetry breaking in non-abelian gauge theories. Phys. Rev. 155, 1554 (1967)
- ATLAS Collaboration, Observation of a new particle in the search for the standard model Higgs boson with the ATLAS detector at the LHC, Phys. Lett. B 716 1–29 (2012). arXiv:1207.7214
- 26. CMS Collaboration, Observation of a new boson with mass near 125 GeV in pp collisions at  $\sqrt{s} = 7$  and 8 TeV. JHEP **06**, 081 (2013). arXiv:1303.4571
- 27. CMS Collaboration, Observation of a new boson at a mass of 125 GeV with the CMS experiment at the LHC. Phys. Lett. B **716**, 30–61 (2012). arXiv:1207.7235
- ATLAS Collaboration, The ATLAS experiment at the CERN large Hadron Collider, JINST 3, S08003 (2008)

References 13

- 29. CMS Collaboration, The CMS experiment at the CERN LHC. JINST 3, S08004 (2008)
- 30. S. Willenbrock, Symmetries of the Standard Model, arXiv:hep-ph/0410370
- 31. P. Schmüser, Feynman-Graphen und Eichtheorien für Experimentalphysiker, vol. 295, Lecture Notes in Physics (Springer, New York, 1988)
- 32. A. Djouadi, The anatomy of electroweak symmetry breaking. I: the Higgs boson in the standard model. Phys. Rep. **457**, 1–216 (2008). arXiv:hep-ph/0503172
- 33. LEP Working Group for Higgs Boson Searches, ALEPH Collaboration, DELPHI Collaboration, L3 Collaboration, OPAL Collaboration, Search for the standard model Higgs boson at LEP, Phys. Lett. B **565**, 61–75 (2003). arXiv:hep-ex/0306033
- 34. ALEPH Collaboration, Final results of the searches for neutral Higgs bosons in  $e^+e^-$  collisions at  $\sqrt{s}$  up to 209 Gev, Phys. Lett. B **526**, 191–205 (2002). arXiv:hep-ex/0201014
- 35. DELPHI Collaboration, Final results from DELPHI on the searches for SM and MSSM neutral Higgs bosons, Eur. Phys. J. C 32, 145–183 (2004). arXiv:hep-ex/0303013
- 36. L3 Collaboration, Standard model Higgs boson with the L3 experiment at LEP, Phys. Lett. B 517, 319–331 (2001). arXiv:hep-ex/0107054
- 37. OPAL Collaboration, Search for the standard model Higgs boson with the OPAL detector at LEP, Eur. Phys. J. C 26, 479–503 (2003). arXiv:hep-ex/0209078
- 38. CDF Collaboration, D0 Collaboration, Higgs boson studies at the Tevatron, Phys. Rev. D **88**(5), 052014 (2013). arXiv:1303.6346
- CDF Collaboration, Combination of searches for the Higgs boson using the full CDF data set, Phys. Rev. D 88(5), 052013 (2013). arXiv:1301.6668
- D0 Collaboration, Combined search for the Higgs boson with the D0 experiment, Phys. Rev. D 88(5), 052011 (2013). arXiv:1303.0823

### Chapter 2

# The Higgs Boson in the Standard Model of Particle Physics

### 2.1 The Principle of Gauge Symmetries

The principle of gauge symmetries can be motivated by the Lagrangian density of the free *Dirac* field, which is covariant under global U(1) gauge transformations of the complex phase of the spinor fields,  $\psi$ :

$$\psi(x) \to \psi'(x) = e^{i\vartheta}\psi(x)$$

$$\overline{\psi}(x) \to \overline{\psi'}(x) = \overline{\psi}(x)e^{-i\vartheta}$$

$$\mathcal{L}'(x) = \overline{\psi'}\left(i\gamma^{\mu}\partial_{\mu} - m\right)\psi'(x) = \overline{\psi}e^{-i\vartheta}\left(i\gamma^{\mu}\partial_{\mu} - m\right)e^{i\vartheta}\psi(x) \qquad (2.1)$$

$$= \overline{\psi}\left(i\gamma^{\mu}\partial_{\mu} - m\right)\psi(x) = \mathcal{L}(x)$$

The U(1) transformation, which only acts on the components of the spinor and not on its arguments is usually called an internal symmetry of the field. The global character of this transformation is imposed by the fact that the phase  $\vartheta$  does not depend on  $\mathbf{x}$  or t. The free choice of  $\vartheta$ , which is inherent to the equations of motion of the Dirac field still requires the phase to be the same at any point in space-time. Extending this global symmetry to a local symmetry, where  $\vartheta$  is allowed to be different in any coordinate in space-time ( $\vartheta \to \vartheta(x)$ ) appears natural, but breaks the covariance of the equation, due to the derivative that appears in the Dirac equation:

$$\psi(x) \to \psi'(x) = e^{i\vartheta(x)}\psi(x) 
\overline{\psi}(x) \to \overline{\psi'}(x) = \overline{\psi}(x)e^{-i\vartheta(x)} 
\mathcal{L}'(x) = \overline{\psi'}\left(i\gamma^{\mu}\partial_{\mu} - m\right)\psi'(x) = \overline{\psi}e^{-i\vartheta}\left(i\gamma^{\mu}\partial_{\mu} - m\right)e^{i\vartheta}\psi(x) 
= \overline{\psi}\left(i\gamma^{\mu}\left(\partial_{\mu} + i\partial_{\mu}\theta\right) - m\right)\psi(x) \neq \mathcal{L}(x)$$
(2.2)

The covariance can however be restored and in fact enforced, by replacing the normal partial derivative by the *covariant derivative*  $\partial_{\mu} \rightarrow D_{\mu} = \partial_{\mu} + ieA_{\mu}$ , where an additional degree of freedom is introduced by the gauge field  $A_{\mu}$ , into which the covariance breaking term,  $i\partial_{\mu}\vartheta$ , can be absorbed. From the imposed covariance requirement on the Lagrangian density

$$\psi(x) \to \psi'(x) = e^{i\vartheta(x)}\psi(x)$$

$$\overline{\psi}(x) \to \overline{\psi'}(x) = \overline{\psi}(x)e^{-i\vartheta(x)}$$

$$D_{\mu}\psi \to (D_{\mu}\psi)'(x) = e^{i\vartheta(x)}(D_{\mu}\psi)(x)$$
(2.3)

the transformation behavior of both the covariant derivative,  $D_{\mu}$ , and the gauge field,  $A_{\mu}$ , can be derived:

$$\begin{split} (D_{\mu}\psi)'(x) &= \left(\partial_{\mu} + ieA'_{\mu}\right)e^{i\vartheta(x)}\psi = e^{i\vartheta(x)}\left(\partial_{\mu} + i\partial_{\mu}\vartheta(x) + ieA'_{\mu}\right)\psi \\ &\equiv e^{i\vartheta(x)}(D_{\mu}\psi)(x) = e^{i\vartheta(x)}\left(\partial_{\mu} + ieA_{\mu}\right)\psi \end{split}$$

$$A_{\mu} \to A'_{\mu} = A_{\mu} - \frac{1}{e} \partial_{\mu} \vartheta(x)$$

$$D_{\mu} \to D'_{\mu} = D_{\mu} - i \partial_{\mu} \vartheta(x)$$

$$(2.4)$$

The transformation behavior of the gauge field,  $A_{\mu}$ , is known from electrodynamics. In the physics interpretation  $A_{\mu}$  can be identified with a mediating particle, that introduces an interaction between fermions with a coupling constant e. It mediates the information of change in phase of the Dirac spinors between two different points  $x_{\mu}$  and  $x'_{\mu}$  in the four dimensional space-time, and thus obtains a geometrical interpretation. With the picture of electrodynamics in mind,  $A_{\mu}$  can be identified with the photon field.

To obtain a dynamic field the Lagrangian density needs to be completed by a term that describes the dynamic behavior of the gauge field. This term should be gauge and *Lorentz* covariant, which is true for the square of the field strength tensor, defined as  $\mathcal{L}_{kin}$  in:

$$\mathcal{L}_{kin} = -\frac{1}{4} F_{\mu\nu} F^{\mu\nu}; \qquad F_{\mu\nu} = \partial_{\mu} A_{\nu} - \partial_{\nu} A_{\mu} = -\frac{i}{e} \left[ D_{\mu}, D_{\nu} \right]$$
 (2.5)

<sup>&</sup>lt;sup>1</sup>Note that in classical formulations  $D_{\mu}$  is sometimes introduced as  $D_{\mu} = \partial_{\mu} - ieA_{\mu}$ . Here it will be introduced with a "+" sign to keep consistency with the canonical formulation of the SM later on.

The *Lorentz* invariance of  $\mathcal{L}_{kin}$  is obvious from the contraction of the *Lorentz* indices. The gauge invariance is demonstrated below:

$$F_{\mu\nu} o F'_{\mu\nu} = \partial_{\mu}A_{\nu} - rac{1}{e}\partial_{\mu}\partial_{
u}\vartheta - \partial_{
u}A_{\mu} + rac{1}{e}\partial_{
u}\partial_{\mu}\vartheta = \partial_{\mu}A_{
u} - \partial_{
u}A_{\mu} = F_{\mu
u}$$

It should be pointed out that the field strength tensor can be obtained from the commutator,  $[\cdot, \cdot]$ , of the covariant derivative, as shown in Eq. (2.5). It should also be pointed out that  $A_{\mu}$  only appears up to second order in  $\mathcal{L}_{kin}$ . This has the important consequence that for the electric field, that will be derived from  $A_{\mu}$  in the Dirac equation, the fundamental principle of linear superposition is obeyed. The full Lagrangian density of a fermion field with interaction reads as:

$$\mathcal{L}(x) = \overline{\psi} \left( i \gamma^{\mu} D_{\mu} - m \right) \psi(x) - \frac{1}{4} F_{\mu\nu} F^{\mu\nu}$$

$$= \overline{\psi} \left( i \gamma^{\mu} (\partial_{\mu} + i e A_{\mu}) - m \right) \psi(x) - \frac{1}{4} F_{\mu\nu} F^{\mu\nu}$$

$$= \underline{\overline{\psi}} \left( i \gamma^{\mu} \partial_{\mu} - m \right) \psi(x) - \underline{e} \overline{\psi} \gamma^{\mu} \psi A^{\mu} - \underline{\frac{1}{4}} F_{\mu\nu} F^{\mu\nu}$$
free fermion field IA gauge (2.6)

where, after some re-ordering of terms, the first part of the Lagrangian density corresponds to the propagation of the free fermion field, the second term (labeled as "IA") to the interaction with the photon field and the third term (labeled as "gauge") to the propagation of the free photon field. The canonical variation just of the kinetic term,  $\mathcal{L}_{kin}$ , of the gauge field returns the *Lorentz* covariant formulation of the *Maxwell* equations in the absence of matter

$$\mathcal{L}_{kin} = -\frac{1}{4} F_{\mu\nu} F^{\mu\nu} = -\frac{1}{4} (\partial_{\mu} A_{\nu} - \partial_{\nu} A_{\mu}) (\partial^{\mu} A^{\nu} - \partial^{\nu} A^{\mu})$$
varied by the field  $A_{\mu}$  (2.7)

$$\partial_{\mu} \left( \frac{\delta \mathcal{L}_{\text{kin}}}{\delta \partial_{\mu} A_{\nu}} \right) - \frac{\delta \mathcal{L}_{\text{kin}}}{\delta A_{\nu}} = 0$$

$$\partial_{\mu}F^{\mu\nu}=0$$

which in the *Lorenz* gauge ( $\partial_{\mu}A^{\mu}=0$ ) further on leads to the *Klein-Gordon* equation for the propagation of a free and massless boson field:

$$\partial_{\nu}\partial^{\nu}A^{\mu} - \partial^{\nu}\underbrace{\partial_{\mu}A^{\mu}}_{} = 0; \qquad (\partial_{\nu}\partial^{\nu} - 0)A^{\mu} = 0$$

$$\partial_{\mu}A^{\mu} = 0 \qquad (2.8)$$

From the transformation behavior  $A_{\mu} \to A'_{\mu} = A_{\mu} - \frac{1}{e} \partial_{\mu} \vartheta(x)$  it is evident that a mass term for the gauge boson,  $A_{\mu}$ , of type

$$\frac{m}{2}A'_{\mu}A'^{\mu} \equiv \frac{m}{2}A_{\mu}A^{\mu} - \frac{m}{e}A^{\mu}\partial_{\mu}\vartheta(x) + \frac{m}{2e^{2}}\partial_{\mu}\vartheta(x)\partial^{\mu}\vartheta(x) \neq \frac{m}{2}A_{\mu}A^{\mu}$$
 (2.9)

in the Lagrangian density breaks local gauge invariance. This is a manifestation of the deeper truth that in naive gauge theories the gauge fields a priori have to be massless. Note that the mass term for the fermion field,  $\psi$ , of type  $\overline{\psi}m\psi$  in Eq. (2.6) does not break gauge invariance.

### 2.1.1 Extension to Non-Abelian Gauge Symmetries

The above explanations refer to the special case of the U(1) symmetry, corresponding to an *Abelian* symmetry group, for which the ordering of the operators is irrelevant. Any extension of this symmetry group, e.g. to higher dimensions, leads to *non-Abelian* symmetry transformations, for which this is not the case any more. The SU(2) symmetry (which is isomorphic to the well known  $\mathcal{O}(3)$  symmetry group of three dimensional rotations) or the SU(3) symmetry are typical examples in particle physics: the  $SU(3)_C$  color symmetry leads to the formulation of *Quantum Chromo Dynamics* (QCD); the  $SU(2)_L$  flavor symmetry of the electroweak isospin will be discussed in the following sections. A general representation of higher dimensional isospin vectors is

$$\psi = \begin{pmatrix} \psi_1 \\ \vdots \\ \psi_n \end{pmatrix} \qquad n \ge N$$

which in principle can be of any dimension  $n \geq N$  (where N is the dimension of the symmetry group). In the examples given above, the isospin vectors would be  $\psi_q = (q_r \ q_g \ q_b)^\mathsf{T}$  for a quark triplet in the case of the strong color isospin, where the components correspond to the three degrees of freedom representing the color charge of the quark (red, green or blue). It would be  $\psi_\ell = (\nu_\ell \ \ell)^\mathsf{T}$  for a lepton doublet, in the case of the weak isospin, where  $\nu_\ell$  corresponds to a neutrino and  $\ell$  to the corresponding charged lepton field.

To investigate the extension of local gauge symmetries to *non-Abelian* symmetry groups the further discussion will be concentrated on the  $SU(2)_L$ , with a spinor,  $\psi$ , with the components  $\psi_{\alpha}$  and a transformation matrix  $G \in SU(2)_L$ . The matrix G has an adjoint matrix  $G^{\dagger}: GG^{\dagger}=1_2$ , which corresponds to the transposed and complex conjugate. As G is an element of a *Lie* group, it can be expressed by its tangential space, spanned by the  $(N^2-1)=3$  generators  $t_a: G=e^{i\vartheta_a t_a}$ , where

 $\vartheta_a$  are three continuous parameters. A typical irreducible representation of these generators in the minimal dimension, two, are the *Pauli* matrices:

$$t_1 = \frac{\sigma_1}{2} = \frac{1}{2} \cdot \begin{pmatrix} 0 & 1 \\ 1 & 0 \end{pmatrix}; \quad t_2 = \frac{\sigma_2}{2} = \frac{1}{2} \cdot \begin{pmatrix} 0 & -i \\ i & 0 \end{pmatrix}; \quad t_3 = \frac{\sigma_3}{2} = \frac{1}{2} \cdot \begin{pmatrix} 1 & 0 \\ 0 & -1 \end{pmatrix}$$

where the *non-Abelian* character of the transformation group is resembled by the fact, that the generator matrices  $t_a$  are non-commuting. For the SU(2) the commutation relations take the general form:

$$[t_a, t_b] = t_a t_b - t_b t_a = i \epsilon_{abc} t_c \neq 0 \tag{2.10}$$

where the totally anti-symmetric Levi-Civita tensor  $\epsilon_{abc}$  corresponds to the structure constants of the SU(2). For different (e.g. higher dimensional) representations also different matrices could be defined, with the only requirement that these new representations should be irreducible and fulfill the commutation relations of Eq. (2.10). For infinitesimal transformations  $\vartheta \equiv \vartheta_a t_a$ , the matrices G and  $G^\dagger$  can be expressed by

$$G = 1_2 + i\vartheta_a t_a = 1_2 + i\vartheta$$
$$G^{\dagger} = 1_2 - i\vartheta_a t_a = 1_2 - i\vartheta$$

which corresponds to the lowest non-trivial Taylor expansion terms of the exponential function. It should be noted that for non-Abelian formulations from this point on  $\vartheta$  corresponds to a matrix composed as a linear combination of the generators  $t_a$  with continuous parameters  $\vartheta_a$ , while for the Abelian case  $\vartheta$  was just a single continuous parameter. The proper choice has to be derived from the context. In the non-Abelian case the gauge transformations of Eq. (2.1) take the form:

$$\psi(x) \to \psi'(x) = G(x)\psi(x) = e^{i\vartheta_a(x)t_a}\psi(x)$$

$$\overline{\psi}(x) \to \overline{\psi'}(x) = \overline{\psi}(x)G^{\dagger}(x) = \overline{\psi}(x)e^{-i\vartheta_a(x)t_a}$$

$$\mathcal{L}'(x) = \overline{\psi'}\left(i\gamma^{\mu}\partial_{\mu} - m\right)\psi'(x) = \overline{\psi}e^{-i\vartheta_a(x)t_a}\left(i\gamma^{\mu}\partial_{\mu} - m\right)e^{i\vartheta_a(x)t_a}\psi(x) \quad (2.11)$$

$$\equiv \overline{\psi}\left(i\gamma^{\mu}D_{\mu} - m\right)\psi(x) = \mathcal{L}(x)$$

which now contains the transformation matrix G, which itself can depend on the spacial coordinates x via the continuous parameters  $\vartheta_a(x)$ . Note that the spinor,  $\psi$ , now has components  $\alpha$  (taking e.g. the values 0 and 1) and that trivial terms like  $i\gamma^{\mu}$  or m implicitly have to be extended by a unit matrix  $1_2$ . The covariant derivative takes the form  $\partial_{\mu} \rightarrow D_{\mu} = \partial_{\mu} + igt_a A^a_{\mu} = \partial_{\mu} + igt_a A^a_{\mu}$ , where  $A_{\mu} \equiv t_a A^a_{\mu}$  again

<sup>&</sup>lt;sup>2</sup>Note that the book follows the convention to sum over re-appearing identical indices as in the case of the *Einstein* sum convention.

corresponds to a  $2 \times 2$ -matrix, built from a linear combination of the *Pauli* matrices. From the covariance requirement on the Lagrangian density

$$\psi(x) \to \psi'(x) = G(x)\psi(x) = e^{i\vartheta_a(x)t_a}\psi(x)$$

$$\overline{\psi}(x) \to \overline{\psi'}(x) = \overline{\psi}(x)G^{\dagger}(x) = \overline{\psi}(x)e^{-i\vartheta_a(x)t_a}$$

$$D_{\mu}\psi \to (D_{\mu}\psi)'(x) = G(x)(D_{\mu}\psi)(x) = e^{i\vartheta_a(x)t_a}(D_{\mu}\psi)(x)$$
(2.12)

again the modification of the transformation behavior of the covariant derivative,  $D_{\mu}$ , and of the gauge field,  $A_{\mu}$ , can be obtained:

$$(D_{\mu}\psi)'(x) = \left(\partial_{\mu} + igA'_{\mu}\right)\psi'(x) = \left(\partial_{\mu} + igA'_{\mu}\right)G\psi(x)$$

$$= \left(\partial_{\mu}G + G\partial_{\mu} + igA'_{\mu}G\right)\psi(x)$$

$$\equiv G(D_{\mu}\psi)(x) = G\left(\partial_{\mu} + igA_{\mu}\right)\psi(x) = \left(G\partial_{\mu} + igGA_{\mu}\right)$$

Note that on the left-hand side of the " $\equiv$ " sign in the above equation the non-commuting operator G is multiplied from the right, while on the right-hand side of the equation, it is multiplied from the left. The transformation behavior of  $A_{\mu}$  turns out to be:

$$A_{\mu} \to A'_{\mu} = GA_{\mu}G^{\dagger} + \frac{i}{g}(\partial_{\mu}G)G^{\dagger}$$

$$A_{\mu} \to A'_{\mu} = A_{\mu} + i[\vartheta, A_{\mu}] - \frac{1}{g}\partial_{\mu}\vartheta$$
(2.13)

where the second formulation of Eq. (2.13) corresponds to infinitesimal transformations  $\vartheta$  and  $[\cdot, \cdot]$  again to the commutator. Note that the first term  $GA_{\mu}G^{\dagger}$  acts like a coordinate transformation in the SU(2) isospace that mixes the components of  $A_{\mu}$ . This transformation behavior is called *adjoint representation*. The transformation behavior for the covariant derivative  $D_{\mu}$  also follows the *adjoint representation* 

$$D_{\mu} \to D'_{\mu} = GD_{\mu}G^{\dagger}$$

$$D_{\mu} \to D'_{\mu} = D_{\mu} + i[\vartheta, D_{\mu}]$$
(2.14)

where again the second formulation corresponds to infinitesimal transformations. The easiest way to understand this is via the relation  $GG^{\dagger}=1$  as outlined below:

$$(D_{\mu}\psi)' = GD_{\mu}\psi = GD_{\mu}\underbrace{G^{+}G}\psi = \underbrace{GD_{\mu}G^{\dagger}}_{D'_{\mu}}\underbrace{G\psi}_{\psi'} = D'_{\mu}\psi'$$

$$\equiv 1_{2} \qquad \qquad \psi'$$

The last missing piece is to determine how the description of the dynamic part of the gauge field changes. For this purpose the field strength tensor as introduced via the commutator in Eq. (2.5) (right) is used:

$$F_{\mu\nu} = -\frac{i}{g} [D_{\mu}, D_{\nu}] = -\frac{i}{g} [(\partial_{\mu} + igA_{\mu}), (\partial_{\nu} + igA_{\nu})]$$
  
=  $\partial_{\mu} A_{\nu} - \partial_{\nu} A_{\mu} + ig[A_{\mu}, A_{\nu}]$  (2.15)

Compared to the *Abelian* case, the field strength tensor gets an additional term from the commutator of  $A_{\mu}$ . The easiest way to derive its transformation behavior in the *non-Abelian* case again is via the commutator relation:

$$\begin{split} F_{\mu\nu} \rightarrow F'_{\mu\nu} &= -\frac{i}{g} [D'_{\mu}, D'_{\nu}] = -\frac{i}{g} \left( G D_{\mu} G^{\dagger} G D_{\nu} G^{\dagger} - G D_{\nu} G^{\dagger} G D_{\mu} G^{\dagger} \right) \\ &= G \left( -\frac{i}{g} [D_{\mu}, D_{\nu}] \right) G^{\dagger} = G F_{\mu\nu} G^{\dagger} \end{split}$$

The kinetic term in the Lagrangian density is required to be an SU(2) singlet and a *Lorentz* scalar. These requirements can be matched by the *ansatz*:

$$\mathcal{L}_{kin} = \text{Tr}\left(F_{\mu\nu}F^{\mu\nu}\right)$$

$$= \text{Tr}\left(t_a F^a_{\mu\nu} \cdot t_b F^{b\mu\nu}\right) = F^a_{\mu\nu} F^{b\mu\nu} \text{Tr}\left(t_a \cdot t_b\right) = F^a_{\mu\nu} F^{b\mu\nu} \frac{1}{2} \delta_{ab} = \frac{1}{2} F^a_{\mu\nu} F^{a\mu\nu}$$

where Tr is the trace in the SU(2) isospace and the *Lorentz* covariance is explicit from the contraction of the *Lorentz* indices. A test of the transformation behavior in the isospace demonstrates that this *ansatz* is justified:

$$\mathcal{L}'_{\text{kin}} = \text{Tr}\left(F'_{\mu\nu}F'^{\mu\nu}\right) = \text{Tr}\left(GF_{\mu\nu}G^{\dagger}GF^{\mu\nu}G^{\dagger}\right) = \text{Tr}\left(GF_{\mu\nu}F^{\mu\nu}G^{\dagger}\right)$$
$$= \text{Tr}\left(F_{\mu\nu}F^{\mu\nu}\right) = \mathcal{L}_{\text{kin}}$$

At the end of this section, the equations of motion for the *non-Abelian SU*(2) shall be given. The Lagrangian density reads as:

$$\mathcal{L}(x) = \overline{\psi} \left( i \gamma^{\mu} D_{\mu} - m \right) \psi(x) - \frac{1}{2} \text{Tr} \left( F^{\mu\nu} F_{\mu\nu} \right)$$

$$= \overline{\psi} \left( i \gamma^{\mu} (\partial_{\mu} + i g A_{\mu}) - m \right) \psi(x) - \frac{1}{2} \text{Tr} \left( F^{\mu\nu} F_{\mu\nu} \right)$$

$$= \overline{\psi}_{\alpha} \left( i \gamma^{\mu} (\partial_{\mu} + i g t_{a} A_{\mu}^{a}) - m \right) \psi_{\alpha}(x) - \frac{1}{4} F_{\mu\nu}^{a} F^{a\mu\nu}$$
(2.16)

where in the last term the individual components have been spelled out explicitly. Like in the *Abelian* case the gauge fields are massless. Mass terms of type  $\frac{m^2}{2}A_{\mu}A^{\mu}$  would break the gauge invariance for the same arguments as given for Eq. (2.9). The variation of  $\mathcal{L}(x)$  by  $\psi$  (resp.  $\overline{\psi}$ ) reveals the equations of motion for fermions:

$$(i\gamma^{\mu}\partial_{\mu} - m)\psi_{\alpha} = g\gamma^{\mu}t_{a}A^{a}_{\mu}\psi_{\alpha}$$

Note that this is a system of two correlated equations for  $\alpha=0,\ 1$ , the spinors  $\psi_\alpha$  are objects with the minimal dimension 4 and corresponding behavior under *Lorentz* transformations and the  $t_a$  are  $2\times 2$  matrices in the corresponding SU(2) isospace, which turns these equations of motion into a rather complex system of equations. The variation by  $A^a_\mu$  reveals the equations of motion for the gauge bosons, which are again given for the gauge fields in absence of fermion fields to allow easy comparison with the *Abelian* example given in Eq. (2.7):

$$\partial_{\nu}F_{a}^{\mu\nu} = -g\epsilon_{abc}A_{b}^{\mu}t_{c}$$

Here the term,  $-g\epsilon_{abc}A^{\mu}_bt_c$  on the right-hand side of the equation introduces the self-coupling of the gauge bosons with the same coupling strength, g, as to the fermions. The fact that g is the same as for the coupling to fermions requires that the coupling to the fermions is universal, which is often referred to as lepton universality. In the SU(2) there are three such equations corresponding to the three generators  $t_a$ , (a=1,2,3) and the associated gauge bosons. They are coupled via the structure constants of the SU(2). Due to the self-coupling the gauge bosons never are freely propagating fields in contrast to the *Abelian* case.

**Table 2.1** Comparison of the most important characteristics of a (left) *Abelian* and (right) *non-Abelian* gauge theory: (first line) the transformation behavior of the (spinor) field, (second line) the covariant derivative, the transformation behavior of the (third line) covariant derivative and (fourth line) gauge field, (fifth line) the transformation behavior of the field strength tensor and (last line) the Lagrangian density

Main Characteristics of Gauge Field Theories		
Abelian	Non-abelian	
$\psi(x) \to \psi'(x) = e^{i\vartheta(x)}\psi(x)$	$\psi(x) \to \psi'(x) = e^{i\vartheta_a(x)t_a}\psi(x)$	
	$=G(x)\psi(x)$	
$\partial_{\mu} \to D_{\mu} = \left(\partial_{\mu} + ieA_{\mu}\right)$	$\partial_{\mu} \to D_{\mu} = \left(\partial_{\mu} + i g t_a A^a_{\mu}\right)$	
	$=\left(\partial_{\mu}+igA_{\mu} ight)$	
$D_{\mu} \to D'_{\mu} = D_{\mu} - i\partial_{\mu}\vartheta(x)$	$D_{\mu} \to D'_{\mu} = D_{\mu} + i[\vartheta, D_{\mu}]$	
	$=GD_{\mu}G^{\dagger}$	
$A_{\mu} \rightarrow A'_{\mu} = A_{\mu} - \frac{1}{e} \partial_{\mu} \vartheta$	$A_{\mu} \rightarrow A'_{\mu} = A_{\mu} + i[\vartheta, A_{\mu}] - \frac{1}{g}\partial_{\mu}\vartheta$	
	$=GA_{\mu}G^{\dagger}+rac{i}{g}(\partial_{\mu}G)G^{\dagger}$	
$F_{\mu\nu} \equiv -\frac{i}{e}[D_{\mu}, D_{\nu}] = \partial_{\mu}A_{\nu} - \partial_{\nu}A_{\mu}$	$F_{\mu\nu} \equiv -\frac{i}{g}[D_{\mu}, D_{\nu}] = \partial_{\mu}A_{\nu} - \partial_{\nu}A_{\mu} + ig[A_{\mu}, A_{\nu}]$	
$F_{\mu\nu}  o F'_{\mu\nu} = F_{\mu\nu}$	$F_{\mu\nu} \to F'_{\mu\nu} = F_{\mu\nu} + i[\vartheta, F_{\mu\nu}]$	
	$=GF_{\mu\nu}G^{\dagger}$	
$\mathcal{L} = \overline{\psi} \left( i \gamma^{\mu} D_{\mu} - m \right) \psi - \frac{1}{4} F_{\mu\nu} F^{\mu\nu}$	$\mathcal{L} = \overline{\psi} \left( i \gamma^{\mu} D_{\mu} - m \right) \psi - \frac{1}{4} F^{a}_{\mu\nu} F^{a\mu\nu}$	
	$= \overline{\psi} \left( i \gamma^{\mu} D_{\mu} - m \right) \psi - \frac{1}{2} \operatorname{Tr} \left( F_{\mu\nu} F^{\mu\nu} \right)$	

Note that the *Abelian* transformation behavior can be obtained from the transformation behavior of the *non-Abelian* case, by requiring that the commutators for the gauge fields is 0. This can be trivially seen for  $A_{\mu}$  and  $F_{\mu\nu}$ . The only non-obvious case of the covariant derivative,  $D_{\mu}$ , is briefly explained in the text

A summary of the most important characteristics of the *Abelian* and *non-Abelian* gauge theories, side by side, is given in Table 2.1. Note that the transformation behavior of the *Abelian* case can be obtained from the *non-Abelian* transformations by the requirement that the commutators for the gauge fields are 0, which can be trivially seen for  $A_{\mu}$  and  $F_{\mu\nu}$ . The only non-obvious check of consistency is the transformation behavior of the covariant derivative,  $D_{\mu}$  for which care has to be taken, when applying the commutator as an operator. The calculation is demonstrated below:

$$\begin{split} D'_{\mu} &= D_{\mu} + i \left( \vartheta D_{\mu} - D_{\mu} \vartheta \right) \\ &= D_{\mu} + i \left( \vartheta \left( \partial_{\mu} + i g A_{\mu} \right) - \left( \partial_{\mu} + i g A_{\mu} \right) \vartheta \right) \\ &= D_{\mu} + \underbrace{i \left( \vartheta \left( \partial_{\mu} + i g A_{\mu} \right) - \vartheta \left( \partial_{\mu} + i g A_{\mu} \right) \right)}_{\equiv 0} - i \partial_{\mu} \vartheta \\ &= D_{\mu} - i \partial_{\mu} \vartheta \end{split}$$

### 2.2 The Electroweak Gauge Theory

In 1914, James Chadwick established that the energy spectrum of the radioactive  $\beta$  decay is not discrete as in the case of  $\alpha$  radiation but continuous [1]. It took another 16 years for Wolfgang Pauli to postulate the existence of the neutrino,  $\nu$ , as another product of the  $\beta$  decay besides to the lepton, which could explain this continuous energy spectrum [2]. The first theory of the weak interactions was formulated by Enrico Fermi in 1933 [3]. In this theory the interaction was described by a four fermion coupling of type

$$\mathcal{H}_{\mathrm{IA}} = G \int d^3x \left( \bar{p}(x) \gamma^{\mu} n(x) \right) \left( \bar{e}(x) \gamma^{\mu} \nu(x) \right) + h.c.$$

where  $\mathcal{H}_{IA}$  corresponds to the *Hamiltonian* function,  $\bar{p}(x)$  to the proton, n(x) to the neutron,  $\bar{e}(x)$  to the electron and  $\nu(x)$  to the neutrino spinor. It followed suit the structure of *quantum electrodynamics*, with a key modification after the discovery that the weak interaction violates parity. Until today the weak interaction is the only interaction that we know of with this peculiar behavior. In 1958 *Richard Feynman* and *Murray Gell-Mann* introduced a model of the weak interaction, in which parity was maximally violated:

$$\mathcal{H}_{IA} = \int d^3x \frac{G}{\sqrt{2}} \left( \bar{p} \gamma^{\mu} (1 - \gamma^5) n \right) \left( \bar{e} \gamma^{\mu} (1 - \gamma^5) \nu \right) \tag{2.17}$$

It takes into account that on the elementary particle level only the left-handed part of particles and the right-handed part of anti-particles take part in the (flavor changing) charged current weak interaction. The special matrix operator  $\gamma^5$  is defined as  $\gamma^5 \equiv i \gamma^0 \gamma^1 \gamma^2 \gamma^3$  and has the following characteristics:

$$\{\gamma^5, \gamma^{\mu}\} = 0$$
  $(\gamma^5)^2 = 1_4$   $(\gamma^5)^{\dagger} = \gamma^5$ 

where  $\{\cdot, \cdot\}$  is the anti-commutator. The second term  $(\gamma^5)^2 = 1_4$  becomes obvious when written out in matrix notation (in the *Dirac* representation):

$$\gamma^5 = \begin{pmatrix} 0 & 1_2 \\ 1_2 & 0 \end{pmatrix}$$

where the elements in this notation correspond to blocks of  $2 \times 2$  sub-matrices. Applied to a spinor with four components  $\gamma^5$  swaps the first two elements with the last two elements. When applied twice the spinor will retain its original form. The terms  $\frac{1}{2}(1\pm\gamma^5)$  are projection operators which project general states on to their right-handed (+) and left-handed (-) components. They have the properties

$$\left(\frac{1}{2}\left(1 \pm \gamma^{5}\right)\right)^{2} = \frac{1}{2}\left(1 \pm \gamma^{5}\right)$$

$$\frac{1}{2}(1 + \gamma^{5}) \cdot \frac{1}{2}(1 - \gamma^{5}) = 0$$
(2.18)

where the first term in Eq. (2.18) is the defining characteristic for a projection operator and the second term indicates, that the two operators are orthogonal to each other. The fact that a single factor  $\frac{1}{2}(1-\gamma^5)$  in the Lagrangian density is sufficient to project out the left-handed state for both the electron and of the neutrino field is demonstrated below:

$$\bar{e}\gamma^{\mu} \left(\frac{1-\gamma^{5}}{2}\right) \nu = \bar{e}\gamma^{\mu} \left(\frac{1-\gamma^{5}}{2}\right)^{2} \nu = \bar{e}\left(\frac{1+\gamma^{5}}{2}\right) \gamma^{\mu} \left(\frac{1-\gamma^{5}}{2}\right) \nu$$
$$= \overline{\left(\left(\frac{1-\gamma^{5}}{2}\right)e\right)} \gamma^{\mu} \left(\frac{1-\gamma^{5}}{2}\right) \nu = \bar{e}_{L}\gamma^{\mu} \nu_{L}$$

The transformation

$$\chi: \quad \psi \to \gamma^5 \psi \quad ; \quad \overline{\psi} \to (\gamma^5 \psi)^{\dagger} \gamma^0 = \psi^{\dagger} \gamma^5 \gamma^0 = -\overline{\psi} \gamma^5$$
(2.19)

is called *chiral* transformation. The projections on to the left- and right-handed states are *eigenstates* of the chiral transformation with the *eigenvalues*  $\mp 1$ :

$$\psi_L \to \gamma^5 \psi_L = -\psi_L$$
  
$$\psi_R \to \gamma^5 \psi_R = +\psi_R$$
 (2.20)

Note that the terms of  $\mathcal{H}_{IA}$  in Eq.(2.17) and terms of type  $\overline{\psi}\gamma^{\mu}\partial_{\mu}\psi$  are invariant under chiral transformations, while terms of type  $\overline{\psi}m\psi$  are not, since they lead to a sign flip. In this picture the introduction of mass terms for fermions would break the chiral symmetry of  $\mathcal{H}$ .

### 2.2.1 Extension to a Theory of Electroweak Interactions

In 1961 Sheldon Lee Glashow managed to develop a gauge field theory that was capable of describing weak and electromagnetic interactions in a unified approach [4]. In this section, this will be explained in detail only for the first generation of leptonic interactions with an electron and a neutrino field, for simplicity reasons. Also for simplicity reasons, this introduction is given in the unitary gauge, in which unphysical degrees of freedom in the theory do not explicitly appear any more and all remaining fields can be identified with physical degrees of freedom. Since the theory does not depend on the choice of the gauge, this choice can be made without restriction. There will be one paragraph in the following sections where the choice of the gauge will play an important role in the argumentation and two examples that will sketch the basic idea of special gauge choices. These appearances will be stated explicitly.

To construct a gauge field theory additional global symmetries have to be introduced into the Lagrangian density, for which then local gauge invariance will be enforced. This is achieved by extending the internal number of degrees of freedom in the Lagrangian density to some higher dimensional space, which, in this case, will be of dimension two. This space is usually called the space of *weak isospin*. Since only left-handed leptons take part in the weak interaction, all fermion fields will be decomposed into their left- and right-handed components. Only the left-handed part of the fields will take part in the (flavor changing) charged current weak interaction. To achieve this only the left-handed leptons will be combined into a doublet in the space of weak isospin.

$$\psi_L = \begin{pmatrix} \nu_L \\ e_L \end{pmatrix} \qquad \psi_R = e_R \tag{2.21}$$

This doublet acts like a spin  $^{1}/_{2}$  object in this hyperspace. The only difference between  $\nu_{L}$  and  $e_{L}$  in the sense of the interaction will be the third component of the weak isospin doublet  $I_{3}$ . The right-handed component of the electron is defined as an isospin singlet  $\psi_{R}=e_{R}$ , with trivial transformation behavior under SU(2) transformations. Since non-trivial SU(2) transformations only act upon the left-handed components of the particles, the symmetry will obtain an index L. The neutrino is still assumed to be massless and to consist only of a left-handed component for simplicity reasons. The actual electron and neutrino fields are linear combinations of the left- and right-handed components:

$$\nu = \nu_L 
e = e_L + e_R$$

The decomposition of a simple Lagrangian density without interaction terms and without mass terms into a left- and right-handed component takes the form

$$\begin{split} \mathcal{L}_{0} &= i\bar{e}\gamma^{\mu}\partial_{\mu}e + i\bar{\nu}\gamma^{\mu}\partial_{\mu}\nu = \\ &= i\bar{e}_{L}\gamma^{\mu}\partial_{\mu}e_{L} + \underline{i\bar{e}_{L}\gamma^{\mu}}\partial_{\mu}e_{R} + \underline{i\bar{e}_{R}\gamma^{\mu}}\partial_{\mu}e_{L} + i\bar{e}_{R}\gamma^{\mu}\partial_{\mu}e_{R} + i\bar{\nu}_{L}\gamma^{\mu}\partial_{\mu}\nu_{L} = \\ &\equiv 0 \qquad \equiv 0 \\ &= i\bar{e}_{L}\gamma^{\mu}\partial_{\mu}e_{L} + i\bar{e}_{R}\gamma^{\mu}\partial_{\mu}e_{R} + i\bar{\nu}\gamma^{\mu}\partial_{\mu}\nu \end{split}$$

where the mixed left- and right-handed terms are 0, since these components are orthogonal to each other. This is explicitly demonstrated in the following equation:

$$i\bar{e}_L\gamma^\mu\partial_\mu e_R=i\bar{e}\Bigg(\frac{1+\gamma^5}{2}\Bigg)\gamma^\mu\partial_\mu\Bigg(\frac{1+\gamma^5}{2}\Bigg)e=i\bar{e}\Bigg(\frac{1+\gamma^5}{2}\Bigg)\Bigg(\frac{1-\gamma^5}{2}\Bigg)\gamma^\mu\partial_\mu e=0$$

Thus the Lagrangian density can be written in a more compact form as

$$\mathcal{L}_{0} = \underbrace{\overline{\psi}_{L} \gamma^{\mu} \partial_{\mu} \psi_{L}}_{\text{doublet}} + \underbrace{\bar{e}_{R} \gamma^{\mu} \partial_{\mu} e_{R}}_{\text{singlet}}$$

where the first term corresponds to the isospin doublet term, as defined in Eq. (2.21) and the second term corresponds to the isospin singlet term. From the isospin doublet term the flavor changing interaction will be derived. The isospin singlet term for the right-handed part of the electron will not take part in this interaction.  $\mathcal{L}_0$  is invariant under global  $SU(2)_L$  gauge transformations of the type:

$$\psi_L \to \psi_L' = G\psi_L \qquad G \in SU(2)_L$$
  
$$\psi_R \to \psi_R' = \psi_R$$

which have been discussed in Sect. 2.1. These transformations correspond to rotations in the weak isospace, with  $(n^2-1)=3$  generators. Under these transformations  $\psi_L$  transforms like a vector while  $\psi_R$  transforms like a scalar. Following the rules as outlined in Sect. 2.1 leads to the introduction of the following covariant derivative and gauge fields:

$$\partial_{\mu} \rightarrow D_{\mu} = \partial_{\mu} + igt_{a}W_{\mu}^{a} = \partial_{\mu} + igW_{\mu} \qquad a = 1, 2, 3$$

$$W_{\mu} \rightarrow W_{\mu}' = W_{\mu} + i[\vartheta, W_{\mu}] - \frac{1}{g}\partial_{\mu}\vartheta \qquad (2.22)$$

$$= GW_{\mu}G^{\dagger} + \frac{i}{g}(\partial_{\mu}G)G^{\dagger}$$

where the second line indicates the transformation behavior of the gauge fields. Note that the gauge field  $W_{\mu}$  is a linear combination of the three components  $W_{\mu}^{a}$ , which

correspond to the generators  $t^a = \frac{\sigma^a}{2}$ . The field strength tensor is also introduced in analogy to Sect. 2.1:

$$W_{\mu\nu} = \frac{i}{g} [D_{\mu}, D_{\nu}] = \partial_{\mu} W_{\nu} - \partial_{\nu} W_{\mu} + ig[W_{\mu}, W_{\nu}]$$

$$W_{\mu\nu}^{a} = \partial_{\mu} W_{\nu}^{a} - \partial_{\nu} W_{\mu}^{a} - g \epsilon^{abc} W_{\mu}^{b}, W_{\nu}^{c}$$
(2.23)

where the second expression corresponds to the component-wise formulation, for which Eq. (2.10) has been used. This leads to a canonical definition of the Lagrangian density as

$$\mathcal{L}^{SU(2)L} = i\overline{\psi}_{L}\gamma^{\mu}D_{\mu}\psi_{L} + i\bar{e}_{R}\gamma^{\mu}\partial_{\mu}e - \frac{1}{2}\operatorname{Tr}\left(W_{\mu\nu}W^{\mu\nu}\right)$$

$$= i\left(\bar{\nu}_{L}\ \bar{e}_{L}\right)\gamma^{\mu}\left(\partial_{\mu} + igt^{a}W_{\mu}^{a}\right)\begin{pmatrix}\nu_{L}\\e_{L}\end{pmatrix} + \bar{e}_{R}\gamma^{\mu}\partial_{\mu}e_{R}$$

$$-\frac{1}{4}\left[\left(\partial_{\mu}W_{\nu}^{a} - \partial_{\nu}W_{\mu}^{a} - g\epsilon^{abc}W_{\mu}^{b}W_{\nu}^{c}\right)\right]$$

$$\cdot\left(\partial^{\mu}W^{\nu a} - \partial^{\nu}W^{\mu a} - g\epsilon^{ade}W^{\mu d}W^{\nu e}\right)\right] \tag{2.24}$$

where the last part of Eq. (2.24) corresponds to the component-wise notation of the compact form, given in the first part of the equation. Since the operators

$$t_{+} = \frac{\sigma_{1} + i\sigma_{2}}{2} = \begin{pmatrix} 0 & 1 \\ 0 & 0 \end{pmatrix} \rightarrow t_{+} \begin{pmatrix} 0 \\ 1 \end{pmatrix} = \begin{pmatrix} 1 \\ 0 \end{pmatrix}$$

$$t_{-} = \frac{\sigma_{1} - i\sigma_{2}}{2} = \begin{pmatrix} 0 & 0 \\ 1 & 0 \end{pmatrix} \rightarrow t_{-} \begin{pmatrix} 1 \\ 0 \end{pmatrix} = \begin{pmatrix} 0 \\ 1 \end{pmatrix} \qquad (2.25)$$

act like the well known ascending and descending operators from quantum mechanics the three gauge fields  $W^a_\mu$  can be rewritten as

$$\begin{split} W_{\mu}^{+} &= \frac{1}{\sqrt{2}} \left( W_{\mu}^{1} - i W_{\mu}^{2} \right) \\ W_{\mu}^{-} &= \frac{1}{\sqrt{2}} \left( W_{\mu}^{1} + i W_{\mu}^{2} \right) \\ W_{\mu}^{a} t^{a} &= \frac{1}{\sqrt{2}} \left( W_{\mu}^{+} t^{+} + W_{\mu}^{-} t^{-} \right) + W_{\mu}^{3} t^{3} \end{split}$$

which leads to the following interacting term of the  $SU(2)_L$  Lagrangian density for left-handed leptons:

$$\begin{split} \mathcal{L}_{\mathrm{IA}}^{SU(2)L} &= i\overline{\psi}_L\gamma^{\mu}D_{\mu}\psi_L = i\overline{\psi}_L\gamma^{\mu}\left(\partial_{\mu} + igt^aW_{\mu}^a\right)\psi_L \\ &= i\overline{\psi}_L\gamma^{\mu}\partial_{\mu}\psi_L - g\overline{\psi}_L\gamma^{\mu}\left[\frac{1}{\sqrt{2}}\left(t^+W_{\mu}^+ + t^-W_{\mu}^-\right) + t^3W_{\mu}^3\right]\psi_L \end{split}$$

$$=\underbrace{i\overline{\psi}_{L}\gamma^{\mu}\partial_{\mu}\psi_{L}}_{\text{KIN}} - \frac{g}{2} \left[ \underbrace{\sqrt{2}\bar{\nu}\left(W_{\mu}^{+}\gamma^{\mu}\right)e_{L}}_{e \rightarrow \nu} + \underbrace{\sqrt{2}\bar{e}_{L}\left(W_{\mu}^{-}\gamma^{\mu}\right)\nu}_{\nu \rightarrow e} + \underbrace{W_{\mu}^{3}\left(\bar{\nu}\gamma^{\mu}\nu - \bar{e}_{L}\gamma^{\mu}e_{L}\right)}_{\text{NC}^{*}} \right]$$

where for the last term the mixing of components due to the *Pauli* matrices has been carried out explicitly. The first term in the equation (labeled by "KIN") corresponds to the kinematic term of the freely propagating leptons (in compact notation), the second term (" $e \rightarrow \nu$ ") to an interaction vertex that leads to the destruction of an electron and the creation of a neutrino, the third term (" $\nu \rightarrow e$ ") to an interaction vertex that leads to the destruction of a neutrino and the creation of an electron. These terms can now be identified with the observed *charged current* reactions. On the other hand the last term ("NC\*") does not yet correspond to the observed electroweak neutral current reaction, as it only couples to the left-handed part of the electron. This means that the electromagnetic interaction is not properly included in this  $SU(2)_L$  Lagrangian density. To achieve this the global U(1) symmetry, which is also inherent to the Lagrangian density, is exploited and the principle of local gauge invariance is extended to a  $SU(2)_L \times U(1)_Y$ <sup>3</sup> symmetry. This implies that in addition to the local  $SU(2)_L$  symmetry, the Lagrangian density should also be invariant under local  $U(1)_Y$  phase transformations. In contrast to the  $SU(2)_L$  transformations, the  $U(1)_Y$  transformations act on both the left-handed component,  $\psi_L$ , and the righthanded component,  $\psi_R$ , of the fields. For the left-handed component, it acts on the doublet as a whole. This additional symmetry requirement leads to one more generator for the  $U(1)_Y$  symmetry group that, in turn, will lead to the introduction of another gauge field

$$B_{\mu}$$
 gauge field 
$$D'_{\mu} \equiv \partial_{\mu} + i g' \frac{Y}{2} B_{\mu}$$
 covariant derivative 
$$B_{\mu\nu} \equiv \partial_{\mu} B_{\nu} - \partial_{\nu} B_{\mu}$$
 field strength tensor

Since the  $U(1)_Y$  symmetry is imposed on the isospin doublet as a whole, it is not independent from the  $SU(2)_L$  symmetry and the gauge fields  $W_\mu$  and  $B_\mu$  will be entangled. This will become more obvious by an explicit entanglement of the coupling constant, g, of the  $SU(2)_L$  with g' later. The constant Y is the hypercharge of the  $SU(2)_L$  singlet or the  $SU(2)_L$  doublet as a whole, which can be different for each object in the isospace, expressing the additional freedom in the *Abelian* over the *non-Abelian* gauge theory, where g is fixed to be the same for all objects in the isospace by the gauge boson self-couplings. In the further discussion the hypercharge is defined such that the electric charge g of each corresponding component of the

 $<sup>^{3}</sup>$ The additional index Y is tribute to the hypercharge Y in the covariant derivative.

isospin singlet or doublet is related to the hypercharge by the *Gell-Mann-Nishijiama* relation:

$$g'$$
 coupling constant  $Y$  hypercharge  $q = I_3 + \frac{Y}{2}$  electric charge

Note the clear distinction between the coupling constant and the charge of an object in this case, which is more obvious here as in *quantum electrodynamics*. The proper choice of  $Y_L = -1$  (left-handed) and  $Y_R = -2$  (right-handed) for the leptons, leads to the electric charges as observed experimentally. An overview of the values for the hypercharge and third component of the weak isospin,  $I_3$ , for the complete first flavor generation of fermions is given in Table 2.2. This peculiar choice of hypercharges is related to the unitary gauge and has been made such that the quantum mechanical charge operator reveals the charges of the elementary particles, like the electron or the proton, as observed by experiment. It is not in contradiction to the principle of gauge invariance that such a choice has to be made. Within the theory, it is only important that a gauge can be found, in which such a choice is possible. In this formulation, the  $SU(2)_L \times U(1)_Y$  Lagrangian density thus takes the form

$$\mathcal{L}^{SU(2)_L \times U(1)_Y} = i \overline{\psi}_L \gamma^\mu \left( \partial_\mu + i g' \frac{Y_L}{2} B_\mu + i g t^a W_\mu^a \right) \psi_L + i \overline{\psi}_R \gamma^\mu \left( \partial_\mu + i g' \frac{Y_R}{2} B_\mu \right) \psi_R$$

$$- \frac{1}{2} \text{Tr} \left( W_{\mu\nu}^a W^{a\mu\nu} \right) - \frac{1}{4} B_{\mu\nu} B^{\mu\nu}$$

$$(2.26)$$

**Table 2.2** Summary of the hypercharge  $(Y_{L/R})$ , third isospin component  $(I_3)$  and electric charge (q) of the particles in the first fermion generation of weak isospin, as obtained from the *Gell-Mann-Nishiyama* relation  $q = I_3 + 1/2 Y$ 

Particle	$SU(2)_L \times U(1)_Y$ Hypercharges					
	Left-handed		Right-handed			
	$Y_L$	$I_3$	$Y_R$	q		
ν	-1	+1/2	_	0		
e		-1/2	-2	-1		
и	-1/3	+1/2	-2/3	+1/3		
d		-1/2	-4/3	-2/3		

with the neutral current component

$$\mathcal{L}^{NC} = -\underbrace{\frac{g}{2}W_{\mu}^{3}\left(\bar{\nu}\gamma_{\mu}\nu - \bar{e}_{L}\gamma_{\mu}e_{L}\right)}_{\text{weak IA}} - \underbrace{\frac{g'}{2}B_{\mu}\left[Y_{L}\left(\bar{\nu}\gamma_{\mu}\nu - \bar{e}_{L}\gamma_{\mu}e_{L}\right) + Y_{R}\bar{e}_{R}\gamma_{\mu}e_{R}\right]}_{\text{em IA}}$$

$$= \underbrace{\left(-\frac{g}{2}W_{\mu}^{3} + \frac{g'}{2}B_{\mu}\right)\!\left(\bar{\nu}\gamma_{\mu}\nu\right) + \left(\frac{g}{2}W_{\mu}^{3} + \frac{g'}{2}B_{\mu}\right)\!\left(\bar{e}_{L}\gamma_{\mu}e_{L}\right) + g'B_{\mu}\left(\bar{e}_{R}\gamma_{\mu}e_{R}\right)}_{\propto Z_{\mu}}$$

As the first term in the last part of this equation has to be proportional to the  $Z_{\mu}$  field, it follows that the gauge fields  $W_{\mu}^3$  and  $B_{\mu}$  do not correspond to the physical Z boson and photon fields. But it can be achieved to construct the physical fields from the original gauge fields from a rotation by the angle  $\theta_W$ , which is referred to as the weak mixing angle angle:

$$\sin \theta_W = \frac{g'}{\sqrt{g^2 + g'^2}} \qquad \cos \theta_W = \frac{g}{\sqrt{g^2 + g'^2}} \qquad \tan \theta_W = \frac{g'}{g}$$

$$Z_\mu = \frac{1}{\sqrt{g^2 + g'^2}} \left( gW_\mu^3 - g'B_\mu \right) = \cos \theta_W W_\mu^3 - \sin \theta_W B_\mu \qquad (2.27)$$

$$A_\mu = \frac{1}{\sqrt{g^2 + g'^2}} \left( gW_\mu^3 + g'B_\mu \right) = \sin \theta_W W_\mu^3 + \cos \theta_W B_\mu$$

After some arithmetic, this term leads to the *neutral current* part of the Lagrangian density in its final form

$$\begin{split} \mathcal{L}^{NC} &= -\frac{\sqrt{g^2 + g'^2}}{2} Z_{\mu} \left( \bar{\nu} \gamma_{\mu} \nu \right) \\ &+ \frac{\sqrt{g^2 + g'^2}}{2} \left[ \left( \cos^2 \theta_W - \sin^2 \theta_W \right) Z_{\mu} + 2 \sin \theta_W \cos \theta_W A_{\mu} \right] \left( \bar{e}_L \gamma_{\mu} e_L \right) \\ &+ \frac{\sqrt{g^2 + g'^2}}{2} \left[ \qquad \qquad -2 \sin^2 \theta_W \ Z_{\mu} + 2 \sin \theta_W \cos \theta_W A_{\mu} \right] \left( \bar{e}_R \gamma_{\mu} e_R \right) \end{split}$$

As can be seen from Eq. (2.28), only the  $Z_{\mu}$  couples to the neutrino. Furthermore the photon has the same coupling to the left- and right-handed part of the electron, which resembles the fact that the photon does not distinguish between left- and right-handed states. This is not the case for the  $Z_{\mu}$  boson. The factor

$$q = \sqrt{g^2 + g'^2} \sin \theta_W \cos \theta_W = \frac{g \cdot g'}{\sqrt{g^2 + g'^2}}$$

can be identified by the electric charge q. Expressed by q and  $\theta_W$  the Lagrangian density takes the form:

$$\begin{split} \mathcal{L}^{SU(2)_L \times U(1)_Y} &= \mathcal{L}^{\text{kin}} + \mathcal{L}^{CC} + \mathcal{L}^{NC} + \mathcal{L}^{\text{gauge}} \\ \\ \mathcal{L}^{\text{kin}} &= i \bar{e} \gamma^\mu \partial_\mu e + i \bar{\nu} \gamma^\mu \partial_\mu \nu \\ \\ \mathcal{L}^{CC} &= -\frac{q}{\sqrt{2} \sin \theta_W} \left[ W_\mu^+ \bar{\nu} \gamma_\mu e_L + W_\mu^- \bar{e}_L \gamma_\mu \nu \right] \\ \\ \mathcal{L}^{NC} &= -\frac{q}{2 \sin \theta_W \cos \theta_W} Z_\mu \left[ \left( \bar{\nu} \gamma_\mu \nu \right) + \left( \bar{e}_L \gamma_\mu e_L \right) \right] - q \left[ A_\mu + \tan \theta_W Z_\mu \right] \left( \bar{e} \gamma_\mu e \right) \end{split}$$

$$\mathcal{L}^{\text{gauge}} = -\left. \frac{1}{2} \text{Tr} \left( W^a_{\mu\nu} W^{a\mu\nu} \right) - \frac{1}{4} B_{\mu\nu} B^{\mu\nu} \right| \begin{array}{c} B_\mu \to A_\mu \\ W^3_\mu \to Z_\mu \end{array}$$

This Lagrangian density describes the full structure of the electroweak interaction: the kinematic terms for the leptons ( $\mathcal{L}^{\rm kin}$ ), the charged current ( $\mathcal{L}^{CC}$ ), the weak and electromagnetic components of the neutral current ( $\mathcal{L}^{NC}$ ) and the kinematic terms of the gauge fields  $W^a_\mu$  and  $A_\mu$  ( $\mathcal{L}^{\rm gauge}$ ). The fact the  $SU(2)_L$  is a *non-Abelian* gauge field theory leads to a characteristic self-coupling of the weak gauge bosons. The rotation by the electroweak mixing angle implies that all types of self couplings will at the same time apply for Z bosons and photons.

The theory thus makes a prediction for the structure of the electroweak interaction, which by construction, is maximally parity violating in the leptonic interaction vertex. The obvious weakness of this theory is that mass terms of the form

$$\overline{\psi} m \psi$$

for the gauge bosons, but also for the weakly interacting leptons are explicitly not gauge invariant. For gauge bosons this has been shown in Eq. (2.9). For the lepton fields this becomes clear from the following calculation

$$\bar{e}m_e e = \overline{(e_R + e_L)} m_e (e_R + e_L) = m_e (\bar{e}_R e_R + \bar{e}_R e_L + \bar{e}_L e_R + \bar{e}_L e_L) 
= m_e (\bar{e}_R e_L + \bar{e}_L e_R)$$
(2.30)

<sup>&</sup>lt;sup>4</sup>The general usage of the variable name "e" for the elementary charge of the electron has been replaced by "q" in this and the following sections to prevent misunderstandings in cases, where "e" is used for other objects, e.g. like the electron spinor.

where  $\bar{e}_R e_R$  and  $\bar{e}_L e_L$  are zero due to the orthogonality property of the projectors. Since  $e_R$  is a  $SU(2)_L$  singlet while  $e_L$  is just a component of the  $SU(2)_L$  doublet  $\psi_L$ , the remaining terms as such do have a non-trivial behavior under  $SU(2)_L$  transformations and are not gauge invariant. This additional complication in the SM only occurs due to the splitting of the fermion fields into a left- and right-handed component. It was therefore obvious since its introduction in 1961 that the  $SU(2)_L \times U(1)_Y$  gauge theory is incomplete and needs to be extended by another theoretical concept, which was suggested to be the concept of *spontaneous symmetry breaking* that will be discussed in detail in the following section.

### 2.3 Electroweak Symmetry Breaking and the Higgs Boson

The expression spontaneous symmetry breaking refers to the situation where a system, described by the Lagrangian density  $\mathcal{L}$ , is invariant under the transformation of a given symmetry group G, while this symmetry is broken by the energy ground state of the system. The simple example of a needle standing upright on its tip has been given in Sect. 1.2: the Lagrangian density of this system is invariant under rotations,  $\varphi$ , around the axis of the needle. But the system is metastable and the needle will fall into an arbitrary direction in  $\varphi$  to end up in the energy ground state. This situation is illustrated in Fig. 1.3 (left). The direction in which the needle will end up lying can not be predicted. All possible angles are degenerate and ignoring frictional energy losses the needle could move around the original axis without further energy costs. This is a general characteristic of the phenomenon. In the context of quantum field theories it is formalized in the Goldstone theorem [5], which states that in a relativistic, covariant quantum field theory, in which symmetries are spontaneously broken, particles with mass zero are created. These particles are called Goldstone bosons. They correspond to the degeneracy of the energy ground state in the simplistic example given in Sect. 1.2.

Goldstone bosons can be elementary particles, which are already part of the Lagrangian density, bound states, which are created within the theory (like the hydrogen atom or *Cooper* pairs) or they can be identified by unphysical excitations or artificial degrees of freedom within the gauge theory, which are usually removed by the choice of a proper gauge.

#### 2.3.1 The Goldstone Model

The *Goldstone* model can be introduced by a field  $\phi$  with a potential  $V(\phi)$  and a Lagrangian density  $\mathcal{L}$  given by

$$\phi = \frac{1}{\sqrt{2}} \left( \phi_1 + i \phi_2 \right)$$

$$V(\phi) = -\mu^2 |\phi|^2 + \lambda |\phi|^4$$
  

$$\mathcal{L}(\phi) = \partial_\mu \phi \partial^\mu \phi^* - V(\phi)$$

 $V(\phi)$  will be referred to as the *Goldstone* potential. For this example an illustration is given in Fig. 1.3 (right). The Lagrangian density  $\mathcal{L}$  is invariant under U(1) transformations  $\phi \to \phi' = e^{i\theta}\phi$ . The energy ground state is where the Hamiltonian

$$\mathcal{H} = \frac{\partial \mathcal{L}}{\partial (\partial_{\mu} \phi)} \partial_{\mu} \phi + \frac{\partial \mathcal{L}}{\partial (\partial^{\mu} \phi^{*})} \partial^{\mu} \phi^{*} - \mathcal{L} = \partial_{\mu} \phi \partial^{\mu} \phi^{*} + V(\phi)$$

is minimal, which is the case for  $|\phi|=\sqrt{\frac{\mu^2}{2\lambda}}$ . This minimum will later on be identified with the non-zero vacuum expectation value

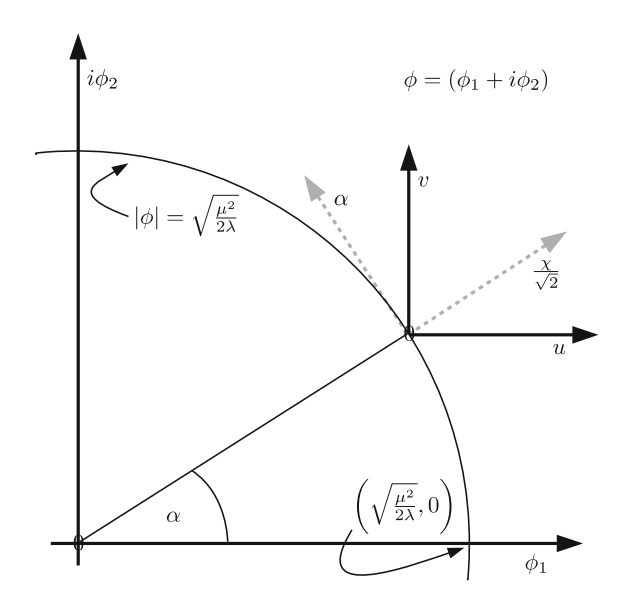
$$v \equiv \sqrt{\frac{\mu^2}{2\lambda}}. (2.31)$$

The ground state is illustrated in Fig. 2.1. An expansion around the ground state in the point  $\left(\sqrt{\frac{\mu^2}{2\lambda}}, 0\right)$  in *Cartesian* coordinates leads to

$$\begin{split} \phi(u,v) &= \sqrt{\frac{\mu^2}{2\lambda}} + \frac{1}{\sqrt{2}} \left( u + iv \right) \\ \mathcal{L} &= \left[ \partial_\mu \phi \partial^\mu \phi^* - V(\phi) \right]_{\phi = \phi(u,v)} = \frac{1}{2} \partial_\mu u \partial^\mu u + \frac{1}{2} \partial_\mu v \partial^\mu v - V'(u,v) \\ V'(u,v) &= \left[ -\mu^2 |\phi|^2 + \lambda |\phi|^4 \right]_{\phi = \phi(u,v)} = -\frac{\mu^4}{4\lambda} + \mu^2 u^2 + \mu \sqrt{\lambda} u \left( u^2 + v^2 \right) \\ &+ \frac{\lambda}{4} \left( u^2 + v^2 \right)^2 \end{split}$$

Note that the  $\varphi$  symmetry around the origin of the potential is not visible any more in this expansion. At the same time a complex structure of terms containing v and u has emerged. The term  $\mu^2 u^2$  formally corresponds to a mass term for the field u, which can be identified with an excitation of the field in the confining direction that leads horizontally out of the minimum, in which V'(u,v) has been developed. The field v, which does not lead out of the minimum of V'(u,v), does not acquire a mass term. This field corresponds to the *Goldstone* boson. Other terms lead to tri-linear and quartic self-couplings of the fields u and v. There are no terms which are linear in u and v. This is obvious from the fact that the field  $\phi$  has been developed in the minimum of the Hamiltonian function, for which the *Taylor* expansion starts with a first non-trivial term in second order. This argument holds for any potential.

Fig. 2.1 Up-view onto the *Goldstone* potential  $V(\phi) = -\mu^2 |\phi|^2 + \lambda |\phi|^4$  as discussed in Sect. 2.3 and illustrated in Fig. 1.3. Both a *Cartesian* and the cylindrical coordinate system as discussed in the text are indicated in the figure. For the examples given in the text the potential is developed in the minimum at  $(\sqrt{\frac{\mu^2}{2\lambda}}, 0)$ 



The symmetry of the system is better represented by cylindrical coordinates, in which the Lagrangian density  $\mathcal{L}$  takes the form

$$\begin{split} \phi(\chi,\alpha) &= e^{i\alpha} \left( \sqrt{\frac{\mu^2}{2\lambda}} + \frac{\chi}{\sqrt{2}} \right) \\ \mathcal{L} &= \left[ \partial_\mu \phi \partial^\mu \phi^* - V(\phi) \right]_{\phi = \phi(\chi,\alpha)} = \frac{1}{2} \partial_\mu \chi \partial^\mu \chi + \left( \sqrt{\frac{\mu^2}{2\lambda}} + \frac{\chi}{\sqrt{2}} \right)^2 \partial_\mu \alpha \partial^\mu \alpha - V'(\chi) \\ V'(\chi) &= \left[ -\mu^2 |\phi|^2 + \lambda |\phi|^4 \right]_{\phi = \phi(\chi)} = -\frac{\mu^4}{4\lambda} + \mu^2 \chi^2 + \mu \sqrt{\lambda} \chi^3 + \frac{\lambda}{4} \chi^4 \end{split}$$

the expressions for the self-coupling terms are simpler, the mass term is created for the real field  $\chi$ . Even though  $\alpha$  does not appear any more in the potential, it corresponds to the *Goldstone* boson. This is an example, where the *Goldstone* boson corresponds to a gauge degree of freedom, which has been removed by the choice of a proper gauge that inherently respects the symmetry of the problem.

# 2.3.2 Extension to a Gauge Theory

The extension of the *Goldstone* model to a gauge theory starts from the introduction of the covariant derivative as described in Sect. 2.1. For simplicity reasons this is

shown for the simple *Goldstone* model in cylindrical coordinates and an *Abelian* gauge symmetry:

$$\mathcal{L} = \left[ \left( \partial_{\mu} + igA_{\mu} \right) \phi \right] \left[ \left( \partial^{\mu} + igA^{\mu} \right) \phi \right]^{*} - V(\phi) - \frac{1}{4} F_{\mu\nu} F^{\mu\nu}|_{\phi(\chi,\alpha)}$$

$$= \left| \frac{1}{\sqrt{2}} \partial_{\mu} \chi e^{i\alpha} + ie^{i\alpha} \left( \sqrt{\frac{\mu^{2}}{\lambda}} + \frac{\chi}{\sqrt{2}} \right) \left( gA_{\mu} + \partial_{\mu} \alpha \right) \right|^{2} - V'(\chi) - \frac{1}{4} F_{\mu\nu} F^{\mu\nu}$$

$$= \frac{1}{2} \partial_{\mu} \chi \partial^{\mu} \chi + \left( \left( \sqrt{\frac{\mu^{2}}{2\lambda}} + \frac{\chi}{\sqrt{2}} \right) \left( gA_{\mu} + \partial_{\mu} \alpha \right) \right)^{2} - V'(\chi) - \frac{1}{4} F_{\mu\nu} F^{\mu\nu}$$

This leads to a quadratic mass term in the gauge field  $A_{\mu}$ , the term  $\partial_{\mu}\alpha$  can be absorbed into  $A_{\mu}$  in the gauge  $A_{\mu} + \partial_{\mu}\theta$  with  $\theta = -\frac{1}{a}\alpha$ . Via  $V'(\chi)$  the field  $\chi$  obtains a mass, too, as described above and appears as a physical field. In this example  $\chi$  plays the role of the physical Higgs boson field in the SM, that will be introduced later. In addition the model obtains characteristic coupling terms of type  $\sim \chi^2 A_\mu A^\mu$  and  $\sim \chi A_\mu A^\mu$  of the Higgs boson field,  $\chi$ , to the gauge field and characteristic self-coupling terms, which originate from the specific form of the Goldstone potential. The introduction of the Goldstone potential and the expansion of the field  $\phi \to \phi(\chi, \alpha)$  in the energy ground state, that is shifted to a non-zero value, has dynamically generated a mass term  $\frac{g^2\mu^2}{2\lambda}A_\mu A^\mu$  for the gauge field  $A_\mu$  from the coupling  $g^2|\phi|^2A_\mu A^\mu$  between  $A_\mu$  and  $\phi$ . This mass term emerges from the coupling of the gauge boson,  $A_{\mu}$ , to the vacuum expectation value  $v = \sqrt{\frac{\mu^2}{\lambda}}$ . As discussed before such a mass term alone would break the gauge symmetry. But the additional presence of the new Higgs boson field,  $\chi$ , and of tri-linear and quartic couplings of  $A_{\mu}$  to  $\chi$  restore and protect the invariance. This leads to firm predictions of the structure of these couplings. This coupling structure is the characteristic of a Higgs boson which is different from a gauge boson or any other particle in this sense.

The field  $\phi$  was originally complex with two degrees of freedom ( $\phi_1$  and  $\phi_2$ ). In the final form the field  $\chi$  is real with only one degree of freedom, while the field of the Golstone boson  $\alpha$  has been completely removed from the Lagrangian density by the choice of a proper gauge. It seems as if the model had lost one degree of freedom. In fact this is not the case. It reappears as an additional degree of freedom of the gauge field  $A_\mu$ : as a massless particle  $A_\mu$  has only two degrees of freedom, which are usually chosen as transverse polarizations. As a massive particle it gains one more degree of freedom of longitudinal polarization. One says that the gauge field has eaten up the additional degree of freedom of the Goldstone boson  $\alpha$  and has acquired mass on it. This shift of degrees of freedom from the Goldstone boson(s) to the gauge field(s) is referred to as the equivalence theorem [6]. It is a main ingredient of the Higgs mechanism.

There are a few concluding remarks on the special choice of the *Goldstone* potential, which might have appeared arbitrary on first sight:

- The *Goldstone* potential as chosen above leads to a symmetry breaking vacuum expectation value in the theory, which is a prerequisite of the model. It only depends on  $|\phi|$  and does not distinguish any direction in space. Furthermore it does not lead to negative infinite energies, which is another prerequisite for the theory to be stable.
- In the example the potential has been cut at order  $|\phi|^4$ . This can be motivated by a dimensional analysis: in natural units the action  $S = \int Ld^4x \sim \hbar$  is dimensionless, x has the dimension [x] = -1 and the partial derivative has the dimension  $[\partial_{\mu}] = +1$ . This gives the field  $\phi$  the dimension  $[\phi] = +1$ . For these reasons, the coupling constants in the potential obtain the dimension  $[\mu] = 1$  and  $[\lambda] = 0$ . Any coupling of negative dimension would turn the theory non-renormalizable. For this reason, it makes sense to stop the power series of the *Goldstone* potential at the lowest needed dimension.

The incorporation of spontaneous symmetry breaking into a gauge theory was the last missing piece of the *Weinberg-Salam* model of electroweak interactions, which led to its completion to the SM. The electroweak sector of the SM will be summarized in the following section.

# 2.4 The Electroweak Sector of the Standard Model of Particle Physics

The  $SU(2)_L \times U(1)_Y$  gauge model as discussed in Sect. 2.2 provides the accurate description of the weak and electromagnetic interactions. Its biggest shortcoming is that the gauge symmetry strictly requires the gauge bosons to be massless. The fact that the W and the Z boson do have a non-vanishing mass implies that the symmetry is not manifest in nature. The solution to this puzzle is to have an energy ground state of the quantum vacuum, which does not obey the symmetry and thus prevents its direct manifestation. The fact that the Lagrangian density as discussed so far does not lead to such a symmetry breaking energy ground state pointed to the existence of a hidden sector in the theory with a new particle that had not yet been observed by the time of its postulation and whose presence implements the spontaneous breaking of the  $SU(2)_L$  symmetry in the quantum vacuum in one or the other way. This part of the theory is called the Higgs sector. Both the  $SU(2)_L \times U(1)_Y$  gauge symmetry and the Higgs model have been introduced in the preceding sections of this chapter. In the following they will be fit together like a zip lock to result in the complete

theory of the SM as formulated since the late 1960s. This construction starts from Eq. (2.29), which is extended by an additional Lagrangian density term

$$\mathcal{L}^{\text{Higgs}} = \partial_{\mu} \phi^{\dagger} \partial^{\mu} \phi - V(\phi)$$

$$V(\phi) = -\mu^{2} \phi^{\dagger} \phi + \lambda \left( \phi^{\dagger} \phi \right)^{2}$$
(2.32)

with a new field

$$\phi = \begin{pmatrix} \phi_+ \\ \phi_0 \end{pmatrix} \qquad \phi^{\dagger} = \begin{pmatrix} \phi_+^* & \phi_0^* \end{pmatrix} \equiv \begin{pmatrix} \phi_- & \phi_0^* \end{pmatrix} \tag{2.33}$$

which should transform like an  $SU(2)_L$  isospin doublet with the coupling constant g and the hypercharge  $Y_\phi=1$  under  $U(1)_Y$  transformations. For the individual components of the doublet this leads to the electric charges of  $q(\phi_0)=0$  and  $q(\phi_+)=+1$  according to the *Gell-Mann-Nishijiama* relation as discussed earlier in this chapter. As an  $SU(2)_L$  doublet  $\phi$  transforms like

$$\begin{array}{ll} \phi & \rightarrow \phi' & = e^{i\vartheta'}G\phi \\ \phi^\dagger \rightarrow \phi'^\dagger & = \phi^\dagger G^\dagger e^{-i\vartheta'} & G = e^{i\vartheta^a t^a} \in SU(2) & \vartheta^a, \vartheta' \in \mathbb{R} \end{array}$$

(as discussed in Sect. 2.1), where  $\vartheta'$  and  $\vartheta^a$  are continuous parameters. Enforcing local gauge invariance of  $\mathcal{L}^{\text{Higgs}}$  under  $SU(2)_L \times U(1)_Y$  transformations again implies the introduction of a covariant derivative

$$\partial_{\mu} \rightarrow D_{\mu} = \partial_{\mu} + ig' \frac{Y_{\phi}}{2} B_{\mu} + igt^{a} W_{\mu}^{a}$$

as for Eq. (2.26). In the next step,  $\phi$  will be expanded in the vicinity of its energy ground state, in the minimum  $v=\sqrt{\frac{\mu^2}{2\lambda}}$  of the Higgs potential

$$\phi = \begin{pmatrix} 0 \\ \sqrt{\frac{\mu^2}{2\lambda}} + \frac{H}{\sqrt{2}} \end{pmatrix}$$

where the new field H has been introduced. Note that the choice to do the expansion around the non-vanishing vacuum expectation value in the lower component of  $\phi$  and the assignment of  $Y_{\phi}$  is a consequence of the choice of the unitary gauge that has been made at the beginning of this chapter. It does not contradict the fact that according to gauge invariance the expansion could in principle be done in any other point in the minimum of the vacuum. The important feature of the theory is that such a choice, as for the unitary gauge, can be found. Since the SM is a gauge invariant theory any other gauge would lead to the same observable quantities, but the correspondence

with the quantum mechanical operators would be non-trivial. Setting the expanded version of  $\phi$  in the kinetic term of  $\mathcal{L}^{\text{Higgs}}$  leads to

$$D_{\mu}\phi^{\dagger}D^{\mu}\phi = \left[ \left[ \frac{1}{\sqrt{2}}\partial_{\mu}H + \left( \sqrt{\frac{\mu^{2}}{2\lambda}} + \frac{H}{\sqrt{2}} \right) \left( igt^{a}W_{\mu}^{a} + ig'\frac{Y_{\phi}}{2}B_{\mu} \right) \right] \begin{pmatrix} 0\\1 \end{pmatrix} \right]^{2}$$

In the last step of this calculation the product of the unit vector of the isospin with the  $t^a$ , (a = +, -, 3) matrices is evaluated in each component:

$$D_{\mu}\phi^{\dagger}D^{\mu}\phi = \left| \left[ \frac{1}{\sqrt{2}} \partial_{\mu}H - \frac{i}{2} \left( gW_{\mu}^{3} - g'B_{\mu} \right) \left( \sqrt{\frac{\mu^{2}}{2\lambda}} + \frac{H}{\sqrt{2}} \right) \right] {0 \choose 1} \right|^{2} + \left| \left( i\frac{g}{2}W_{\mu}^{+} \left( \sqrt{\frac{\mu^{2}}{2\lambda}} + \frac{H}{\sqrt{2}} \right) \right) {1 \choose 0} \right|^{2}$$

$$(2.34)$$

The following remarks should help to understand Eq. (2.34): (i) the ascending operator  $t^+$ , which belongs to the field  $W_\mu^+$  has shifted the unit vector of the down component up; (ii) the descending operator  $t^-$ , which belongs to the field  $W_\mu^-$  evaluated to the unit vector of the down component is zero; (iii) the operator  $t^3$  evaluated on the unit vector of the down component has flipped the sign of the term associated with  $W_\mu^3$ , according to the structure of the *Pauli* matrix  $\sigma_3$ . Also note that

$$\left(gW_{\mu}^{3} - g'B_{\mu}\right) \equiv \sqrt{g^{2} + g'^{2}}Z_{\mu}$$
 (2.35)

according to the definitions in Eq. (2.27). The evaluation of the absolute value squared finally results in

$$D_{\mu}\phi^{\dagger}D^{\mu}\phi = \frac{1}{2}\partial_{\mu}H\partial^{\mu}H + \frac{g^{2} + g'^{2}}{4}\left(\sqrt{\frac{\mu^{2}}{2\lambda}} + \frac{H}{\sqrt{2}}\right)^{2}Z_{\mu}Z^{\mu} + \frac{g^{2}}{4}\left(\sqrt{\frac{\mu^{2}}{2\lambda}} + \frac{H}{\sqrt{2}}\right)^{2}W_{\mu}^{+}W^{\mu-}$$
(2.36)

thus generating mass terms for the gauge fields  $Z_{\mu}$ ,  $W_{\mu}^{+}$  and  $W_{\mu}^{-}$  from the coupling to the quantum vacuum, v. As in the simplified example of Sect. 2.3, a new physical field, H, emerges as a radial excitation of  $\phi$  in the quantum vacuum. This Higgs field acquires a mass on its own given by the potential  $V(\phi)$ . As discussed before this is independent from the specific form of the *Goldstone* potential. The couplings of the

gauge bosons  $Z_{\mu}$ ,  $W_{\mu}^{+}$  and  $W_{\mu}^{-}$  to H protect the gauge invariance in the theory. The masses of the gauge bosons can be read off from the equations to be

$$\left(\frac{g}{2}\right)^2 v^2 W_{\mu}^+ W^{\mu -} \equiv m_W^2 W_{\mu}^+ W^{\mu -}$$

$$\left(\frac{\sqrt{g^2 + g'^2}}{2}\right)^2 v^2 Z_{\mu} Z^{\mu} \equiv m_Z^2 Z_{\mu} Z^{\mu}$$
(2.37)

which appears like a quartic coupling of the gauge bosons to the non-vanishing quantum vacuum, equivalent to the quartic Higgs coupling. Equation (2.37) illustrates how from an underlying theory, like the SM, effective phenomenological parameters like  $m_W$  and  $m_Z$ , can be further resolved to give deeper insights into the dynamic processes of nature. Equation (2.37) furthermore leads to the relation

$$\rho \equiv \frac{m_W^2}{m_Z^2 \cdot \cos^2 \theta_W} = 1 \tag{2.38}$$

From this relation, an accurate constraint on  $\cos\theta_W$  and a firm prediction of  $m_Z > m_W$  arise. Note for the evaluation of the absolute value of Eq. (2.34) that the second term in the absolute value, which is proportional to  $W_\mu^+$ , is also proportional to the upper unit vector, while the first term is proportional to the lower unit vector. This is why there are no mixed terms between these two parts in the absolute value. The same is true for the kinetic term in the first part of the absolute value, which is purely real, and the second term, which is proportional to  $Z_\mu$  and purely imaginary, which again implies that there are no mixed terms.

It has been discussed in the previous section how in the Higgs mechanism the *Goldstone* bosons are eaten up and commit their degrees of freedom to the gauge bosons, which in turn become massive. Though this has not been shown explicitly this is also the case here: the general complex  $SU(2)_L$  doublet field  $\phi$  has four (scalar) degrees of freedom, of which three get eaten up by the  $W_\mu^+, W_\mu^-$  and  $Z_\mu$  boson. One degree of freedom remains and turns into a real field: the Higgs boson field, H.

The vacuum expectation value v can be obtained from Eq. (2.37) and the relation between the mass of the W boson,  $m_W$ , and the Fermi constant,  $G_F$ , which has been very accurately determined from muon lifetime measurements [7]:

$$\frac{1}{2}gv = m_W = \sqrt{\frac{\sqrt{2}g^2}{8G_F}}$$
 ;  $v = \frac{1}{\sqrt{\sqrt{2}G_F}} = 246.22 \text{ GeV}$ 

The value of v = 246.22 GeV [8] sets the scale of electroweak symmetry breaking. This knowledge allows the replacement of the self-coupling  $\lambda$  in the *Goldstone* potential, leaving only the mass of the Higgs boson  $m_H$  undetermined.

### 2.4.1 Custodial Symmetry

The Lagrangian density of the Higgs boson sector

$$\mathcal{L}^{\text{Higgs}} = (D_{\mu}\phi)^{\dagger} D^{\mu}\phi - V(\phi)$$

$$V(\phi) = -\mu^{2}\phi^{\dagger}\phi + \lambda \left(\phi^{\dagger}\phi\right)^{2}$$

$$D_{\mu}\phi = \left(\partial_{\mu} + ig'\frac{Y_{\phi}}{2}B_{\mu} + igt^{a}W_{\mu}^{a}\right)\phi$$
(2.39)

does not only have a local  $SU(2)_L \times U(1)_Y$  symmetry, which has been introduced by construction, but also an approximate larger global symmetry, which happens to be present by accident. This can be seen if the Higgs doublet field,  $\phi$ , and its charge conjugate

$$\phi_c = 2it_2\phi^* = \begin{pmatrix} \phi_0^* \\ -\phi_- \end{pmatrix} \tag{2.40}$$

are combined into a bi-doublet matrix

$$\Phi = \frac{1}{\sqrt{2}} \left( \phi_c \ \phi \right) = \frac{1}{\sqrt{2}} \left( \begin{array}{c} \phi_0^* \ \phi_+ \\ -\phi_- \ \phi_0 \end{array} \right) \qquad \Phi^{\dagger} = \frac{1}{\sqrt{2}} \left( \begin{array}{c} \phi_0 \ -\phi_+ \\ \phi_- \ \phi_0^* \end{array} \right) \tag{2.41}$$

The definition of  $\phi_c$  is in analogy to the charge conjugation of spinors. It obtains the hypercharge  $Y_{\phi_c} = -Y_{\phi} = -1$ . It is a feasible exercise to show, that  $\phi_c$  has an  $SU(2)_L \times U(1)_Y$  transformation behavior, which is equivalent to  $\phi$ . In the matrix representation  $\phi_c$ , corresponds to the first column and  $\phi$  to the second column of the matrix  $\Phi$ . Note that there is no such correspondence any more for  $\Phi^{\dagger}$ . In this notation Eq. (2.39) can be obtained from

$$\mathcal{L}^{\text{Higgs}} = \text{Tr}\left((D_{\mu}\Phi)^{\dagger}D^{\mu}\Phi\right) - V(\phi)$$

$$V(\phi) = -\mu^{2}\text{Tr}\left(\Phi^{\dagger}\Phi\right) + \lambda\left(\text{Tr}\left(\Phi^{\dagger}\Phi\right)\right)^{2}$$

$$D_{\mu}\Phi = \left(\partial_{\mu}\Phi - \frac{ig'}{2}B_{\mu}\Phi\sigma_{3} + \frac{ig}{2}W_{\mu}^{a}\sigma_{a}\Phi\right)$$

$$\left(D_{\mu}\Phi\right)^{\dagger} = \left(\partial_{\mu}\Phi^{\dagger} + \frac{ig'}{2}B_{\mu}\sigma_{3}\Phi^{\dagger} - \frac{ig}{2}W_{\mu}^{a}\Phi^{\dagger}\sigma_{a}\right)$$

$$(2.42)$$

which can be verified when evaluating the term

$$\operatorname{Tr}\left(\Phi^{\dagger}\Phi\right) = \operatorname{Tr}\left(\frac{1}{2} \begin{pmatrix} \phi_0^*\phi_0 + \phi_+\phi_- & 0\\ 0 & \phi_+\phi_- + \phi_0^*\phi_0 \end{pmatrix}\right)$$

$$= \phi_+\phi_- + \phi_0^*\phi_0 \equiv \phi^{\dagger}\phi$$
(2.43)

There is one subtlety in this notation to be noted: the fact, that  $Y_{\phi_c} = -Y_{\phi}$  has lead to the introduction of a minus sign and the multiplication with  $\sigma_3$  from the right in  $D_{\mu}\Phi$  for the term in the covariant derivative, which is affected by the hypercharge. In this case it is important that  $\sigma_3$  is multiplied from the right. In this notation the transformation behavior of  $SU(2)_L \times U(1)_Y$  of  $\Phi$  is given by

$$SU(2)_L: \quad \Phi \to L\Phi$$
 
$$U(1)_Y: \quad \Phi \to \Phi e^{-\frac{i}{2}\sigma_3\vartheta}$$

where L is equivalent to the transformation matrix G as introduced in Sect. 2.1.1 (the change from G to L in the notation will become clear in the next paragraph) and the *Pauli* matrix  $\sigma_3$  has again been introduced due to the opposite hypercharges of  $\phi$  and  $\phi_c$ . The global  $SU(2)_L$  symmetry of  $\mathcal{L}^{\text{Higgs}}$  in this notation can be trivially verified from

$$\operatorname{Tr}\left(\left(D_{\mu}\Phi\right)^{\dagger}D^{\mu}\Phi\right) \to \operatorname{Tr}\left(\left(D_{\mu}\Phi\right)^{\dagger}\underbrace{L^{\dagger}L}D^{\mu}\Phi\right) = \operatorname{Tr}\left(\left(D_{\mu}\Phi\right)^{\dagger}D^{\mu}\Phi\right)$$

$$\equiv 1$$

$$V(\phi) \qquad \to V(L\phi) = -\mu^{2}\operatorname{Tr}\left(\Phi^{\dagger}\underbrace{L^{\dagger}L}\Phi\right) + \lambda\left(\operatorname{Tr}\left(\Phi^{\dagger}\underbrace{L^{\dagger}L}\Phi\right)\right)^{2} = V(\phi)$$

$$= 1 \qquad = 1$$

which is not much of a surprise, since a global  $SU(2)_L$  is part of the construction of the local  $SU(2)_L$  symmetry. The non trivial additional symmetry enters via the transformation

$$SU(2)_R: \Phi \to \Phi R$$

where the SU(2) transformation matrix is multiplied from the right, corresponding to rotations in a right-handed coordinate system. It is indeed non-trivial to show that  $\mathcal{L}^{\text{Higgs}}$  is also invariant under such global transformations. It has to be done by explicitly checking the relations

$$\operatorname{Tr}\left(\left(D_{\mu}\Phi\right)^{\dagger}D^{\mu}\Phi\right) \to \operatorname{Tr}\left(R^{\dagger}\left(D_{\mu}\Phi\right)^{\dagger}D^{\mu}\Phi R\right) \approx \operatorname{Tr}\left(\left(D_{\mu}\Phi\right)^{\dagger}D^{\mu}\Phi\right)$$

$$V(\phi) \qquad \to V(\phi R) = -\mu^{2}\operatorname{Tr}\left(R^{\dagger}\Phi^{\dagger}\Phi R\right) + \lambda\left(\operatorname{Tr}\left(R^{\dagger}\Phi^{\dagger}\Phi R\right)\right)^{2} = V(\phi)$$

$$(2.44)$$

which will be done in the following paragraphs. It should first be noted that the matrix  $\Phi^{\dagger}\Phi$  will play a special role, which is why it has been written out explicitly in Eq.(2.43). In a first step, the invariance of the term  $\text{Tr}\left(\sigma_a^{\dagger}\Phi^{\dagger}\Phi\sigma_a\right)$  will be discussed, which appears several times in Eq.(2.44). Expressed in the basis of the  $SU(2)_R$  generators the rotations R are linear combinations of the form  $R^{(\dagger)} = 1_2 \pm \sum \vartheta_a \sigma_a$ , a = 1, 2, 3. When multiplied from the left or right the transformation will lead to terms of type  $A: 1_2\Phi^{\dagger}\Phi 1_2$ ,  $B: 1_2\Phi^{\dagger}\Phi\sigma_a$ ,  $C: \sigma_a\Phi^{\dagger}\Phi 1_2$ ,

 $D: \sigma_a \Phi^{\dagger} \Phi \sigma_b$ . Multiplication with  $\sigma_1$  from the left (right) swaps the rows (columns) of  $\Phi^{\dagger}\Phi$ . The same is true for the multiplication with  $\sigma_2$  apart from additional factors of i and -i that will appear in the elements of the matrix. The multiplication with  $\sigma_3$ from the left (right) adds a minus sign to all elements in the lower row (last column) of  $\Phi^{\dagger}\Phi$ . This completes the ingredients needed to check the invariance of  $V(\Phi)$  in Eq. (2.44): terms of type A are trivially invariant; terms of type B and C will lead to a swap of rows or columns, which will shift the off-diagonal zero elements in  $\Phi^{\dagger}\Phi$  on the diagonal, these terms have thus no effect on the trace; for terms of type D, three cases have to be distinguished: (i) if  $\sigma_3$  is multiplied from left and right the minus sign applied once to the lower row and once to the last column leaves the lower right element and thus the trace unchanged; (ii) if  $\sigma_3$  and  $\sigma_{1,2}$  appear in the product, this will result in an effective swap of a row or a column and thus again have no effect on the trace; (iii) if combinations of  $\sigma_{1,2}$  appear in the product the swap of rows and columns will swap the upper left with the lower right diagonal element and thus again leave the trace invariant. This is also true for the additional factors of i and -ithat might appear in the diagonal elements depending on the occurrences of  $\sigma_2$ . To translate these findings into the test of  $\operatorname{Tr}\left(R^{\dagger}\left(D_{\mu}\Phi\right)^{\dagger}D^{\mu}\Phi R\right)$  the product will be written out explicitly

$$\operatorname{Tr}\left(R^{\dagger}\left(\partial_{\mu}\Phi^{\dagger} + \frac{ig'}{2}B_{\mu}\sigma_{3}\Phi^{\dagger} - \frac{ig}{2}\Phi^{\dagger}\sigma_{a}W_{\mu}^{a}\right)\left(\partial_{\mu}\Phi - \frac{ig'}{2}B_{\mu}\Phi\sigma_{3} + \frac{ig}{2}\sigma_{a}W_{\mu}^{a}\Phi\right)R\right) \tag{2.45}$$

Not the whole calculation will be done here. Instead, it will be shown in a first step that the derivative part of Eq. (2.44) is exactly true for g'=0. In this case Eq. (2.45) leads to three different types of traces,  $A': \operatorname{Tr}(R^{\dagger}\Phi^{\dagger}\Phi R)$ ,  $B': \operatorname{Tr}(R^{\dagger}\Phi^{\dagger}\sigma_{a}\Phi R)$  and  $C': \operatorname{Tr}(R^{\dagger}\Phi^{\dagger}\sigma_{a}\sigma_{a'}\Phi R)$ . The invariance of type A' has been demonstrated above, type C' can be mapped into A', due to the orthogonality of the *Pauli* matrices,  $\sigma_{a}\sigma_{a'}=\delta_{aa'}$ . The only non trivial case to check are the traces of type B'. This can be done explicitly for each  $\sigma_{a}$ , a=1,2,3 and leads to the result of  $\operatorname{Tr}(\Phi^{\dagger}\sigma_{a}\Phi)=0$ ,  $\forall a$ . Since the rotation by R will be without influence on the trace, as demonstrated above, these terms will not contribute to the overall trace.

In a second step, an example is given to demonstrate that this invariance is not exact in the case of  $g'\neq 0$ . In this case, the product of the middle terms in Eq. (2.45) will lead to a trace of type  ${\rm Tr}\left(R^\dagger\sigma_3\Phi^\dagger\Phi\sigma_3R\right)$ . To give an example where the invariance is broken from the expansions of  $R^{(\dagger)}=1_2\pm\sum\vartheta_a\sigma_a$  the term is chosen, where  $\sigma_2$  is multiplied from left and right. This term leads to

$$\operatorname{Tr}\left(\sigma_{2}\sigma_{3}\Phi^{\dagger}\Phi\sigma_{3}\sigma_{2}\right) \propto \operatorname{Tr}\left(\sigma_{1}\Phi^{\dagger}\Phi(-1)\sigma_{1}\right) = -\operatorname{Tr}\left(\Phi^{\dagger}\Phi\right)$$

The residual minus sign demonstrates that those terms containing  $\sigma_3$  in general violate the exact symmetry. Since g' is small the symmetry is still approximately valid. The fact that Eq. (2.44) holds, implies that  $\mathcal{L}^{\text{Higgs}}$  has an additional approximate global symmetry of type

$$SU(2)_L \times SU(2)_R : \Phi \to L\Phi R$$

When the Higgs field  $\phi$  acquires the non-vanishing vacuum expectation value in matrix notation this is expressed by the matrix

$$\langle \Phi \rangle = \frac{1}{2} \begin{pmatrix} v & 0 \\ 0 & v \end{pmatrix}$$

which breaks both global symmetries  $SU(2)_L$  and  $SU(2)_R$  since

$$L\langle\Phi\rangle \neq \langle\Phi\rangle \qquad \langle\Phi\rangle R \neq \langle\Phi\rangle$$

But it leaves a sub-group  $SU(2)_{L+R}$  unbroken in which  $R=L^{\dagger}$  since

$$L\langle\Phi\rangle L^{\dagger} = \langle\Phi\rangle$$

Either  $SU(2)_R$  or  $SU(2)_{L+R}$  is referred to as custodial symmetry [9, 10]. It has been shown that this symmetry is non-trivial. It is only approximate and appears due to the special structure of  $\Phi$ , which allows Eq. (2.44) to be true. Since SU(2) is a three dimensional group, the number of broken generators from  $SU(2)_L \times SU(2)_R$ to  $SU(2)_{L+R}$  is 3+3-3=3. These give rise to three Goldstone bosons, which in turn give mass to the  $W^+$ ,  $W^-$  and Z boson, as demonstrated with the calculations leading to Eq. (2.37). It can be shown that in the limit  $g' \to 0$  the three heavy gauge bosons transform like a triplet in the three dimensional adjoint space of  $SU(2)_{L+R}$ , which explains why  $m_Z$  and  $m_W$  are so close to each other. In the limit of  $g' \to 0$ they would even be the same and the difference only occurs due to the small violation of the exact symmetry by q' as can be seen from Eq. (2.37). The custodial symmetry also protects the relation of Eq. (2.38) from large higher-order corrections, which would move  $\rho$  away from being  $\mathcal{O}(1)$ . This is where the exceptional name of this symmetry originates from. A similar custodial symmetry can be found in the sector of Higgs quark Yukawa couplings, under the assumption that the quark masses are the same, as will be briefly discussed at the end of the following section. Indeed, the violations of these custodial symmetries by g' and by the difference between the masses of the b- and the top quark were exploited in the global parameter fits that had been used to estimate  $m_t$  and  $m_H$  from their loop contributions to the electroweak precision data taken at LEP as will be discussed in Sect. 3.2.

# 2.4.2 Giving Masses to Fermions

As has been discussed before, also naive mass terms of fermions are violating the local  $SU(2)_L \times U(1)_Y$  gauge symmetry, due to their unequal splitting in left- and right-handed parts. Giving a mass to the leptons without breaking the gauge symmetry can also be achieved dynamically by adding a coupling of the lepton doublet to the

Higgs boson field,  $\phi$ . This is demonstrated for the electron-neutrino doublet in the following paragraphs. The corresponding term in the Lagrangian density is

$$\mathcal{L}_{e}^{\text{Yukawa}} = -y_{e} \left( \bar{e}_{R} \phi^{\dagger} \psi_{L} \right) + y_{e}^{*} \left( \overline{\psi}_{L} \phi e_{R} \right) \qquad \psi_{L} = \begin{pmatrix} \nu \\ e_{L} \end{pmatrix}$$

which corresponds to a common Yukawa coupling with the coupling constant  $y_e$ . The Lagrangian density  $\mathcal{L}^{Yukawa}$  transforms like a  $SU(2)_L \times U(1)_Y$  singlet as will be discussed with the following arguments: (i) both  $\phi$  and  $\psi_L$ , are  $SU(2)_L$  doublets, but their product is a  $SU(2)_L$  singlet as well as  $e_R$ . Therefore, the product of the three elements also transforms like a  $SU(2)_L$  singlet; (ii) the  $U(1)_Y$  transformation behavior is described by the product

$$e^{\pm i\frac{g'}{2}(Y_R+Y_\phi-Y_L)\vartheta'}$$

where the minus sign in front of  $Y_L$  comes from the fact that  $\phi$  and  $\psi_L$  are always adjoint to each other, and which in the configuration  $Y_L = -Y_\phi = -1$  and  $Y_R = -2$ , as given in Table 2.2, always equals to 1. Correspondingly, the product of the three elements will also transform like a  $U(1)_Y$  singlet. The coupling constant  $y_e$  can be chosen to be real. Any complex phase could be absorbed into a phase of  $e_R$ , which is also true for the quarks that will be discussed later. Again expanding the field  $\phi$  in its energy ground state

$$\mathcal{L}_{e}^{\text{Yukawa}} = -y_{e} \left( \sqrt{\frac{\mu^{2}}{2\lambda}} + \frac{H}{\sqrt{2}} \right) (\bar{e}_{R}e_{L} + \bar{e}_{L}e_{R}) = -m_{e} \left( 1 + \frac{1}{v} \frac{H}{\sqrt{2}} \right) \bar{e}e$$

leads to a mass term for the coupling lepton. The *Yukawa* coupling is determined by  $y_e = m_e/v$  and thus proportional to the mass of the lepton and the inverse of the vacuum expectation value, v. Mass terms for down-type quarks can be introduced into the theory in complete analogy, as will be demonstrated for the first flavor generation quark doublet: in this case the *Yukawa* coupling takes the form

$$\mathcal{L}_{d}^{\text{Yukawa}} = -y_{d} \left( \bar{d}_{R} \phi^{\dagger} \psi_{L} \right) + y_{d} \left( \overline{\psi}_{L} \phi d_{R} \right) \qquad \psi_{L} = \begin{pmatrix} u_{L} \\ d_{L} \end{pmatrix}$$
 (2.46)

There is one more subtlety when introducing mass terms for up-type fermions in general: since  $\phi$  is developed in its lower component, in the unitary gauge, it can only serve to give mass terms for the fields in the lower component of the doublet. Since neutrinos have been assumed to be massless throughout these considerations, this did not become apparent for the lepton doublet. For the quark doublet it can not be ignored any more. The way how to obtain mass terms for the upper components of the doublets is again not a priori given. It would be possible to introduce a second Higgs doublet field,  $\tilde{\phi}$ , to serve this purpose. In the minimal SM it is achieved via

the charge conjugate of  $\phi$ , as defined in Eq. (2.40). In this formalism, the *Yukawa* coupling to the up-type quark can be introduced as

$$\mathcal{L}_{u}^{\text{Yukawa}} = -y_{u} \left( \bar{u}_{R} \phi_{c}^{\dagger} \psi_{L} \right) + y_{u} \left( \overline{\psi}_{L} \phi_{c} u_{R} \right) \qquad \psi_{L} = \begin{pmatrix} u_{L} \\ d_{L} \end{pmatrix}$$
 (2.47)

All further considerations, including the check for the  $SU(2)_L \times U(1)_Y$  transformation behavior are in analogy to the case of the lepton doublet. The hypercharges of the corresponding quark singlets and doublets are given in Table 2.2.

As discussed for the pure Higgs sector of the Lagrangian density,  $\mathcal{L}^{\text{Higgs}}$ , before, in Sect. 2.4.1, there is also a custodial symmetry in the Higgs *Yukawa* sector for quarks, under the assumption that the quarks in the doublet have equal mass (i.e.  $y_u = y_d = y$ ). This can be seen if the right-handed quarks are grouped into a global  $SU(2)_R$  doublet  $\psi_R = (u_R d_R)$ . In this notation, Eqs. (2.46) and (2.47) can be rewritten in a compact form as

$$\mathcal{L}_{q}^{\text{Yukawa}} = -\sqrt{2}y \left( \overline{\psi}_{R} \Phi^{\dagger} \psi_{L} \right)$$

using the matrix notation for  $\Phi$  as introduced in Sect. 2.4.1. From the transformation behavior of  $\psi_{L,R}$  under the global  $SU(2)_{L,R}$  transformations the invariance of  $\mathcal{L}_q^{\text{Yukawa}}$  under global  $SU(2)_L \times SU(2)_R$  transformations can easily be seen from

$$\begin{split} SU(2)_L: & \psi_L \to L \ \psi_L & \psi_R \to \psi_R \\ SU(2)_R: & \psi_R \to R^\dagger \psi_R & \psi_L \to \psi_L \\ SU(2)_L \times SU(2)_R: & \overline{\psi}_R \Phi^\dagger \psi_L \to \overline{\left(R^\dagger \psi_R\right)} \left(L \Phi R\right)^\dagger L \psi_L = \overline{\psi}_R \underbrace{RR^\dagger}_{} \Phi^\dagger \underbrace{L^\dagger L}_{} \psi_L = \overline{\psi}_R \Phi^\dagger \psi_L \end{split}$$

This completes the discussion on the first generation of weak isospin doublets including quarks. The last peculiarity of the electroweak interaction that will be discussed in this context is not crucial for the discussion of electroweak symmetry breaking and mass generation, while it adds to the distinctiveness of the electroweak interaction in general. From the observation of decays like

$$n \to p \ e^- \ \bar{\nu}_e$$
 and  $\Lambda^0 \to p \ e^- \ \bar{\nu}_e$ 

it is obvious that the weak interaction allows transitions between the upper and lower components of an isospin doublet not only within the same, but also across different isospin doublets. In this case, the decay  $n \to p \ e^- \ \bar{\nu}_e$ , is an example for a normal transition from a d-quark to a u-quark within the same doublet. The decay  $\Lambda^0 \to p \ e^- \ \bar{\nu}_e$  is an example for a transition from an s-quark to a u-quark, which is a transition across two distinct doublets. Another important experimental observation is that these transitions seem to be only allowed via the coupling to the W and between up- and down-type elements of the doublets. So called flavor

changing neutral currents (FCNC), e.g. from an *s*-quark to a *d*-quark, seem to be highly suppressed.

In the SM, this behavior can be understood if the mass *eigenstates* of the quarks are not the same as the  $SU(2)_L$  flavor *eigenstates*. When only considering the two weak isospin doublets for u-, d-, s- and c-quarks, this can be achieved by a unitary rotation of the *eigenstates* against each other

$$\begin{pmatrix} d' \\ s' \end{pmatrix} = \begin{pmatrix} \cos \varphi_{12} & \sin \varphi_{12} \\ -\sin \varphi_{12} & \cos \varphi_{12} \end{pmatrix} \cdot \begin{pmatrix} d \\ s \end{pmatrix}$$

where  $\varphi_{12} = 13.04(5)^{\circ}$  [8] corresponds to the *Cabbibo* angle, which indicates the amount by which the  $SU(2)_L$  flavor basis is rotated against the basis of mass *eigenstates*. It is thereby convention to express this rotation in the down-type components of the doublets, while it would be equivalent and lead to the same predictions to express the rotation in the up-type components. This rotation also protects the theory from FCNC (at tree level) via the *Glashow-Iliopoulus-Maiani* or GIM mechanism [11], which implies that such processes can only appear at higher orders in the SM.

The extension of the fermion fields to three generations of quark doublets leads to the introduction of the *Cabbibo-Kobayashi-Maskawa* or *CKM* matrix as an extension of the simple two dimensional rotation via the *Cabbibo* angle [12]. In the standard parametrization, this rotation matrix of the complex spinor fields reads as

$$\begin{split} M_{\text{CKM}} &= \begin{pmatrix} V_{ud} & V_{us} & V_{ub} \\ V_{cd} & V_{cs} & V_{cb} \\ V_{td} & V_{ts} & V_{tb} \end{pmatrix} \\ &= \begin{pmatrix} 1 & 0 & 0 \\ 0 & c_{23} & s_{23} \\ 0 & c_{23} & -s_{23} \end{pmatrix} \cdot \begin{pmatrix} c_{13} & 0 & s_{13}e^{-i\delta_{13}} \\ 0 & 1 & 0 \\ -s_{13}e^{-i\delta_{13}} & 0 & c_{23} \end{pmatrix} \cdot \begin{pmatrix} c_{12} & s_{12} & 0 \\ -s_{12} & c_{12} & 0 \\ 0 & 0 & 1 \end{pmatrix} \\ &= \begin{pmatrix} c_{12}c_{13} & s_{12}c_{13} & s_{13}e^{-i\delta_{13}} \\ -s_{12}c_{23} - c_{12}s_{23}s_{13}e^{i\delta_{13}} & 12c_{23} - s_{12}s_{23}s_{13}e^{i\delta_{13}} & s_{23}c_{13} \\ 12s_{23} - c_{12}c_{23}c_{13}e^{i\delta_{13}} & -c_{12}s_{23} - c_{12}c_{23}s_{13}e^{i\delta_{13}} & c_{23}c_{13} \end{pmatrix} \end{split}$$

$$c_{ij} = \cos \varphi_{ij} \; ; \; s_{ij} = \sin \varphi_{ij} \; (ij = 12, 13, 23)$$

where the three real angles  $\varphi_{ij}$  correspond to the *Euler* angles in three dimensions (corresponding to the three generations of weak isospin doublets) and  $\delta_{13}$  corresponds to a complex phase, which remains also in the unitary gauge. The complex phase,  $\delta_{13}$ , is the parameter that determines direct CP violation in the SM. If it were equal to zero, direct CP violation would not be allowed. But since  $\delta_{13}$  itself is only a parameter which has to be determined by experiment it carries no further predictive

power of the SM beyond incorporating the possibility of direct *CP* violation in the theory. It is a peculiarity of the electroweak interaction that, in spite of the origin of the quark masses being related to the electroweak sector of the SM, the *eigenstates* of the electroweak interaction of the quarks are not the same as their mass *eigenstates*.

### 2.4.3 Summary and Conclusions

The complete Lagrangian density of the electroweak sector of the SM, which for reasons of simplicity is only given for the first generation of leptons, reads as:

$$\mathcal{L}^{\text{SM}} = \mathcal{L}_{\text{kin}}^{\text{Lepton}} + \mathcal{L}_{\text{IA}}^{\textit{CC}} + \mathcal{L}_{\text{IA}}^{\textit{NC}} + \mathcal{L}_{\text{kin}}^{\text{Gauge}} + \mathcal{L}_{\text{kin}}^{\text{Higgs}} + \mathcal{L}_{V(\phi)}^{\text{Higgs}} + \mathcal{L}_{e}^{\text{Yukawa}}$$

$$\mathcal{L}_{\rm kin}^{\rm Lepton} = i\bar{e}\gamma^{\mu}\partial_{\mu}e + i\bar{\nu}\gamma^{\mu}\partial_{\mu}\nu$$

$$\mathcal{L}_{\mathrm{IA}}^{CC} = -\frac{q}{\sqrt{2}\sin\theta_W} \left[ W_\mu^+ \bar{\nu} \gamma^\mu e_L + W_\mu^- \bar{e}_L \gamma^\mu \nu \right]$$

$$\mathcal{L}_{\mathrm{IA}}^{NC} = -\frac{q}{2\sin\theta_{W}\cos\theta_{W}}Z_{\mu}\left[\left(\bar{\nu}\gamma^{\mu}\nu\right) + \left(\bar{e}_{L}\gamma^{\mu}e_{L}\right)\right] - q\left[A_{\mu} + \tan\theta_{W}Z_{\mu}\right]\left(\bar{e}\gamma^{\mu}e\right)$$

$$\mathcal{L}_{\mathrm{kin}}^{\mathrm{Gauge}} = -\left.\frac{1}{2}\mathrm{Tr}\left(W_{\mu\nu}^{a}W^{a\mu\nu}\right) - \frac{1}{4}B_{\mu\nu}B^{\mu\nu}\right| \begin{array}{c} B_{\mu} \to A_{\mu} \\ W_{\mu}^{3} \to Z_{\mu} \end{array}$$

$$L_{\rm kin}^{\rm Higgs} = \frac{1}{2} \partial_{\mu} H \partial^{\mu} H + \left(1 + \frac{1}{v} \frac{H}{\sqrt{2}}\right)^{2} m_{W}^{2} W_{\mu}^{+} W^{\mu -} + \left(1 + \frac{1}{v} \frac{H}{\sqrt{2}}\right)^{2} m_{Z}^{2} Z_{\mu} Z^{\mu}$$
(2.48)

$$\mathcal{L}_{V(\phi)}^{\rm Higgs} = -\frac{\mu^2 v^2}{2} + \mu^2 \left(\frac{H}{\sqrt{2}}\right)^2 + 2\frac{\mu^2}{v} \left(\frac{H}{\sqrt{2}}\right)^3 + \frac{\mu^2}{2v^2} \left(\frac{H}{\sqrt{2}}\right)^4$$

$$\mathcal{L}_e^{\text{Yukawa}} = -\left(1 + \frac{1}{v}\frac{H}{\sqrt{2}}\right) m_e \bar{e} e$$

The parts, which only contain the Higgs boson field, H, in  $\mathcal{L}_{V(\phi)}^{\text{Higgs}} + \mathcal{L}_{\text{kin}}^{\text{Higgs}}$  correspond to the *Klein-Gordon* equation for a scalar boson with a tri-linear and a quartic self-coupling given by the explicit choice of the *Goldstone* potential. Due to the self-coupling, there is no free Higgs boson field. A few more consequences of the explicit coupling structure will be further discussed in Sect. 3.1, together with the

triviality constraint within the SM. In  $\mathcal{L}_{V(\phi)}^{\mathrm{Higgs}}$  the mass of the Higgs boson field, H, can be read off as

$$m_H^2 \equiv 2\mu^2 \tag{2.49}$$

The coupling of the Higgs boson to fermions, heavy gauge bosons and to itself, expressed by  $m_H$  and v, can be read off from the Lagrangian density to be

$$\begin{split} f_{H\to ff} &= i\frac{m_f}{v} \qquad \text{(Fermions)} \\ f_{H\to VV} &= i\frac{2m_V^2}{v} \qquad \text{(Heavy Bosons trilinear)} \\ f_{HH\to VV} &= i\frac{2m_V^2}{v^2} \qquad \text{(Heavy Bosons quartic)} \\ f_{H\to HH} &= i\frac{3m_H^2}{v} \qquad \text{($H$ Boson trilinear)} \\ f_{HH\to HH} &= i\frac{3m_H^2}{v^2} \qquad \text{($H$ Boson quartic)} \end{split}$$

Note that since H is an indistinguishable particle, each appearance, n, in the scattering vertex needs to be taken into account by a combinatorial factor  $^1/_{n!}$ , in the description of the elementary scattering process, according to the *Feynman* rules [13]. This leads to an additional factor of 2! for  $f_{HH\to VV}$ , of 3! for  $f_{H\to HH}$  and of 4! for  $f_{HH\to HH}$ . Both in the case of self-couplings and in the case of the coupling to gauge bosons the tri-linear and quartic couplings have the same strength, with the only difference that the quartic couplings are suppressed by one additional factor of  $^1/_v$ . Further on, in contrast to the fermionic couplings, which depend linearly on the mass of the fermions,  $m_f$ , the bosonic couplings are proportional to the masses of the bosons squared. As has been discussed before this coupling structure constitutes a characteristic property of a Higgs boson. While with more stringency for the coupling to gauge bosons than for the coupling to fermions, it constitutes a unique coupling behavior, which is non-universal among fermion generations.

The individual non-trivial steps towards the full electroweak theory are summarized below:

- In the first step, the Lagrangian density has been extended into the two-dimensional  $SU(2)_L$  weak isospace, which is comprehensible only for the left-handed components of matter. The neutrino and the left-handed component of the electron have been combined into an isospin doublet  $\psi_L = (\nu e_L)^\mathsf{T}$ , for which local  $SU(2)_L$  gauge invariance has been enforced. This has led to a description of the weak theory. The right-handed part of the electron,  $e_R$ , which does not take part in the weak interaction behaves like a singlet under  $SU(2)_L$  transformations.
- To also obtain a description for the electromagnetic force in addition local invariance has been required for the global  $U(1)_Y$  symmetry of the Lagrangian density, which acts on the left-handed  $SU(2)_L$  doublet,  $\psi_L$ , as a whole, and on the right-handed  $SU(2)_L$  singlet,  $e_R$ , with the different hypercharges  $Y_L$  and  $Y_R$ . These

- two local gauge invariance requirements have led to the structure of electroweak interactions and to the four gauge fields  $B_{\mu}$  and  $W_{\mu}^{a}$ , a=1,2,3.
- To achieve that the gauge coupling to the  $\nu$  is governed by only a single physical field, the Z boson field, the fields  $B_{\mu}$  and  $W_{\mu}^3$  have been transformed into the fields  $A_{\mu}$  and  $Z_{\mu}$ . This was possible by a trivial rotation in the plane of the neutral gauge fields by the weak mixing angle  $\theta_W$ .
- Up to this point the main issue of the model was, that local gauge symmetries require all gauge boson fields to be massless, while the  $W^+$ ,  $W^-$  and Z bosons of the weak interaction have been measured to be massive. This finding implies that the  $SU(2)_L$  symmetry can not be manifest in the Lagrangian density. The symmetry can still be immanent, but hidden, if it is broken in the energy ground state of the system, which corresponds to the quantum vacuum.
- Since all fields and interactions in the Lagrangian density up to this point obey the  $SU(2)_L$  symmetry the incorporation of an energy ground state, which breaks the symmetry implied the postulation of a new weak isospin doublet field,  $\phi$ , with a self-coupling and a potential imparting this property to the quantum vacuum. The simplest potential, with these properties, which is bound from below, does not distinguish any direction in weak isospace and still leads to a renormalizable theory is the *Goldstone* potential defined in Eq. (2.32).
- The requirement of local  $SU(2)_L$  gauge invariance to this field leads to a mass term for the three  $SU(2)_L$  gauge bosons, in the energy ground state of the quantum vacuum. The mass terms appear as a coupling of the gauge bosons to the non-zero expectation value of the quantum vacuum, v. Three out of four degrees of freedom of the complex  $SU(2)_L$  doublet field,  $\phi$ , are eaten up by the gauge fields, which in turn obtain an additional degree of freedom of longitudinal polarization, each, due to the gained mass. One degree of freedom remains in the model, which in unitary gauge can be expressed by the single real field H.
- The field H is called the Higgs boson field. As a single scalar field it obeys the  $Klein\,Gordon$  equation and thus is a boson. It obtains a mass due to its self-coupling with the potential  $V(\phi) \to V(H)$ . This mass term,  $\propto H^2$  appears naturally and irrespective of the exact form of the potential, from the first non-trivial term of the Taylor expansion of the Lagrangian density, when developed in the minimum of the energy ground state. The physical Higgs boson field, H, can be viewed as the radial excitation of the Higgs doublet field,  $\phi$ , in the minimum of the Goldstone potential.
- The gauge invariance violating transformation behavior of the mass terms of the heavy gauge bosons is compensated by additional coupling terms of the bosons to the new physical Higgs boson field, H. This coupling is  $\propto m_V^2$ .
- For fermions the problem of masses is different and it only occurs due to the chiral nature of the weak interaction coupling to fermions, which requires the splitting of fermions into left-handed SU(2)<sub>L</sub> doublets and right-handed SU(2)<sub>L</sub> singlets. It is this distinction and the different behavior under SU(2)<sub>L</sub> transformations, of left- and right-handed particle components which leads to the breaking of the local SU(2)<sub>L</sub> gauge symmetry for fermion mass terms. Despite of its different nature also this problem can be solved by the coupling of the involved fermion fields to

the new Higgs boson field,  $\phi$ , e.g. via a Yukawa coupling,  $\propto \bar{e}_R \phi \psi_L$ . As in the case of the massive gauge bosons the mass terms appear from the coupling to the non-zero vacuum expectation value, v. Also here the gauge symmetry breaking behavior of the mass terms is compensated by additional coupling terms of the fermions to the new physical Higgs boson field, H. This coupling is  $\propto m_f$ .

• The vacuum expectation value, v, is developed in the lower component of  $\phi$ . This only allows to give mass terms to the lower components of the fermion doublets. In the minimal SM, mass terms for the upper components of the fermion doublets can be obtained from the charge conjugate of  $\phi$ ,  $\phi_c$ . This is not possible in *supersymmetric* extensions of the SM, were  $\phi$  has to fit into the structure of a larger multiplet.

These non-trivial points extend the Weinberg-Salam model of electroweak interactions to the electroweak sector of the SM as a complete theory. It contains the physical 21 fields for the neutrinos, the left- and right-handed components of the leptons and quarks, as constituents of matter, the gauge fields  $Z_{\mu}$ ,  $W_{\mu}^{+}$ ,  $W_{\mu}^{-}$  and  $A_{\mu}$ as mediators of the electromagnetic and weak interaction, and the Higgs field H.

In this collection of fields the Higgs boson plays a special role in the theory: it is the only particle with spin 0. In the theory this is expressed by the fact that it is a scalar field with a single external degree of freedom, in contrast to a spinoror vector field. The Higgs boson is neither a constituent of matter, like the fermion fields, nor is it a force mediating gauge field. It is omnipresent as an excitation of the non-zero expectation value in the quantum vacuum. In this sense it is similar to the omnipresent aether in the closing of the 19th century. This omnipresence is manifest in the non-zero masses of the particles, which couple to the non-zero vacuum expectation value, v, and to the excitations of the quantum vacuum, H, in the same way. A brief summary of all involved fields in the electroweak sector of the SM is given in Table 2.3.

Table 2.3 Summary of all fields that appear in the electroweak sector of the SM								
Spin 0	Higgs Fie	Higgs Field						
	Н	Н						
Spin 1/2	Leptons <sup>†</sup>	Leptons <sup>†</sup>			Quarks <sup>†</sup>			
	$\nu_e$	$ u_{\mu}$	$\nu_{ au}$	и	c	t		
	e	$\mu$	$\tau$	d	S	b		
Spin 1	Gauge Fi	Gauge Fields						
	W <sup>+</sup> /-	Z	γ					

All gauge fields have spin 1, the fields corresponding to the elementary constituents of matter, the leptons and quarks have spin 1/2. † Note that the lepton and quark fields describing elementary particles with a finite mass have a left-handed and a right-handed component, of which only the left-handed component is taking part in the weak charged current interaction. The Higgs boson is the only field in the SM that has spin 0

References 51

### References

 C. Jensen, Controversy and Consensus: Nuclear Beta Decay 1911–1934 (Birkhäuser Verlag, Basel, 1992)

- 2. W. Pauli, Dear Radioactive Ladies and Gentlemen. Phys. Today 31N9 27(1978)
- 3. E. Fermi, Tentativo di una Teoria Dei Raggi. Il Nuovo Cimento 11(1), 1–19 (1934)
- 4. S. Glashow, Partial symmetries of weak interactions. Nucl. Phys. 22, 579-588 (1961)
- 5. J. Goldstone, A. Salam, S. Weinberg, Broken symmetries. Phys. Rev. 127, 965–970 (1962)
- 6. J.M. Cornwall, D.N. Levin, G. Tiktopoulos, Derivation of Gauge Invariance from High-Energy Unitarity Bounds on the S-Matrix. Phys. Rev. D 10, 1145 (1974)
- 7. T. van Ritbergen, R.G. Stuart, On the precise determination of the fermi coupling constant from the Muon lifetime. Nucl. Phys. B **564**, 343–390 (2000). arXiv:hep-ph/9904240
- Chin. Phys. C Review of particle physics. 38, 090001 (2014). doi:10.1088/1674-1137/38/9/ 090001
- 9. M. Veltman, Limit on mass differences in the Weinberg model. Nucl. Phys. B 123, 89 (1977)
- P. Sikivie, L. Susskind, M.B. Voloshin et al., Isospin breaking in technicolor models. Nucl. Phys. B 173, 189 (1980)
- S.L. Glashow, J. Iliopoulos, L. Maiani, Weak interactions with Lepton-Hadron symmetry. Phys. Rev. D2, 1285–1292 (1970)
- M. Kobayashi, T. Maskawa, CP violation in the renormalizable theory of weak interaction. Prog. Theor. Phys. 49, 652–657 (1973)
- 13. G. 't Hooft, M. Veltman, DIAGRAMMAR. NATO Sci. Ser. **B4**, 177–322 (1974)

# Chapter 3 Higgs Boson Searches Before the Advent of the Large Hadron Collider

### 3.1 Constraints Within the Theory

The electroweak sector of the SM, as summarized for the first generation of leptons in Eq. (2.48) has 17 open parameters, which can be chosen to be: (i) the coupling constants g and g', usually expressed by the electric charge, q, and the electroweak mixing angle,  $\sin \theta_W$ ; (ii) the mass of the W boson,  $m_W$ , and the mass of the Higgs boson,  $m_H$ ; (iii) three lepton masses and six quark masses (proportional to their coupling strengths,  $y_i$ , to the Higgs boson field); (iv) and finally the three *Euler* angles and the complex phase of the *CKM* matrix. The mass of the Z boson,  $m_Z$ , and the self-coupling of the *Goldstone* potential,  $\lambda$ , are fixed via the relations

$$m_Z = \frac{m_W}{\cos \theta_W}; \qquad \lambda = \frac{m_H^2}{4v^2}; \tag{3.1}$$

Fifteen out of these 17 parameters are related to the phenomenology of electroweak symmetry breaking, which introduces all masses, mixing angles,  $\varphi_{ij}$ , and the phase  $\delta_{13}$  into the theory as effective parameters. The common belief is that the SM is a low energy approximation of a more fundamental theory, which will allow for a deeper understanding of the electroweak symmetry breaking mechanism. In this perspective the masses, mixing angles and phase,  $\delta_{13}$ , resemble our current ignorance for this underlying mechanism and would themselves be composed of a smaller set of more fundamental parameters, which govern the behavior in the low energy limit.

Apart from the mass of the Higgs boson,  $m_H$ , all parameters of the SM had been determined from measurements well before the discovery of the Higgs boson. A summary of all SM parameters as introduced above and their uncertainties is given in Table 3.1. In the course of this book q will be discussed in *Lorentz-Heavyside* units related to the dimensionless fine structure constant  $\alpha \approx 1/137$  by  $q = \sqrt{4\pi\alpha}$ . The only parameter that would have to be added for the inclusion of the strong interaction to complete the parameters of the SM is the strong coupling constant,  $g_s$ . Some of

Table 3.1	Free parameters	of the electroweak	sector of the	SM [1]

	Parameters of	of the SM	
Couplings			
Electric charge	$q = \sqrt{4\pi\alpha}$	0.3028221(31)	
Mixing angle	$\sin \theta_W$	0.23122(15)	
Boson masses			
W	$W = m_W = 80.385(15)$		GeV
Higgs	$m_H$ 40–1600		GeV <sup>†</sup>
Fermion masses			
Leptons			
e	$m_e$	510.998928(11)	keV
$\mu$	$m_{\mu}$	105.6583715(35)	MeV
τ	$m_{ au}$	1.77682(16)	GeV
Quarks		<u> </u>	
и	$m_u$	1.7–3.1	MeV
d	$m_d$	4.1–5.7	MeV
С	$m_c$	$1.29\pm_{0.11}^{0.05}$	GeV
S	$m_s$	$0.1\pm_{0.02}^{0.03}$	GeV
t	$m_t$	173.21(87)	GeV
b	$b$ $m_b$		GeV
CKM angles and phase			
arphi12		13.04(5)	0
$\varphi_{13}$		0.201(11)	0
$\varphi_{23}$		2.38(6)	0
$\delta_{13}$		1.20(8)	rad

The breaking mechanism of the symmetry introduces all masses, the mixing angles,  $\varphi_{ij}$  corresponding to the rotation of the *eigenstates* of the weak isospin against the mass *eigenstates* in the quark sector and the complex phase of the *CKM* matrix,  $\delta_{13}$ . The electric charge, q, is given in *Lorentz-Heavyside* units related to the dimensionless fine structure constant  $\alpha \approx 1/137$  by  $q = \sqrt{4\pi\alpha}$ . † The boundaries on  $m_H$  correspond to values that have been obtained from simplified calculations of the *triviality* and *stability bounds*, as discussed in this section, assuming that the SM is valid up to the TeV scale

the parameters, like the masses of the electron or the muon, are directly observable and known from measurement to very high precision. The electroweak mixing angle,  $\theta_W$ , the quark masses and the parameters of the *CKM* matrix on the other hand are not directly observable.

Even if the mass of the Higgs boson is a priori undetermined, its range is not completely unconstrained in the SM. The constraints originate from the physical bounding of scattering amplitudes, e.g. for elastic  $W^+W^- \to W^+W^-$  scattering, or from the validity of higher-order corrections to the parameters  $\mu$  and  $\lambda$  of the *Goldstone* potential. Three examples will be given in this section. The argumentation follows the description given in [2, 3]. It should be noted that all boundaries that will be discussed rely on the assumption that the SM is valid up to a certain scale. They indicate the range of  $m_H$ , for which the SM can be sustained as a self-consistent

theory. The observation of a Higgs boson with a mass outside the given range would indicate the non-applicability of the SM and in most cases the breakdown of the perturbation series, from which the boundaries have been obtained.

### 3.1.1 The Unitarity Bound

In the SM, the scattering amplitudes of the longitudinal components of the gauge bosons  $Z_L$  and  $W_L$  grow with their momenta. It is obvious that this growth has to be tamed in one or the other way with increasing energy, not to violate the unitarity of the scattering process. This is shown explicitly for the case of elastic  $W^+W^- \to W^+W^-$  scattering. For center-of-mass energies  $s \gg m_W^2$  the scattering amplitude of this process will be dominated by the longitudinal component of the W boson and takes the form [2]

$$A(W^+W^- \to W^+W^-) \xrightarrow{s \gg m_W^2} \frac{1}{v^2} \left[ s + t - \frac{s^2}{s - m_H^2} - \frac{t^2}{t - m_H^2} \right]$$

where v and  $m_H$  are the vacuum expectation value and the Higgs boson mass and s and t are the *Mandelstam* variables corresponding to the center-of-mass energy and the momentum transfer in the scattering vertex squared. According to the equivalence theorem of the *Goldstone* theory this scattering amplitude can be expressed by the *Goldstone* bosons, W', that have been eaten up in the unitary gauge, to give mass to the W boson, and re-appeared as the additional longitudinal polarization degrees of freedom:

$$A(W'^+W'^- \to W'^+W'^-) = -\left[2\frac{m_H^2}{v^2} + \left(\frac{m_H^2}{v}\right)^2 \frac{1}{s - m_H^2} + \left(\frac{m_H^2}{v}\right)^2 \frac{1}{t - m_H^2}\right]$$
(3.2)

The unitarity argument is based on the optical theorem, which relates the scattering amplitude to the total cross section at small scattering angles [4]. For its quantification it is most suited to decompose the scattering amplitude into partial waves  $a_J$  of orbital angular momentum J. For a  $2 \to 2$  scattering process the partial wave amplitude  $a_J$  can be obtained from the transformation

$$a_J(s) = \frac{1}{32\pi} \int_{-1}^{1} d\cos\theta^* P_J(\cos\theta^*) A(s, \theta^*) = \frac{1}{16\pi s} \int_{-s}^{0} dt P_J(t) A(s, t)$$

$$t = (p_{\mu}^* - p_{\mu}^{\prime *}) = -\left(|\vec{p^*}|^2 + |\vec{p^{\prime *}}|^2 - 2|\vec{p^*}||\vec{p^{\prime *}}|\cos\theta^*\right) = -2\left(\sqrt{s}/2\right)^2 \left(1 - \cos\theta^*\right)$$
  
$$d\cos\theta^* = 2/sdt; \qquad \cos\theta^* = -1 \Rightarrow t = -s; \qquad \cos\theta^* = +1 \Rightarrow t = 0$$

where  $P_J$  corresponds to the  $J^{\text{th}}$  Legendre polynomial,  $p^*$ ,  $p'^*$  correspond to the in-coming and out-going momentum of one of the scattering particles, and  $\theta^*$  to the scattering angle, each expressed in the center-of-mass system of the two-body scattering (which has been made explicit by the superscript "\*"). The variable transformations in the lower part of the equation have been added to make it easier to follow the transformation from  $\cos \theta^*$  to t.

According to the optical theorem the cross section is given by the imaginary part of the scattering amplitude in the forward direction, which leads to the unitarity condition

$$|a_J|^2 = \text{Im}(a_J)$$
  
 $|\text{Re}(a_J)|^2 + |\text{Im}(a_J)|^2 = \text{Im}(a_J)$   
 $|\text{Re}(a_J)|^2 + (\text{Im}(a_J) - \frac{1}{2})^2 = \frac{1}{4}$ 

This condition corresponds to a circle with radius  $^1/_2$  around the point  $(0, ^1/_2)$  in the complex plane,  $\mathbb C$ . It implies the unitarity constraint of  $|\operatorname{Re}(a_J)| < ^1/_2$ . Taking the partial wave for J=0 of the scattering amplitude  $A(W'^+W'^-\to W'^+W'^-)$  as given in Eq. (3.2) (with  $P_0(\cos\theta^*)=P_0(t)=1$ ) translates this constraint into a simple boundary condition for the mass of the Higgs boson,  $m_H$ ,

$$|a_0| = \frac{1}{16\pi s} \int_{-s}^0 dt |A| = \frac{m_H^2}{16\pi v^2} \left[ 2 + \frac{m_H^2}{s - m_H^2} + \frac{m_H^2}{s} \log \left( \frac{s}{m_H^2} + 1 \right) \right]$$

$$\xrightarrow{s \gg m_H^2} \frac{m_H^2}{8\pi v^2} < \frac{1}{2}$$

which results in an upper bound for the mass of the Higgs boson of

$$m_H \lesssim \sqrt{4\pi} \cdot v = 870 \,\text{GeV}$$
 (Unitarity Bound) (3.3)

The above discussion can also be led with the assumption that  $m_H$  is very large and out of reach of current accelerators (expressed by the limit  $s \ll m_H$ ). This leads to an estimate of

$$|a_0| \xrightarrow{s \ll m_H^2} \frac{s}{32\pi v^2} < \frac{1}{2}; \qquad \sqrt{s} \lesssim \sqrt{16\pi} \cdot v = 1.7 \text{ TeV}$$

corresponding to a boundary on the center-of-mass energy, above which new physics phenomena have to set in to prevent unitarity violation in the  $W^+W^- \to W^+W^-$  scattering amplitude.

This discussion has only been based on the  $W^+W^- \to W^+W^-$  scattering process. In a more global analysis it can be extended to include the scattering amplitudes of elastic  $Z_LZ_L$ , HH,  $Z_LH$ ,  $W_L^+Z_L$  and  $W_L^+H$  scattering, which leads to a slightly stronger constraint of  $m_H \lesssim 700\,\text{GeV}$  or correspondingly to a limit on the validity of the SM of  $\sqrt{s} \lesssim 1.2\,\text{TeV}$ , in case of the absence of a Higgs boson [2].

It should be noted that these estimates have been made at tree level in perturbation theory, which is not applicable any more in the case of large Higgs boson masses, leading to a large self-coupling  $\lambda$  of the Higgs boson. To be clear about this limitation the boundary is often called *perturbative* or *tree-level unitarity bound*.

### 3.1.2 The Goldstone Potential at Higher Orders

The following inherent constraints of the SM are derived from the high energy behavior of the parameters  $\lambda$  and  $\mu$  in the *Goldstone* potential. This behavior is determined by loop corrections, which can be taken into account to fixed order by renormalization group equations. At one-loop accuracy the renormalization group equation of the Higgs boson quartic self-coupling,  $\lambda$ , is given by [2]

$$\frac{d\lambda}{d \log Q^2} = \frac{1}{16\pi^2} \left[ \underbrace{\frac{12\lambda^2}{Higgs} + \underbrace{6\lambda y_t^2 - 3y_t^4}_{top \text{ quark}} - \underbrace{\frac{3}{2}\lambda \left(3g'^2 + g^2\right) + \frac{3}{16} \left(2g'^4 + \left(g'^2 + g^2\right)^2\right)}_{gauge \text{ bosons}} + \dots \right]$$
(3.4)

where g and g' correspond to the electromagnetic and the weak coupling constants and  $y_t = m_t/v$  to the *Yukawa* coupling of the *top* quark to the Higgs boson. Since the coupling of the Higgs boson is proportional to the mass or to the mass squared, the high energy behavior of  $\lambda$  will be driven by the loop contributions of the heaviest objects that the Higgs boson couples to.

For  $m_H^2$  much larger than a given scale,  $Q^2$ , Eq. (3.4) will be dominated by the first term (labeled by "Higgs"), which simplifies the equation to

$$\frac{\mathrm{d}\lambda}{\mathrm{d}\log Q^2} = \frac{3}{4\pi^2}\lambda^2(Q^2)$$

This equation can easily be solved by separation of variables. Evaluated at the scale of electroweak symmetry breaking v as a reference it has the solution

$$\frac{4\pi^2}{3} \frac{\mathrm{d}\lambda}{\lambda^2} = \mathrm{d}\log Q^2$$

$$\frac{4\pi^2}{3} \left( \frac{1}{\lambda(v^2)} - \frac{1}{\lambda(Q^2)} \right) = \log \left( \frac{Q^2}{v^2} \right)$$

$$\lambda(Q^2) - \lambda(v^2) = \frac{3}{4\pi^2} \lambda(Q^2) \lambda(v^2) \log \left( \frac{Q^2}{v^2} \right)$$

$$\lambda(Q^2) = \frac{\lambda(v^2)}{1 - \frac{3}{4\pi^2} \lambda(v^2) \log \left( \frac{Q^2}{v^2} \right)}$$
(3.5)

For small values of  $Q^2 \ll v^2$ , the  $\log \left( \frac{Q^2}{v^2} \right)$  in the denominator of Eq.(3.5) is negative, thus leading to a large positive denominator. The smaller  $Q^2$  with respect to  $v^2$  the larger the denominator will be, damping  $\lambda$  to zero. For  $Q^2 \lesssim v^2$  Eq.(3.5) reaches a point, where the denominator approaches zero. The value of  $\lambda$  will grow to infinitely large values, which renders the theory non-perturbative. This point that is reached at

$$Q_{\text{Landau}}^2 \lesssim v^2 \cdot 10^{\frac{4\pi^2}{3\lambda}} = v^2 \cdot 10^{\frac{16\pi^2 v^2}{3m_H^2}}$$

is called the *Landau* pole, where  $\lambda(v^2)$  has been evaluated from Eq.(3.1). Beyond this pole the logarithm will change sign,  $\lambda$  will take negative values and the theory will not be physical any more.

A growth with the momentum scale  $Q^2$  is a general behavior for any  $\phi^4$ -theory as in the case of  $\mathcal{L}^{\mathrm{Higgs}}$ . For a bare  $\phi^4$ -theory the requirement to be perturbative at all scales forces the coupling term  $\lambda$  to be zero, which means that the theory is without coupling and therefore trivial.

Depending on the scale to which the theory should remain perturbative the *Landau* pole can be used to obtain an upper bound on the mass of the Higgs boson corresponding to

$$m_H \lesssim \sqrt{\frac{16\pi^2}{3 \cdot \log\left(Q_{\rm Landau}^2/v^2\right)}} \cdot v$$
  
 $m_H(\Lambda \sim 10^{-3} \, {\rm GeV}) \lesssim 1.6 \, {\rm TeV}$ 
  
 $m_H(\Lambda \sim 10^{16} \, {\rm GeV}) \lesssim 340 \, {\rm GeV}$  (Triviality Bound). (3.6)

In literature this bound is referred to as the *triviality bound*. For small values of  $m_H^2 \ll v$ , Eq. (3.4) will be dominated by those terms, which do not depend on  $\lambda$ , since  $\lambda$  will be small according to Eq. (3.1). These terms have a gauge boson component, which contributes with a positive sign and a *top* quark component, which contributes with a negative sign. In this case the equation and corresponding solution becomes:

$$\begin{split} \frac{\mathrm{d}\lambda}{\mathrm{d}\log Q^2} &= \frac{1}{16\pi^2} \left[ -3y_t^4 + \frac{3}{16} \left( 2g'^4 + \left( g'^2 + g^2 \right)^2 \right) \right] \\ \mathrm{d}\lambda &= \frac{1}{16\pi^2} \left[ -3y_t^4 + \frac{3}{16} \left( 2g'^4 + \left( g'^2 + g^2 \right)^2 \right) \right] \cdot \mathrm{d}\log Q^2 \\ \lambda(Q^2) &= \lambda(v^2) + \frac{1}{16\pi^2} \left[ -3\frac{m_t^4}{v^4} + \frac{3}{16} \left( 2g'^4 + \left( g'^2 + g^2 \right)^2 \right) \right] \log \left( \mathcal{Q}^2/v^2 \right) \end{split}$$
(3.7)

If  $m_H$  falls below a certain value,  $\lambda$  will turn negative, the *Goldstone* potential, will lose its minimum and will not be bound any more from below. The requirement  $\lambda(Q^2) \geq 0$  leads to a lower bound for  $m_H$ :

$$m_H \gtrsim \sqrt{\left(\frac{3m_t^4}{4\pi^2v^2} - \frac{3v^2}{64\pi^2}\left(2g'^4 + \left(g'^2 + g^2\right)^2\right)\right)\log\left(Q^2/v^2\right)}$$

$$m_H(\Lambda \sim 10^{-3} \, {\rm GeV}) \gtrsim 40 \, {\rm GeV}$$
  
 $m_H(\Lambda \sim 10^{16} \, {\rm GeV}) \gtrsim 160 \, {\rm GeV}$  (Stability Bound)

where again  $\lambda(v^2)$  has been evaluated from Eq. (3.1). In the literature this bound is referred to as the *stability bound*. The above discussion has been simple to give the principle idea of the argumentation. A complete analysis of the stability bound is more evolved, including the effect of the renormalization group on the complete *Goldstone* potential. There is a region of meta-stability, where a global minimum different from the minimum at  $v=246.22\,\mathrm{GeV}$  can emerge. The stability of the electroweak quantum vacuum then depends on the tunneling probability from the local into the global minimum. In contrast to the unitarity bound the triviality and stability bounds depend on the scale  $\Lambda$ , up to which the SM is assumed (or required) to remain valid without any further contribution of new physics. These bounds as a function of  $\Lambda$  are shown in Fig. 3.1. Also shown in the figure are the 10 and 1 % levels of fine-tuning of the higher-order corrections to the parameter  $\mu=m_H/\sqrt{2}$  that are needed to obtain

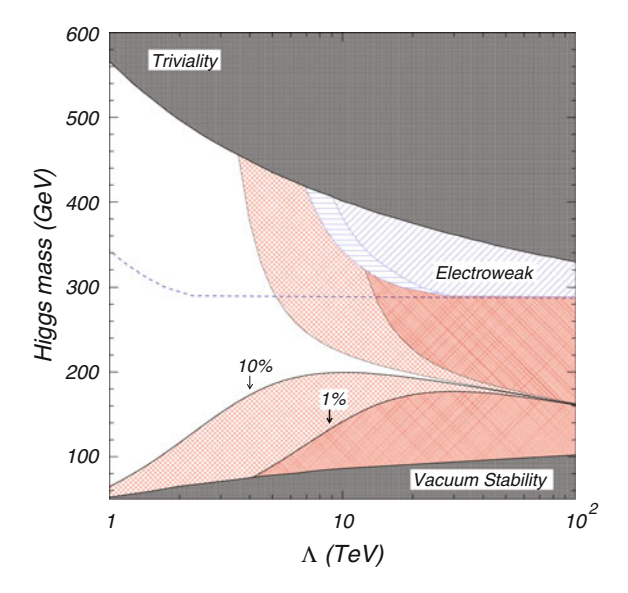


Fig. 3.1 Stability and triviality bounds on  $m_H$ , depending on the scale up to which the SM is assumed to be valid without any further contribution of new physics. Also shown are regions determined from electroweak precision measurements that will be discussed in Sect. 3.2 (hatched blue line) and regions of 10 and 1 % of fine-tuning, corresponding to the level at which the bare value of  $\mu$  and higher-order corrections have to cancel each other to lead to an observable Higgs boson mass at the scale of electroweak symmetry breaking of  $v = 246.22 \,\text{GeV}$  (hatched red areas) [3]

a physical mass of the Higgs boson at the scale of electroweak symmetry breaking, including higher order corrections. In the literature this phenomenon is referred to as the fine-tuning or naturalness problem. The name naturalness problem, is motivated by the fact that the bare mass of the Higgs boson would have to be by many orders of magnitude larger than the physically observable Higgs boson mass to compensate the large corrections by higher-order terms. In this context a fine-tuning level of 1 % means that the bare mass of the Higgs boson and the corrections due to higher orders would have to compensate each other by 99 %, so that the physically observable mass of the Higgs boson corresponds only to 1 % of the bare value of  $\mu$  before higher-order corrections. According to Fig. 3.1, both a physical mass of the Higgs boson smaller than 130 GeV, as well as larger then 300 GeV implies fine-tuning by more than 10 % if the SM remains without any signs of new physics beyond a scale of  $\Lambda \approx 5 \,\text{TeV}$ .

### 3.2 Indirect Constraints from Electroweak Precision Measurements

Particles which cannot be directly observed at lower energy scales still have an indirect influence on observable quantities due to higher-order corrections in loops. These corrections can result in shifts of particle masses, coupling constants, branching ratios or production cross sections, depending on whether they appear in propagator terms, in the vertices or in the legs of a given leading-order process. The circumstance that higher-order corrections can depend both, on the mass of the top quark and on the mass of the SM Higgs boson has been utilized to predict these masses, even before the discovery of each of these particles had been made. This has been done in a global analysis of a number of observables that had been measured with very high precision in  $e^+e^-$  collisions at the Stanford Linear Accelerator (SLAC) and the LEP collider [5]. Two examples of loop corrections, via which the top quark influences the decay of the Z boson into b-quarks in  $e^+e^-$  collisions, are shown in Fig. 3.2. Some more examples of loop corrections to the bosonic propagator, via which both the Higgs boson, and the top quark have influence on the mass of the W and Z boson, are shown in Fig. 3.3.

### 3.2.1 Electroweak Precision Observables

Since the effect of loop corrections sets in at higher order, they are small (typically less than 1% for electroweak corrections) and become significant only for observables which can be measured with an equally high precision. The observables in question have been:

- the mass,  $m_Z$ , and decay width,  $\Gamma_Z$ , of the Z boson; the hadronic pole cross section,  $\sigma_{\rm had}^0$ , of the process  $ee \to q\bar{q}$ ;

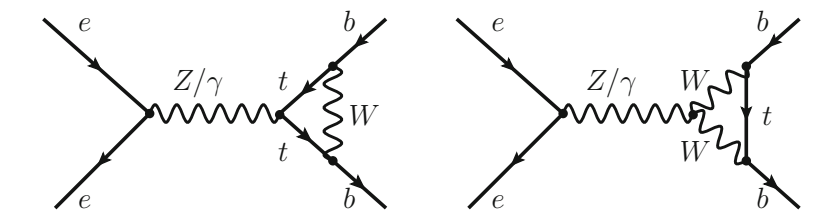


Fig. 3.2 Two examples of higher-order corrections via which the *top* quark influences the decay of the Z boson into b-quarks in  $e^+e^-$  collisions at *LEP*. The shown diagrams appear as corrections  $\mathcal{O}(\alpha^2)$ , to the leading-order process, which is  $\mathcal{O}(\alpha)$  (where  $\alpha = q^2/4\pi$  refers to the fine structure constant). Since  $\alpha \approx 1/137$ , this results in corrections to the leading-order process, which are  $\mathcal{O}(1\%)$ 



**Fig. 3.3** Schematic sketch for higher-order corrections to the propagator of the heavy gauge bosons. In the left and middle sub-figure the exchange of a virtual Higgs boson is shown. In the sub-figure on the right a fermion anti-fermion pair is running in the loop

- the ratio to the hadronic decay width,  $R_f^0 = \frac{\Gamma_f}{\Gamma_{q\bar{q}}}$  for the decay width for *b*-quarks  $(R_b^0)$ , *c*-quarks  $(R_c^0)$  and leptons  $(R_l^0)$  (excluding *top* quarks from  $\Gamma_{q\bar{q}}$ , which were not yet discovered by that time);
- the asymmetry  $A_{FB}^{0,X} = \frac{\sigma_F^X \sigma_B^X}{\sigma_F^X + \sigma_B^X}$  of the forward and backward decay of Z bosons into b-quarks  $(A_{FB}^{0,b})$ , c-quarks  $(A_{FB}^{0,c})$  and leptons  $(A_{FB}^{0,l})$ , where "forward" refers to the direction of the  $e^-$  for particles and to the direction of the  $e^+$  for anti-particles; the asymmetry  $A_X = \frac{g_{LX}^2 g_{RX}^2}{g_{LX}^2 + g_{RX}^2}$  of the coupling to left- and right-handed leptons for b-quarks  $(A_b)$ , c-quarks  $(A_c)$  and leptons  $(A_l)$ . The observable  $A_l$  could be
- the asymmetry  $A_X = \frac{g_{LX} g_{RX}}{g_{LX}^2 + g_{RX}^2}$  of the coupling to left- and right-handed leptons for *b*-quarks  $(A_b)$ , *c*-quarks  $(A_c)$  and leptons  $(A_l)$ . The observable  $A_l$  could be directly measured at the *SLAC* Large Detector (SLD), which was operated with polarized beams. At the *LEP* experiments, which did not have access to polarized beams, the distinction between left- and right-handed leptons was made in final state decays making use of the polarization of  $\tau$ -leptons;
- the effective electroweak mixing angle,  $\sin^2\theta_{\rm eff}^{\rm lep}$ , determined from  $q\bar{q}$  charge asymmetry measurements.

For all measurements referring to leptons, lepton universality had been assumed and the observables had been corrected for initial and final state *QED* radiation and final state *QCD* radiation.<sup>1</sup> To indicate where such corrections had been applied to

<sup>&</sup>lt;sup>1</sup>The *QED* corrections had been calculated up to  $\mathcal{O}(\alpha^3)$ , including initial and final state interference effects up to  $\mathcal{O}(\alpha)$ . The *QCD* corrections had been calculated up to  $\mathcal{O}(\alpha_s^3)$  and  $\mathcal{O}(\alpha \cdot \alpha_s)$ , with  $\alpha_s$  being the strong coupling constant. *QCD* corrections are necessary for all observables which imply the presence of quarks in the final state.

the measured observables, the observables had been marked by a superscript "0". Since these quantities do not correspond to the directly measured observables any more, they were referred to as *pseudo-observables* in the literature. The wealth of high precision calculations that have been applied to correct the measurements, give an idea of the great effort, that has been made to reach a theoretical uncertainty on the predictions of these observables that matches the experimental precision of the analyzed data. This high level of theoretical and experimental precision is a prerequisite for any analysis trying to make use of the contributions of higher-order corrections to observable quantities as in this case.

After the *LEP-I* running period, these measurements have been complemented by a precise measurement of the mass,  $m_W$ , and the decay width,  $\Gamma_W$ , of the W boson as measured in the *LEP-II* running period [6] and at the *Tevatron* [7, 8] and by the measurement of the *top* quark mass,  $m_t$ , as measured at the *Tevatron* [9]. In addition the obtained results have been crosschecked with data obtained from experiments operated at much lower energy scales, like the measurement of atomic parity violation in cesium [10], measurements of the electroweak mixing angle in Møller scattering at the *E-158* experiment [11, 12] and the ratio of the neutral to charged current scattering cross section measured by the *NuTeV* collaboration [13].

A summary of all measurements that have been used in the global analysis to constrain  $m_H$  and  $m_t$  are summarized in Table 3.2. The relative uncertainty of the high precision measurements at the Z-pole mass (including systematic uncertainties) ranges from  $\mathcal{O}(10^{-5})$ , for  $m_Z$ ,  $\mathcal{O}(10^{-4})$ , for  $m_W$ , to  $\mathcal{O}(10^{-2})$ , for  $\Gamma_W$ .

### 3.2.2 Statistical Model

The statistical model, from which the constraints on  $m_t$  and  $m_H$  were determined, was based on an estimate of higher-order corrections to Eq. (2.38)

$$m_W^2 = \frac{m_Z^2}{2} \left( 1 + \sqrt{1 - 4 \frac{\alpha \pi}{\sqrt{2} G_F m_Z^2} \cdot \frac{1}{1 - \Delta r}} \right)$$

For the calculations the corrections had been parametrized by  $\Delta r = \Delta \alpha + \Delta r_W$ , where  $\Delta \alpha$  refers to higher-order vertex corrections to  $\alpha$  due to vacuum polarization effects. This term had been further split into contributions from leptonic, *top* quark and light quark loops,  $\Delta \alpha = \Delta \alpha_{\rm lep} + \Delta \alpha_{\rm top} + \Delta \alpha_{\rm had}^{(5)}$ , according to the challenges imposed by the calculations. The dependency on  $m_t$  and  $m_H$  enters via higher-order corrections to the W boson propagator, as sketched in Fig. 3.3 and parametrized by the term  $\Delta r_W$ . At one-loop level  $\Delta r_W(m_t, m_H)$  takes the form

$$\Delta r_W(m_t, m_H) \simeq \frac{\alpha}{\pi \sin^2 \theta_W} \left( -\frac{3}{16} \frac{\cos^2 \theta_W}{\sin^2 \theta_W} \frac{m_t^2}{m_W^2} + \frac{11}{24} \log \left( {^{m_H}/_{m_Z}} \right) \right)$$

**Table 3.2** (Pseudo-)Observables that have been used as input for the global SM analysis performed by the *LEP* Electroweak Working Group as given in [6]

<u> </u>						
(Pseudo-)observable	Measured value	Fit result	$(\mathcal{O}_{\mathrm{meas}} - \mathcal{O}_{\mathrm{fit}})/\sigma_{\mathrm{meas}}$			
	Z-pole Electroweak	Precision Observables				
$\Delta \alpha_{\rm had}^{(5)}(m_Z)$	$0.02750 \pm 0.00033$	0.02759	-0.3			
$m_Z$ [GeV]	$91.1875 \pm 0.0021$	91.1874	0.0			
$\Gamma_Z$ [GeV]*	$2.4952 \pm 0.0023$	2.4959	-0.3			
$\sigma_{\rm had}^0$ [nb]	$41.540 \pm 0.037$	41.478	1.7			
$R_l^0$	$20.767 \pm 0.025$	20.742	0.7			
$R_b^0$	$0.21629 \pm 0.00066$	0.21579	1.0			
$R_c^0$	$0.1721 \pm 0.0030$	0.1723	-0.1			
$\overline{A_{FB}^{0,l}}$	$0.0171 \pm 0.0010$	0.0164	0.7			
$R_{l}^{0}$ $R_{b}^{0}$ $R_{c}^{0}$ $A_{FB}^{0,l}$ $A_{FB}^{0,l}$ $A_{FB}^{0,c}$	$0.0992 \pm 0.0016$	0.1038	-2.9			
$A_{FB}^{0,c}$	$0.0707 \pm 0.0035$	0.0742	-1.0			
$\mathcal{A}_l(\mathcal{P}_{\ll})^{\dagger}$	$0.1465 \pm 0.0033$	0.1481	-0.5			
$A_b$	$0.923 \pm 0.020$	0.935	-0.6			
$A_c$	$0.670 \pm 0.027$	0.668	0.1			
$\sin^2 \theta_{\rm eff}^{\rm lep}$	$0.2324 \pm 0.0012$	0.231439	0.8			
$\mathcal{A}_l(\mathrm{SLD})^{\star\dagger}$	$0.1513 \pm 0.0021$	0.1481	1.6			
Additional High Energy Measurements						
$m_W$ [GeV]* <sup>†</sup>	80.385± 0.015	80.377	0.5			
$\Gamma_W$ [GeV]	$2.085 \pm 0.042$	2.092	-0.2			
$m_t$ [GeV]*	$173.2 \pm 0.9$	173.3	-0.1			
Crosscheck with Low Energy Measurements						
$Q_W(Cs)$	$-72.74 \pm 0.46$	-72.909	0.4			
$\sin^2\theta_{\overline{MS}}(M_Z)$	$0.2330 \pm 0.0015$	0.02311	1.3			
$g_{\nu Lud}^2$	$0.30005 \pm 0.00137$	0.30397	2.9			
$g_{\nu Rud}^2$	$0.03076 \pm 0.00110$	0.03011	0.6			

In the second column the measured value and the uncertainty for each observable are given (including theoretical uncertainties). The result of the  $\chi^2$  minimization based on only the Z-pole high precision data (upper part of the table) and the compatibility of this result with the data are shown in the third and fourth column. The most sensitive single (pseudo-)observables for the determination of  $m_t$  (log( $^mH/_{\rm GeV}$ )) have been indicated by a  $\star$  (†)

where  $m_t$  ( $m_H$ ) enters the calculation with a quadratic (logarithmic) dependency. Since the leading-order relation of Eq. (2.38) is protected by a custodial symmetry, as discussed in Sect. 2.4.1,  $\Delta r_W$  is expected to be small to all orders in perturbation theory, such that the leading-order dependency, with which  $m_t$  and  $m_H$  enter the calculation would not be subject any more to significant changes after corrections of even higher order. The stronger dependency, in return, gives the stronger predictive power to the estimate of  $m_t$ .

For the final estimate the complete fermionic and bosonic two-loop corrections to the propagator term had been used, including contributions of  $\mathcal{O}(\alpha \cdot \alpha_s)$  in cases

where quarks are involved. For the vertex correction the complete fermionic two-loop corrections for the calculation of  $\sin^2\theta_{\rm eff}^{\rm lep}$  had been calculated, including three-loop contributions from the top quark. The remaining theoretical uncertainties due to missing higher orders had been estimated to be 4 MeV on  $m_W$  and  $4.9 \times 10^{-5}$ on  $\sin^2 \theta_{\rm eff}^{lep}$  and thus negligible compared to the experimental uncertainty or theoretical uncertainties from the light quark component of the vacuum polarization term. The correction term  $\Delta \alpha_{\rm lep}(m_Z) = 0.03150$  had been calculated to third-order accuracy with negligible remaining uncertainty, the term  $\Delta \alpha_{top} = -0.00007(1)$  had been determined at second-order accuracy together with the corrections to  $m_W$ . For light quark loops a diagrammatic approach to calculate  $\Delta \alpha_{\rm had}^{(5)}$  is not viable since at such low energy scales perturbative QCD is not applicable any more. Therefore,  $\Delta\alpha_{\rm had}^{(5)}=0.02750\pm0.00033$ , had been taken from an independent measurement of the hadronic cross section in  $e^+e^-$  collisions based on the data of the experiments BES, CMD-II and CLOE, which had been operated at lower center-of-mass energies. The theoretical uncertainties on the prediction of  $m_t$  (log( $^{m_H}/_{\text{GeV}}$ )) due to  $\Delta\alpha_{had}^{(5)}$  were  $\mathcal{O}(0.2\,\text{GeV})$  ( $\mathcal{O}(0.1)$ ), resulting in the dominant uncertainty on the theoretical description.

For the statistical inference, a five parameter minimum  $\chi^2$  fit had been applied with  $\Delta\alpha_{\rm had}^{(5)}(m_Z)$ ,  $\alpha_s(m_Z)$ ,  $m_Z$ ,  $m_t$  and  $\log(^{m_H}/_{\rm GeV})$  as parameters of interest following the parametric dependencies of the observables in the theoretical model. In the main analysis the  $\chi^2$  minimization had been applied only to the input value of  $\Delta\alpha_{\rm had}^{(5)}$  and to the fourteen Z pole measurements, as listed in the upper part of Table 3.2. With these fifteen input variables and the five parameters of interest, the minimization is left with 10 degrees of freedom. The result of the minimization is shown in the third column of Table 3.2. In the fourth column of the table, the compatibility of the minimization result with the data is shown, expressed by the difference between the measured value and the central value of the fit divided by the combined theoretical and experimental uncertainty of the measurement. This analysis constitutes the constraint only of the high precision Z pole measurements made at *LEP* and *SLAC* on  $m_t$  and  $\log(m_H/_{\text{GeV}})$ . In an expansion of the analysis the minimization had been augmented by the most precise measurements of  $m_W$ ,  $\Gamma_W$  and  $m_t$ , as listed in the middle part of Table 3.2, which had been obtained from the LEP-II data taking period and from the Tevatron experiments. The observables from the low energy experiments, which are listed in the lower part of Table 3.2 have been found to have only little influence on the final result and have only been used to crosscheck the results of the main analysis. The observables being used as input for the minimization can be combined into three groups:

- observables, which are among the five parameters of interest, like  $\Delta \alpha_{\rm had}^{(5)}$ ,  $m_Z$  and  $m_t$ . These observables naturally lead to the most direct constraints on the corresponding parameters;
- observables, which have a high sensitivity to the electroweak radiative corrections and are therefore important for the determination of the five parameters of interest;

observables, which compared to their experimental uncertainty, do not have a
strong parametric dependency on the five parameters of interest, but are of relevance to test other important properties of the SM, like the number of fermion
generations and the quantum numbers of weak isopin and electric charge. These
observables were kept in the minimization procedure to guarantee that these important properties are sustained. Examples for such observables are σ<sup>0</sup><sub>had</sub> and most of
the left-right and forward-backward asymmetries for quarks.

To obtain an estimate of the single observable sensitivity for the determination of  $m_t$  (log( $^mH/_{\text{GeV}}$ )) the partial derivative of the parametrization with respect to  $m_t$  (log( $^mH/_{\text{GeV}}$ )) for each of the eighteen observables had been multiplied with an estimate for the uncertainty on  $m_t$  (log( $^mH/_{\text{GeV}}$ )) and compared to the experimental uncertainty of the corresponding observable. For this estimate for  $m_t$  the uncertainty had been chosen to be 4.3 GeV. For log( $^mH/_{\text{GeV}}$ ) the uncertainty had been chosen to be 0.2, which for a central value of  $m_H \approx 150 \,\text{GeV}$  corresponds to a variation by  $\pm 50 \,\text{GeV}$ . In this way  $m_t$ ,  $m_W$  and  $A_t$  (SLD) had been found to be the most sensitive single observables for the estimate of  $m_t$  (with  $\Gamma_Z$  and  $A_{FB}^{0,b}$  being the next most sensitive observables, when restricted to only the Z-pole measurements). For the estimate of  $\log(^mH/_{\text{GeV}})$   $m_W$ ,  $A_t$  (SLD) and  $A_{FB}^{0,b}$  have been found to be the most sensitive single observables (with  $A_t$  ( $P_T$ ) being the next most sensitive observable, when restricted to the Z-pole measurements). It should be noted that these estimates are approximate and do not take the correlations of the measurements into account.

## 3.2.3 Results of the Likelihood Analysis

The results of the minimization in the main analysis, when using only the high precision Z-pole observables as inputs, are shown in Table 3.3. The minimization procedure results in a  $\chi^2$  of 16 for 10 degrees of freedom, corresponding to a  $\chi^2$  probability of 9.9%. The largest (positive) correlation among the parameters of interest in the minimization emerges between the two most interesting parameters  $m_t$  and  $\log(^{m_H}/_{\rm GeV})$ , with 89%. The fit results in a prediction of  $m_t=173\pm11.5\,{\rm GeV}$  (with an uncertainty of 7%) and a constraint of  $m_H=111\pm^{160}_{90}\,{\rm GeV}$ . It is remarkable how well the analysis of only the Z-pole measurements predicted the mass of the top quark  $m_t$ , which was not yet known by the time of the first publication of the fit results

Adding  $m_W$ ,  $\Gamma_W$  and  $m_t$  to the input observables increased the  $\chi^2$  to 18.3 for 13 degrees of freedom, corresponding to a  $\chi^2$  probability of 15%. The correlation between  $m_t$  and  $\log(^{m_H}/_{\rm GeV})$  was reduced to 67%, while it remained the largest correlation among all parameters of interest. The prediction of  $m_t$  changed to 178.5  $\pm$  3.9 GeV (with a much reduced uncertainty, due to the constraint of the direct measurement) and the constraint of  $m_H$  changed to 129 $\pm_{40}^{74}$  GeV.

The  $\chi^2$  probability is not exceptionally high, but still demonstrates good compatibility of the high precision observables with the predictions of the SM. A closer

taking period a	s input as given in [5]					
Parameter	Best fit value	$\Delta \alpha_{\rm had}^{(5)}(m_Z)$	$\alpha_s(m_Z)$	$m_Z$	$m_t$	$\log(^mH/\text{GeV})$
$\Delta \alpha_{\rm had}^{(5)}(m_Z)$	$0.02759 \pm 0.00035$	1.0				
$\alpha_s(m_Z)$	$0.1190 \pm 0.0027$	-0.04	1.0			
$m_Z$	$91.1874 \pm 0.0021$	-0.01	-0.03	1.0		
$m_t$	$173 \pm 11.5$	-0.03	0.19	-0.07	1.0	
$\log(m_H/_{\rm GeV})$	$2.05 \pm 0.385$	-0.29	0.25	-0.02	0.89	1.0

**Table 3.3** Most probable values and correlation matrix for the parameters of interest from the  $\chi^2$ minimization only with  $\Delta\alpha_{\rm had}^{(5)}(m_Z)$  and the high precision Z-pole observables of the *LEP-I* data taking period as input as given in [5]

The  $\chi^2$ /ndf of this minimization is 16/10, corresponding to a  $\chi^2$  probability of 9.9 %. The most probable value of  $\log(^mH/\text{GeV}) = 2.05 \pm 0.385$  corresponds to a value of  $m_H = 111 \pm \frac{160}{90}$  GeV.

look into the differences between the fit result and the measurements, shown in Table 3.2 reveals a difference of  $+1.7\sigma_{\rm meas}$  for  $\sigma^0_{\rm had}$  (which is not very sensitive to the determination of  $m_t$  or  $m_H$ ), a difference of  $+1.6\sigma_{\rm meas}$  for  $\mathcal{A}_l({\rm SLD})$ , a difference of  $-2.9\sigma_{\rm meas}$  for  $A_{FB}^{0,b}$  and a difference of  $+2.9\sigma_{\rm meas}$  for the coupling  $g^2_{\nu Lud}$  in neutrino-nucleon scattering. Of those only  $A_{FB}^{0,b}$  and  $g^2_{\nu Lud}$  are really worrisome when considering the number of observables and the size of the differences. The issue with the large difference on  $g^2_{\nu Lud}$  has been resolved by a reassessment of nuclear effects in the determination of  $\sin^2\theta_W$  in [14]. The difference of  $A_{FB}^{0,b}$  has been discussed in detail in [5] and no issues have been found neither with the prediction nor with the measurement. So the difference has been considered as a result of a fluctuation, which is especially unfortunate since  $A_{FB}^{0,b}$  turns out to be one of the most sensitive variables, in the determination of both  $m_t$  and  $m_H$ . It is this measurement which takes the largest responsibility on the increased value of  $\chi^2$ , enhanced by  $\mathcal{A}_l({\rm SLD})$  (with a difference of  $+1.6\sigma_{\rm meas}$ ) pulling the result of the minimization into the opposite direction. It has been tested, that dropping  $A_{FB}^{0,b}$  or  $\mathcal{A}_l({\rm SLD})$  individually or both at the same time in the minimization procedure, while significantly improving the value of  $\chi^2/ndf$  (to 8.7/11 corresponding to a  $\chi^2$  probability of 65 %, when both observables are dropped) changes the most probable value of  $m_H$  by less than one sigma of the obtained fit uncertainty when compared to the most probable value as obtained when including both observables. More details can be found in [5].

While the high precision Z-pole measurements have been unchanged since their publication in 2005, the measurements of  $m_W$  and  $m_t$  from the *Tevatron* had been regularly updated. The last update of the analysis that had been made in March 2012, shortly before the discovery of the new particle at the *LHC*, is shown in Fig. 3.4 (left), with  $m_t$  on the x-axis and  $m_W$  on the y-axis. The red dashed line in the figure corresponds to the 68% confidence level (CL) contour of the fit to the *LEP-I* and *SLAC* data only. This contour corresponds to the constraints as obtained from the main analysis, as described above. The blue continuous line corresponds to the 68% CL contour of the combination of the direct measurements of  $m_W$  from *LEP-II* and the direct measurements of  $m_W$  and  $m_t$  from the *Tevatron* experiments. The agreement

between the indirect constraints and the direct measurements is remarkable. Also shown is the relationship between  $m_W$  and  $m_t$  as predicted in the SM for a given value of  $m_H$ , in the mass range between 114 and 1000 GeV. The (bright) yellow shaded area indicates the ranges of  $m_H$  that had already been excluded by the searches at the LHC by that time, while the (dark) green shaded areas indicate the regions that were still allowed. Obviously the indirect constraints and even more the direct measurements of  $m_W$  and  $m_t$  favored a light over a heavy Higgs boson. Accurate measurements of these three masses will constitute a strong test of the SM in future. As discussed before the largest theoretical uncertainty in the analysis of the high precision Z-pole data is the contribution of light quarks to the fine structure constant  $\alpha(m_Z)$ . The arrow labeled by  $\Delta \alpha$  in the figure indicates the size and direction of the effect of a change of  $\alpha(m_Z)$  by  $+1\sigma$  of the estimate of this uncertainty on the lines of constant  $m_H$ .

In Fig. 3.4 (right) the difference of the  $\chi^2$  function with respect to the global minimum,  $\Delta \chi^2$ , is shown, as a function of  $m_H$ , based on the Z-pole measurements and the direct measurements of  $m_W$ ,  $\Gamma_W$  and  $m_t$  from *LEP-II* and the *Tevatron* experiments. It corresponds, in a good approximation, to a parabola with a minimum at  $m_H = 94\pm_{24}^{29}$  GeV. From the scan of  $\Delta \chi^2$  an upper limit of  $m_H \leq 152$  GeV at 95 % CL could be derived. The (bright) yellow shaded areas in the figure correspond to regions of  $m_H$  that were experimentally already excluded by the searches at *LEP* and at the *LHC*, by that time. The red dashed line indicates the effect of a different

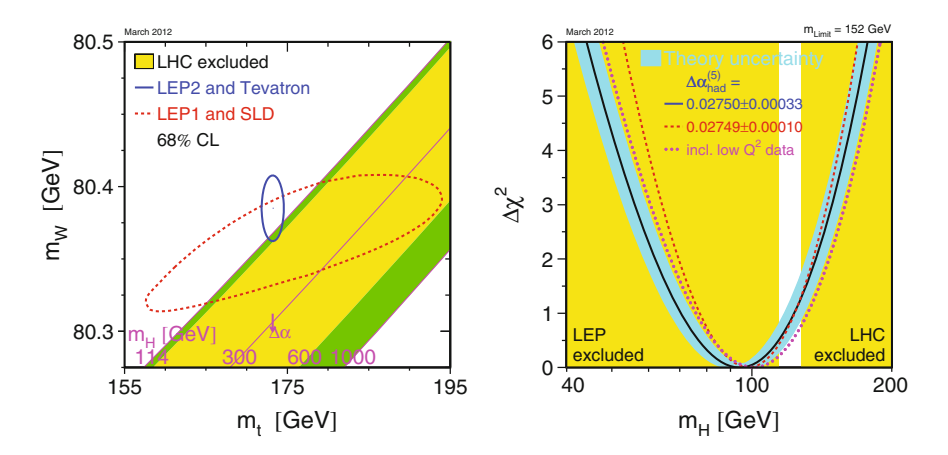


Fig. 3.4 Results of the indirect constraints of the high precision measurements at *SLAC*, *LEP* and *Tevatron* [5]. On the left the indirect constraint on  $m_W$  and  $m_t$  is shown in comparison to the direct measurements at *LEP-II* and the *Tevatron*. On the right the difference of the  $\chi^2$  value of the minimization based on the high precision *Z*-pole measurements,  $m_W$ ,  $\Gamma_W$  and  $m_t$  with respect to the global minimum,  $\Delta \chi^2$ , is shown, as a function of  $m_H$ . These plots have been updated several times to resemble the most up to date inputs from *LEP-II* and *Tevatron*. The last update has been made in March 2012, shortly before the discovery of the new particle at the *LHC*. A more detailed description of the plots is given in the text

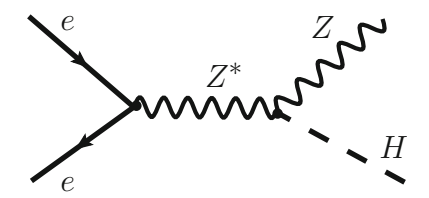
input value of  $\Delta\alpha_{\rm had}^{(5)}$  and the magenta dotted line the effect of including the low energy measurements listed in the lower part of Table 3.2. It should be noted though that the *NuTeV* data should not be considered valid any more as previously discussed in this section. Since their beginning the global fits of the SM to the electroweak high precision (pseudo-)observables from *LEP*, *SLAC* and the *Tevatron* experiments favored low values of  $m_H \approx 100\,\text{GeV}$ . This was one of the main motivations for the direct searches for the Higgs boson at *LEP*, which will be discussed in the next section. The most recent fit before the discovery of the new particle at the *LHC*, as shown in Fig. 3.4, was compatible within  $\approx 1\sigma$  with the allowed mass range between 120 GeV and 130 GeV given by the searches at the *LHC* experiments, by that time. The prediction of  $m_t$  and  $m_H$  before the discovery of the *top* quark and the Higgs boson constitutes a great triumph of the predictive power of the SM.

### 3.3 Direct Searches at the Large Electron Positron Collider

The LEP collider had been operated at a center-of-mass energy corresponding to  $m_Z$  from 1989 until 1995. After this period it was subject to a substantial energy upgrade to open the kinematic phasespace for W boson pair production and to further investigate the electroweak sector of the SM. The LEP-II data taking period lasted from 1996 until 2000 [15]. During this time the LEP collider produced a dataset of 2.461 fb<sup>-1</sup> of  $e^+e^-$  collisions at center-of-mass energies of  $\sqrt{s} \ge 189\,\text{GeV}$ , including a subset of 0.536 fb<sup>-1</sup> at center-of-mass energies of  $\sqrt{s} \ge 206\,\text{GeV}$ . On this dataset the four LEP experiments conducted a direct search for the SM Higgs boson [16] which set path and defined the statistical framework for all subsequent searches in the following years. This framework will be discussed in the context of the SM Higgs boson searches at LEP in more detail in this section.

Since the Higgs boson coupling is proportional to the particle masses the dominant production mode at LEP was in association with Z bosons as illustrated in Fig. 3.5. The accessible range of  $m_H \lesssim (\sqrt{s} - m_Z) \approx 116\,\text{GeV}$  was given by the maximal center-of-mass energy of the collisions that could be achieved by the accelerator. The main decay channel of the SM Higgs boson in this mass range is into b-quarks with a branching fraction of 70 % at  $m_H = 115\,\text{GeV}$ , followed by the next largest branching fraction of 7.65 % for the decay into  $\tau$ -leptons [17]. Therefore, the main search

Fig. 3.5 Schematic view of Higgs boson production in association with a Z boson, which was the main mode for SM Higgs boson production in  $e^+e^-$  collisions at LEP



channel was in the final state with four jets,  $Z(q\bar{q})H(b\bar{b})$ , complemented by the final states  $Z(\nu\nu)H(b\bar{b})$ ,  $Z(\ell\ell)H(b\bar{b})$  (where  $\ell$  stands for an electron, muon or  $\tau$ -lepton), and  $Z(q\bar{q})H(\tau\tau)$ , indicating the final state particles in braces. Main backgrounds for these searches were made up from diphoton, WW and ZZ production. For the search, the data of all four *LEP* experiments had been combined into one single analysis. From each experiment the data, the number of expected background events and the number of expected signal events had been provided in the form of two-dimensional distributions, given as a function of the reconstructed invariant mass of the Higgs boson candidate,  $m_H^{\rm rec}$ , and one additional variable, into which several quantities had been combined to distinguish the signal from the main backgrounds. The expected signal and background processes had been obtained from simulation using Monte-Carlo methods and taking all known effects of selection inefficiencies and object resolutions into account to best knowledge, including potential non-Gaussian effects. The expected number of signal events had been provided for several hypotheses of  $m_H$ . To obtain estimates also for values of  $m_H$  that had not been fully simulated linear template interpolation methods had been applied [18].

#### 3.3.1 Statistical Framework

The statistical inference of the search had been made in form of a classical hypothesis test, where the presence of a SM Higgs boson signal with a given mass,  $m_H$ , in addition to the expected background from non-SM Higgs boson events had been considered as the "signal plus background" (s+b)-hypothesis, while the presence only of the expected non-SM Higgs boson processes was referred to as the "background only" (b)-hypothesis. As test statistic a likelihood ratio had been chosen defined as

$$Q = \frac{\mathcal{L}_{s+b}}{\mathcal{L}_{b}} = \prod_{k=1}^{N} \left( e^{-s_{k}} \cdot \prod_{j=1}^{n_{k}} \frac{s_{k} S_{kj} + b_{k} B_{kj}}{b_{k} B_{kj}} \right)$$

$$\mathcal{L}_{s+b} = \prod_{k=1}^{N} \left( \frac{(s_{k} + b_{k})^{n_{k}}}{n_{k}!} e^{-(s_{k} + b_{k})} \cdot \prod_{j=1}^{n_{k}} \frac{s_{k} S_{kj} + b_{k} B_{kj}}{s_{k} + b_{k}} \right)$$

$$\mathcal{L}_{b} = \prod_{k=1}^{N} \left( \frac{b_{k}^{n_{k}}}{n_{k}!} e^{-b_{k}} \cdot \prod_{j=1}^{n_{k}} \frac{b_{k} B_{kj}}{b_{k}} \right)$$
(3.8)

where k runs over all independent measurements provided per experiment, run period or decay channel,  $n_k$  corresponds to the observed number of events and  $s_k$  and  $b_k$  to the expected number of signal and background events per measurement. Since the individual measurements were provided as binned distributions the quantities  $S_{kj}$  and  $B_{kj}$  correspond to the probability functions to observe a given event j in a given bin, based on the signal or background hypothesis. The index j thus runs

over all events for a given measurement, k. The two likelihood functions  $\mathcal{L}_{s+b}$  and  $\mathcal{L}_b$  were constructed from *Poisson* distributions for each measurement based on the (s+b)- and the b-hypothesis. In the likelihood functions  $s_k$  and  $S_{kj}$  did depend on the hypothesis of  $m_H$ .

Systematic uncertainties were incorporated in the form of nuisance parameters, e.g. replacing the parameter  $b_k$ , for the normalization of a background process by a product with a log-normal probability density function

$$b_k \to b_k \cdot f(\theta_k, \sigma_k, x) = \begin{cases} \frac{b_k}{\sqrt{2\pi}x\sigma_k} e^{-(\ln(x) - \theta_k)^2/\sigma_k^2} & x > 0\\ 0 & x \le 0 \end{cases}$$
(3.9)

where  $\theta_k$ , corresponds to the best known value of  $b_k$  and  $\sigma_k$  to its uncertainty. The variable x in this function will be integrated out in the further steps of the statistical inference as will be discussed in the following paragraphs. The likelihood functions of Eq. (3.8) were thus extended by a product with a term of the type of Eq. (3.9) for each considered uncertainty. Typical probability density functions for the incorporation of nuisance parameters for background normalizations (which are bound to be  $\geq 0$ ) are log-normal distributions as given above or truncated Gaussian distributions.

For convenience in the minimization procedure usually the logarithmic form of the test statistic is used

$$q = -2\ln Q = 2\sum_{k=1}^{N} \left( s_k - \sum_{j=1}^{n_k} \ln \left( 1 + \frac{s_k S_{kj}}{b_k B_{kj}} \right) \right)$$
(3.10)

which corresponds to the difference in  $\chi^2$  for the comparison between  $\mathcal{L}_{s+b}$  and  $\mathcal{L}_b$  in the limit of high statistics, according to the central limit theorem of de Moivre and Laplace. In this representation each event in the analysis contributes with a certain weight depending on whether it is more signal- or background-like. If the full dataset is more (s+b)- than b-like, Q will be >1 and q<0. If the full dataset will be more b-like, q will be >0 correspondingly. The more (s+b)-like the dataset is the smaller the quantity q will be. Within the dataset an event which is more signal- than background-like will contribute with a larger weight  $\ln\left(1+\frac{s_kS_{kj}}{b_kB_{kj}}\right)$  to the sum of q.

For data the test statistic, q, can be obtained as a single number, which may vary as a function of the tested hypothesis for  $m_H$ . For the estimation of q the nuisance parameters are evaluated at their a priori best known values  $\theta_k$ . For an assessment on whether the obtained value of q does point to an observation of signal or not, it

<sup>&</sup>lt;sup>2</sup>To be accurate in the test statistic as used by the *LEP* experiments the probability functions,  $f(\theta_k, \sigma_k, x)$  to obtained a measured value x for a true value  $\theta_k$  were translated into a probability function  $\tilde{f}(x, \sigma_k, \theta_k)$  to have a true value of  $\theta_k$  for a measured value of x using *Bayes'* theorem. It was thus a frequentist-bayesian hybrid *ansatz*. This was still true for the test statistic as used by the *Tevatron* experiments but not any more for the test statistic as used by the *LHC* experiments, where  $f(\theta_k, \sigma_k, x)$  was used e.g. as given in Eq. (3.9) and estimates for the true value of  $\theta_k$ , for each hypothesis were obtained from the corresponding fit.

needs to be compared to the expectation based on the (s + b)- and the b-hypothesis. These expectations and their uncertainties are derived from probability density functions, which are obtained from a large number of pseudo-experiments, based on the expected number of events in each bin of the input distributions, according to the corresponding hypothesis. For the creation of each pseudo-experiment a random value is determined from each likelihood function in Eq. (3.8) to form a value of q. For the determination of q not only the expectation values,  $\theta_k$ , of the nuisance parameters, but also their uncertainties,  $\sigma_k$ , are taken into account. To illustrate how this works, an example will be given for a normalization uncertainty of a given background process  $b_k$ : assume that in the likelihood functions  $\mathcal{L}_b$  and  $\mathcal{L}_{s+b}$  the fixed values for  $b_k$  have been replaced by probability density functions as given in Eq. (3.9). Prior to the creation of each pseudo-experiment, a random value  $b'_k$  is chosen according to this probability density function. This procedure is equivalent to the numerical integration of the variable x in Eq. (3.9). Since the probability density function is normalized to unity the integration leaves the expected over all vields unchanged. Normalization uncertainties which are correlated across measurements, measurement bins or experiments, like theoretical uncertainties or uncertainties on the measured luminosity, are evaluated based on the same random number. With the values of  $b'_{k}$  the pseudo-experiment is created in a subsequent step. The creation of pseudo-experiments to determine the expected values of q thus takes all uncertainties due to limited knowledge of parameters and their correlations in the statistical model fully into account. The process, in which the uncertainties on the nuisance parameters are integrated out numerically during the creation of the pseudo-experiments is called marginalization. In this example it would require  $n_k$  random numbers for each independent measurement plus  $n_k$  additional random numbers for each uncorrelated nuisance parameter for each measurement.<sup>4</sup>

Ideally the number of pseudo-experiments for both the (s+b)- and the b-hypothesis is large to obtain a reliable estimate of the probability density functions. Depending on the expense of computing time for the generation of a single pseudo-experiment several millions of pseudo-experiments can be created. The mean or the median of these distributions for the (s+b)- and b-hypothesis are chosen to define the expected value of q for each hypothesis. The uncertainty on the expected value is obtained from the double sided 68 and 95% quantiles of the corresponding probability density function. The median, which shows a more stable behavior against statistical fluctuations than the mean, is usually the preferred choice for the expected value of q. Typical probability density functions for the LEP search to obtain a certain value of q for the b- and (s+b)-hypothesis and the observed value,  $q_{obs}$ , for three different values of  $m_H$  are shown in Fig. 3.6. Important integrals for the statistical inference are

<sup>&</sup>lt;sup>3</sup> In the frequentist-bayesian hybrid *ansatz* as described in Footnote 2 each value of x in this integration corresponds to a pseudo-measurement of the true value of  $\theta_k$ .

<sup>&</sup>lt;sup>4</sup>In practice the marginalization can take place prior to the determination of the probability density functions for q, leading to an additional broadening of the probability density functions due to all possible values of  $b'_{\nu}$ , with the same result as described above.

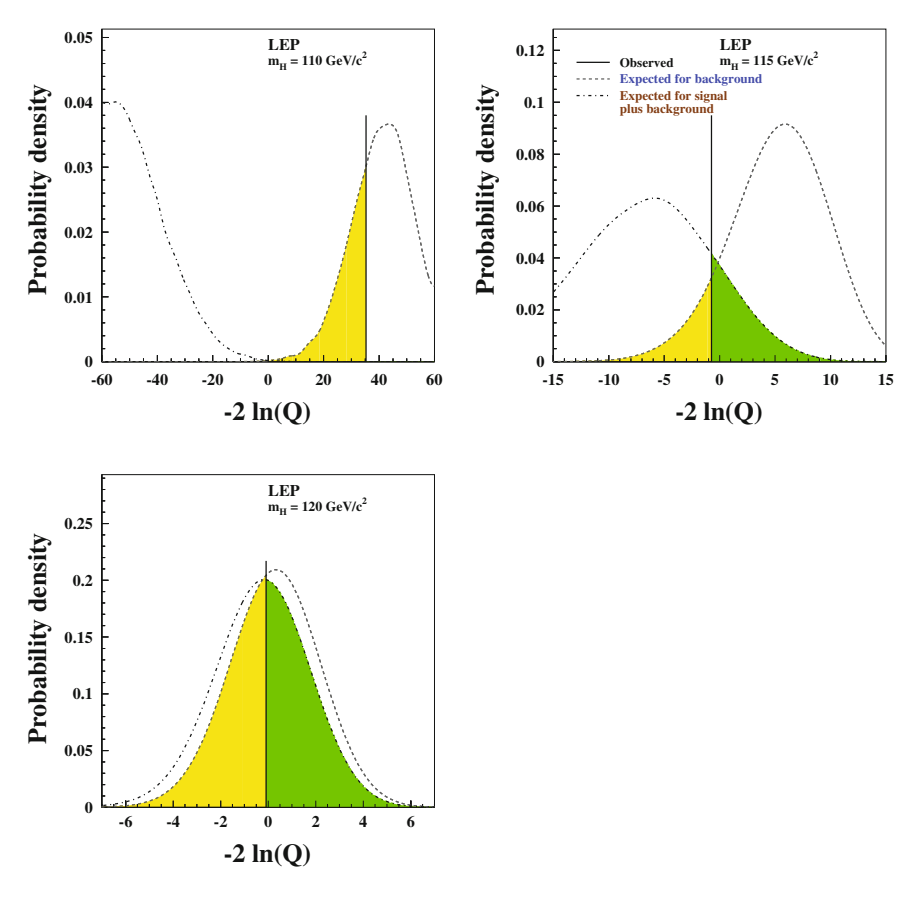


Fig. 3.6 Observed (black horizontal line) test statistic  $q=-2 \ln Q$  as defined in the text and probability density functions to obtain certain values of q for the (blue, dashed curve) b- and (brown, dash-dotted curve) (s+b)-hypothesis [15]. Values of q for an (s+b)-like dataset are <0, values for a b-like dataset are >0. The (bright) yellow area corresponds to the integral of the probability density function for the b-hypothesis from the left ( $-\infty$ ), the (dark) green area to the integral of the probability density function for the (s+b)-hypothesis from the right ( $+\infty$ ). These integrals are further discussed in the text. The probability density functions are shown for three different values of  $m_H$ 

$$(1 - CL_b) = \int_{-\infty}^{q_{\text{obs}}} \mathcal{P}_b \quad (p\text{-value})$$

$$CL_b = \int_{q_{\text{obs}}}^{+\infty} \mathcal{P}_b \quad (CL_b \text{ confidence})$$

$$CL_{s+b} = \int_{q_{\text{obs}}}^{+\infty} \mathcal{P}_{s+b} \quad (CL_{s+b} \text{ confidence})$$

$$CL_s = \frac{CL_{s+b}}{CL_b} \quad (CL_s \text{ confidence})$$

$$(3.11)$$

where  $\mathcal{P}_b$  corresponds to the probability density function for the *b*-hypothesis, shown as blue, dashed curves, and  $\mathcal{P}_{s+b}$  to the probability density function for the (s+b)-

hypothesis, shown as brown, dash-dotted curves, in the figure. Two of the integrals of Eq. (3.11) are also indicated by colored areas in the figure: the background confidence,  $(1 - CL_b)$ , or p-value, indicated by the (bright) yellow areas, corresponds to the probability that a value of  $q \le q_{\rm obs}$  (i.e. more (s+b)-like than observed) might be obtained from the b-hypothesis just due to statistical fluctuations in the measurement bins. This is a measure of the probability to incorrectly assign the outcome of the experiment to the (s+b)-hypothesis, while it belongs to the b-hypothesis (statistically the error of first kind). The value  $CL_{s+b}$ , indicated by the (dark) green area in the figure, corresponds to the probability to miss a discovery by incorrectly assigning the outcome of the experiment to the b-hypothesis, while it belongs to the (s+b)-hypothesis (error of second kind). All integrals of Eq. (3.11) are  $\leq 1$ .

The p-value is used to establish an excess of signal over the b-hypothesis. The  $CL_{s+b}$  value is used to exclude the (s+b)-hypothesis, if it falls below a predefined threshold. This threshold is arbitrary and corresponds to the level of confidence (CL), with which the hypothesis is rejected. In particle physics usually a value of 0.05 is chosen corresponding to a 95 % CL. This means that the probability that the experimental outcome might lead to a value of  $q \ge q_{obs}$  (i.e. more b-like than observed) and that the exclusion of an actually true (s + b)-hypothesis is  $\leq 5\%$ . It should be kept in mind, that with this convention there is still a 5% chance that the (s+b)-hypothesis in the end turns out to be true even if it is excluded at 95 % CL. The more separate the probability density functions for the two hypotheses are the better the measurement is suited to assign them, without misidentification. Figure 3.6 gives an impression how much the potential to separate the two hypotheses degraded when m<sub>H</sub> reached the kinematic limit, which was a tribute to the fact that the production cross section for the SM Higgs boson approached zero. For  $m_H = 120 \,\mathrm{GeV}$  the two hypotheses turned out to be nearly indistinguishable. The sensitivity reaching out beyond the kinematic boundary is due to the fact that the Higgs boson could still be produced virtually and decay into the visible decay products, which washes out the kinematic boundary to some extent.

In practice the  $CL_{s+b}$  value is not used for exclusions in particle physics, the reason being illustrated by the example of the test statistics for  $m_H = 120 \,\mathrm{GeV}$ in Fig. 3.6 (lower left). As discussed above in this case the analysis does not have the power to distinguish between the (s + b)- and the b-hypothesis. Since both probability density functions,  $\mathcal{P}_b$  and  $\mathcal{P}_{s+b}$  are nearly identical a fluctuation that leads to a value of  $CL_{s+b} \leq 0.05$  has the same statistical meaning for the (s + b)as for the b-hypothesis. It should not lead to a 95 % CL exclusion of the (s + b)hypothesis where on the other hand the b-hypothesis would still be trusted without doubt. Moreover an experiment should not exclude the presence of a signal if it is not sensitive to observe it. To prevent this unwanted behavior of the  $CL_{s+b}$  value, the exclusion judgment is usually made based on the  $CL_s$  value as defined in Eq. (3.11) [19, 20]. This value will always be larger or equal to the value of  $CL_{s+b}$ . It is thus a more conservative estimate in the sense that an exclusion based on  $CL_s$  will always imply an exclusion based on  $CL_{s+b}$ . In cases like the test for  $m_H = 110 \,\mathrm{GeV}$  the  $CL_s$  value will approach the  $CL_{s+b}$  value from above, since the integral of  $CL_b$  will go to 1 from below. In cases like the test for  $m_H = 120 \,\text{GeV}$  on the other hand the  $CL_s$  value will be close to 1 and thus prevent the unwanted behavior of the  $CL_{s+b}$  value.

#### 3.3.2 Direct Search Results

The test statistic q as a function of the tested values of  $m_H$  is shown in Fig. 3.7 (upper left). Shown are the observed value (black solid line), the median (blue dashed line), 68 % quantile (darker green band) and 95 % quantile (brighter yellow band) of the expected probability density function for the b-hypothesis, and the median (brown dash-dotted line) of the expected probability density function for the (s + b)hypothesis. The sub-figures in Fig. 3.6 can be viewed as horizontal slices through this distribution for  $m_H = 110 \,\text{GeV}$ , 115 GeV and 120 GeV correspondingly. As discussed before, an (s + b)-like (b-like) dataset corresponds to negative (positive) values of q, as can also be seen from the course of the expected medians for the two hypotheses. The larger the distance between the medians of the expected probability density functions of the two hypotheses, the higher the power of the analysis to distinguish between them. As can be seen from this sub-figure, the power of the LEP experiments to observe the signal of a SM Higgs boson at 95 % CL, corresponding to a deviation below the bright yellow band, did not reach to values of  $m_H$  beyond  $\gtrsim 114\,\text{GeV}$ . For lower masses the discovery potential grew rapidly, due to the clean signature and the rising  $H \to b\bar{b}$  branching fraction on the one hand and the drop of the cross section for the main background of diboson pair production on the other hand. The sub-figure points to a mild excess in the data, which leads to values of q < 0 for a mass range of  $m_H > 115$  GeV with a shallow minimum around 116 GeV, where the observed values of q also have a crossing point with the median of the probability density function for the (s + b)-hypothesis.

This behavior translates into the p-value as a function of  $m_H$ , which is shown in a mass range between 80 and 120 GeV in Fig. 3.7 (upper right). The expected median of the p-value for a dataset compatible with the b-hypothesis is 0.5, as indicated by the blue dashed horizontal line in the figure. Also indicated by horizontal lines are the p-values corresponding to a significance of  $2\sigma$  and  $3\sigma$ . Around  $m_H \approx 98 \,\mathrm{GeV}$  a deviation is observed, which corresponds to a  $2.3\sigma$  excess above the b-hypothesis for the given value of  $m_H$ . This excess is not compatible with the expectation for the SM Higgs boson, which should be by orders of magnitude larger than observed. This can be seen from the expected p-value for the (s+b)-hypothesis, indicated by the brown dash-dotted line with the bands corresponding to the 68 and 95 % CL uncertainties, which falls below the displayed axis range already for values of  $m_H \lesssim 115 \, \text{GeV}$ . Another much less significant deviation, which is compatible with the expectation for a SM Higgs boson is observed at  $m_H \approx 115 \, \text{GeV}$ , but this deviation is not significant. The crossing point of the expected median for the (s + b)-hypothesis shows that no observation beyond the  $2\sigma$  level is expected for a SM Higgs boson with a mass of  $m_H \gtrsim 116 \, \text{GeV}$ . It is noteworthy that the  $2.3\sigma$  deviation at  $m_H \approx 98 \, \text{GeV}$  seemed

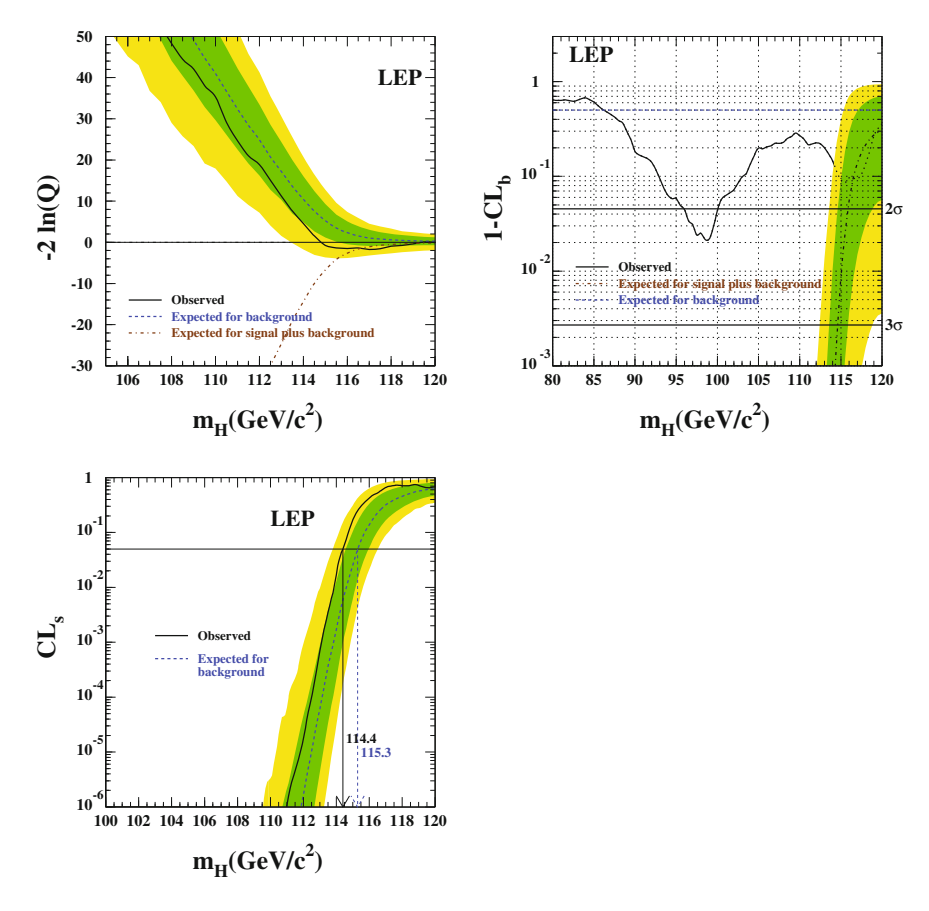


Fig. 3.7 The test statistic  $q = -2 \ln Q$  (upper left), p-value  $(1 - CL_b, upper right)$  and  $CL_s$  value (lower left), as function of the test mass  $m_H$  [15]. Values of q < 0 (q > 0) indicate (s + b)-(b-)likeness of the analyzed data. The horizontal lines in the p-value plot indicate the line of full compatibility with the b-hypothesis (dashed line at  $1 - CL_b = 0.5$ ) and the p-value for a  $2\sigma$  and  $3\sigma$  excess over the b-hypothesis. The horizontal line in the  $CL_s$  plot indicates the value of  $CL_s = 0.05$ , which corresponds to the 95 % CL exclusion limit. The intercept points with the expected median, for the b-hypothesis and with the observed  $CL_s$  values determine the expected and observed 95 % CL lower limits on the mass of the SM Higgs boson that can be obtained from the LEP data

to build up equally in all four experiments, while the deviation at  $m_H \approx 116 \, \text{GeV}$  was only seen in one of the *LEP* experiments.

The fact that no significant signal had been observed is expressed by a 95 % CL lower limit on  $m_H$ , which is based on the  $CL_s$  value as discussed in Eq. (3.11). In Fig. 3.7 (lower left) the value of  $CL_s$  is shown as a function of  $m_H$ . The horizontal line indicates the value of  $CL_s = 0.05$ , corresponding to the 95 % CL exclusion. The crossing point of the observed  $CL_s$  line is at  $m_H = 114.4$  GeV, which corresponds to the yellow shaded area on the left of Fig. 3.4 (right). The crossing point of the median

of the expectation for the *b*-hypothesis lies at  $m_H = 115.3 \,\text{GeV}$ . The fact that the observed limit is slightly weaker than expected for the *b*-hypothesis corresponds to the slight excess seen in the data.

# **3.4 Direct Searches at the Tevatron Proton Anti-Proton Collider**

Searches for the SM Higgs boson had also been conducted at the *Tevatron p \bar{p}* collider from 2010 on. The *Tevatron* has been operated at a center-of-mass energy of  $\sqrt{s} = 1.96\,\text{TeV}$  for the proton anti-proton collisions. For a hadron collider the center-of-mass energy,  $\sqrt{s}$ , of the hadron hadron collision translates into significantly lower center-of-mass energies,  $\sqrt{\hat{s}}$ , on the parton level, depending on the parton distribution functions evaluated at the energy scale at which the hard scattering process is taking place. A more detailed discussion will be given in Sect. 4.1.1. E.g. the production of a Higgs boson with a mass of  $m_H = 125\,\text{GeV}$  requires a mean fraction of the (anti-)proton momentum of

$$\langle x \rangle = \sqrt{\frac{m_H}{\sqrt{s}}} = \sqrt{\frac{125 \,\text{GeV}}{1.96 \,\text{TeV}}} \approx 0.25$$

The reduction of center-of-mass energy in the step from hadron to parton scattering limited the experimental reach of the searches at the Tevatron to Higgs boson masses below  $m_H \lesssim 200 \, \text{GeV}$ . The kinematic reach was maximal in quark anti-quark annihilation processes, where the valence quarks took part in the hard scattering process. Therefore, the main production channel was Higgs boson production in association with a W or Z boson. In the accessible range of  $m_H$  the main decay channels were into b-quarks in the regime of  $m_H \lesssim 130\,\mathrm{GeV}$  and into W bosons already slightly below the threshold where this decay is energetically allowed. The last publication on searches for the SM Higgs boson at the *Tevatron* has been made in 2013 [21]. It has been based on all modes relevant for SM Higgs boson production at hadron colliders: gluon fusion, vector boson fusion and Higgs boson production in association with vector bosons or top quark pairs, and the decay channels into b-quarks,  $\tau$ -leptons, W bosons, Z bosons or photons. A detailed discussion of these production modes and decay channels will be given in Sect. 4.2.1. The results correspond to the combination of all search channels that have been analyzed at both Tevatron experiments, CDF and D0, and based on the full dataset with a luminosity of 10 fb<sup>-1</sup> collected with each of the two experiments.

For the statistical inference the strategy and methods as developed for the *LEP* search had been adopted, as described in Sect. 3.3.1. To maximize the search potential and in light of increased computing power and the availability of more powerful minimization tools, the test statistic of Eq. (3.10) had been modified such that the

likelihood functions  $\mathcal{L}_{s+b}$  and  $\mathcal{L}_b$  were minimized before the marginalization<sup>5</sup> to find the most probable values,  $\hat{\theta}_k$ , of all nuisance parameters,  $\theta_k$ , for the given dataset, varying the nuisance parameters within their a priori uncertainties. This treatment allowed for the uncertainties in the analyses to be further constrained a posteriori by the data themselves. In extreme cases nuisance parameters e.g. for the normalization of a background process that was difficult to estimate otherwise, could even be left a priori unconstrained, to obtain an a posteriori constraint during the prior minimization procedure. These fits could become very complex with hundreds of parameters to minimize, which in turn significantly increased the computing power needed for the evaluation of the pseudo-experiments.

The results of the combined search are shown in Fig. 3.8. The test statistic q (here labeled as Log-Likelihood Ratio) as a function of the tested values of  $m_H$  is shown in Fig. 3.8 (left). The plot can be directly compared to Fig. 3.7 (upper left) for  $m_H \lesssim 120 \,\text{GeV}$ . As discussed before, negative (positive) values of  $q = -2 \ln Q$ correspond to the dataset being more compatible with the (s + b)- (b-)hypothesis. The black dashed line with the uncertainty band (labeled as LLR<sub>b</sub>) corresponds to the expectation for the b-hypothesis, the red dashed line (labeled as  $LLR_{s+b}$ ) to the expectation for the (s + b)-hypothesis, estimated at each point of  $m_H$ . The solid black line corresponds to the observed value of q. The publication by *Tevatron* had been made after the discovery of the new particle at the LHC on 4 July 2012. Therefore the expectation in the presence of a SM Higgs boson at a fixed mass of  $m_H = 125 \,\mathrm{GeV}$  had been added to the figures as a blue dash-dotted line. As can be seen for a mass around 160 GeV, where the decay channel into W bosons opens up, the sensitivity of the *Tevatron* searches increases rapidly, while the (s+b)-hypothesis in this range of  $m_H$  is disfavored by the observed values of q. This behavior is driven by the non-observation of a signal in the decay channel into W bosons. In a mass range around 120 GeV the observation falls below the  $-2\sigma$  band of the b-hypothesis, which roughly corresponds to the expectation in the presence of a SM Higgs boson with  $m_H = 125 \,\text{GeV}$ , as can be concluded from a comparison with the course of the blue dash-dotted line. The same trend can be seen from the p-value shown in Fig. 3.8 (right). The observation scratches the edge of a  $3\sigma$  evidence, while an effect not larger than  $2\sigma$  would be expected from the SM. The observation is compatible with the expectation for a SM Higgs boson at  $m_H = 125 \,\text{GeV}$  within  $1\sigma$ . An (s+b)like deviation from the b-hypothesis at  $m_H \approx 95 \, \text{GeV}$  as visible in Fig. 3.7 (upper right) could not be confirmed despite the similar production mechanism and the same dominant decay channel into b-quarks. The comparison of the p-value from both experiments in this mass range (Fig. 3.7 upper right and Fig. 3.8 right) reveals that the Tevatron experiments were by far less sensitive to observe such a deviation.

<sup>&</sup>lt;sup>5</sup> While this statement is true for the example given above in practice the minimization could also happen after the marginalization step to find the most probable values of the  $b'_k$  and their uncertainties. See Footnote 4 for a comment on when the marginalization can take place.

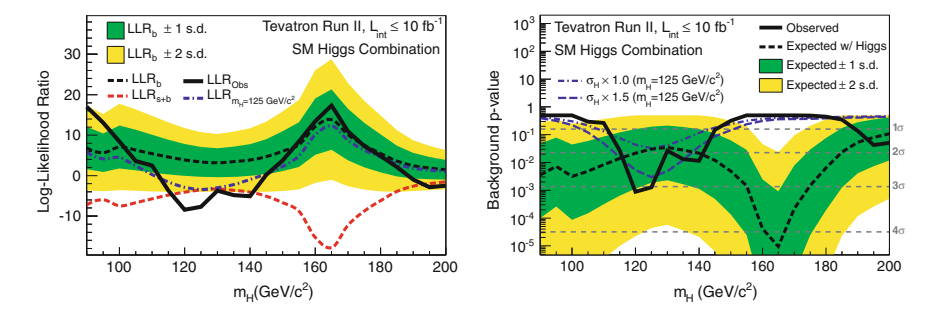


**Fig. 3.8** (*Left*) test statistic  $q=-2\ln Q$  (here labeled as Log-Likelihood Ratio) and (*right*) p-value, as function of  $m_H$  for values between 90 and 200 GeV [21]. In the left plot the *black dashed line* (labeled as LLR<sub>b</sub>) corresponds to the expectation for the b-hypothesis, the red dashed line (labeled as LLR<sub>s+b</sub>) to the expectation for the (s+b)-hypothesis. The *blue dash-dotted line* in both sub-figures corresponds to the expectation in the presence of the SM Higgs boson with  $m_H=125\,\text{GeV}$ , the *solid black curve* to the observed values

#### References

- Particle Data Group, Review of particle physics. Chin. Phys. C C38, 090001 (2014). doi:10. 1088/1674-1137/38/9/090001
- A. Djouadi, The anatomy of electroweak symmetry breaking. I: the Higgs boson in the standard model. Phys. Rep. 457, 1–216 (2008). arXiv:hep-ph/0503172
- C.F. Kolda, H. Murayama, The Higgs mass and new physics scales in the minimal standard model. JHEP 0007, 035 (2000). arXiv:hep-ph/0003170
- 4. R.G. Newton, Optical theorem and beyond. Am. J. Phys. **44**(7), 639–642 (1976)
- ALEPH Collaboration, DELPHI Collaboration, L3 Collaboration, OPAL Collaboration, SLD Collaboration, LEP Electroweak Working Group, SLD Electroweak Group, SLD Heavy Flavour Group, Precision electroweak measurements on the Z resonance. Phys. Rep. 427, 257–454 (2006). arXiv:hep-ex/0509008
- ALEPH Collaboration, DELPHI Collaboration, L3 Collaboration, OPAL Collaboration, LEP Electroweak Working Group, Electroweak measurements in electron-positron collisions at Wboson-pair energies at Lep. Phys. Rep. 532, 119–244 (2013). arXiv:1302.3415
- CDF Collaboration, D0 Collaboration, Tevatron Electroweak Working Group, Update of the Combination of CDF and D0 Results for the Mass of the W boson (2012). arXiv:1204.0042
- CDF Collaboration, D0 Collaboration, Tevatron Electroweak Working Group, Combination of CDF and D0 Results on the Width of the W boson, arXiv:1003.2826
- CDF Collaboration, D0 Collaboration, Combination of the top-quark mass measurements from the tevatron collider. Phys. Rev. D86, 092003 (2012). arXiv:1207.1069
- J. Ginges, V. Flambaum, Violations of fundamental symmetries in atoms and tests of unification theories of elementary particles. Phys. Rep. 397, 63–154 (2004). arXiv:physics/0309054
- SLAC E158 Collaboration, Observation of parity non-conservation in Møller scattering. Phys. Rev. Lett. 92, 181602 (2004). arXiv:hep-ex/0312035
- SLAC E158 Collaboration, Precision measurement of the weak mixing angle in M
  øller scattering. Phys. Rev. Lett. 95, 081601 (2005). arXiv:hep-ex/0504049
- NuTeV Collaboration, A precise determination of electroweak parameters in neutrino nucleon scattering. Phys. Rev. Lett. 88, 091802 (2002). arXiv:hep-ex/0110059
- W. Bentz, I. Cloet, J. Londergan et al., Reassessment of the NuTeV determination of the weak mixing angle. Phys. Lett. B693, 462–466 (2010). arXiv:0908.3198

References 79

15. R. Assmann, M. Lamont, S. Myers, A brief history of the LEP collider. Nucl. Phys. Proc. Suppl. **109B**, 17–31 (2002)

- LEP Working Group for Higgs Boson Searches, ALEPH Collaboration, DELPHI Collaboration, L3 Collaboration, OPAL Collaboration, Search for the standard model Higgs boson at LEP. Phys. Lett. B565, 61–75 (2003). arXiv:hep-ex/0306033
- LHC Higgs Cross Section Working Group, Handbook of LHC Higgs cross sections: 3. Higgs properties. arXiv:1307.1347
- 18. A.L. Read, Linear interpolation of histograms. Nucl. Instrum. Methods A425, 357-360 (1999)
- 19. A. Read, Modified frequentist analysis of search results (the  $CL_s$  Method). Technical report CERN-OPEN-2000-005, CERN (2000)
- 20. A.L. Read, Presentation of search results: the  $CL_s$  technique. J. Phys. **G28**, 2693–2704 (2002)
- 21. CDF Collaboration, D0 Collaboration, Higgs boson studies at the tevatron. Phys. Rev. **D88**(5), 052014 (2013). arXiv:1303.6346

# Chapter 4 Discovery of the Higgs Boson at the Large Hadron Collider

#### 4.1 Setting up the Scene for Discovery

#### 4.1.1 The Large Hadron Collider

The *LEP* collider, stopped operation after the 2 November 2000 to give space for the construction of the *LHC*, which uses the same tunnel and infrastructure. In contrast to *LEP* the *LHC* is a hadron hadron collider, designed to accelerate beams of protons (or heavy ions) to energies up to 7 TeV each, thus reaching out to center-of-mass energies of the proton proton collisions up to 14 TeV. The acceleration is reached via radio frequency in the MHz range generated with klystrons and filtered by cavities to obtain the proper wavelengths for acceleration. Analogue to accelerated charges in antennas the projectiles loose energy due to synchrotron radiation, when forced on a predefined path. In the case of circular acceleration this energy loss is given by

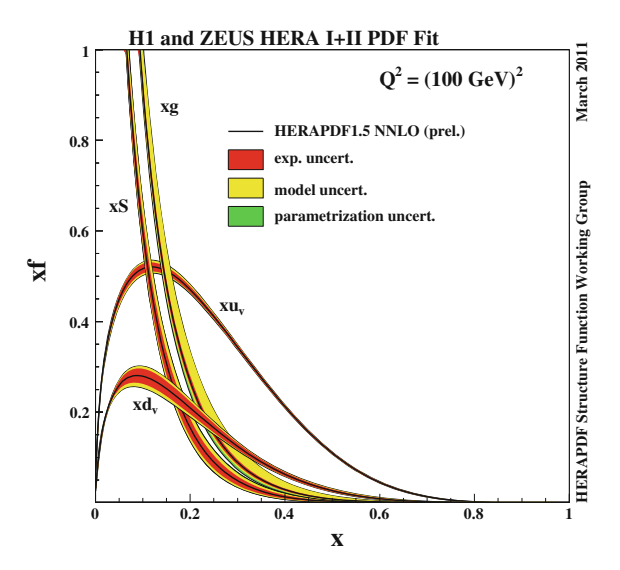
$$\mathcal{P}_{\text{sync}} = \frac{q^2}{6\pi R^2} \gamma^4 = \frac{q^2}{6\pi R^2} \left(\frac{E}{m}\right)^4$$

where q corresponds to the charge of the projectile, R to the radius of the accelerator and  $\gamma = E/m$  to the gamma factor of the system of the accelerated projectile with respect to the laboratory frame. The  $\gamma$  factor in this equation introduces a dependency of the energy loss per revolution cycle on the mass of the projectile to the power of  $m^{-4}$ , which explains the gain in switching from electrons to protons: the factor of  $m_p/m_e \approx 2000$  in the mass of the accelerated particles suppresses the energy loss per revolution cycle due to synchrotron radiation from  $\approx 500\,\mathrm{kW}$  per cycle to a negligible level. The switch of the particle type to be accelerated has two important consequences that will be discussed in the following: it is inherent to proton proton collisions that the center-of-mass energy of the collision cannot be completely transferred into the hard scattering process. Instead the proton momentum has to be folded with the probability to find a certain parton with momentum fraction

x inside the proton. These probabilities can be obtained from parton density functions that have e.g. been determined in deep inelastic scattering experiments at the HERA accelerator [1] making use of OCD factorization theorems like [2]. Typical parton density functions evaluated at the energy scale of  $Q^2 = (100 \,\text{GeV})^2$ , are shown in Fig. 4.1. Unless stated differently center-of-mass energies will always refer to the proton proton collisions throughout this chapter. The second consequence is of more technical nature: the larger mass of the accelerated particles requires strong magnetic dipole fields to keep the protons on their foreseen trajectories. For the LHC this is assured by 1232 helium cooled superconducting dipole magnets, which can reach magnetic field strengths of up to 8.3 T. These fields are obtained from coils with 160 windings and currents of up to 11.8 kA. At the maximum field strength in these magnets an energy density of 500 kJ/m is stored. Due to the high currents the coils of the magnets have to be kept in place by support structures that have to cope with a pressure of 200 000 t/m. With the choice of superconducting magnets the power consumption of the complex can be kept at a manageable level: it is designed to be operated with a power consumption of  $\approx$ 120 MW, compared to the power production of  $\approx 1200 \,\mathrm{MW}$  of a typical atomic power plant. In turn the accelerator is run at a calculated risk that one or several of the superconducting magnets might quench, i.e. that they locally loose their superconducting quality and lead to the spontaneous deposition of the complete stored energy into electrical power and finally heat. To keep also this risk at a manageable level and to protect the accelerator from serious damage, sophisticated quench monitoring and protection systems had been installed.

The protons are accelerated in *bunched* structures, which are naturally imposed by the wells of the accelerating radio frequency waves. They are brought to collision at several interaction points. The nominal collision times are often called *bunch crossings*. Since collisions with high momentum transfer have a very small probability

Fig. 4.1 Parton distributions functions (x f) at the scale  $Q^2 = (100 \,\text{GeV})^2$ , as determined from the data collected at the HERA accelerator [1]. This corresponds to the energy scale relevant for the production of the SM Higgs boson with  $m_H \approx 100 \, \text{GeV}$ . Shown are the probability density for observing a valence quark ( $xu_v$  and  $xd_v$ ), a sea quark (xS) or a gluon (xg), multiplied by the momentum fraction of the parton relative to the proton, x



to occur it is one of the main goals during the operation of the accelerator to bring as many protons into collision during these bunch crossings as possible. This is achieved by maximizing the number of protons per bunch, and the frequency, with which the bunches are brought to collision. The rate of proton proton collisions, the (instantaneous) luminosity, is therefore one of the most important parameters of the accelerator apart from its energy. It is defined in analogy to the brightness of a light source and usually measured in units of (collisions) cm<sup>-2</sup>s<sup>-1</sup>. The typical number of protons per bunch in 2011/2012 was  $\mathcal{O}(10^{11})$ , the bunch crossing rate at the interaction points was 20 MHz, corresponding to a timespan between two subsequent bunch crossings of 50 ns. These specifications corresponded to instantaneous luminosities up to  $3.5 \times 10^{33}$  cm<sup>-2</sup>s<sup>-1</sup> ( $7.7 \times 10^{33}$  cm<sup>-2</sup>s<sup>-1</sup>) in 2011 (2012). Since the probability of a hard scattering process to occur is also measured in terms of a cross section, i.e. in units of an area, luminosities can be translated into units, which are slightly more intuitive for a particle physicist

$$\mathcal{L} = 10^{33} \, \text{cm}^{-2} \text{s}^{-1} \equiv 1 \, \text{nb}^{-1} \text{s}^{-1}$$

This implies that a process with a cross section of 1 nb has an expected rate of one Hz, a pair of *top* quarks with a production cross section of  $\approx$ 250 pb at 8 TeV would be produced any four seconds, supporting the view of the *LHC* being a factory for the production of *top* quarks.

The high density of protons per bunch led to a mean number of  $\langle N_{IA} \rangle = 9$  (21) proton proton interactions per bunch crossing in 2011 (2012). Out of these usually one interaction corresponds to a hard scattering process of interest, while the others correspond to low energy and diffractive scattering processes. This can be inferred from the extremely low probability of a scattering process with high momentum transfer to occur. All other interactions but the one, which corresponds to the hard scattering process are usually referred to as *pileup*. Their presence complicates the identification and reconstruction of the hard scattering process and requires dedicated methods to identify those objects that have been genuinely produced during the hard scattering process, as will be discussed later.

## 4.1.2 Main Experiments and Event Reconstruction

To collect the collision data, among other experiments, two main multipurpose detectors have been built, with their origin in one of the nominal interaction points of the accelerator. The coordinate system used by the experiments is right-handed with the y-axis pointing to the top and the z-axis pointing along the axis of the proton beams. To optimally address their physics cases the detectors have been laid out to contain all observable energy produced during a proton proton collision at 14 TeV center-of-mass energy and to provide reliable energy (transverse momentum) measurements of all neutral (and charged) particles emerging from these collisions. The plane transverse to the beam axis thereby is of special importance, for two reasons: (i) there

is no residual momentum in the transverse plane expected in the initial state of the collision, which via momentum conservation translates into the final state. This is usually not the case along the *z*-axis, where the initial momentum of the scattering partons in the proton due to the step from the proton level to the parton level is a priori not known; (ii) for the same reason the system of the hard scattering process can be boosted along the *z*-axis, but quantities, which are defined in the transverse plane are not affect by such boosts, i.e. to first approximation they are the same in the center-of-mass system of the collision and in the laboratory frame. For these reasons the particles emerging from the collisions are usually characterized by the following three quantities:

transverse momentum 
$$p_T$$
 azimuthal angle  $\phi$  pseudorapidity  $\eta = -\ln{(\tan{(\theta/2)})}$ 

where  $\phi$  is measured in the transverse plane and the polar angle,  $\theta$ , with respect to the z-axis of the coordinate system. In contrast to  $\theta$ , the pseudorapidity,  $\eta$ , is approximately form invariant under *Lorentz* boosts along the z-axis thus that all three quantities retain their intuitive geometrical meaning irrespective of the residual boost of the scattering system along the axis of the proton beams. The classical method to measure the (transverse) momenta of charged particles is via their bending due to the *Lorentz* force in magnetic fields (parallel to the beam axis):

$$\vec{p}_T = q \cdot \vec{r} \times \vec{B}; \qquad \frac{\delta p_T}{p_T} = \frac{(\delta B \oplus \delta r)}{q \cdot |\vec{r}| \cdot |\vec{B}|}$$

where  $\vec{p}_T$  corresponds to the transverse momentum of the charged particle, with charge q,  $\vec{r}$  to the bending radius and  $\vec{B}$  to the strength of the magnetic field. To achieve high relative momentum resolution it is obvious that both the uncertainty,  $\delta B$ , of the magnetic field strength as well as the resolution,  $\delta r$ , of the bending radius of the reconstructed trajectory of the particle have to be known with best possible precision. Usually  $\delta B$  can be determined with high precision, leaving the over all precision limited by  $\delta r$ . The relative precision of the (transverse) particle momentum can be further increased if the magnetic field strength, B, is very high or if the detector is large enough to measure even largest bending radii, r, with a large lever arm. Both concepts have been followed up: the ATLAS detector has been build as a barrel detector with 22 m diameter and 45 m length [3]. It is thus equipped with a large lever arm to measure highest momentum tracks reconstructed from the traces that charged particles leave along their trajectories in the active detector material, due to their ionizing effect. In the design several magnetic systems provide independent measurements of the particle momentum, among those an inner solenoid magnet with a field strength of 2.5 T, with field lines parallel to the proton beam direction and an outer toroid magnet with a field strength of up to 4T, with a circular field in the transverse plane. From inside out the detector comprises: (i) a silicon pixel detector to identify the vertex of the hard scattering process; (ii) silicon strip detectors

and multi-wire chambers to measure the bending of tracks and thus the transverse momenta of the charged particles emerging from the collision, inside the superconducting solenoid magnet; (iii) and a lead liquid argon sampling calorimeter, which is read out with different granularity to account for an electromagnetic and a hadronic section outside the magnet and complemented by an iron plastic scintillator hadronic sampling calorimeter in the barrel region. The momenta of a particle that penetrates the whole detector can be measured from three bending radii of its trajectory: there is the bending in the transverse plane in the inner and outer field of the solenoid magnet. In addition there is the bending parallel to the beam direction in the field of the toroid magnet. A sketch of the *ATLAS* detector and all its components is shown in Fig. 4.2 (upper part). A strength of the *ATLAS* detector lies in the excellent highly granular lead liquid argon calorimeter with fine lateral segmentation, which affords to be located outside the solenoid magnet, following a classical design pattern and in the redundancy that allows for a reliable measurement of even highest momenta. A weakness might arise from the inhomogeneity and complexity of the detector.

The CMS detector follows a concept, which is by far more compact and in addition more homogeneous than the ATLAS detector [4]. Compared to ATLAS the CMS detector has nearly twice the weight in a third of its extension. The main feature of CMS is a large superconducting solenoid magnet with roughly 6 m diameter and the capability to reach a magnetic field strength of up to 3.8 T, with field lines parallel to the proton beam direction. In contrast to ATLAS this magnet comprises not only the inner track detector but also all parts of the main calorimetry, thus preventing energy loss due to multiple scattering of electromagnetic particles in the solenoid coil before reaching the calorimeters. The momenta of charged particles are measured using an all silicon pixel and strip track detector covering the range of  $|\eta|$  < 2.5 (corresp. to  $10^{\circ} < \theta < 170^{\circ}$ ). The inner track detector consists of  $200 \,\mathrm{m}^2$  of active silicon detector material, making it one of the largest silicon track detectors that has ever been build so far, and resembling the choice to stick to a single detector technology for track finding in the design. The inner track detector is surrounded by a lead tungstate crystal electromagnetic calorimeter (ECAL), with a thickness of  $X_0 = 28$ radiation lengths, for electromagnetic showers, and an excellent energy resolution, completed by a brass-scintillator hadron calorimeter (HCAL), with a thickness of  $\lambda_i = 10$  interaction lengths for the energy loss of hadrons, both used to measure particle energy deposits and consisting of a barrel assembly and two endcaps. The choice of lead tungstate for the ECAL guarantees high energy resolution and a large stopping power for electromagnetic particles, which is of importance for the compact design of the detector, inside the solenoid coil. On the other hand it requires careful monitoring of the temperature and irradiation damage to the crystals. The ECAL and HCAL extend to  $|\eta| < 3.0$  (corresp. to  $5^{\circ} < \theta < 175^{\circ}$ ). A steel-quartz-fiber *Cherenkov* forward detector extends the calorimetric coverage to  $|\eta| < 5.0$  (corresp. to  $1^{\circ} < \theta < 179^{\circ}$ ).

The *CMS* detector offers a single track momentum resolution of  $\delta p_p = 0.5\%$  for the track of a 10 GeV charged particle, in the inner track detector, an energy resolution of  $\delta E_E = 1\%$  for an electron or photon with an energy of 30 GeV in the *ECAL* and an energy resolution of  $\delta E_E = 10\%$  for a single charged pion with

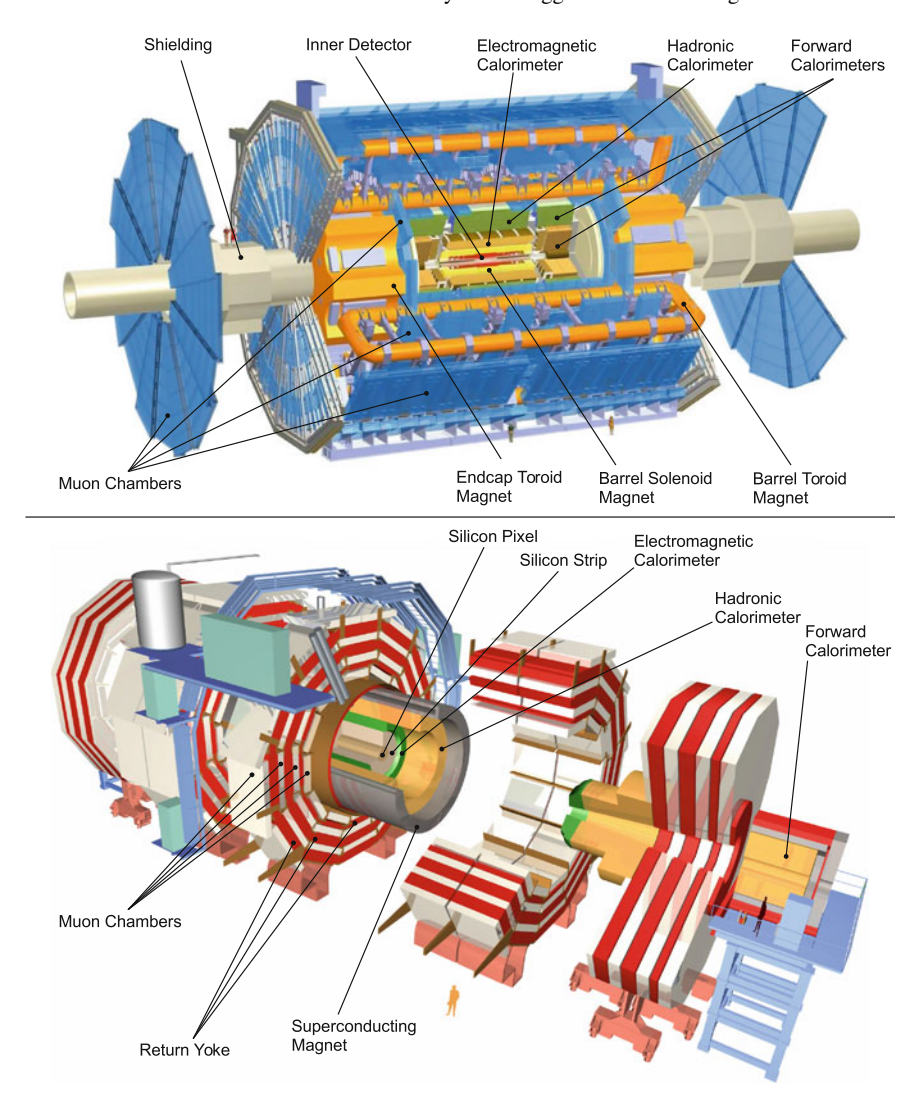


Fig. 4.2 Schematic views of the (top) ATLAS [3] and (bottom) CMS [4] detector

an energy of 100 GeV in the *HCAL*. These energies are typical for the analyses that will be discussed in the following. Outside the magnet the field lines are closed by an iron return yoke, which is instrumented with gas-ionizing detectors of different technologies and optimized for momentum resolution or fast readout for the online selection of interesting events, to form the muon system. Since the return yoke fills roughly twice the volume of the detector inside the magnet the magnetic field strength is approximately half and pointing to the opposite direction of the inner magnetic field. Since the field strength that can be maximally reached in saturated

iron corresponds to 2 T the field strength in the inner detector in this way defines the final size of the detector. The track of a muon, that penetrates the full detector is correspondingly bent like an "S" in the transverse plane. For a transverse momentum of up to a few 100 GeV the momentum resolution of all charged particles and thus also for muons is dominated by the precision of the inner track detector, while beyond the muon system takes over. The momentum resolution of a 1 TeV track in the muon system alone is 10 %. A muon from the hard interaction process has to have an energy of at least 4 GeV to guarantee that it will penetrate the inner detector and reach the muon system. A schematic view of the *CMS* detector is shown in Fig. 4.2 (lower part).

All information that is read out from the detector during a bunch crossing is called an event. If the whole CMS detector were read out with uncompressed information of all readout channels at the nominal interaction rate of 20 MHz this would correspond to a data volume of  $\approx$ 1 PB/s. This huge flow of information is reduced to a manageable level by a three level trigger and online selection system. Each level of this system is tuned for fast decision taking, whether to keep or to discard the event starting from a coarse readout of the detector by custom hardware processors, up to software implemented algorithms, which make use of nearly the complete readout of the detector with full granularity. Since at each trigger level non-interesting events are discarded, each proceeding trigger level can afford more processing time on the remaining events. During the decision taking the whole information for all interesting events is buffered in readout pipelines. Typical numbers for the output rate at each trigger level are  $100\,\mathrm{kHz}$  ( $\approx 100\,\mathrm{GB/s}$ ) after level one,  $5\,\mathrm{kHz}$  ( $\approx 5\,\mathrm{GB/s}$ ) after level two and 300 Hz ( $\approx$ 500 MB/s) after level three. The latter finally corresponds to the rate with which readout information is written to tape. The whole system can be configured with a large menu of interesting event signatures that will compete with each other within the available band width. This design guarantees a dead time free readout of all interesting signatures. A similar trigger system has been laid out by the ATLAS collaboration.

The two main assets of the *CMS* detector lie in the all silicon inner track detector and in the high resolution crystal ECAL, inside the coil of the solenoid magnet, such that its superior resolution is not too much compromised by pre-showering and energy loss in front of the calorimeter. The compromise to the compact design choice and the expensive ECAL is the HCAL with a thickness of only  $\lambda_i = 10$  interaction lengths and no granularity in the lateral readout. It turned out though that the potential weakness of the HCAL could be largely compensated with the help of the excellent inner track detector exploiting a dedicated *particle flow* algorithm [5, 6], with the aim to reconstruct the full path of all particles emerging from the hard scattering process on their way through the detector. The particle flow algorithm, which extends the classical reconstruction, is based on the optimal determination of all independently measured energy deposits in each individual detector component, as energy clusters of different granularity in the ECAL and HCAL, and tracks in the inner and outer track detectors.

In a first step these energy deposits are linked across all detector components. This procedure starts from tracks in the inner detector, which are extrapolated through the

active calorimeter material up to the first layers of the outer tracking chambers of the muon system. Energy clusters in the calorimeters, which are crossed by the extrapolated trajectories are linked to the corresponding tracks. Ambiguities after linking are resolved according to the expected resolution in the calorimeters and the track detector. Energy deposits in the calorimeters which significantly exceed the track momentum are associated to neutral electromagnetic or hadronic particles. If the extrapolated trajectory can be matched to a track in the muon system or at least to a track segment and if the measured energies along the trajectory in the calorimeter are compatible with the signature of a minimal ionizing particle, these energy deposits are removed from the list of reconstructed objects and refitted to obtain the best estimate for the energy and momentum of a combined reconstructed muon track [7]. Linked energy clusters and tracks, which are compatible with each other within the uncertainty of the track momentum measurement are also removed from the list of reconstructed objects and refitted to obtain the best estimate of the combined object, taking the resolution of the calorimeters and the track detector at the given energy into account. This method assures that the energy or momentum measurement of the combined object is driven by the detector component with the best expected resolution, with a smooth transition between the detector components. Tracks that can be linked to one or more energy clusters in the ECAL only, are reconstructed as electrons. The reconstruction takes photons due to bremsstrahlung into account [8, 9]. Tracks that can be linked to energy clusters in the ECAL and HCAL are reconstructed as charged hadrons. Energy clusters in the calorimeters that are not linked to any track are reconstructed as photons, if linked to clusters in the ECAL only, and neutral hadrons if linked to clusters in the HCAL only or to clusters in the ECAL and HCAL.

The result of the particle flow algorithm is a complete, unambiguous list of reconstructed particles categorized into muons, electrons, charged and neutral hadrons, which are the usual input for any further analysis. The particle flow algorithm allows trivially to associate all charged particles to a reconstructed vertex that can be identified with the hard interaction vertex or with pileup. The vertex of the hard interaction usually is chosen to be the one, with the highest transverse momentum squared,  $\sum \vec{p}_T^2$ , summed over all emerging tracks associated to it.

Quarks and gluons, which are involved in the hard interaction, due to their color charge are produced together with a large number of additional quarks and gluons, which freeze out into color neutral hadrons during a subsequent hadronization phase. These particle sprays are usually clustered and collimated due to the high momentum transfer of the hard scattering process. This allows to determine the four momentum of a single jet object composed from all individual reconstructed particles that it contains. For all analyses described in the following this has been done using the anti- $k_t$  clustering algorithm with an opening parameter of y = 0.5, as described in [10]. The four momentum of this jet can be correlated back to the four momentum of the initial quark or gluon with a finite resolution [11].

As mentioned in Sect. 1.3 throughout the text there will be an emphasize on the measurements that have been made with the *CMS* detector. Where available the public results from the *ATLAS* collaboration will be given for comparison at the end

of the corresponding sections. It should be mentioned that the concept of having two independent experiments to crosscheck each others results has been an important design choice for the construction of the *LHC*. As discussed both experiments are complementary in their layout, but have demonstrated a comparable performance for the search for the SM Higgs boson that will be discussed in the following.

#### 4.1.3 First Measurements of Known Standard Model Processes

The construction of the *LHC* took from 2000 till 2008. The accelerator started operation at 10 September 2008 but suffered from a major incidence during a quench, that could not be controlled, only 9 days later. This incidence affected 100 dipole magnets and set free 6t of helium, which evaporated into the tunnel system. A total of 53 superconducting magnets got seriously damaged or destroyed. When technicians entered the affected tunnel sections for the first time two days after the incident they entered a snow landscape due to the evaporated helium that had condensed the air humidity on the walls of the tunnel system. The repair took another year and on the 20 November 2009 the accelerator could finally be restarted. As a consequence of the incidence the quench protection system had been significantly improved and the energy of the proton beams had been reduced to 3.5 TeV each in 2011, leading to proton proton collisions at a center-of-mass energy of 7 TeV. This reduction significantly reduced the danger of uncontrolled quenches. This time the restart was a full success, which led to a first data taking period with  $\approx 5 \, \mathrm{fb}^{-1}$  of collected proton proton collisions in both main experiments in 2011. For 2012 the decision was taken to increase the center-of-mass energy from 7 to 8 TeV. At this center-of-mass energy another dataset with  $\approx 20\,\mathrm{fb^{-1}}$  of proton proton collisions per experiment could be collected. These conditions set the scene for the hunt for the SM Higgs boson.

This hunt started off with an unprecedented campaign to find back and establish all known and predicted processes of the SM, starting from the production of Z and W bosons, via the production of top quarks in pairs  $(t\bar{t})$  and as single quarks up to the pair production of W and Z bosons. The measurements were complemented by theoretical predictions usually at a precision of up to NNLO in the strong coupling constant,  $\alpha_s$ , which had been obtained in long lasting and challenging calculations over many years. A snapshot of the knowledge and control that could be gained based on these well established sectors of the SM is shown in Figs. 4.3 and 4.4. In Fig. 4.3 the cross section of single W boson, single Z boson and top quark pair production, are shown, inclusively and in association with additional jets. The first measurements of the inclusive W and Z boson production cross section [14] as well as the first measurement of the  $t\bar{t}$  production cross section [15] at a center-of-mass energy of 7 TeV with the CMS experiment were based on a luminosity of  $\approx 3 \,\mathrm{pb}^{-1}$  ( $\approx 0.012 \,\%$ of the total collected dataset of the years 2011 and 2012). These measurements in the first place probe the QCD based production in proton proton collisions (i.e. the sector of strong interactions in the SM) and the understanding of the proton. The production of W and Z bosons in association with jets are furthermore important

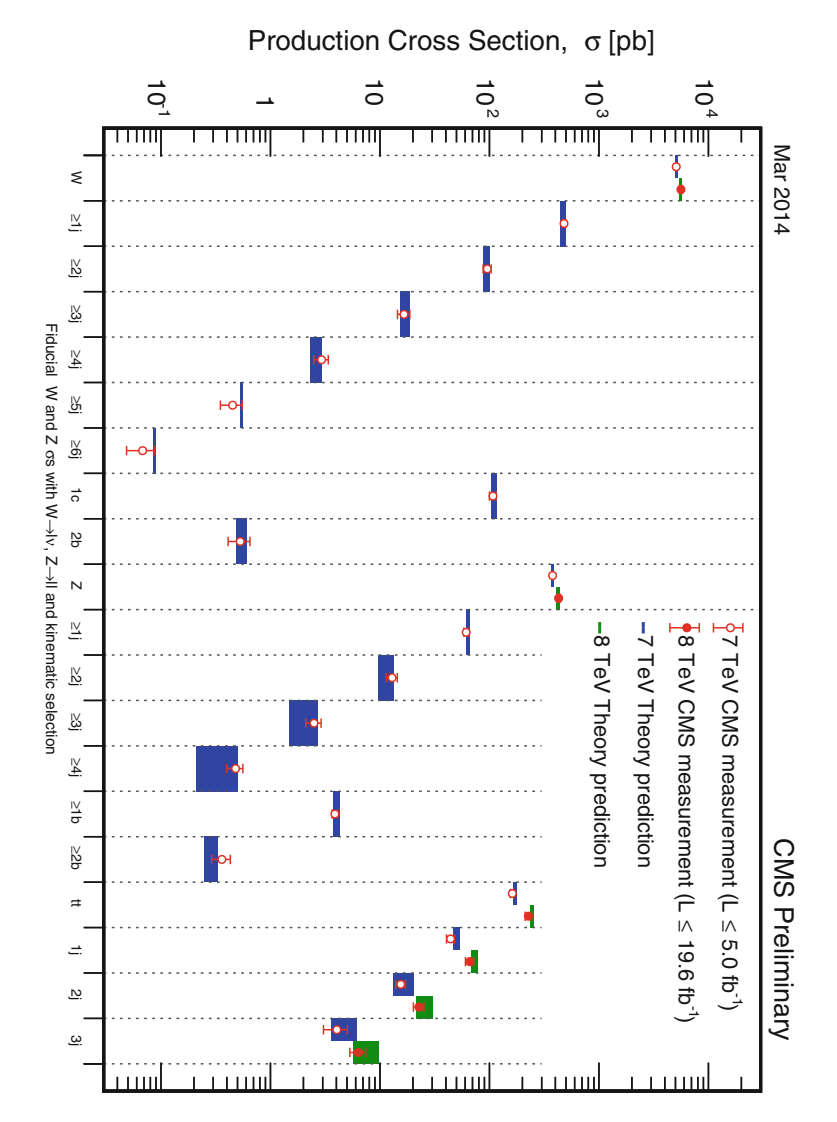


Fig. 4.3 Snapshot of the understanding of the SM that had been achieved, here given for measurements of the CMS collaboration, based on the data collected in 2011 and 2012, before the discovery of the Higgs boson [12]. Shown are the measured cross sections for single W or Z boson production and for top quark pair production in association with additional jets and the corresponding predictions of the SM

background processes first for all measurements concerned with  $t\bar{t}$  production, and in the next instance for the search for the SM Higgs boson, as will be discussed in the following sections. The impressive agreement between the measurements and the predictions based on the SM spans over six orders of magnitude. In Fig. 4.4 the

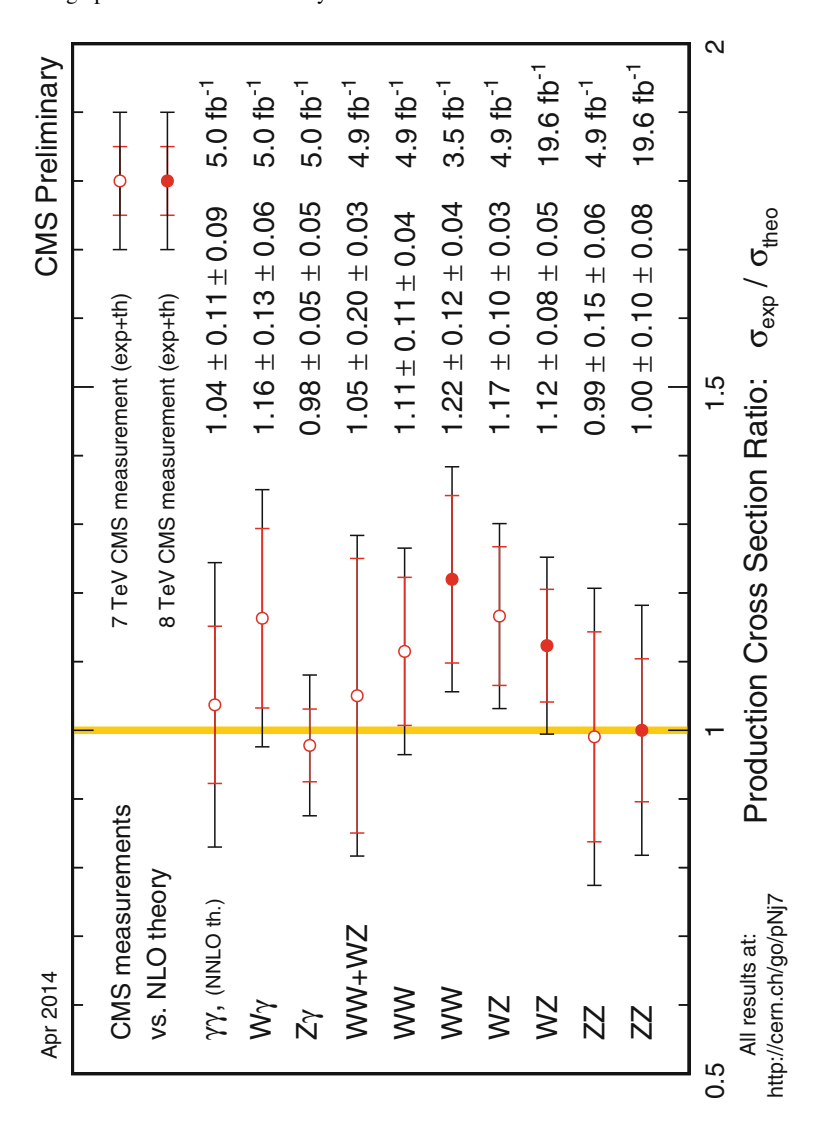


Fig. 4.4 Snapshot of the understanding of the SM that had been achieved, here given for measurements of the *CMS* collaboration, based on the data collected in 2011 and 2012, before the discovery of the Higgs boson [13]. Shown is the ratio of the measured ( $\sigma_{exp}$ ) over the predicted ( $\sigma_{theo}$ ) cross section for several processes of inclusive diboson production

ratio of the measured ( $\sigma_{\rm exp}$ ) over the predicted ( $\sigma_{\rm theo}$ ) cross section is shown for several processes of diboson production. These measurements together with the first measurement of single *top* quark production at the *LHC* [16] probe the weak sector of the SM as discussed in Sect. 2.2. Also here the agreement between the measurements and the predictions based on the SM is remarkable, maybe with a slight tendency for

an enhanced production of dibosons in cases where W bosons are involved, which only shines through since these production modes consistently appear slightly higher than expected.

## 4.2 The Eve of the Hunt for the Higgs Boson

#### 4.2.1 Decay Channels and Production Modes

The search for the SM Higgs boson seriously started in 2011, when enough events had been accumulated to gain relevant sensitivity. It was conducted in a mass range from  $m_H = 110$  up to 1000 GeV, which was motivated by the unsuccessful preceding searches at LEP and at the Tevatron and by the theoretical boundaries as discussed in Sect. 3.1. The branching fractions as used for the search are shown in Fig. 4.5 [17]. In Fig. 4.5 (left), the total decay width,  $\Gamma_H$ , as a function of  $m_H$  is shown. Since the Higgs boson coupling is proportional to the mass of the decay products the decay width grows with increasing values of  $m_H$ , as the decay into successively heavier particles becomes energetically accessible. The first jump in  $\Gamma_H$  at  $m_H \approx 160 \, \text{GeV}$ corresponds to the decay channels into W and Z bosons. This jump is additionally enhanced by the fact that the coupling of the Higgs boson to the massive vector bosons is proportional to the vector boson mass squared. A further increase can be seen at  $m_H \approx 350 \, \text{GeV}$ , where the decay channel into top quarks opens up. In Fig. 4.5 (right) the decay fractions as derived from the total and partial decay widths are shown. It illustrates a rich phenomenology with several competing decay channels for lower values of  $m_H$ , while above their kinematic thresholds the decay into W, Z bosons

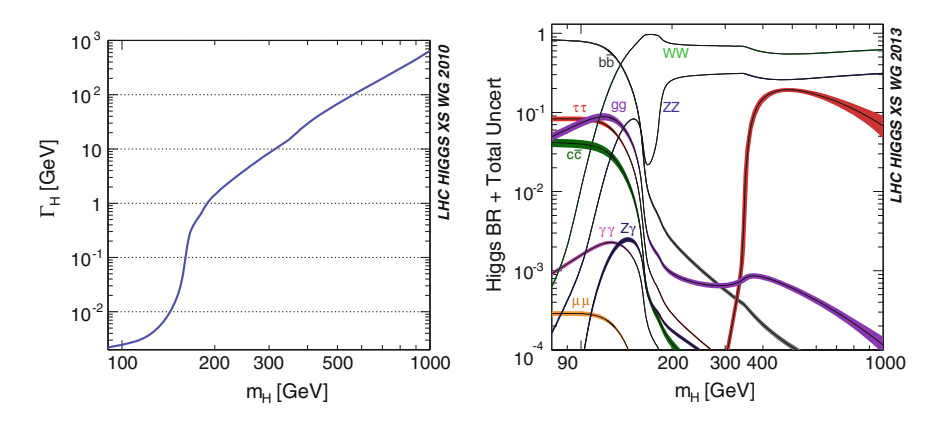


Fig. 4.5 Expected (*left*) decay width ( $\Gamma_H$ ) and (*right*) branching fractions (*BR*) of the SM Higgs boson for values from  $m_H = 90 \, \text{GeV}$  up to  $1000 \, \text{GeV}$ . On the *right* the bands correspond to the uncertainties of the expected values. The *curve* with the *red band* that rises at  $m_H \approx 300 \, \text{GeV}$  corresponds to the decay into *top* quarks ( $t\bar{t}$ ) [17, 18]

and finally into *top* quarks gain dominance over all other decay channels. The bands in the figure correspond to the total theoretical uncertainty of each decay fraction taking into account finite mass effects and uncertainties in the calculation of  $\alpha_s$  as well as the effects of missing higher orders in the calculations, added linearly. For  $m_H \approx 125\,\text{GeV}$  these uncertainties for the energetically and at the *LHC* accessible decay channels are typically  $\mathcal{O}(5\,\%)$  [18].

The LHC search program for the SM Higgs boson comprised five main decay channels: the decay into (i) W bosons  $(H \to WW)$ , (ii) Z bosons  $(H \to ZZ)$ , (iii) photons  $(H \to \gamma \gamma)$ , (iv) b-quarks  $(H \to b\bar{b})$  and (v)  $\tau$ -leptons  $(H \to \tau \tau)$ . This choice guaranteed complete coverage of the whole relevant mass range down to lowest values of  $m_H$ , including all main decay channels, which are obviously accessible at the *LHC*. It contains decay channels into vector bosons and fermions, quarks and leptons to equal parts catching all most important characteristics of the coupling structure of the SM Higgs boson that can be studied at the LHC. In the low mass regime the decay channel into b-quarks is dominant, followed by the decay into  $\tau$ -leptons, giving access to the couplings to quarks and leptons. The decay into photons appears unintuitive at first sight, since photons are massless objects (even protected by the intact  $U(1)_Y$  symmetry). But the coupling occurs at higher order in perturbation theory and not at tree level as for the other decay channels. The contributing leading-order diagrams proceed via a fermion or a W boson loop, as shown in Fig. 4.6. Note that in loops always the coupling to the heaviest particle dominates, leading to a dominant role of the top quark in the fermion loop. The same is true when resolving the effective coupling to gluons, which follows the same line of argumentation and plays a more important role in the discussion of the production

At 8 TeV center-of-mass energy and for  $m_H \approx 100 \, \text{GeV}$  the required fraction of the parton momentum over the proton momentum is  $\langle x \rangle \approx 0.11$ . In Fig. 4.1 the probability to observe a valence quark  $(xu_v \text{ and } xd_v)$  sea quark (xS) or gluon (xg) for a given value of the parton momentum fraction, x, are shown at a scale of

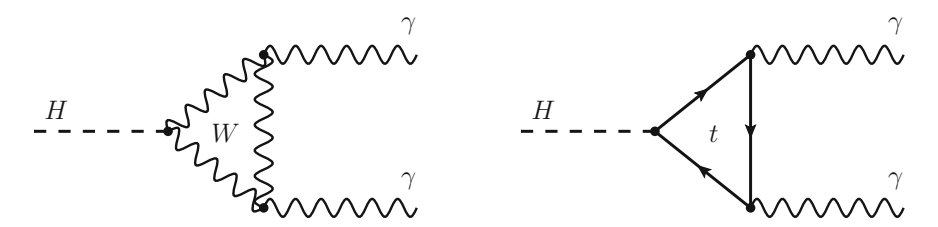
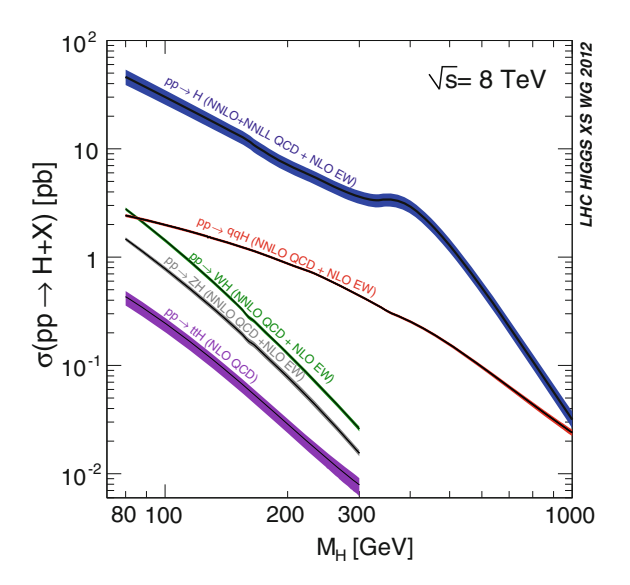


Fig. 4.6 Sketch of the leading-order contributions to the decay of the SM Higgs boson into two photons  $(\gamma)$ , via a (left) W boson or (right) top quark loop. For the bosonic loop only the W boson is of relevance, since the photon couples to the charge of the W boson. For the fermionic loop in principle each fermion can contribute, but the dominant contribution is via the heaviest particle that runs in the loop. In cross section calculations the fermion loop enters with a minus sign, leading to a destructive interference terms and lowering the overall decay rate into photons, in the SM. This will be further discussed in Sect. 5.3

Fig. 4.7 Expected cross section for SM Higgs boson production at 8 TeV, split by production modes, as determined from [17, 19, 20]. The curve on the top (with the *blue band*) corresponds to  $qq \rightarrow H$ production, followed by  $(red) qq \rightarrow H$  production and Higgs boson production in association with (green) W bosons, (brown) Z bosons and (magenta)  $t\bar{t}$  pairs. The bands correspond to the theoretical uncertainties



 $Q^2 = (100 \,\mathrm{GeV})^2$ . The figure illustrates the overwhelming dominance of gluons over quarks as initial partons of the hard scattering process, which is in contrast to the *Tevatron*, where much larger values of  $\langle x \rangle \approx 0.25$  had to be probed to reach out to a similarly large energies. Consequently the dominant mode for the production of SM Higgs bosons at the LHC is gluon fusion  $(qq \rightarrow H)$  as shown in Fig. 4.7 [17, 19, 20]. This is the case although the effective coupling of the SM Higgs boson to gluons proceeds only at one-loop level and not at tree level, as discussed before. The next important production mode is via vector boson fusion  $(qq \rightarrow H)$ , which over the gluon fusion exhibits a specific event signature, emerging from the scattered quarks, from which the vector bosons are radiated off, and characterized by two well separated jets in the forward and backward direction of the detector with no further hadronic activity in between. Less prominent production modes are Higgs *strahlung*, which results in the production of Higgs bosons in association with Z(ZH) or W(WH) bosons (the most important production mode at LEP and at the Tevtron) and Higgs strahlung in association with top quark pairs  $(t\bar{t}H)$ . Typical diagrams for these processes are shown in Fig. 4.8.

The expected cross section for each production mode as used for the final *CMS* publications based on the *LHC* run-1 dataset of the years 2011 and 2012 are shown in Table 4.1. All but the cross section for the production in association with *top* quark pairs have been calculated in NNLO in the strong coupling constant  $\alpha_s$  and at NLO in the fine structure constant  $\alpha$ . The production cross section in association with *top* quark pairs has been calculated at NLO precision in  $\alpha_s$ . The first uncertainty in the table corresponds to the uncertainty due to missing higher orders in the perturbation series, usually estimated by a variation of the renormalization and factorization scales by a factor of two. It is  $\mathcal{O}(7\,\%)$  for gluon fusion and  $\mathcal{O}(1\,\%)$  and below for

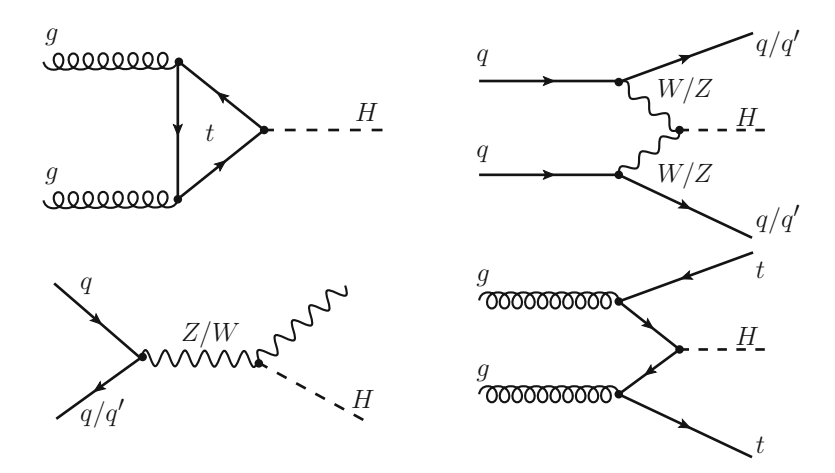


Fig. 4.8 Sketch of typical processes for Higgs boson production at the *LHC*: (upper left) the dominant production mode via gluon fusion  $(gg \rightarrow H)$ , (upper right) vector boson fusion  $(qq \rightarrow H)$ , (lower left) Higgs boson production in association with vector bosons (ZH, WH) and (lower right) Higgs boson production in association with top quark pairs  $(t\bar{t}H)$ 

**Table 4.1** (Left) Cross section for the production modes of the SM Higgs boson, in proton proton collisions at a center-of-mass energy of 8 TeV and (right) branching fractions (BR) of the SM Higgs boson, each for  $m_H = 125$  GeV, as determined from [17, 19, 20]

Process	Cross section $\sqrt{s} = 8 \text{ TeV}, m_H = 125 \text{ GeV}$	Final state	BR $\Gamma_H = 4.04 \mathrm{MeV}$
$gg \rightarrow H$	$19.52 \pm 1.47 \pm 1.40 \mathrm{pb}$	$\gamma\gamma$	0.00229
$qq \rightarrow H$	$1.578 \pm 0.003 \pm 0.043 \mathrm{pb}$	WW	0.216 (0.0106)
WH	$0.6966 \pm 0.0023 \pm 0.024 \mathrm{pb}$	ZZ	0.0266 (0.000126)
ZH	$0.3943 \pm 0.0061 \pm 0.014 \mathrm{pb}$	$b\bar{b}$	0.577
tτ̄Η	$0.1302 \pm 0.0085 \pm 0.010 \mathrm{pb}$	$\tau\tau$	0.0637

On the left the first uncertainty corresponds to missing higher-order corrections, the second uncertainty to insufficient knowledge of the parton density functions. On the right the values in braces correspond to the decay chains with electrons and muons in the final state. The uncertainty on the branching fractions is  $\mathcal{O}(5\%)$ 

vector boson fusion and Higgs boson production in association with vector bosons. The larger uncertainties on the production cross section via gluon fusion can be explained from the fact that this production mode sets in only at one-loop level in  $\alpha_s$  in contrast to the vector boson related production modes. The second uncertainty in the table corresponds to the limited knowledge of the parton density functions in the proton. It is again  $\mathcal{O}(7\%)$  for gluon fusion and  $\mathcal{O}(3\%)$  for the vector boson related production modes. As can be seen from the table the vector boson fusion process and the production in association with vector bosons are known with remarkable precision (with the largest uncertainty from the insufficient knowledge of the quark

density functions at medium parton momentum fraction x), while the knowledge of the gluon fusion process is still moderate despite of the large effort that went into the calculation of higher orders. This underlines the importance of higher-order calculations for the estimation of the production rates of purely QCD induced processes. All production modes sum up to a total cross section of  $\approx$ 22 pb in proton proton collisions at 8 TeV center-of-mass energy, compared to a roughly  $10 \times$  larger cross section for the production of top quark pairs with  $\approx$ 250 pb and a cross section for the production of single top quarks of  $\approx$ 80 pb. For a center-of-mass energy of 7 TeV the cross section for the production of the SM Higgs boson decreases by  $\approx$ 20 %, for a center-of-mass energy of (13) 14 TeV it increases by a factor of (2.25) 2.5.

#### 4.2.2 First Searches and Statistical Methods

Searches for the SM Higgs boson were first published by the *ATLAS* and *CMS* collaborations based on the complete 7 TeV dataset with roughly 5 fb<sup>-1</sup> for each experiment, in 2011 [21, 22]. All searches had been performed "blind", which means that the strategies for event selection, crosscheck of the normalization and kinematic distributions of background processes and signal extraction methods as well as the determination of reconstruction efficiencies and calibration constants were defined by the analysts without knowing the data in the signal region of the search. This procedure shall guarantee that the analysts are not influenced in their decision taking by the appearance or non-appearance of a potential signal in the data. These decisions are taken to best knowledge in theory and simulation and according to the assessment of control of the data in predefined background control regions. After the analysts have declared the analysis to be final it is "frozen" and the signal region is "unblinded". After this "unblinding" step, the analysis is not allowed to be changed any more.

The results of the searches were presented in form of upper limits on the production cross section,  $\sigma$ , in terms of the cross section,  $\sigma_{SM}$ , as expected by the SM for a given value of  $m_H$ . For these limits again the search strategy and statistical methods as developed for the searches at LEP were adopted to the needs and the technological developments by that time. Theoretical and experimental uncertainties were implemented in form of nuisance parameters  $\theta$  in the definition of the likelihood functions. Analogue to Eq. (3.10) the test statistic was defined as a likelihood ratio,

$$q_{\mu} = \frac{\mathcal{L}\left(n|\mu \cdot s(\hat{\theta}_{k,\mu}) + b(\hat{\theta}_{k,\mu})\right)}{\mathcal{L}\left(n|\hat{\mu} \cdot s(\hat{\theta}_{k}) + b(\hat{\theta}_{k})\right)} \qquad 0 \le \hat{\mu} < \mu$$
(4.1)

but this time estimated for a given test value of  $\mu = \sigma/\sigma_{SM}$  for the (s+b)-hypothesis (indicated by the subscript  $q_{\mu}$  in the equation) where, as in the *Tevatron* definition a fit to the data was applied prior to any further statistical inference to determine

the most probable values,  $\hat{\mu}$  for  $\mu$  and  $\hat{\theta}_{k,(\mu)}$  for the nuisance parameters,  $\theta_{k,(\mu)}$ (for the given test value of  $\mu$ ). The ratio  $\mu$  is called signal strength. In contrast to the Tevatron definition, the signal strength was not explicitly set to 0 for the b-hypothesis in the denominator of the likelihood ratio. Instead it was allowed to vary between 0 and the fixed test value,  $\mu$ , in the numerator. In this way the  $\hat{\theta}_k$  correspond to the absolute minima and the  $\hat{\theta}_{k,\mu}$  to the minima for the fixed test value of  $\mu$ . This definition turns the likelihood ratio into a profile likelihood function and allows to use asymptotic  $\chi^2$  formulae in the further statistical inference [23], preventing the CPU intensive evaluation of thousands of toys, as in the case of the *Tevatron* test statistic. The confidence intervals  $CL_{s+b}$ ,  $CL_b$  and the ratio of confidence intervals  $CL_s$  remained the same as defined in Eq. (3.11). If  $CL_s \leq \alpha$  for  $\mu = 1$  and a given value of  $m_H$ , this mass point was considered excluded at the  $(1-\alpha)$  CL. The expected exclusion in the absence of a SM Higgs boson for a given value of  $m_H$ was also used to quantify the "exclusion sensitivity" of a given analysis, in terms of multiples of  $\sigma_{SM}$ . The conventional value for  $\alpha$  was chosen to be 0.05, translating into exclusion statements at 95 % CL as in previous searches. For the quantification of an access the test statistic

$$q_0 = \frac{\mathcal{L}\left(n|b(\hat{\theta}_{k,0})\right)}{\mathcal{L}\left(n|\hat{\mu}\cdot s(\hat{\theta}_k) + b(\hat{\theta}_k)\right)} \qquad 0 \le \hat{\mu}$$

$$(4.2)$$

as a special case of Eq. (4.1) for  $\mu=0$  was used to obtain the p-value, with slightly modified boundary conditions for  $\hat{\mu}$ . The limits as published at the eve of the discovery in July 2012 are shown in Figs. 4.9 and 4.10. They correspond to the full dataset that had been analyzed by that time with a center-of-mass energy of 7 TeV, corresponding to a luminosity of approximately  $5\,\mathrm{fb^{-1}}$  for each experiment. In the upper parts of the figures the 95 % CL exclusion limits as measured by the ATLAS and the CMS experiment are shown. The black points connected by the black line correspond to the observed 95 % CL upper limit on the production cross section in terms of  $\sigma_{\mathrm{SM}}$ . The median expected limit in the absence of a SM Higgs boson for a given value of  $m_H$  (corresponding to the b-hypothesis) is shown as dashed line with the  $1\sigma$  ( $2\sigma$ ) uncertainty indicated by the dark green (bright yellow) band. For a fixed value of  $m_H$  the expected limit and its uncertainties correspond to the median and the 68 and 95 % quantiles of a distribution equivalent to the distributions for the background only hypothesis as shown in Fig. 3.6.

For the *CMS* experiment the expected exclusion limit at 95% CL ranged from 118 to 543 GeV. The observed exclusion limit was in a range from 127 to 600 GeV. In a range between 118 and 127 GeV the presence of a SM Higgs boson could not be excluded and even in a slightly narrower range, between 121 and 126 GeV, the observed limit exceeded the expected limit by more than  $2\sigma$ . This excess had its maximum at a value of  $m_H \simeq 124$  GeV with a p-value of 0.001, corresponding to a significance of  $3.1\sigma$ . As can be seen from the bottom of Figs. 4.9 and 4.10 this excess in the data was strongest in the  $H \to \gamma \gamma$  decay channel for both experiments. At the

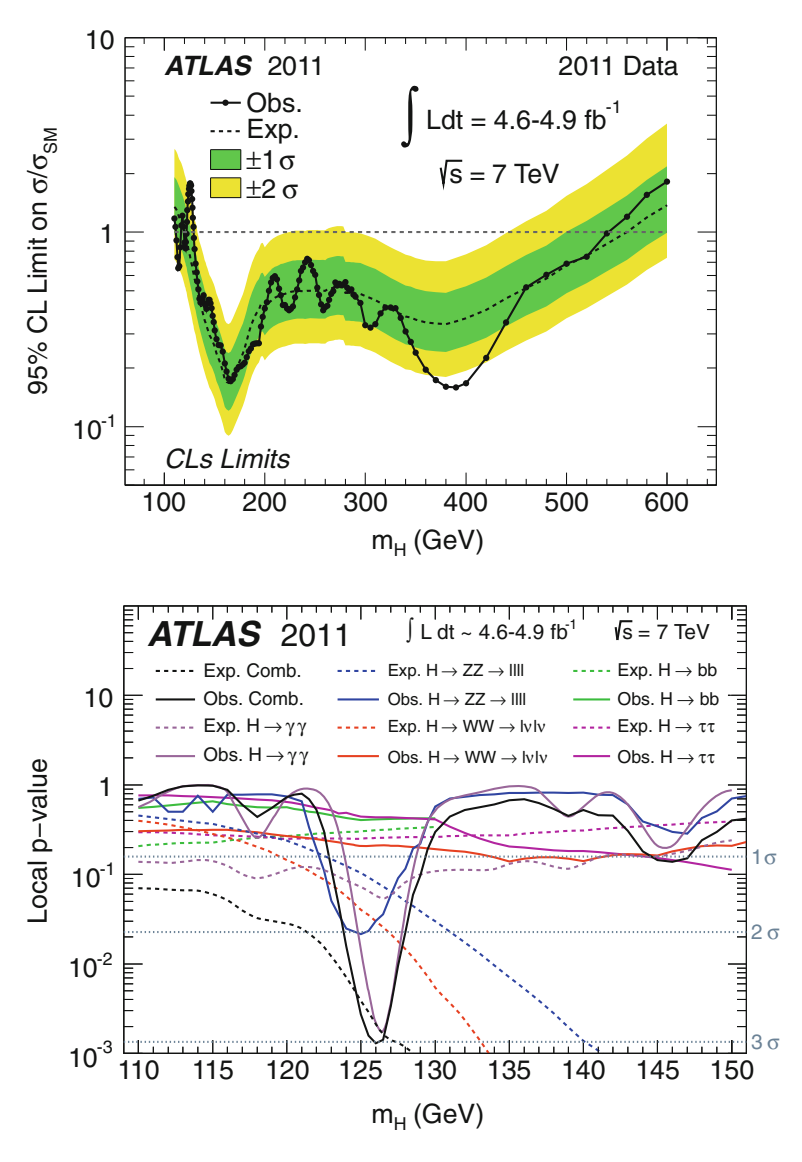


**Fig. 4.9** (*Top*) exclusion contour and (*bottom*) *p*-values for the search for the SM Higgs boson with masses from 110 to 600 (150) GeV, based on the 7 TeV dataset taken in 2011 and corresponding to a luminosity of  $\approx$ 5 fb<sup>-1</sup>, collected with the *ATLAS* experiment [21]

eve of the discovery in July 2012 the situation was the following: clear exclusions had been set for finding a SM Higgs boson at higher masses, mostly driven by the dominant high mass decay channels into vector bosons; there were hints of a signal, which were not conclusive yet; and there were more data at the higher center-of-mass energy of 8 TeV to be analyzed.

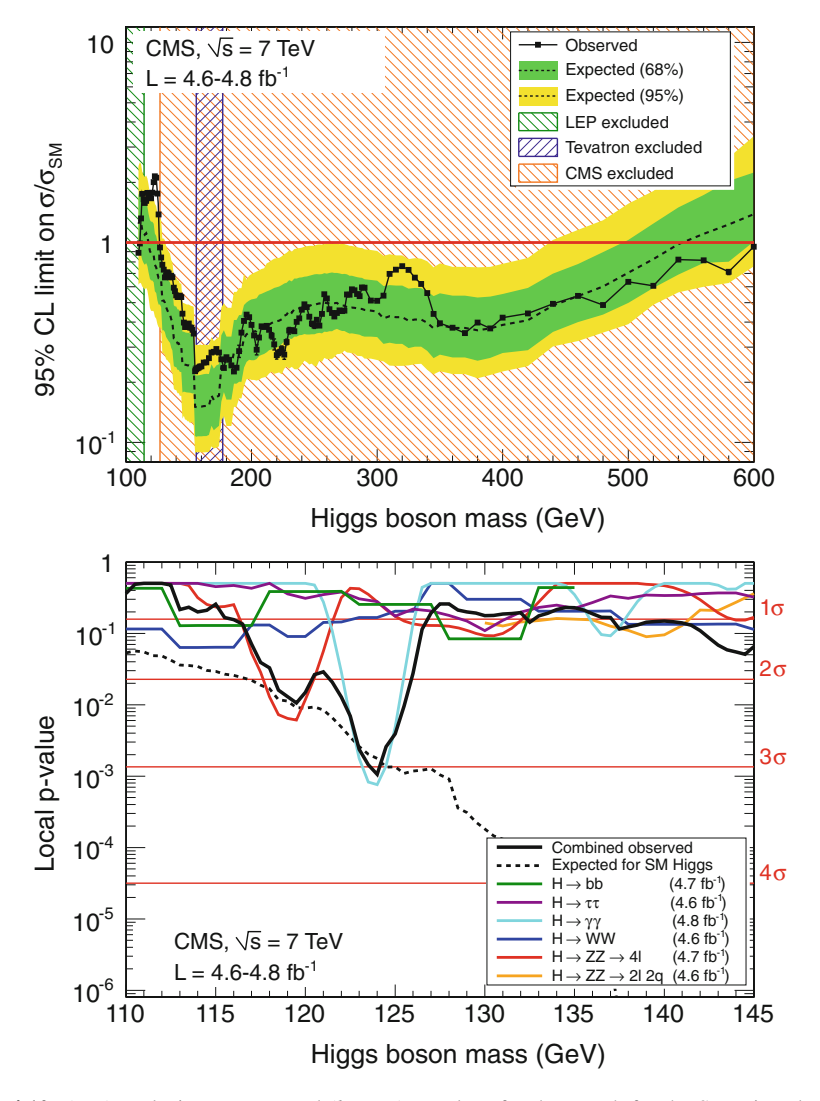


**Fig. 4.10** (*Top*) exclusion contour and (*bottom*) *p*-values for the search for the SM Higgs boson with masses from 110 to 600 (145) GeV, based on the 7 TeV dataset taken in 2011 and corresponding to a luminosity of  $\approx 5 \, \mathrm{fb}^{-1}$ , collected with the *CMS* experiment [22]. In the exclusion contour of *CMS* also the excluded mass values from *LEP* and *Tevatron* by that time are indicated

# **4.3** The Discovery of a New Particle in the Bosonic Decay Channels

In July 2012 both experiments *ATLAS* and *CMS* had analyzed the first 5 fb<sup>-1</sup> of proton proton collision data at the higher center-of-mass energy of 8 TeV. On 4 of July 2012 the discovery of a new boson was announced in a CERN seminar prior

to the *International Conference of High Energy Physics (ICHEP)* in Melbourne, Australia [24–26]. The evidence that had shown up in the 7 TeV data already, was confirmed. The excess had shown up in two independent decay channels and in both experiments at approximately the same position of  $m_H \approx 125\,\text{GeV}$ , and the combined measurements of all search channels for each individual experiment had reached the  $5\sigma$  level. The local p-value of the final publication based on the same dataset for each of the experiments, as a function of  $m_H$ , is shown in Fig. 4.11.

The figure shows that for each experiment the discovery was driven by the  $H \to \gamma\gamma$  and  $H \to ZZ$  decay channels, which have a relative mass resolution between 1–2% in  $m_H$ . In the case of *CMS* the  $H \to \gamma\gamma$  decay channel alone reached a significance of >4 $\sigma$ , followed by the  $H \to ZZ$  decay channel with a significance of >3 $\sigma$  at about the same value of  $m_H$ . Both excesses are supported by an expected broad excess of  $\approx 2\sigma$  in the  $H \to WW$  decay channel. The combination of all decay channels added up to the 5 $\sigma$  excess that had been reported. For *ATLAS* the situation was similar, while the excess was a bit larger and a small difference in  $m_H$  was observed between the  $H \to \gamma\gamma$  and the  $H \to ZZ$  signal.

It is worth mentioning that the discovery could only be established in the decay channels into bosons, which also most radically challenge the concept of local gauge symmetries. Note that the problem of the SM with mass terms for fermions is only introduced by the fact that the W boson couples only to left-handed fermions, and that this problem could in principle be solved differently from the solution that has been explained in Chap. 2. The question, whether the Higgs mechanism as introduced in Chap. 2 would also solve the problem of fermion masses in the SM still remained unanswered: the two fermionic decay channels that were in the reach of the LHC,  $H \to b\bar{b}$  and  $H \to \tau\tau$  did not show any significant excess, which was a tribute to the fact that both channels had not reached the sensitivity yet, to be able to see the excess for a SM like Higgs boson. Indeed both decay channels at both experiments were just around the corner to give a more conclusive answer to this question. Indirect conclusions could be drawn from the over all consistency of the production and bosonic decay structure, since both the main production process, via gluon fusion  $(qq \rightarrow H)$  and the loop induced decay into photons would proceed (at least partially) via a fermionic loop, as depicted in Figs. 4.6 and 4.8.

The fact that the new particle was a boson was clear from its confirmed observation in the decay channels into photons or Z bosons, which are both bosons with spin 1. These two decay channels also fixed the mass of the new particle, with the high precision of a few hundred MeV to  $m_H=125\,\mathrm{GeV}$  and thus the predicted production cross section to the  $\approx\!22\,\mathrm{pb}$  at 8 TeV that have been discussed in Sect. 4.1. With the mass of the new boson, when interpreted as the Higgs boson of the SM, the last ambiguity of the SM was resolved.

In the wake of this discovery several updated results with increasing luminosity have been presented at conferences, investigating the development of the excess and first properties of the new boson, based on preliminary alignment and calibration constants of the detectors, that had been used during data taking. The first data taking period of the LHC was completed by the end of 2012 with a total amount of  $5\,\mathrm{fb}^{-1}$ , taken at  $7\,\mathrm{TeV}$ , and  $20\,\mathrm{fb}^{-1}$ , taken at  $8\,\mathrm{TeV}$  center-of-mass energy. At this

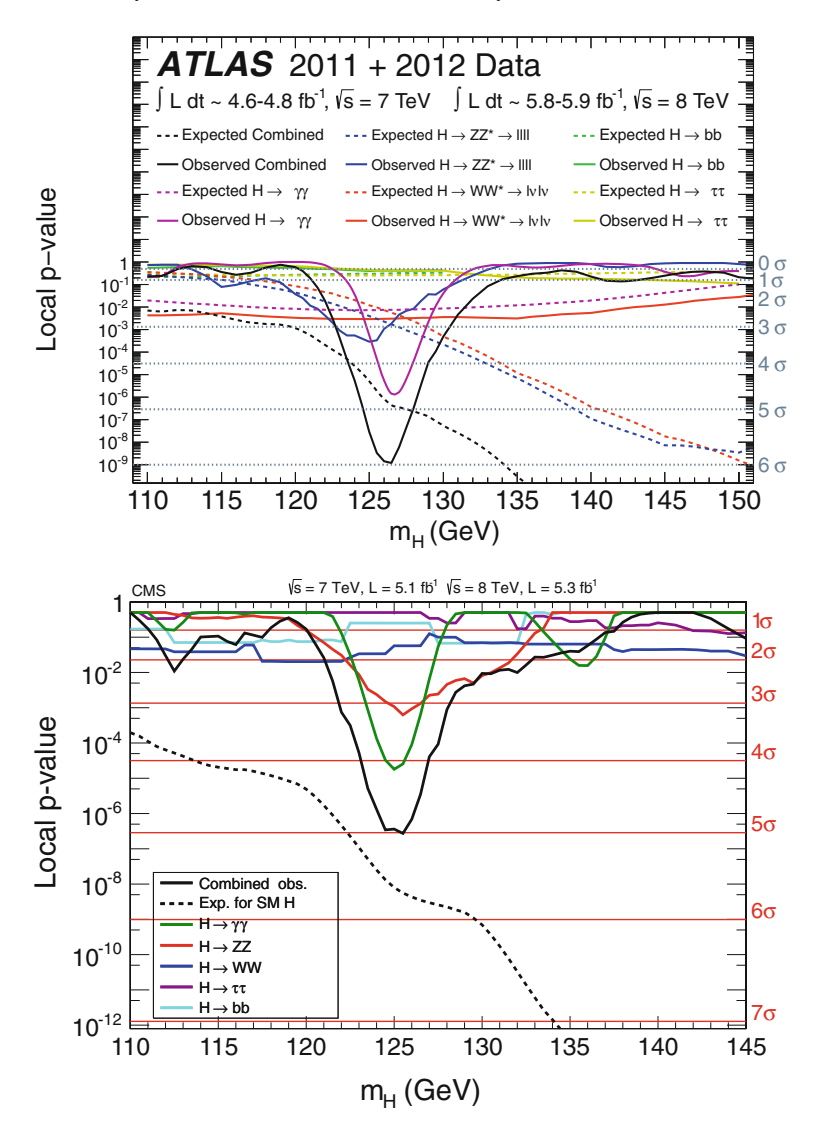


**Fig. 4.11** Local *p*-value based on the data analyzed by the time of the discovery announcement by both experiments, (top) ATLAS [24] and (bottom) CMS [25, 26], on 4 July 2012, based on 5 fb<sup>-1</sup> of data at 7 TeV and 5 fb<sup>-1</sup> of data at 8 TeV center-of-mass energy

time the *LHC* entered an upgrade phase to restart a new measurement program with increased instantaneous luminosity and increased center-of-mass energy of 13 TeV, with the aim to collect  $300\,{\rm fb^{-1}}$  in a second period of three years data taking from 2015 on. These data should allow to measure the properties of the new boson at an accuracy level of  $\mathcal{O}(3-5\,\%)$  across all main decay channels.

In Spring 2014 the CMS experiment published the complete and final set of analyses in the five main decay channels that had been presented by the time of discovery, based on the full dataset of the first data taking period of 2011 and 2012 [27–31]. These results exploit the final calibration and alignment of the detector and most refined analysis strategies, which represent the best understanding of the data and lay path for analyses strategies from 2015 on. For the re-analysis the data had been "re-blinded" to prevent selection biases. The analyses have been increased in complexity, more elaborate signal extraction methods have been applied and the event categorization has been increased to further exploit the characteristics of SM Higgs boson production. In addition more analysis channels and an inclusive analysis for Higgs boson production in association with top quark pairs have been published. Compared to the preliminary results they give a good and instructive example of what can be achieved by the careful analysis of a closed high quality dataset in the timespan of one year. These publications give the final word of the CMS experiment on the first data taking period of the LHC. The following discussion will be based on these final results. For the decay channels which have been part of the discovery the simplifications that had been made by the time of the discovery will be briefly discussed at the end of the corresponding sections. The results will be compared to the results by the ATLAS collaboration where available.

#### 4.3.1 The Signal in the $H \rightarrow \gamma \gamma$ Decay Channel

The search for the SM Higgs boson in the decay channel into two photons for low values of  $m_H$  [27] is one of the analyses that the CMS detector with its excellent ECAL has been built for. The signature of this decay channel consists of two high energetic isolated high transverse momentum photons that are reconstructed as clusters in the ECAL. The term isolated indicates that no significant hadronic activity in the vicinity of the reconstructed photons is expected, since neither the Higgs boson, nor the photons carry color charge and thus do not take part in the strong interaction.

The strength of this decay channel lies in the clear and easy to reconstruct signature and in the high resolution of the invariant diphoton mass,  $m_{\gamma\gamma}$  that can be achieved, which is of the order of  $\mathcal{O}(1\text{--}2\,\%)$ . Difficulties arise from the large background from non-resonant QCD diphoton production or single photon production in association with jets, of which fragments might be misidentified as a second photon. For a mass of the SM Higgs boson of  $m_H=125\,\text{GeV}$  the branching fraction of this decay channel is  $BR(H\to\gamma\gamma)=0.00229$  leading to an expectation of  $\approx 1000$  signal events in the 8 TeV dataset, not taking any reconstruction or selection inefficiencies into account. The naively expected signal over background ratio (S/B) is  $\mathcal{O}(1/10)$ , depending on the exact kinematics and topology of the events.

To maximize the sensitivity of the analysis, the standard reconstruction techniques of *CMS* had been refined in several aspects. The final calibration of the reconstructed photons had been obtained from a multivariate regression method mapping the reconstructed onto the true photon energy in simulated events. This calibration had been

validated with well reconstructed and identified  $Z \rightarrow ee$  events, where the electrons had been reconstructed and selected as if they were photons. In a comparison between data and simulation an overall good agreement had been found as a function of the photon kinematics and several reconstruction related quantities. Correction factors and additional smearing coefficients had been derived and applied to account for small residual imperfections of the detector description in the simulation.

The photons for the analysis had been selected to have transverse momenta of  $p_T^{\gamma} > 33(25)\,\text{GeV}$  for the (sub-)leading photon in addition to some loose selection criteria based on the shape of the reconstructed photon clusters, the energy in the hadronic calorimeter sections behind the reconstructed photons and a veto on the reconstructed photon of being an electron. The latter can be easily achieved by requiring that no charged particle track is pointing towards the reconstructed cluster in the calorimeter. Any further identification had been left to a multivariate event classifier based on a *boosted decision tree* (BDT) technique [32–34] for photon identification (photon ID BDT score), with the following additional information as input: the shape of the reconstructed photon shower in the *ECAL* and in the preshower detector; the energy deposits in the vicinity of the reconstructed photon; the median of the energy density in the detector per unit area (a variable related to the amount of pileup in the event); the pseudorapidity,  $\eta$ , and the energy of the reconstructed photon cluster in the *ECAL* as well as of the fully reconstructed photon.

The photon ID BDT score had been validated comparing  $Z \to \mu\mu\gamma$  or  $Z \to ee$  events with the simulation, where in the latter case the electron veto had been removed from the selection and, as for the validation of the photon energy calibration before, the electrons had been reconstructed as if they were photons. A comparison of the photon ID BDT score as obtained in data with the simulation composed of  $\gamma$ - $\gamma$ ,  $\gamma$ -jet and jet-jet events is shown in Fig. 4.12 (left). In the figure the black points with the error bars correspond to the data and the black line with the dark (purple) shaded band to the simulation. The expected photon ID BDT score for the  $H \to \gamma\gamma$  signal is also shown by a red line. Note that in this figure the number of expected  $H \to \gamma\gamma$  events has to be read off from the second axis on the right of the figure. In the final event selection only those photons were considered, for which the photon ID BDT score was above an optimized threshold, which was found to retain 99 % of all signal events, rejecting roughly a quarter of the events in data.

The resolution of  $m_{\gamma\gamma}$  does not only depend on the energy resolution of the reconstructed photon clusters, but also on the calculation of the opening angle of the two photons, which itself depends on the correct choice of the vertex of the hard interaction. For this analysis the standard choice of the hard interaction vertex had been replaced by a channel specific multivariate selection method, to assign a probability of the chosen vertex to be correct (vertex probability estimate). To achieve this, in a first step a multivariate discriminator had been build using not only the  $\sum \vec{p}_T^2$  of the emerging tracks as input, as used by the standard choice, but also the sum of the  $p_T$  of the emerging tracks projected onto the direction of the reconstructed diphoton pair in the transverse plane,  $-\sum (\vec{p}_T \cdot \hat{n}_T^{\gamma\gamma})$ , and the asymmetry between

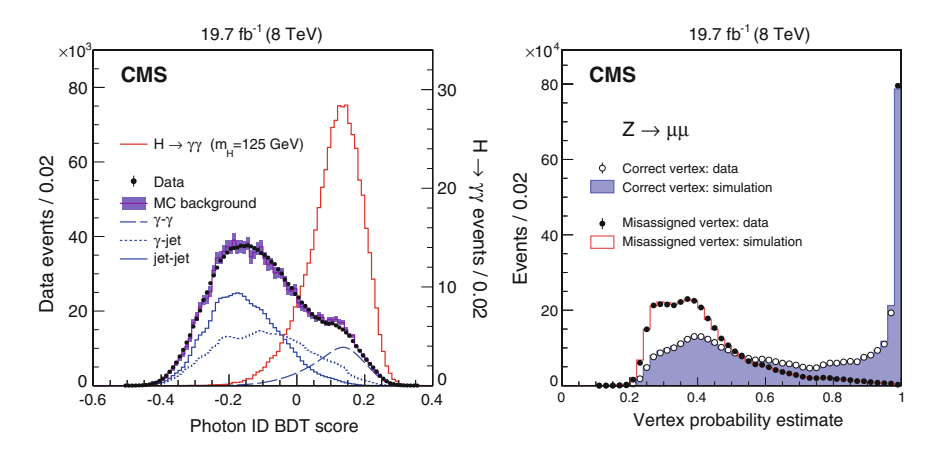


**Fig. 4.12** (*Left*) Multivariate discriminant of the photon identification (labeled as "photon ID BDT score") and (*right*) estimate for the probability to identify the vertex of the hard interaction (labeled as "vertex probability estimate") for the 8 TeV dataset [27]. In the figure on the *right* the comparison of the simulation with  $Z \to \mu\mu$  events is shown, split into the fraction of events where the vertex of the hard interaction has been correctly assigned, and events where this is not the case. More details of this crosscheck are given in the text

the summed transverse momentum in the vertex and the transverse momentum of the diphoton system,

$$\mathcal{A}_{\text{vtx}}^{\gamma\gamma} = \frac{\left|\sum \vec{p}_T\right| - |\vec{p}_T^{\gamma\gamma}|}{\left|\sum \vec{p}_T\right| + |\vec{p}_T^{\gamma\gamma}|}$$

where the additional information was motivated by the idea that the transverse momentum summed over the charged tracks in the correct interaction vertex should balance the transverse momentum of the diphoton system.

The output of this discriminator for the vertices with the three highest scores, the distances between the vertex with the highest score and the vertices with second and third highest score, the total number of reconstructed vertices, the transverse momentum,  $p_T^{\gamma\gamma}$ , of the diphoton system and the information whether none, one or both photons had tracks from an intermediate  $\gamma \to ee$  conversion associated, had been fed into another multivariate classifier to obtain the final vertex probability estimate for finding the vertex of the hard interaction. As a function of  $p_T^{\gamma\gamma}$  this discriminator has a steep rise and reaches a plateau at a probability of about 96%, for the 8 TeV dataset. Integrated over  $p_T^{\gamma\gamma}$  the probability to assign the correct vertex had been found to be 85% on the 7 TeV dataset and 80% on the 8 TeV dataset, where the loss in efficiency in the 8 TeV dataset could be attributed to the increased pileup in the events.

The vertex probability estimate had been validated comparing the data in dedicated control samples with the simulation. These control samples consisted e.g. of a clean selection of  $Z \to \mu\mu$  events, from which the charged particle tracks belonging to the reconstructed muons had been used to identify the vertex of the hard interaction.

In the subsequent step these tracks had been removed from the reconstructed event and the vertex identification procedure as described above had been applied on the remaining event. A comparison of the data with the simulation, both for events for which the proper vertex could be assigned and for events, where this was not the case, are shown in Fig. 4.12 (right). The open points with the error bars correspond to the data for the events where the vertex of the hard interaction could be identified, the black points with the error bars correspond to the events, where this was not the case. These have to be compared with the open red and filled blue histograms correspondingly. The correlation of the vertex probability estimate with the actual probability to find the vertex of the hard interaction can be assessed from the display of both event classes, which becomes more obvious from the crossing point of both distributions at the value of 0.5 or from the dominance of correct vertex associations at the value of 1.0. A very good agreement between data and simulation can be seen over the whole range in both event classes, which demonstrates that the vertex probability estimate is well under control.

For the final statistical inference, events with two well identified photons were selected with a transverse momentum of  $p_T^{\gamma} > m_{\gamma\gamma}/3$  ( $m_{\gamma\gamma}/4$ ) for the (sub)-leading photon. In the rare case of multiple diphoton candidates, the one with the highest  $p_T^{\gamma_1}$  +  $p_T^{\gamma_2}$  was chosen. The use of the  $p_T^{\gamma}$  thresholds divided by  $m_{\gamma\gamma}$  prevents distortions at the low end of the  $m_{\gamma\gamma}$  spectrum, that would occur if fixed thresholds would have been applied. The discriminating variable was chosen to be  $m_{\gamma\gamma}$  in a mass range of  $100 < m_{\gamma\gamma} < 180 \,\text{GeV}$ . To increase the sensitivity of the analysis the events were divided into categories exploiting specific characteristics of the SM Higgs boson production modes or characterizing the event according to the expected signal to background fraction (S/B) and resolution of  $m_{\gamma\gamma}$ . The classification according to the characteristics of the production modes,  $qq \rightarrow H$ , VH and  $t\bar{t}H$  affected only 1 % of all selected events and should rather be taken as laid out for future analyses from 2015 on. The classification of the remaining 99 % of the events was made based on another multivariate discriminator (diphoton BDT classifier score), built from the following input variables: the photon transverse momenta,  $p_T^{\gamma}/m_{\gamma\gamma}$ ; pseudorapidity,  $\eta$ , and the value of the photon ID BDT score of each photon; the cosine of the angle between the two photons in the transverse plane; an estimator of the expected relative resolution of  $m_{\gamma\gamma}$  under the hypothesis of selecting the correct or a wrong interaction vertex; and the value of the vertex probability estimate. This multivariate discriminator for the 8 TeV dataset is shown in Fig. 4.13, where the discriminator has been transformed to be flat for the combined signal contribution. In the figure the black points with error bars correspond to the data and the blue open histogram to the expectation from the simulation. The split of the signal sample by SM Higgs boson production modes is indicated by filled histograms in various shades of red. Note that in this figure again the number of  $H \to \gamma \gamma$  events has to be read off from the additional axis on the right.

Dashed horizontal lines indicate the thresholds that had been chosen for the event categorization, where the event category with the highest S/B ratio and the best resolution in  $m_{\gamma\gamma}$  can be found on the right of the distribution, with the highest values of the diphoton BDT classifier score. Events with a small score, corresponding to the

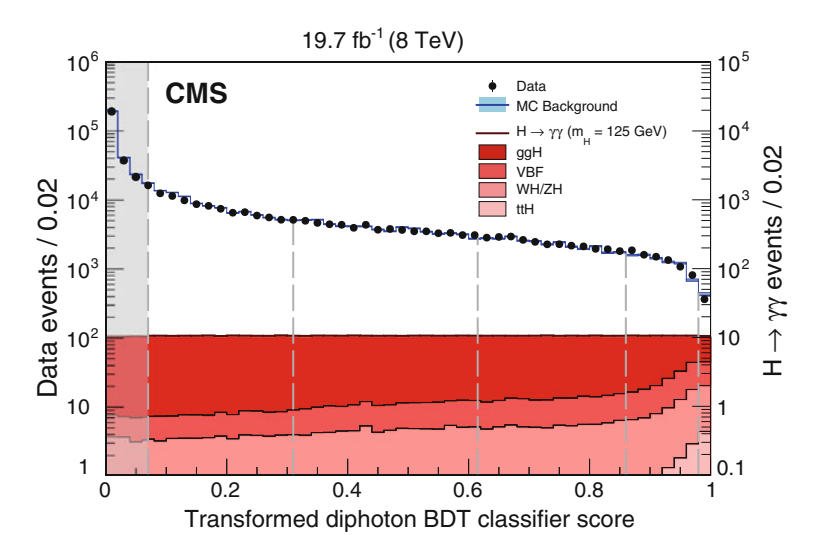


**Fig. 4.13** Multivariate discriminant for the classification of 99% of the diphoton events, which had not been classified according to the production mode (diphoton BDT classifier score) [27]. The event classes are defined by thresholds on the diphoton BDT classifier score, as indicated by the *dashed horizontal lines* in the figure. The events in the *shaded area* on the *left side* of the plot had not been considered for the further statistical inference

shaded area on the left of the figure, were not considered for the further statistical inference. In the best event category the signal over background fraction from the bare number of events across the whole mass range is  $S/B \approx 1/40$ , rapidly decreasing for the less sensitive event categories.

Similar categorizations were derived in the  $qq \rightarrow H$  classified events, as far as the number of selected events in this event category allowed, resulting in a total of 25 independent event categories for the combined 7 and 8 TeV dataset. The largest expected purity of a single production mode with respect to the other production modes was reached in the  $t\bar{t}H$  tagged event categories with usually  $\gtrsim 90\%$ . On the combined dataset these event categories had an expectation of  $\approx$ 2.5 background events within the expected resolution in the vicinity of  $m_{\gamma\gamma} \approx 125 \,\text{GeV}$  and  $\approx 1.3 \,\text{SM}$ Higgs boson events, while  $\approx$ 5 events had been observed. The most sensitive inclusive event category on the 8 TeV dataset (as indicated in Fig. 4.13) had an expected fraction of 75.7 % for  $gg \to H$  events and 11.9 % of  $gg \to H$  events when compared to the sum of all SM Higgs boson production modes. In the vicinity of  $m_{\gamma\gamma} \approx 125\,\mathrm{GeV}$ the expected number of background events was  $\approx$ 5 and the expected number of SM Higgs boson events  $\approx$ 6, resulting in an S/B ratio in the mass region of interest of  $\approx$ 1. The comparison to  $S/B \approx 1/40$ , when determined from the event numbers in this event category across the whole mass range, as indicated above, underlines the importance of the mass resolution in this analysis. On the other hand the resolution of  $m_{\gamma\gamma}$  must be controlled to an excellent level, which constitutes one of the main challenges of this analysis.

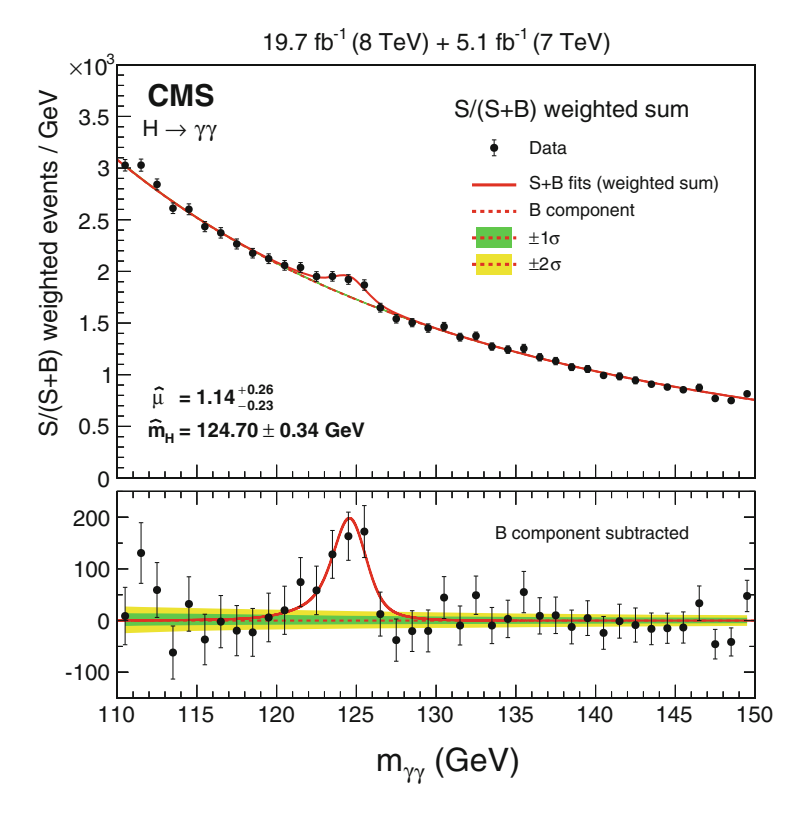


Fig. 4.14 Final distribution of  $m_{\gamma\gamma}$ , that has been used for the statistical inference, summed over all 25 event categories, which have been weighted by the expected S/(S+B), in the vicinity of the peak at  $m_H \approx 125\,\text{GeV}$  [27]. In the *lower panel* the expectation from the *b*-hypothesis has been subtracted from the plot in the *upper part* of the figure.

The  $m_{\gamma\gamma}$  distribution for all selected events summed over all 25 event categories and weighted by the S/(S+B) ratio in each event category is shown in Fig. 4.14. The weighting roughly resembles the event weights in the test statistic in the statistical inference as discussed in Sect. 3.4. The black points with the error bars correspond to the weighted data events. The continuous and dashed red line with the bright yellow and dark green bands corresponds to the models for the (s+b)- and b-hypothesis and the one and two  $\sigma$  uncertainty of the b-hypothesis after applying an unbinned maximum likelihood fit as used for the signal extraction. Both, the models for the (s+b)- and b-hypothesis are analytical thus that no assumptions about the shape of the background distribution enter into the statistical inference other than being of non-peaking nature. Uncertainties on the assumed background modeling had been carefully estimated and added in form of a discrete nuisance parameter to the likelihood model. In the lower panel of the figure the same events are shown, where the expectation from the b-hypothesis has been subtracted from the weighted data events. A clear signal is visible on top of a huge background, which has been quantified by

the *p*-value to correspond to an observed (expected) significance of  $5.7\sigma$  ( $5.2\sigma$ ) at  $\hat{m}_H = 124.7\,\text{GeV}$  on the combined dataset. These significances correspond to an observed value of  $\hat{\mu} = 1.14 \pm 0.25$ , well compatible with the expectation of  $\mu = 1$  as predicted by the SM. Evaluated at  $m_H = 125.0\,\text{GeV}$  the observed (expected) significance changes to  $5.6\sigma$  ( $5.3\sigma$ ), corresponding to a value of  $\hat{\mu}|_{125\,\text{GeV}} = 1.12 \pm 0.24$ .

Compared to the analysis as published by the time of the discovery, apart from the increased number of events, the photon energy calibration on the final dataset had been revised introducing a time dependent calibration, which resulted in an improvement of the  $m_{\gamma\gamma}$  resolution up to  $\approx 40$  % in the mass range of  $m_{\gamma\gamma} \approx 125$  GeV. Keeping in mind the importance of the  $m_{\gamma\gamma}$  resolution this constitutes a substantial improvement of the analysis. The multivariate discriminators had been retrained and adjusted to maximize the expected sensitivity of the analysis. In addition the number of event categories had been increased from 11 to 25 and the assessment of the uncertainty on the background modeling had been significantly improved.

Two crosscheck analyses had been made to validate the event classification and the signal extraction method and in both cases similar results with less sensitivity had been obtained. When split into the 7 (8) TeV dataset the values for  $\mu$  were found to be  $\hat{\mu}=2.22\pm0.59~(0.90\pm0.25)$ . As already observed by the time of the discovery the signal in the 7 TeV dataset was higher than expected from the SM, while in the 8 TeV dataset it turned out to be slightly below, which can both be attributed to statistical fluctuations. When checked across 24 out of the 25 independent event categories of the analysis of the 7 and 8 TeV dataset, the  $\chi^2$  probability of the obtained values of  $\hat{\mu}_{\rm cat}$  for each category was found to be 74 %. From the plot shown in Fig. 4.14, even though sitting on top of a huge pedestal of background events the discovery of the new particle in the  $H \to \gamma \gamma$  decay channel is indisputable.

### 4.3.2 The Signal in the $H \rightarrow ZZ$ Decay Channel

Also the analysis in the decay channel into two Z bosons,  $H \to ZZ$  [28], is straight forward. Several sub-decay channels of the ZZ system are accessible, of which the decay into four leptons (where the term lepton refers to an electron or muon throughout this section) is often referred to as *golden channel* for the following reasons: the event signature with four isolated leptons with high transverse momentum can be easily identified; the event rate of all known background processes in the SM is low and the leptons can be reconstructed with high accuracy. In addition the final state with the four leptons preserves all kinematic information of the decay in the reconstructed final state, which allows further detailed studies of the properties of the new particle.

As the  $H \to \gamma \gamma$  decay channel the  $H \to ZZ \to 4\ell$  decay channel is characterized by an excellent relative resolution of the four lepton invariant mass,  $m_{4\ell}$ ,

<sup>&</sup>lt;sup>1</sup>In one category the fit did not converge due to the limited number of events. This event category is thus not part of the compatibility test.

between 1–2 %, but unlike the  $H \to \gamma \gamma$  decay channel across most of the interesting range of  $m_{4\ell}$  it furthermore profits from a very good S/B ratio. Challenges in this decay channel arise from the low branching fraction of  $BR(H \to ZZ \to 4\ell) = 1.26 \times 10^{-4}$ , corresponding to a total of not more than  $\approx 50$  signal events before reconstruction and selection in the 8 TeV dataset. Consequently the highest priority in this decay channel must be assigned to the most efficient reconstruction and selection of these few events over a small background. Backgrounds constitute from diboson production, single Z boson production in association with jets, where parts from the jets might be misidentified as leptons originating from another Z boson and from top quark pair production where again, leptons and misidentified jets might accidentally be interpreted as originating from Z bosons.

Three sub-channels were considered: (i) the decay channel into  $4\mu$  (with the best resolution of  $m_{4\ell}$ ); (ii) the decay channel into  $2\mu 2e$  and; (iii) the decay channel into 4e. In the analysis electrons were required to have a transverse momentum of  $p_T(e) > 7 \,\text{GeV}$  and to be fully contained within the geometrical acceptance of the ECAL defined by  $|\eta(e)| < 2.5$ . The distinction of true electrons from jet fragments and detector noise, which might accidentally have been reconstructed as electrons, was performed with the help of a multivariate discriminant. Muons were required to have a transverse momentum of  $p_T(\mu) > 5 \,\text{GeV}$  and to be contained within the geometrical acceptance of the muon system, defined by  $|\eta(\mu)| < 2.4$ . Both electrons and muons were required to be isolated, again motivated by the fact that they should originate from a color neutral Z boson. The isolation requirement was based on the sum of the transverse momenta (energies) of all reconstructed charged (and neutral) particles in the vicinity of the lepton. Of the charged particles only those were considered, which originated from the hard interaction vertex, which in this analysis was chosen according to the standard selection as described in Sect. 4.1.2. The energy from neutral particles in the isolation requirement was corrected for contributions from pileup, which otherwise might degrade the efficiency of the selection. This correction was based on an estimate of the median of the energy originating from pileup, distributed across the detector (in the case of electrons) or from the sum of transverse momentum, of charged tracks that have been associated to vertices from pileup, which was then translated into an estimate for the neutral energy, using the expected ratio of neutral to charged particles in proton proton collisions. Finally, the sums of the energy were divided by the transverse momenta of the corresponding leptons. In order to suppress leptons from charged kaon and pion in-flight decays or muons from cosmic rays the impact parameter of the lepton candidates relative to the hard interaction vertex was required to be smaller than 4 times the uncertainty of this estimate. Selection efficiencies, energy scales and resolutions were monitored and residual corrections were derived with the help of  $Z \to \ell \ell$  events or low mass resonances like the  $J/\psi$  and the  $\Upsilon$  to reach out to the lowest lepton transverse momenta with the monitoring. To improve the resolution of the two and four lepton invariant mass, an algorithm was applied to identify photons that might have been radiated off from a selected lepton in a final state radiation, bremsstrahlung process. The efficiency of correctly identifying such photons had been estimated to be  $\approx$ 50 % for a purity of  $\approx$ 80 %. The recovery of radiated photon energies lead to an efficiency

gain of  $\approx 3\%$ , 2%, 1% in  $4\mu$ ,  $2\mu 2e$  and 4e events. It might be surprising that muons seem to be more affected by final state radiation of *bremsstrahlung* photons than electrons. This can be understood by two means: (i) indeed the transverse momentum of muons and their bending in the 3.8 T magnetic field of the *CMS* detector is not so small, such that *bremsstrahlung* also for muons occurs more often than one might naively expect; (ii) in the case of electrons the energy radiated off via *bremsstrahlung* is already re-captured by the electron reconstruction algorithm, for which this was an explicit design requirement.

The first step of selecting  $H \to ZZ \to 4\ell$  events was to require four well identified and isolated leptons originating from the same reconstructed vertex of the hard interaction. Candidates of Z bosons were then formed from same flavor opposite charge leptons. When forming the Z boson candidates final state radiation photons were taken into account if they brought the mass of the Z boson candidate closer to the nominal Z boson mass, up to a maximum value of  $m_{\ell\ell\gamma}=100\,\text{GeV}$ . This affected 9%, 4.6%, 1.5% of all  $H \to ZZ \to 4\mu$ ,  $H \to ZZ \to 2\mu 2e$  and  $H \to ZZ \to 4e$  events according to the simulation. Again the larger effect on events containing muons can be explained by the reconstruction algorithms.

For  $m_H < 2m_Z$  one Z boson has to be produced off-shell. Of all possible oppositecharge lepton pairs in the event, the one with the invariant mass closest to  $m_Z$  was declared as  $Z_1$ . The mass of this Z boson candidate was required to lie within  $40 < m_{Z_1} < 120 \,\text{GeV}$ . Then all remaining leptons were used to form a second Z boson candidate referred to as  $Z_2$ . The chosen  $Z_2$  candidate was required to satisfy an invariant dilepton mass requirement of  $12 < m_{Z_2} < 120 \,\text{GeV}$ . If more than one  $Z_2$  candidate satisfied all object criteria the one with the highest scalar sum of the lepton transverse momenta was chosen. Among the four selected leptons forming the two Z boson candidates the transverse momentum of at least one lepton was required to fulfill a transverse momentum requirement of  $p_T(\ell) > 20 \,\text{GeV}$  and the transverse momentum of another lepton was required to be  $p_T(\ell) > 10 \,\mathrm{GeV}$ , to guarantee that the selected leptons fulfilled the criteria of the online selection. Furthermore it was required that the invariant mass of any same flavor opposite charge pair of the selected leptons be  $m_{\ell^+\ell^-} > 4 \, \text{GeV}$  to prevent that the leptons might have originated from low mass resonances, heavy flavor quark decays, or jet fragments. Finally, the search range was restricted to  $m_{4\ell} > 100 \,\text{GeV}$ .

The geometrical acceptance, reconstruction and selection efficiency for SM Higgs boson events with this selection rapidly increases as a function of  $m_H$  up to the kinematic edge of  $m_H \approx 2m_Z$ , where it roughly flattens out. For  $m_H \approx 125\,\text{GeV}$  the over all acceptance, reconstruction and selection efficiency was found to be  $\approx 62\,\%$ , 43 %, 30 % for SM Higgs boson events in the  $4\mu$ ,  $2\mu 2e$  and 4e final state, where the acceptance has been estimated from the simulation of the  $gg \to H$  production mode with  $|\eta(\ell)| < 5$  and  $m_{\ell^+\ell^-} > 1\,\text{GeV}$  for each Z boson on the level of the simulated hard scattering process. The relative four lepton mass resolution at  $m_{4\ell} \approx 125\,\text{GeV}$  was estimated to be  $\approx 1\,\%$ ,  $1.5\,\%$ ,  $2\,\%$ , in the  $4\mu$ ,  $2\mu 2e$  and 4e final state. For electrons and muons it could individually be monitored using the resolution at  $m_Z$  from events containing single inclusive Z bosons. The invariant dilepton mass

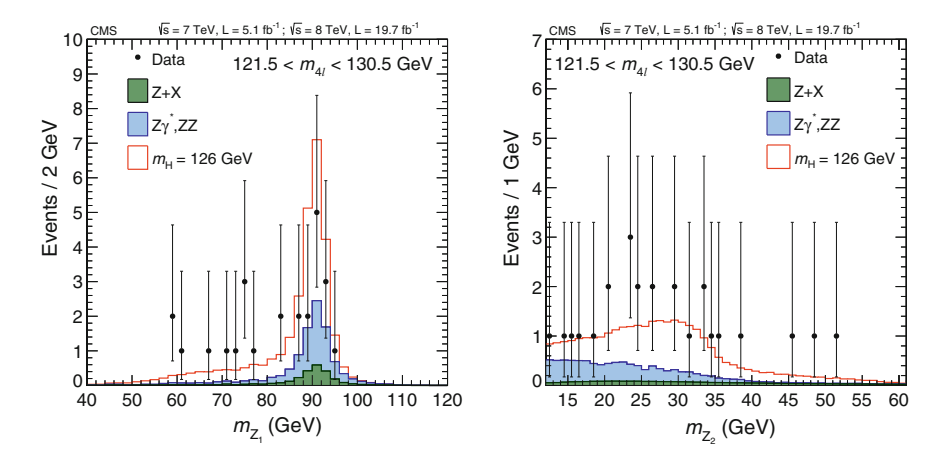


Fig. 4.15 Invariant dilepton mass of the two reconstructed Z boson candidates, (left) the one with the closest value of  $m_{\ell^+\ell^-}$  to  $m_Z$  ( $Z_1$ ) and (right) the one which is expected to be produced off-shell ( $Z_2$ ) [28]. For these figures four-lepton events have been selected in a range of 121.5  $< m_{4\ell} < 130.5 \,\text{GeV}$ 

of the two reconstructed Z boson candidates, for those events that have been selected in a window of  $121.5 < m_{4\ell} < 130.5$  GeV, is shown in Fig. 4.15.

To increase the sensitivity of the event selection also for this analysis a classification of the events was made according to their production mode. The events were classified into a dijet event category and a 0/1-jet event category, according to a linear discriminant,  $\mathcal{D}_{\rm jet}$ , combining the two most discriminating variables, the difference of the pseudorapidity,  $|\Delta\eta_{jj}|$ , and the invariant mass,  $m_{jj}$ , of the two leading jets corresponding to the outgoing jets in the  $qq \to H$  production mode. The discriminant was constructed to maximize the separation between the production modes of  $gg \to H$  and  $qq \to H$ . With the help of this discriminant the expected fraction of  $qq \to H$  events with respect to all signal events could be increased from 4% (in the 0/1-jet event category) to 30% (in the dijet event category). Nevertheless the signal events in each event category were still dominated by the  $gg \to H$  production mode (with 93% in the 0/1-jet event category and 53% in the dijet event category).

To set the scope of the enterprise to separate out the  $qq \to H$  production mode by this event categorization note that the number of expected signal events in this production mode is  $\approx 1.5$  before any event categorization on the combined 7 and 8 TeV dataset. Accordingly also in this decay channel the categorization corresponding to SM Higgs boson production modes can be viewed rather as a preparation step for the upcoming data taking period from 2015 on. The most obvious discriminating variable to separate between the SM Higgs boson signal and the non SM Higgs boson background is the four lepton invariant mass,  $m_{4\ell}$ , as shown in a mass range from 70 GeV to 1 TeV, for the full dataset of the 2011 and 2012 data taking period in Fig. 4.16. The black points with error bars correspond to the data, the filled blue histogram to the expected  $Z\gamma^*$  and ZZ background and the open histogram to the expectation for

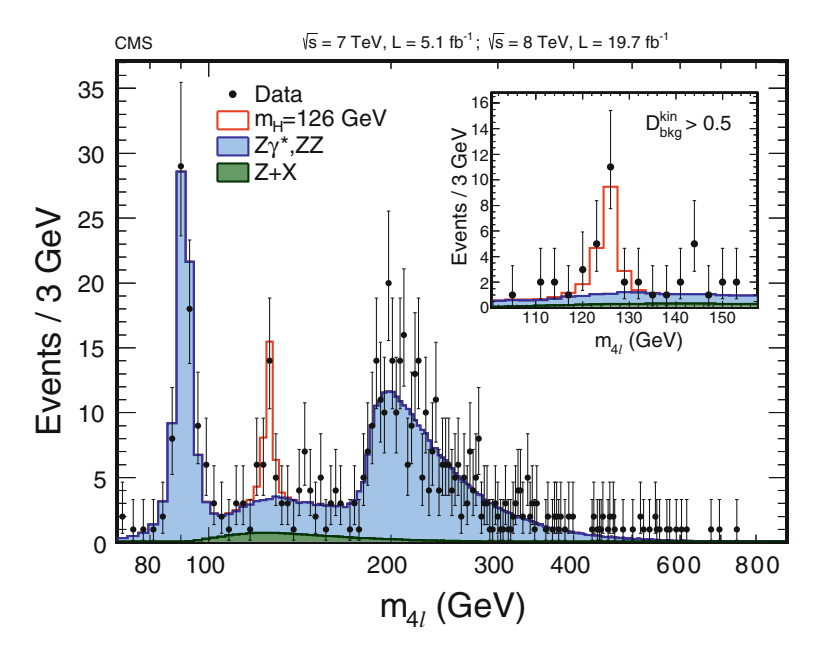


Fig. 4.16 Invariant four lepton mass,  $m_{4\ell}$ , in the range from 70 GeV up to 1 TeV [28]. The *black points* with error bars correspond to the data, the filled *blue* histogram corresponds to the expected  $Z\gamma^*$  and ZZ background and the open histogram to the expectation for a SM Higgs boson with  $m_H = 126$  GeV. In the inlet the distribution in the mass range from 100 to 160 GeV is shown for the subset of events with  $\mathcal{D}_{bkg}^{kin} > 0.5$  as explained in the text

a SM Higgs boson with  $m_H=126\,\mathrm{GeV}$ . The peaks at 90 and 180 GeV correspond to  $Z\gamma^*$  and ZZ production. In addition to  $m_{4\ell}$  the full angular information,  $\Omega$ , of the decay was exploited consisting of five angles, as illustrated in Fig. 4.17: (i) the angle  $\theta^*$  of the  $H\to ZZ$  decay in the restframe of the Higgs boson candidate; (ii) the two decay angles  $\theta_{1,2}$  of the leptons in the corresponding Z boson restframes; (iii) the azimuthal angle  $\phi$ , between the decay planes of the two Z bosons; and the azimuthal angle  $\phi_1$  between the flight direction of one Z boson (conventionally chosen to be  $Z_1$ ) and the  $H\to ZZ$  decay plane. Probability density functions for a given set of leptons to lead to a corresponding configuration of azimuthal and decay angles were derived from the integral kernels of the leading-order matrix element calculations for  $gg\to H$  production and for the main backgrounds of non resonant  $qq\to ZZ$  and  $gg\to ZZ$  production, including interference effects between the final state leptons. These probability density functions were then combined into a discriminant of the form:

$$\mathcal{D}_{\text{bkg}}^{\text{kin}} = \frac{\mathcal{P}_{0^{+}}^{\text{kin}}}{\mathcal{P}_{0^{+}}^{\text{kin}} + \mathcal{P}_{\text{bkg}}^{\text{kin}}} = \left[1 + \frac{\mathcal{P}_{\text{bkg}}^{\text{kin}}(m_{Z_{1}}, m_{Z_{2}}, \vec{\Omega}|m_{4\ell})}{\mathcal{P}_{0^{+}}^{\text{kin}}(m_{Z_{1}}, m_{Z_{2}}, \vec{\Omega}|m_{4\ell})}\right]^{-1}$$
(4.3)

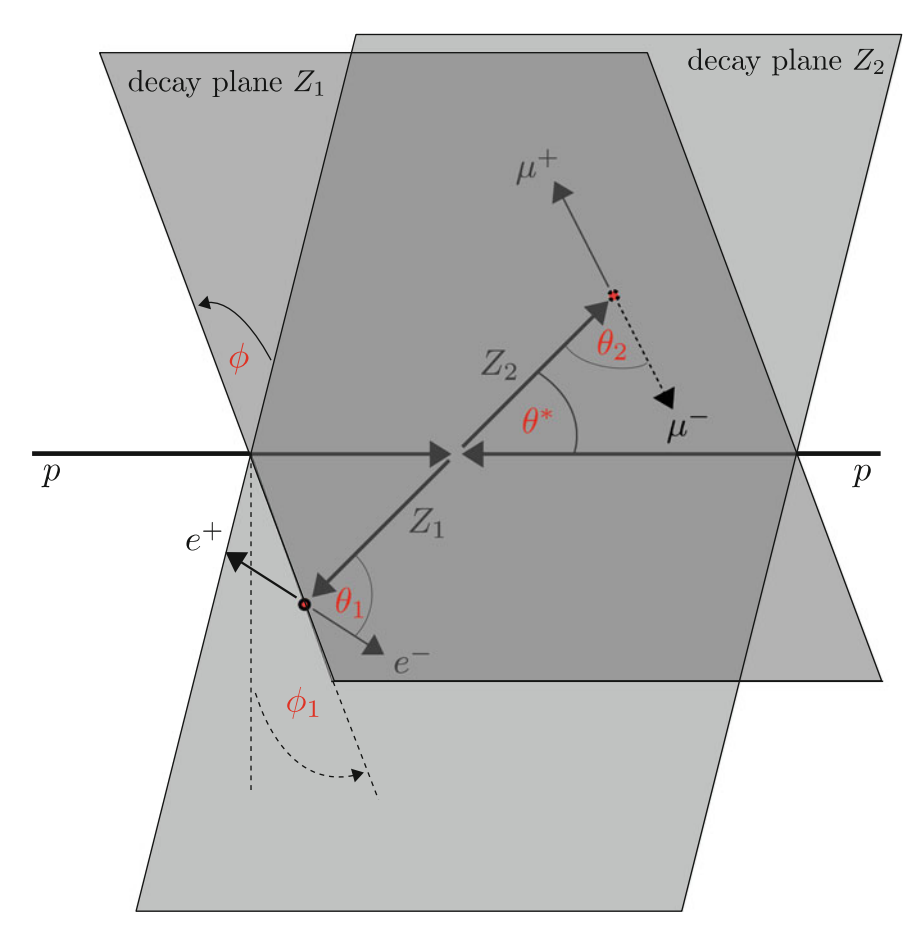


Fig. 4.17 Angles in the  $H \to ZZ \to 4\ell$  decay system as defined in the text

where  $\mathcal{P}_{0^+}^{\mathrm{kin}}$  corresponds to the probability for the leptons to end up in the given angular configuration in the case of signal and  $\mathcal{P}_{\mathrm{bkg}}^{\mathrm{kin}}$  corresponds to the same probability in the case of ZZ background. In Eq. (4.3) the index  $0^+$  indicates the spin 0 and CP even character of the SM Higgs boson signal, which is encoded in the angular distributions.

Defined in this way the variable  $\mathcal{D}_{\rm bkg}^{\rm kin}$  carries no discriminating power based on  $m_{4\ell}$  between the signal and background contributions, which motivates its use as a second discriminating variable. In the inlet of Fig. 4.16 the distribution in the mass range from 100 to 160 GeV is shown for the subset of events with  $\mathcal{D}_{\rm bkg}^{\rm kin} > 0.5$ . With this restriction both prominent peaks of the  $Z\gamma^*$  and ZZ background can be effectively suppressed, while the signal at  $m_{4\ell}=126$  GeV remains. Finally, in the 0/1-jet event category the transverse momentum of the four lepton system,  $p_T^{4\ell}$  and

in the dijet event category the linear discriminant  $\mathcal{D}_{jet}$  were chosen to define the following three dimensional likelihood functions

$$\mathcal{L}_{3D}^{\mu} \equiv \begin{cases} \mathcal{P}(m_{4\ell}|m_H, \Gamma_H) \cdot \mathcal{P}(\mathcal{D}_{\text{bkg}}^{\text{kin}}|m_{4\ell}) \cdot \mathcal{P}(p_T^{4\ell}|m_{4\ell}) & (0/1\text{-jet}) \\ \\ \mathcal{P}(m_{4\ell}|m_H, \Gamma_H) \cdot \mathcal{P}(\mathcal{D}_{\text{bkg}}^{\text{kin}}|m_{4\ell}) \cdot \mathcal{P}(\mathcal{D}_{\text{jet}}|m_{4\ell}) & (\text{dijet}) \end{cases}$$
(4.4)

as input for an unbinned maximum likelihood fit, for the five signal components  $(gg \to H, qq \to H, ZH, WH, t\bar{t}H)$  and three background processes  $(qq \to ZZ, gg \to ZZ)$  and (z + X), where (z + Z) denotes the corresponding probability density function and the upper part of Eq. (4.4) was used for the 0/1-jet event category, while the lower part of Eq. (4.4) was used in the dijet event category. In this likelihood function the first factor in the triple product is derived from the (z + Z) spectrum, the second factor from the expected angular distributions of the leptons and the third factor from the transverse momentum spectrum or the likeliness of being a vector boson fusion event.

Based on these likelihood functions and on the test statistic as defined in Eq. (4.2) a signal could be established with an observed (expected) significance of  $6.8\sigma$  ( $6.7\sigma$ ) for  $\hat{m}_H=125.7\,\mathrm{GeV}$ . The observed significance corresponds to a value of  $\hat{\mu}=0.93\pm0.25\,\mathrm{(stat.)}\pm0.11\,\mathrm{(syst.)}$ , where the pure statistical uncertainty has been obtained from the maximum likelihood fit neglecting all systematic uncertainties. The value of  $\mu$  has been found to be well compatible when split into the 7 and 8 TeV dataset. Also here from the peak of  $m_{4\ell}$  in Fig. 4.16 the discovery of the new particle is without any doubt. Evaluated at  $m_H=125.0\,\mathrm{GeV}$  the observed (expected) significance changes to  $6.5\sigma$  ( $6.3\sigma$ ), corresponding to a value of  $\hat{\mu}|_{125\,\mathrm{GeV}}=1.00\pm0.29$ , where the change in  $\mu$  and in the expected significance is mostly due to the steep rise of the branching fraction as a function of  $m_H$ , at the point where this decay channel opens up energetically. The change in the observed significance is due to the fact, that  $m_H=125.0\,\mathrm{GeV}$  does not correspond to the most probable value of  $m_H$  for this decay channel.

Compared to the analysis as published by the time of the discovery apart from the increased number of events, the split into event categories had been introduced and the signal extraction via the likelihood function as defined in Eq. (4.4) had been extended by the third term, which also distinguishes between the event categories. The gain in sensitivity due to this change was between 10–15 %.

# 4.3.3 Evidence of the Signal in the $H \rightarrow WW$ Decay Channel

With a value of  $BR(H \to WW \to 2\ell 2\nu) = 0.0106$  in the final state with two leptons (where lepton again refers to an electron or muon in this section) the decay channel into two W bosons,  $H \to WW$ , has the largest branching fraction of the bosonic decay channels, leading to an expectation of  $\approx 5000$  SM Higgs boson events

before reconstruction and selection in the 8 TeV dataset. The signature consists of two isolated leptons, which can be of same or different flavor and missing transverse energy due to the escape of the neutrinos, which are part of the decay, from detection. The escape of the neutrinos also marks one of the challenges of this decay channel, since it will not allow the full reconstruction of  $m_H$ . This will lead to a rather broad than peaked excess over a given background distribution. In the analysis the resolution of  $m_H$  was found to be  $\mathcal{O}(20\,\%)$  [29], which is roughly ten times worse than in the two high resolution channels that have been discussed before.

To increase the sensitivity of the analysis also here the events had been split in event categories to distinguish events with leptons of same flavor (ee and  $\mu\mu$ ) from events with leptons of different flavor  $(e\mu)$  on the one hand, and to distinguish events with zero or one jet on the other hand. This categorization has been implied to address different background processes individually, which gain dominance in one or the other event category. The most important background processes arise from: nonresonant WW production (which is very weakly constrained both experimentally and theoretically); single Z boson production (especially in the same flavor event categories); and  $t\bar{t}$  production (especially in the 1-jet event categories). In the final publication independent analyses had also been performed in two additional dijet event categories, addressing the  $qq \rightarrow H$  and WH production mode. For the latter the W boson was assumed to decay hadronically, leading to the two additional jets in the event. Furthermore two additional three lepton event categories had been introduced, to address the WH production mode with three leptonically decaying W bosons in the final state and the ZH production mode where the Z boson and one of the W bosons in the final state decay leptonically, while the second W boson decays hadronically. But these analyses were of no relevance for the discovery on the available dataset and are more of importance in view of the future layout of  $H \rightarrow WW$  analyses from 2015 on.

For the main analysis electrons and muons were reconstructed and identified as described in Sect. 4.1.2. Also for this analysis both leptons were required to be isolated and the effect of pileup was taken into account not to compromise the efficiency of this selection requirement. Events were selected if they contained exactly two isolated leptons with (sub-)leading  $p_T^{\ell} > 20(10)$  GeV. The escape of the neutrinos can be indirectly observed, when assuming energy and momentum conservation, from the momentum of all visible particles in the detector, which should balance the vectorial sum of the momentum of all undetected particles. This is not possible in beam direction, since the residual longitudinal momentum of the partons in the hard scattering process is not known. But it is possible in the transverse plane of the scattering process, which should not show any residual momentum as discussed in Sect. 4.1.1. Correspondingly the negative vectorial sum of the transverse momentum of all reconstructed particles in the detector is defined as missing transverse momentum (or missing transverse energy),  $E_T^{\text{miss}}$ . It is one of the most difficult quantities to control experimentally for several reasons: (i) it only allows statements about the vectorial sum of all particles that have escaped detection, e.g. the transverse momentum of each of the two neutrinos in the  $H \to WW \to 2\nu 2\ell$  decay individually can not be resolved; (ii) it requires the efficient reconstruction of all objects of the hard scattering process and the complete coverage of the whole solid angle, e.g. all particles that escape detection through the beam pipe in forward or backward direction of the scattering process will deteriorate the measurement; (iii) it requires the most accurate energy (or momentum) measurements of each reconstructed object, any mis-measurement will be picked up as missing energy (or momentum) in the vectorial sum; (iv) the resolution of  $E_T^{
m miss}$  will suffer from the presence of additional pileup. The typical resolution of  $E_T^{
m miss}$  determined from all reconstructed particles in the CMS detector varies between 7, 12 and 15 GeV for pileup corresponding to 0, 9, 21 additional interactions. To assure the presence of enough missing transverse energy in the event the  $E_T^{\rm miss}$  reconstructed from all particle flow candidates in the event was required to be above 20 GeV. To suppress background from  $Z \to \tau \tau$ events, where the missing transverse energy due to neutrinos from leptonic  $\tau$ -decays are expected to be more aligned with the direction of the leptons, the projection of  $E_T^{\text{miss}}$  perpendicular to the direction of the leading lepton was used instead of the plain value of  $E_T^{\text{miss}}$ , when it was found to point into the direction of the leading lepton within a cone of size  $\pi/2$ . To cope with the problem of mis-measured energies in the detector an alternative version of  $E_T^{\rm miss}$  was calculated, based only on tracks instead of all reconstructed particle flow candidates in the detector, with the reasoning that for low energies the transverse momentum measurement from tracks is more accurate than the energy measured in the calorimeters. In the selection the requirement of  $E_T^{\text{miss}} > 20 \,\text{GeV}$  was applied to the version of  $E_T^{\text{miss}}$ , that yielded the smaller value. Further on, the invariant mass of the dilepton system was required to be  $m_{\ell\ell} > 12 \,\text{GeV}$ , the transverse momentum of the dilepton system to be  $p_T^{\ell\ell} > 30 \,\text{GeV}$ and the transverse mass, which was defined as

$$m_T = \sqrt{2p_T^{\ell\ell} E_T^{\text{miss}} \left(1 - \cos\phi(\ell\ell, \vec{E}_T^{\text{miss}})\right)}$$

to be  $m_T > 30\,\mathrm{GeV}$ , where  $\phi(\ell\ell,\vec{E}_T^{\mathrm{miss}})$  refers to the angle between the direction of the dilepton system in the transverse plane and the missing transverse energy. To cope with the large background due to single Z boson production in the same flavor event categories, these requirements were tightened up to  $m_{\ell\ell} > 20\,\mathrm{GeV}$  and  $p_T^\ell > 15\,\mathrm{GeV}$  for the sub-leading lepton. In addition, events where the angle between the direction of the dilepton system and the direction of the leading jet with  $p_T > 15\,\mathrm{GeV}$  in the transverse plane was larger than  $165^\circ$  and events with an invariant dilepton mass,  $m_{\ell\ell}$ , within a window of  $\pm 15\,\mathrm{GeV}$  around the nominal mass of the Z boson were rejected, an additional multivariate discriminator was used to suppress off-shell Z boson production, and the  $E_T^{\mathrm{miss}}$  cut was increased with increasing number of reconstructed vertices in the event. Events with top quark pairs were suppressed exploiting the probability of jets to originate from a b-quark.

In the leptonic decay channel the W bosons in the final state reveal sensitivity to the spin of their parent particle, which can be used to distinguish SM Higgs boson events from the dominant residual background of non-resonant WW production. This fact is illustrated in Fig. 4.18: in the restframe of the SM Higgs boson the two

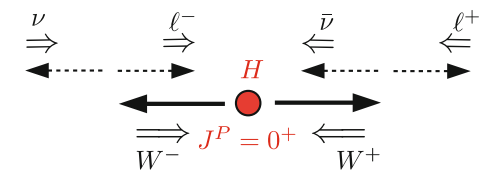


**Fig. 4.18** Spin structure for the decay of the SM Higgs boson into two W bosons. To comply with the spin 0 in the initial state the spins of the two W bosons have to add up to spin 0 as well. In the subsequent decays of the W bosons the half-integer spins of the leptons also have to add up to the spin of their parent particles. The (anti-) neutrino is purely (right-) left-handed and thus defines the direction of flight for the corresponding charged lepton

W bosons decay back to back. Since the SM Higgs boson is a spin 0 particle the spins of the two W bosons have to add up to 0 as well. Also in the restframe of the subsequent decays of the W bosons the resulting lepton  $(\ell^-/\ell^+)$  and neutrino  $(\nu/\bar{\nu})$  emerge with a back to back topology and their spins have to add up to the spin of the corresponding W boson. Since the neutrinos are massless (which holds to very good approximation for all considerations throughout this document) and since  $W^{(+)-}$  bosons only couple to (right-)left-handed (anti-)neutrinos, the latter will fly (in) against the direction of the W bosons spin. In the decay chain of an original spin 0 particle the spins of the W bosons will point in opposite directions and the two leptons (and neutrinos) will fly in the same direction in the restframe of the mother particle. This can be observed via a smaller opening angle,  $\phi_{\ell\ell}$ , between the two leptons, a smaller invariant dilepton mass,  $m_{\ell\ell}$ , and a smaller transverse mass,  $m_T$ , than for non-resonant WW production, which is produced without any characteristic spin polarization.

The invariant mass of the dilepton system,  $m_{\ell\ell}$ , and the transverse mass,  $m_T$ , in the different flavor  $(e\mu)$  event categories are shown in Fig. 4.19. To obtain these figures the 0-jet and the 1-jet event category have been combined with a weight according to the expected S/(S+B) ratio. The black points with error bars correspond to the data and the stacked filled histograms to the expected number of events from the known non-SM Higgs boson processes. The light blue histogram at the bottom corresponds to the most important background from non-resonant WW production, which is expected to dominate the event sample after the selection described above. The shapes and normalizations of all background processes had been carefully crosschecked with data in several dedicated sideband regions and good agreement had been found. Residual uncertainties, e.g. due to a limited number of events in the control regions had been taken into account in form of nuisance parameters in the maximum likelihood fit prior to the statistical inference. The normalization of the background from non-resonant WW production, which is weakly constrained from experimental measurements had been left as a free parameter to have it constrained in the fit. The open histogram stacked on top of the expected number of events from non-SM Higgs boson processes corresponds to the expectation for a SM Higgs boson with  $m_H = 125 \, \text{GeV}$ , in accordance with the findings in the  $H \to ZZ$ and the  $H \to \gamma \gamma$  decay channels. The excess of the data over the expectation from

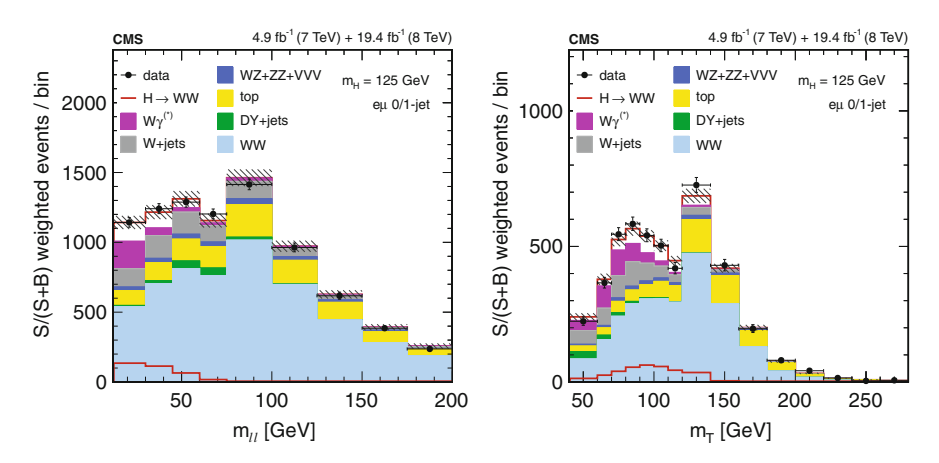


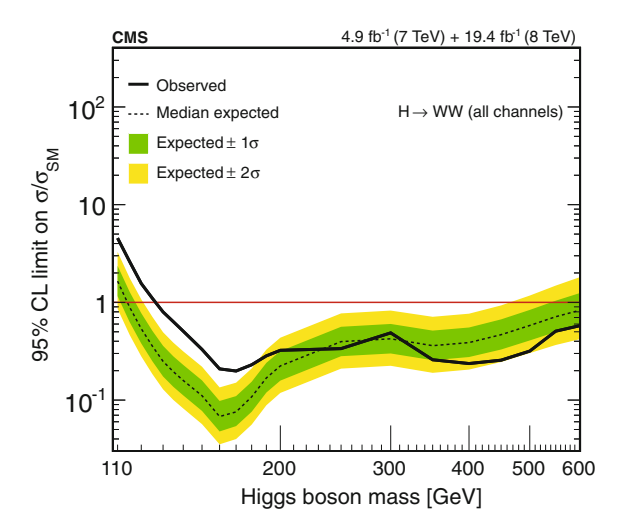
Fig. 4.19 (*Left*) Invariant dilepton mass,  $m_{\ell\ell}$ , and (*right*) transverse mass,  $m_T$ , in the  $H \to WW$  decay channel, in the different flavor ( $e\mu$ ) event categories, after the event selection as described in the text [29]. For these figures the 0- and the 1-jet event category have been combined weighted by their expected S/(S+B) ratio

the non-SM Higgs boson events is clearly visible and can be well explained by the shape and event yield predicted for a SM Higgs boson with  $m_H = 125 \,\text{GeV}$ .

Ignoring the shape information and concentrating on the analyses for  $m_H$  = 125 GeV, 506 events are observed after the final selection in the  $e\mu$  0-jet event category for  $429\pm34$  expected non-SM Higgs boson events and  $88\pm19$  (2.19 $\pm0.22$ ) expected SM Higgs boson events in the  $gg \to H (qq \to H + VH)$  production mode, in the 8 TeV dataset. In the  $e\mu$  1-jet event category 228 events are observed for 209  $\pm$  14 expected non-SM Higgs boson events and 37  $\pm$  12 (6.53  $\pm$  0.53) expected Higgs boson events in the  $gg \rightarrow H (qq \rightarrow H + VH)$  production mode, in the 8TeV dataset. This corresponds to a S/B ratio of  $\approx 1/5$  in both event categories and a fraction of  $\approx 2.5\%$  (15%) of SM Higgs boson events from the  $qq \rightarrow H$  and VHproduction mode with respect to the number of all expected SM Higgs boson events in the 0-(1-)jet event category. These event numbers demonstrate the power of the analysis to infer the presence of a SM Higgs boson already, from a pure counting experiment, after the final selection. This has indeed been used by the time of the discovery and as an additional crosscheck in the final publication, while the final inference has been performed taking the shape information as shown in Fig. 4.19, for all four event categories into account in a binned maximum likelihood fit. This has been done based on the two most discriminating shapes,  $m_{\ell\ell}$  and  $m_T$ , which have been combined into two-dimensional templates with 9 bins in  $m_{\ell\ell}$  and 14 bins in  $m_T$ for all signal contributions and all backgrounds as indicated in Fig. 4.19.

Due to its superior exclusion power across a large mass range, the 95 % CL limit on the production cross section times branching fraction,  $BR(H \to WW)$  of the SM Higgs boson in the range from 110 to 600 GeV had been chosen as the main result of this analysis, as shown in Fig. 4.20. In the figure the solid black line indicates the

Fig. 4.20 95% CL upper limits on the production cross section times branching fraction  $BR(H \to WW)$  of the SM Higgs boson in the mass range from 110 to 600 GeV as determined from the binned maximum likelihood fit in the  $H \to WW$  decay channel on the combined dataset [29]



observed exclusion limit while the dashed black line with the dark green and bright yellow band indicates the median and the 68 and 95% quantiles of the expected exclusion limits for the b-hypothesis. For these results also the production mode specific analyses have been used that have not been discussed in this section, since they have only the effect of a few per cent on the result. As can be seen from the figure the analysis did reach the sensitivity to exclude the SM Higgs boson at 95 % CL for  $m_H \gtrsim 115 \,\mathrm{GeV}$ , while it only excludes SM Higgs boson masses up to 130 GeV. Instead a broad excess is observed, which in a mass range from 110 to 180 GeV exceeds the  $2\sigma$  uncertainty band of the expectation for the b-hypothesis. This excess is compatible with the expectation in the presence of a SM Higgs boson with  $m_H =$ 125 GeV, where the broadness is caused by the poor mass resolution in this decay channel. The observed (expected) significance of this excess can be quantified to be 4.3 $\sigma$  (5.8 $\sigma$ ), corresponding to a most probable value of  $\hat{\mu} = 0.72 \pm 0.19$ , for  $m_H = 125.7 \,\text{GeV}$ . For the publication this mass value had been chosen, since it corresponds to the most probable value of  $m_H$  in the  $H \rightarrow ZZ$  decay channel that had already been published by that time. Evaluated at  $m_H = 125.0 \,\mathrm{GeV}$  the observed (expected) significance changes to  $4.7\sigma$  (5.4 $\sigma$ ), corresponding to a value of  $\hat{\mu}|_{125\,\mathrm{GeV}} = 0.83 \pm 0.21$ , where the change in  $\mu$  and in the expected significance is mostly due to the steep rise of the branching fraction as a function of  $m_H$ , at the point where this decay channel opens up energetically, as in the case of the  $H \to ZZ$  decay channel. Compared to the publication by the time of the discovery, the analysis has been extended by the sub-decay mode specific event classes and the main analysis has been extended from a counting experiment to the shape based signal extraction as described above. This change has improved the sensitivity of the search by  $\mathcal{O}(20\%)$ .

2012, and based on the final dataset corresponding to 25 fb						
		$10{\rm fb^{-1}}$	$25{\rm fb}^{-1}$			
		Significance $(\sigma)$	Significance $(\sigma)$	$\hat{\mu}$		
ATLAS	$H \to \gamma \gamma$	4.5 (2.5) [24]	5.2 (4.6) [35]	$1.17 \pm 0.27$		
	$H \rightarrow ZZ$	3.6 (2.7) [24]	8.1 (6.2) [36]	$1.44 \pm 0.37$		
	$H \rightarrow WW$	2.8 (2.3) [24]	6.1 (5.8) [37]	$1.09 \pm 0.21$		
CMS	$H \rightarrow \gamma \gamma$	4.1 (2.8) [25]	5.7 (5.2) [27]	$1.14 \pm 0.25$		
	$H \rightarrow ZZ$	3.2 (3.8) [25]	6.8 (6.7) [28]	$0.93 \pm 0.27$		
	$H \rightarrow WW$	1.6 (2.5) [25]	4.3 (5.8) [29]	$0.72 \pm 0.19$		

**Table 4.2** Significance and most probable value of the observed signal strength parameter  $\hat{\mu}$ , for the decay channels into bosons, as published by the *ATLAS* and *CMS* collaboration, based on the dataset of  $10\,\mathrm{fb^{-1}}$ , that had been collected by the time of the discovery announcement at 4 July 2012, and based on the final dataset corresponding to  $25\,\mathrm{fb^{-1}}$ 

The values in braces correspond to the expected significance, indicating the sensitivity of the corresponding analyses to establish the signal. On the final dataset the values from the *CMS* collaboration have been given for the best fit value of  $m_H$  in the  $H \to \gamma \gamma$  and  $H \to ZZ$  decay channel. The results from the *ATLAS* collaboration have been given at a fixed value of  $m_H = 125.4\,\mathrm{GeV}$ 

#### 4.3.4 Conclusions on the Bosonic Decay Channels

The observed significances, in each of the three bosonic decay channels, which have been discussed in the previous sections are summarized in Table 4.2. The significances given for  $10\,\mathrm{fb}^{-1}$  correspond to the published values, based on the dataset that had been collected by the time of the discovery announcement, on 4 July 2012. The significances and values of  $\hat{\mu}$  given for  $25\,\mathrm{fb}^{-1}$  correspond to the final analyses on the full dataset of the *LHC* run-1 data taking period. The results of the *ATLAS* collaboration are given in the upper part of the table, the results of the *CMS* collaboration in the lower part. Also given in braces is the expected significance, as a measure of the sensitivity of each analysis to establish the signal.

As discussed in the previous sections the sensitivity depends on the exact value of  $m_H$ , an effect which is stronger for the  $H \to ZZ$  and the  $H \to WW$  decay channel, for which the rise of the branching fraction as a function of  $m_H$  is relatively steep. The numbers given in the table correspond to the values of  $m_H$ , as used for the original publications by collaborations. For the ATLAS collaboration these values are  $m_H = 126.0 \,\mathrm{GeV}$  for the significances in all decay channels as published by the time of the discovery and  $m_H = 125.4 \,\mathrm{GeV}$  for significances and values of  $\hat{\mu}$ for all decay channels on the final dataset. For the CMS collaboration the values are  $m_H = 125.5 \,\mathrm{GeV}$  for the significances in all decay channels as published by the time of the discovery,  $m_H = 124.7 \,\text{GeV}$  on the final dataset in the  $H \to \gamma \gamma$  decay channel and  $m_H = 125.7 \,\text{GeV}$  on the final dataset in the  $H \to ZZ$  and  $H \to WW$ decay channel, as discussed in the previous sections. In all analyses the sensitivity to make a discovery of the SM Higgs boson with a mass of  $\approx$ 125 GeV with a statistical significance of more than  $5\sigma$  has been reached with the exception of the  $H \to \gamma\gamma$ analysis of the ATLAS collaboration. The signal has been established in all, but the analysis in the  $H \to WW$  decay channel of the CMS collaboration, in which still a

strong evidence is observed. For the analyses that have been performed by the *CMS* collaboration the appearance of the signal can be seen from Figs. 4.14, 4.16 and 4.19.

The expected value for the signal strength parameter  $\mu$  in the SM is one. The values as found in each decay channel are well compatible with each other and with the expectation of the SM. The compatibility of the *ATLAS* results with the SM expectation is  $\chi^2_{\rm ATLAS}/ndf = 1.96/3$ , corresponding to a  $\chi^2$  probability of 42%, for the *CMS* results it is  $\chi^2_{\rm CMS}/ndf = 0.91/3$ , corresponding to a  $\chi^2$  probability of 58%, for the values of  $\hat{\mu}$  evaluated at the same value of  $m_H = 125.0\,{\rm GeV}$ . The results of both experiments combined have a compatibility with the SM expectation of  $\chi^2_{\rm LHC}/ndf = 2.86/6$ , corresponding to a  $\chi^2$  probability of 49%.

Treating all channels as independent measurements and ignoring correlations between systematic uncertainties across decay channels or experiments a value for  $\hat{\mu}$  for each individual and a combination of both experiments can be obtained from the weighted mean of the individual measurements. For the results from the ALTAS experiment the weighted mean reveals a value of  $\langle \hat{\mu} \rangle_{ATLAS} = 1.17 \pm 0.15$ . For the results from the CMS experiment a value of  $\langle \hat{\mu} \rangle_{\text{CMS}} = 0.97 \pm 0.14$  is obtained. For both experiments combined the value is  $\langle \hat{\mu} \rangle_{LHC} = 1.06 \pm 0.10$ . Correlated across all decay channels for a single experiment is e.g. the uncertainty on the luminosity (typically  $\mathcal{O}(2-3\%)$ ). Correlated across the experiments are the uncertainties related to the Higgs boson production cross section (typically  $\mathcal{O}(3-10\%)$ ), as discussed in Sect. 4.2. Since these correlations have been ignored the weighted mean should only be viewed as an approximation for a combined most probable value,  $\hat{\mu}$ , which would have to take correlations and non-Gaussian tails in the probability distributions into account. Such a combined analysis for the CMS results will be discussed in Chap. 5, which allows a comparison of this approximation with the result of the properly combined analyses.

It is assuring that in the  $H \to \gamma \gamma$  and  $H \to ZZ$  high resolution channels, in which the mass of the new boson can be determined precisely, the signal is observed at the same value of  $m_H \approx 125\,\text{GeV}$ , which is true for both experiments. In the  $H \to WW$  decay channel where the mass resolution is worse the observed excess is well compatible with the presence of the SM Higgs boson with  $m_H = 125\,\text{GeV}$ , while the presence of a SM Higgs boson with  $m_H \gtrsim 130\,\text{GeV}$  can be excluded at 95% CL, as has been shown for the measurement of the CMS collaboration. An exact mass measurement from the two high resolution channels based on the CMS results will be discussed in Chap. 5.

These findings confirm the discovery that had been announced in 2012 and impresses in many aspects: (i) the short timespan that has elapsed between the discovery, the first preliminary results based on the full dataset and the final publications; (ii) the consistency between the preliminary results and the results of the final publications, which demonstrate how well the data had already been under control by the time of data taking; (iii) the consistency of the findings with the expectation for a single Higgs boson, with a yield as predicted by the SM, which points out the quality of the theory. The latter point will be discussed further in Chap. 5. The results are found to be consistent across all decay channels and to be consistent between the two experiments. They conclude the hunt for the elusive SM Higgs boson based on

the available dataset of the years 2011 and 2012, in the three main bosonic decay channels, with the confirmation of the discovery. In the golden  $H \to ZZ \to 4\ell$  decay channel this discovery has been made only with a hand full of events,  $\mathcal{O}(20)$ , which points to the fact that only the upcoming data taking periods of the *LHC* will really open an era of high precision measurements in the Higgs boson sector. From the discovery in the bosonic decay channels the bosonic nature of the new particle is evident. A more detailed analysis of its properties will be discussed in Chap. 5. Up to this point one question still remained unanswered, which is the coupling of the new particle to fermions.

# **4.4** Signs of the New Particle in the Fermionic Decay Channels

As discussed in Chap. 2, in the SM the problem of massive fermions is independent from the more fundamental problem of massive gauge bosons. It only occurs due to the chiral coupling of the W boson to the weak isospin: in Chap. 2 this becomes evident from the distinction between left- and right-handed fermions, in isospin doublets and singlets, which then leads to a mixture of fields belonging to singlet and doublet components, when introducing mass terms, as demonstrated in Eq. (2.30). This explicitly breaks the gauge symmetry unless compensated by an adequate counter part in the theory. In the minimal SM as discussed in Chap. 2, such counterparts can be obtained by introducing a Yukawa coupling of all massive fermions that take part in the weak interaction to the isospin doublet field,  $\phi$ , which naturally results in the introduction of mass terms together with compensating coupling terms of the fermions to the physical Higgs field, H. Since an equivalent mechanism with a similar result could be thought of, the question of the coupling of the new boson to fermions sustains its impact even if the coupling to bosons came out as expected in the SM. A common example of an equivalent ansatz to obtain mass terms for fermions is the extension of the Higgs sector by a second Higgs doublet field  $\phi$ , which governs the mass generation for up-type fermions independently from the mass generation for down-type fermions. Such an extension is e.g. a necessary ingredient for each supersymmetric extension of the SM, as discussed in Sect. 1.1.

For  $m_H \lesssim 160\,\text{GeV}$  there are two obvious choices to search for the SM Higgs boson at the *LHC* in decay channels into fermions, exploiting the coupling to b-quarks or the coupling to  $\tau$ -leptons as can be seen from Fig. 4.5.<sup>2</sup> The prerequisite of  $m_H \lesssim 160\,\text{GeV}$  prevents that the Higgs boson will predominantly decay into vector bosons and *top* quarks. At these masses the decay channel into b-quarks is dominant over all other decay channels, since the b-quark is the heaviest particle for which the decay is energetically allowed. It therefore naively might appear as the most promising search channel. In reality both fermionic decay channels are challenging,

<sup>&</sup>lt;sup>2</sup>The figure also shows that in a mass range of  $160 \lesssim m_H \lesssim 350 \,\text{GeV}$  a measurement of a coupling of the SM Higgs boson to fermions would have been without hope.

mostly due to the low mass of their decay products, which makes them difficult to distinguish from background processes, which are not as highly suppressed as in the  $H \to WW$  and  $H \to ZZ$  analyses. Moreover the reconstruction is too difficult to reach a resolution in  $m_H$  that could compete with the resolution in the  $H \to \gamma\gamma$  or  $H \to ZZ$  decay channel. Due to this circumstance by the time of the discovery the question of the coupling of the new particle to fermions was still unanswered, as can be seen from Fig. 4.11. Indeed it can be viewed as a second breakthrough that this question could be addressed, only one year after the discovery, in 2013.

#### 4.4.1 The Coupling to Leptons

#### $\tau$ -Leptons

The most promising channel to establish the coupling of the Higgs boson to fermions turned out to be the  $H\to \tau\tau$  decay channel. As the heavy brother of the electron and the muon the  $\tau$ -lepton is the heaviest known lepton with a mass of 1.77682(16) GeV [38]. It decays via the weak interaction with a lifetime corresponding to a decay length of  $c\tau=87.11\,\mu\text{m}$ . Since its mass exceeds the mass of light mesons, unlike its lighter lepton companions, it has the special feature that it can decay into hadrons. This motivates the separation of the di- $\tau$  final state into six exclusive decay channels ee,  $\mu\mu$ ,  $e\mu$ ,  $e\tau_h$ ,  $\mu\tau_h$  and  $\tau_h\tau_h$  corresponding to the reconstructed final state particles, where  $\tau_h$  refers to a hadronic decay of the  $\tau$ -lepton. The branching fractions of the  $\tau$ -lepton decays, which are most relevant for the analysis are listed in Table 4.3.

In CMS hadronically decaying  $\tau$ -leptons are reconstructed from isolated jets either as three-prong decays or as one-prong decays with one or two additional  $\pi^0$  candidates, <sup>3</sup> corresponding to the  $\tau$ -decay modes via a  $\rho$  or an  $a_1$  resonance [39]. The term "prong" here refers to a charged particle, which could be a pion or a kaon. The weak decay of the  $\tau_h$  is accompanied by one  $\nu_{\tau}$ , whose energy cannot be detected. The invariant mass of the visible decay products of the reconstructed  $\tau_h$ -leptons,  $m_{\rm vis}^{\tau_h}$ , in the  $\mu\tau_h$  decay channel in the analysis is shown in Fig. 4.21 (left) [30]. The black points with the error bars correspond to the data and the stacked histograms in different colors to the contributions of various SM background processes. Electroweak processes,  $t\bar{t}$  events or QCD multijet events might contain genuine  $\tau_h$ -leptons, electrons, muons or jets that have been misidentified as  $\tau_h$ . The dominating contribution from  $Z \to \tau \tau \to \mu \tau_h$  events has been further split in the fractions of simulated three-prong decays and one-prong decays with and without additional neutral pions. The sharp peak in the distribution at 0.2 GeV corresponds to the invariant mass of the single charged pion from  $\tau \to \pi \nu$  decays, reconstructed as one-prong without additional  $\pi^0$  candidate. The broad peak that ranges from 0.4 to 1.4 GeV is composed

<sup>&</sup>lt;sup>3</sup>In the detector the immediate  $\pi^0 \to \gamma \gamma$  decay leads to the presence of additional photons in the vicinity of the reconstructed prong.

BR (%)

 $\tau$ -lepton decay

1 2	
$ au^-  o h^- h^- h^+  u_ au$	9.8
$\tau^- \to a_1^- \nu_\tau \to \pi^- \nu_\tau 2\pi^0$	9.3
$\tau^- \to \rho^- \nu_\tau \to \pi^- \nu_\tau \pi^0$	25.5
$\tau^- \to \pi^- \nu_{\tau}$	10.8
$ au^-  o e^- \overline{ u}_e  u_ au$	17.8
$\tau^- \to \mu^- \overline{\nu}_\mu \nu_\tau$	17.4
In this table h refers to a not further specified charged	hadron, which could e.g. be a pion or a kaon
	CMC 10.7 fb-1 at 0.TaV

**Table 4.3** Decay channels of the  $\tau$ -lepton, which are most relevant for the analysis [38]

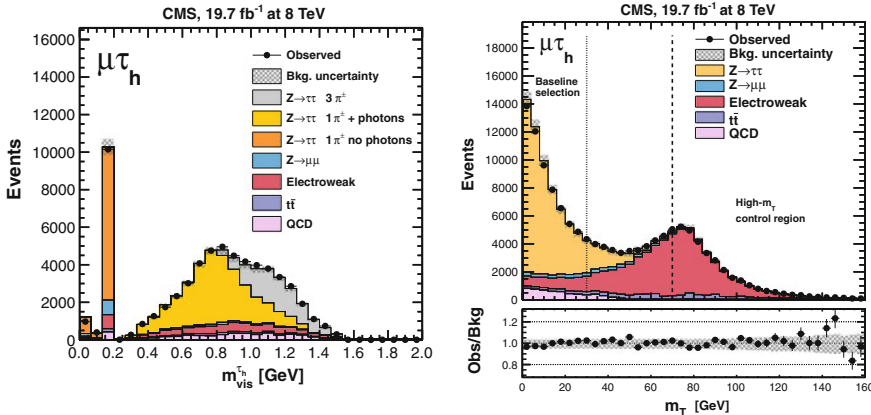


**Fig. 4.21** (*Left*) Visible mass of the reconstructed hadronic  $\tau_h$ -candidate,  $m_{\text{vis}}^{\tau_h}$  and (right) transverse mass,  $m_T$ , in the  $\mu\tau_h$  decay channel, which is driving the sensitivity of the analysis. Both quantities are shown after an inclusive event selection for the 8 TeV dataset [30]. The contribution of the SM Higgs boson signal at this selection level is expected to be negligible

of the one-prong decays with additional  $\pi^0$  candidates and of the three-prong decays. Also indicated in the figure is a hatched band corresponding to the uncertainty of the prediction of the SM, after applying the fit that has been used for the signal extraction. An excellent agreement between data and simulation is observed, which illustrates the level control that has been reached over the reconstruction of  $\tau_h$ -decays. A first feeling of two main uncertainties in the analysis in the  $H \to \tau \tau$  decay channel, the uncertainty on the reconstruction efficiency in each decay mode of the  $\tau_h$  and the uncertainty on the energy calibration of the visible parts of the decay can already be obtained from this figure.

According to Table 4.1 (right) the coupling of the SM Higgs boson to  $\tau$ -leptons, with  $BR(H \to \tau\tau) = 0.0637$ , only yields the second largest branching fraction of relevance for the Higgs discovery program of the LHC, which is significantly smaller than the branching fraction into b-quarks. On the other hand the  $H \to \tau\tau$ decay channel provides the cleaner signature with isolated high  $p_T$  leptons in the final state and the superior control over the dominating irreducible background, which in this case is not composed of QCD multijet production, but of Z boson production in the di- $\tau$  final state. The delicacy of this background arises from its high similarity to the signal, from which it can only be distinguished by the different spin and CP properties and (more promising) by the invariant mass. For  $m_H \approx 90\,\text{GeV}$ , the analysis practically turns into a counting experiment to establish an excess of events on top of the yield of  $Z \to \tau\tau$  events, which therefore has to be controlled to an excellent level. For  $m_H \neq 90\,\text{GeV}$  additional discriminating power can be gained from the expected differences in the shape of the invariant mass peaks. But also this requires a good control over the line shape of both the  $H \to \tau\tau$  signal and the  $Z \to \tau\tau$  background.

Control over the line shape of  $Z \to \tau \tau$  events can be achieved from data exploiting the *embedding* method: this method relies on the fact that due to the much smaller mass and the thus dramatically reduced coupling of the SM Higgs boson to muons  $Z \to \mu\mu$  events can be viewed as a literally background free sideband region in data. Due to lepton universality of the gauge coupling these events to very good approximation resemble the event kinematics, jet topology and event pileup as in the di- $\tau$  signal region. In addition  $Z \to \mu\mu$  events can be selected with large statistics and very high purity (of usually more than 98 % in typical inclusive selections). The basic idea of the embedding procedure is to interpret the four vector of the reconstructed muons as  $\tau$ -leptons and only to determine the well known decay of the  $\tau$ -leptons from the simulation. Other important background processes are: the production of  $t\bar{t}$  events (especially in the  $e\mu$  final state); W boson production in association with additional jets (W+jet), as shown in Fig. 4.3; and diboson production (usually subsumed into electroweak backgrounds in this section), as shown in Fig. 4.4;  $Z \to \ell\ell$  production with electrons or muons in the final state (especially in the subsequent ee and  $\mu\mu$  decay channels); and to a much smaller degree, the production of QCD multijet events, which is highly suppressed by the selection of two isolated leptons and remains of importance only due to its large production cross section.

The number of expected SM Higgs boson events with  $m_H=125\,\mathrm{GeV}$  in the  $H\to\tau\tau$  decay channel amounts to  $\approx 30\,000$  before reconstruction and selection in the 8 TeV dataset. For a baseline selection two high  $p_T$  isolated leptons were required according to the decay channel with a typical transverse momentum of  $p_T>30\,\mathrm{GeV}$  for  $\tau_h$ -leptons and  $p_T>20\,(20-24)\,\mathrm{GeV}$  for the muon (electron) in the  $\mu\tau_h$  ( $e\tau_h$ ) decay channel,  $p_T>20\,(10)\,\mathrm{GeV}$  for the (sub-)leading lepton in the ee,  $e\mu$  and  $\mu\mu$  decay channel, and  $p_T>45\,\mathrm{GeV}$  in the  $\tau_h\tau_h$  decay channel, in the corresponding geometrical acceptance of the detector. In each case the level of isolation of the leptons was determined from the transverse momentum (or energy) of the reconstructed particles in the vicinity of the lepton, relatively to the transverse momentum of the lepton in the case of electrons and muons and by its absolute value in the case of  $\tau_h$ -leptons. For these estimates the energy in the vicinity of the lepton was corrected for the effects of pileup as described in the previous sections. In the  $\mu\tau_h$  and  $e\tau_h$  channel, the background from W+ jets events was reduced by a requirement of

$$m_T = \sqrt{2p_T(\ell)E_T^{\text{miss}} (1 - \cos \Delta \phi)} < 30 \,\text{GeV}$$
 (4.5)

on the transverse mass,  $m_T$ , where  $p_T(\ell)$  corresponds to the transverse momentum of the electron or muon and  $\Delta\phi$  to the azimuthal angle between the electron or muon and the direction of  $E_T^{\text{miss}}$ . The control over this variable in the  $\mu\tau_h$  decay channel is illustrated in Fig. 4.21 (right), where also the selection requirements for the signal region (labeled as "Baseline selection") and for a high  $m_T$  sideband region, to control the normalization of W+jets events, are indicated. The black points with the error bars correspond to the data and the stacked histograms in different colors to the contributions of various SM background processes. The selection requirement of Eq. (4.5) is indicated by the fine dashed line in the upper part of the figure. It is clearly visible how the transverse mass separates two distinct processes: W+jets events, with high transverse mass (around  $m_W$ , indicated by the label "Electroweak" in the figure) and signal like  $Z \to \tau \tau$  events, with low transverse mass. This can be understood from the fact in W+jets events the neutrino originates from the decay of the real heavy W boson, while the neutrinos of the  $\tau$ -lepton decays originate from virtual W boson decays at the much lower scale of  $m_{\tau}$  and collinear with the visible decay products. In the lower part of the figure the ratio of the data over the expectation from the simulation is shown. In both sub-figures the systematic uncertainty as obtained after the fit that has been used for the signal extraction is shown by a hatched band.

In the  $e\mu$  decay channel, the more important background from  $t\bar{t}$  events was reduced using a BDT discriminant exploiting kinematic variables, related to the  $e\mu$  system and  $E_T^{\text{miss}}$ , the distance of closest approach between each corresponding lepton and the vertex of the hard interaction, and the probability of the leading jet in the event to be initiated by a b-quark.

With the amount of the *LHC* run-1 data of the years 2011 and 2012 there was no sensitivity, yet, to make use of the spin or CP nature of the SM Higgs boson to distinguish signal from background. Thus the invariant mass of the di- $\tau$  system,  $m_{\tau\tau}$ , was the most important quantity for this purpose. The reconstruction of  $m_{\tau\tau}$  is complicated by the presence of the two to four neutrinos in the decay chains, depending on the final state of the di- $\tau$  system, which can only be measured via  $E_T^{\text{miss}}$  under the assumption that they are the only sources of  $E_T^{\text{miss}}$  in the event. The simplest estimate of  $m_{\tau\tau}$  is obtained, ignoring the contributions from the neutrinos in the decay chain right away using the invariant mass only of the visible decay products of each  $\tau$ -lepton,  $m_{\text{vis}}$ . While this is a robust estimate it misses all energy that is carried away by the neutrinos and is thus deteriorated in terms of its response and resolution with respect to the true di- $\tau$  mass.

A simple improvement can be achieved by the collinear approximation [40, 41], which relies on the additional assumption, that the  $\tau$ -leptons are highly enough boosted, such that the flight direction of the neutrinos coincides with the flight direction of the visible  $\tau$ -decay products. In this case the momentum sum of all neutrinos of the two  $\tau$ -lepton decays can be inferred from  $E_T^{\rm miss}$  via a simple system of two linear equations

$$E_{T,x}^{\text{miss}} = p_{\tau_1}^{\nu} \cdot \sin \vartheta_{\tau_1} \cos \varphi_{\tau_1} + p_{\tau_2}^{\nu} \cdot \sin \vartheta_{\tau_2} \cos \varphi_{\tau_2}$$

$$E_{T,y}^{\text{miss}} = p_{\tau_1}^{\nu} \cdot \sin \vartheta_{\tau_1} \sin \varphi_{\tau_1} + p_{\tau_2}^{\nu} \cdot \sin \vartheta_{\tau_2} \sin \varphi_{\tau_2}$$

$$(4.6)$$

where  $E_{T,x,y}^{\text{miss}}$  correspond to the x and y component of  $E_T^{\text{miss}}$ ,  $p_{\tau_i}^{\nu}$  to the summed momenta of all neutrinos and  $\vartheta_{\tau_i}$  and  $\varphi_{\tau_i}$  to the polar and azimuthal angle of  $\vec{p}_{\tau_i}^{\nu}$ , belonging to  $\tau_i$ . The solution for  $p_{\tau_i}^{\nu}$  takes the form

$$p_{\tau_1}^{\nu} = \frac{E_{T,x}^{\text{miss}} \cdot \sin \varphi_{\tau_2} - E_{T,y}^{\text{miss}} \cdot \cos \varphi_{\tau_2}}{\sin \vartheta_{\tau_1} \sin(\varphi_{\tau_1} - \varphi_{\tau_2})} \quad p_{\tau_2}^{\nu} = -\frac{E_{T,x}^{\text{miss}} \cdot \sin \varphi_{\tau_1} - E_{T,y}^{\text{miss}} \cdot \cos \varphi_{\tau_1}}{\sin \vartheta_{\tau_2} \sin(\varphi_{\tau_1} - \varphi_{\tau_2})}$$
(4.7)

and  $m_{\tau\tau}$  can be calculated as

$$m_{ au au} = rac{m_{ ext{vis}}}{\sqrt{x_{ au_1}x_{ au_2}}}, \qquad x_{ au_i} = rac{p_{ au_i}^{ ext{vis}}}{p_{ au_i}^{ ext{vis}} + p_{ au_i}^
u}$$

where  $p_{\tau_i}^{\rm vis}$  corresponds to the summed momenta of the visible decay products of  $\tau_i$ . The drawback of the collinear approximation is that it requires a boost of the  $\tau$ -leptons to lead to a good estimate of  $m_{\tau\tau}$  and that the system in Eq.(4.6) turns degenerate when the two  $\tau$ -leptons emerge in a back to back configuration in the transverse plain. In this case the solutions given in Eq.(4.7) diverge, resembling the fact that  $p_{\tau_1}^{\nu}$  and  $p_{\tau_2}^{\nu}$  could become infinitely large compensating each other by a small fraction consistent with the measurement of  $E_T^{\rm miss}$ .

To further improve on the estimate of  $m_{\tau\tau}$  the CMS collaboration has followed an analytical likelihood approach that will be described in the following paragraphs: six variables are needed to fully describe the hadronic decay of a  $\tau$ -lepton. These can be chosen to be the azimuthal and polar angle of the decay in the  $\tau$  restframe, the invariant mass of the visible decay products,  $m_{vis}$ , and the three coordinates of the boost into the  $\tau$  restframe. For the leptonic decays these parameters have to be extended by a seventh parameter, which can be chosen to be the invariant mass of the two neutrinos,  $m_{\nu\nu}$ , in the decay. These parameters have to be matched against the four observable components of the visible decay products, which leaves 2 (3) parameters undetermined. In the likelihood approach these undetermined parameters were chosen to be: (i) the  $\tau$ -energy fraction of the visible decay products in the laboratory frame, x; (ii) the azimuthal angle of the  $\tau$ -lepton in the laboratory frame,  $\phi$ , and; (iii) the invariant mass of the neutrino system,  $m_{\nu\nu}$ , in the case of leptonic decays. These 2 (3) undetermined variables per  $\tau$ -lepton add up to 4 (6) undetermined variables for the di- $\tau$  system, depending on the decay channel. Under the assumption that there are no other sources of missing energy in the event, additional information on the neutrinos in the decay can be inferred from the x- and y-component of  $E_T^{\text{miss}}$ .

With these ingredients the likelihood function is composed as a product of three terms: two terms corresponding to the probability of the visible decay products of each  $\tau$ -lepton to be compatible with the expected kinematics of the decay, and one more term, which quantifies the compatibility of the resulting kinematics of the neutrinos from the two decays with the measurement of  $E_T^{\rm miss}$ . Each term can be expressed by an analytical form: the kinematics of the hadronic decay of the

 $\tau$ -lepton had been expressed by the phasespace kinematics of a two body decay in the  $\tau$  restframe, treating the sum of the momenta of all visible decay products as a single particle [38]

 $\mathcal{L}_{\tau_h} = \frac{\mathrm{d}\Gamma}{\mathrm{d}x} \propto \frac{1}{1 - m_{\mathrm{vis}}^2 / m_{\tau}^2} \tag{4.8}$ 

where the kinematic allowed phasespace is given by  $m_{\rm vis}^2/m_\tau^2 \le x \le 1$  and x corresponds to the energy fraction of the visible decay product(s) with respect to the total energy in the  $\tau$  restframe. Extensive checks had been made to assure that this approach was in sufficient agreement with the complete matrix element calculation, including spin and CP information of the decay as implemented in simulation programs as given in [42]. For the leptonic decay the leading-order matrix element in the  $\tau$  restframe had been used as given in [43]

$$\mathcal{L}_{\tau_{\ell}} = \frac{\mathrm{d}\Gamma}{\mathrm{d}x\,\mathrm{d}m_{\nu\nu}} \propto \frac{m_{\nu\nu}}{4m_{\tau}^2} \left[ (m_{\tau}^2 + 2m_{\nu\nu}^2)(m_{\tau}^2 - m_{\nu\nu}^2) \right] \tag{4.9}$$

where the kinematic allowed phasespace is given by  $0 \le x \le 1$  and  $0 \le m_{\nu\nu} \le m_{\tau}\sqrt{1-x}$  and x has the same meaning as for Eq. (4.8). The compatibility of the neutrino kinematics in the decay with the observed  $E_T^{\text{miss}}$  in the event had been inferred from a Gaussian model of the  $E_T^{\text{miss}}$  resolution in x and y

$$\mathcal{L}_{\nu}(E_{T,x}^{\text{miss}}, E_{T,y}^{\text{miss}}) = \frac{1}{2\pi\sqrt{|V|}} \times \exp\left(-\frac{1}{2} \left(\frac{E_{T,x}^{\text{miss}} - \sum p_{x}^{\nu}}{E_{T,y}^{\text{miss}} - \sum p_{y}^{\nu}}\right)^{T} \cdot V^{-1} \cdot \left(\frac{E_{T,x}^{\text{miss}} - \sum p_{x}^{\nu}}{E_{T,y}^{\text{miss}} - \sum p_{y}^{\nu}}\right)\right)$$
(4.10)

where  $E_{T,x,y}^{\text{miss}}$  and  $\sum p_{x,y}^{\nu}$  correspond to the x and y component of  $E_T^{\text{miss}}$  and of the sum of the momenta of the neutrinos in the decay, and  $V^{-1}$  and |V| to the inverse and the determinant of the covariance matrix of  $E_T^{\text{miss}}$ , which can be estimated from the reconstructed particle flow objects, on an event by event basis. The integral over the product of the individual likelihoods for the corresponding decay then reads as

$$\mathcal{P}(m_{\tau\tau}^{j}) = \int \delta \left( m_{\tau\tau}^{j} - m_{\tau\tau}(\vec{y}_{\tau_{1}}, \vec{x}_{\tau_{1}}, \vec{y}_{\tau_{2}}, \vec{x}_{\tau_{2}}) \right) \mathcal{L}_{\tau_{h/\ell}} \cdot \mathcal{L}_{\tau_{h/\ell}} \cdot \mathcal{L}_{\nu}(E_{T,x}^{\text{miss}}, E_{T,y}^{\text{miss}}) d\vec{x}_{\tau_{1}} d\vec{x}_{\tau_{2}}$$
(4.11)

where  $\vec{y}_{\tau_i}$  corresponds to the measured four vectors of the visible decay products and  $\vec{x}_{\tau_i} = (\phi, x, m_{\nu\nu})_{\tau_i}$  for each  $\tau_i$ . The value  $\mathcal{P}(m_{\tau\tau}^j)$  gives the probability of the kinematics of the visible decay products,  $\vec{y}_{\tau_i}$ , and  $E_T^{\text{miss}}$  to be compatible with the hypothesis of a decay into two  $\tau$ -leptons, for a given value of  $m_{\tau\tau}^j$ . The dependency of the likelihood on  $m_{\nu\nu,\tau_i}$  in the case of leptonic decays is evident from Eq. (4.9). The dependency on  $x_{\tau_i}$  enters via the integration boundaries of Eqs. (4.8) and (4.9),

the dependency on  $\phi_{\tau_i}$  enters via Eq. (4.10). The value  $\hat{m}_{\tau\tau}^j$  that leads to a maximum of  $\mathcal{P}(m_{\tau\tau}^j)$  in a wide scan of values of  $m_{\tau\tau}^j$  is chosen to be the best estimate of  $m_{\tau\tau}$  under the hypothesis of a di- $\tau$  decay.

With this reconstruction method a resolution of  $m_{\tau\tau}$  had been achieved, which is superior to the invariant mass only of the visible decay products,  $m_{\rm vis}$ , and comparable to the collinear approximation. Over the collinear approximation it has the advantage that it does not rely on the di- $\tau$  system to be boosted and that it always leads to a valid solution. Depending on the kinematics of the di- $\tau$  system the resolution of  $m_{\tau\tau}$  is approximately 10%, 15%, 20% in the  $\tau_h\tau_h$ ,  $\ell\tau_h$ ,  $\ell\ell$  decay channels. In Fig. 4.22  $m_{\rm vis}$  and  $m_{\tau\tau}$  as calculated from the maximum likelihood approach, as described above, are shown in the  $\mu\tau_h$  decay channel. The full histogram corresponds to simulated events of the most important background process of  $Z \to \tau\tau$  production and the open histogram to simulated events of the  $H \to \tau\tau$  signal process for a mass of  $m_H = 125$  GeV. For the comparison of the shapes of the distributions both samples have been normalized to unit area. The figure indicates the difficulty to separate the two processes and how the separation between the two peaks increases when going from  $m_{\rm vis}$  to the maximum likelihood approach. Also the most probable values of the peaks are closer to the nominal masses of the Z boson and  $m_H = 125$  GeV.

To increase the sensitivity of the analysis, the selected events were further divided into categories of zero, one and two jets, in each of the six inclusive decay channels with a further sub-categorization according to the  $p_T$  of the (leading) lepton in the final state and the reconstructed  $p_T$  of the Higgs boson candidate, estimated from the  $p_T$  of the leptons and  $E_T^{\rm miss}$ . These distinctions resulted in 27 event categories

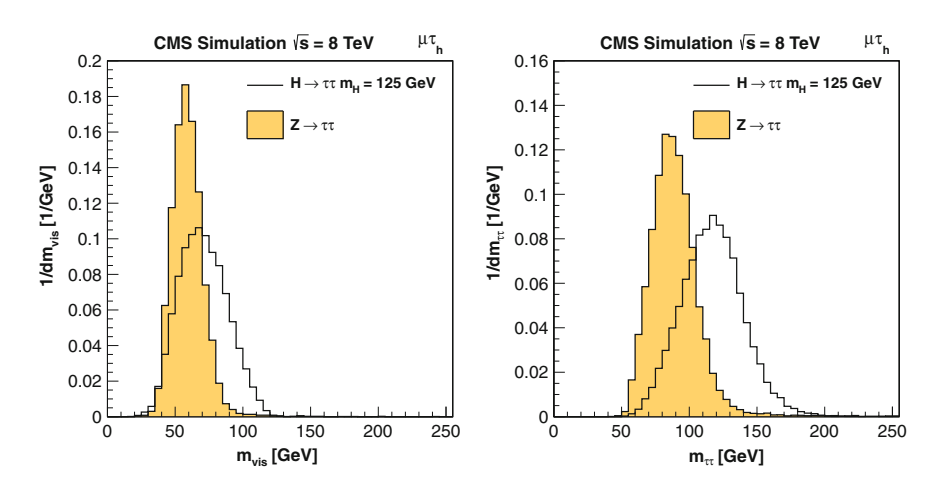
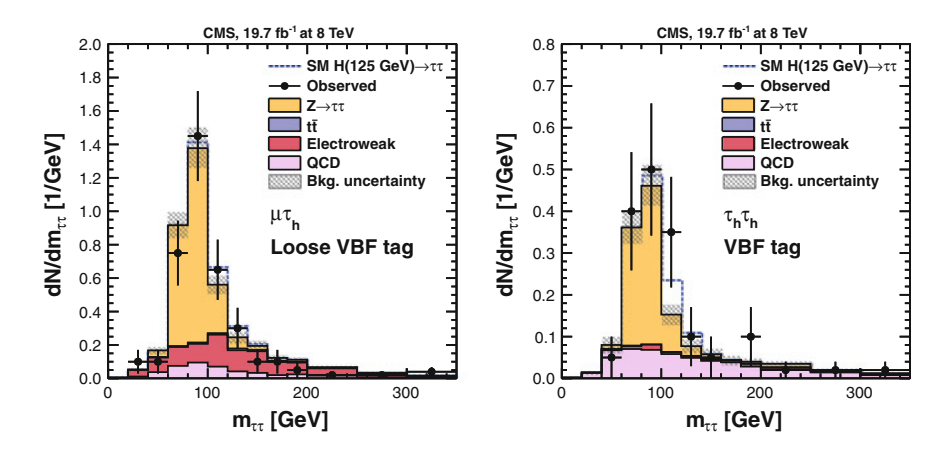


Fig. 4.22 Reconstructed invariant mass of the di- $\tau$  system, (*left*) using the invariant mass of the visible decay products,  $m_{\rm vis}$  and (*right*) using the maximum likelihood approach as described in the text [30]. Shown are simulated events for the most important background process of  $Z \to \tau \tau$  and for the signal process of  $H \to \tau \tau$  for  $m_H = 125 \, {\rm GeV}$  for a center-of-mass energy of 8 TeV in the  $\mu \tau_h$  decay channel, normalized to unit area

on the 8 TeV dataset and a similar, but slightly smaller number of event categories on the 7 TeV dataset. The smaller number of event categories on the 7 TeV dataset is explained by the smaller number of events in this dataset, which restricts the possibility to further categorize. With the large number of initial signal events ( $\approx 2.100$ events in the vector boson fusion (VBF) production mode before reconstruction and selection!), the  $H \to \tau \tau$  decay channel was the only channel, which allowed realistically to tag signal events in the VBF production mode, in the two jet event categories. The typical fraction of signal events in the VBF production mode with respect to all other production modes in these event categories was expected to be  $\approx$ 80 %. At the same time these are the most sensitive single event categories of the analysis (with an exclusion sensitivity at  $m_H = 125 \,\mathrm{GeV}$  of  $\approx 0.5 \times \sigma_{\mathrm{SM}}$ ). The invariant mass in the  $\mu \tau_h$  and in the  $\tau_h \tau_h$  decay channel, in a loose VBF event category, with the largest expected S/B ratio are shown in Fig. 4.23. The black points with error bars correspond to the data and the filled histograms, stacked on top of each other to the events from all expected SM background processes. The uncertainties of the background prediction are indicated by a hatched band.

In these event categories the expected signal contribution, indicated by the open dashed line histogram, on top of the background expectation starts to become visible already, by eye. The one jet event categories are designed to select signal events in the  $gg \to gH$  production mode with a Higgs boson with high  $p_T$ , recoiling against the selected high  $p_T$  jet. In these event categories the additional jet and the high  $p_T$  of the recoiling di- $\tau$  system lead to a significant reduction of the background from  $Z \to \tau \tau$  events. In addition the high  $p_T$  of the recoiling di- $\tau$  system leads



**Fig. 4.23** Reconstructed invariant mass of the di- $\tau$  system,  $m_{\tau\tau}$ , for the (*left*)  $\mu\tau_h$  and (*right*)  $\tau_h\tau_h$  decay channel in a loose vector boson fusion (VBF) tagged event category, with the largest S/B ratios [30]. The *black points* with the error bars correspond to the data. The different colors of the filled histograms indicate the expected composition of the SM background processes. The *blue open dashed* histogram on top of the expected background distribution corresponds to the expected signal for a SM Higgs boson with  $m_H = 125\,\text{GeV}$ 

to a better resolution of  $E_T^{\rm miss}$  which translates into a better resolution of  $m_{\tau\tau}$ . The one jet event categories yield the second most sensitive single event categories (with an exclusion sensitivity at  $m_H=125\,{\rm GeV}$  only slightly worse than the VBF event categories). They contain much more events than the two jet event categories, but also more background events, and are complementary to the two jet event categories in that sense.

The zero jet event categories yield an exclusion sensitivity of the single event categories of typically 2 to  $4 \times \sigma_{SM}$  at  $m_H = 125$  GeV. The most important role of these event categories lies in the in-situ inter-category cross-calibration of the most important uncertainties in the analysis, like the  $\tau_h$ -energy scale or the  $\tau_h$ -reconstruction and selection efficiency, which have already been discussed at the beginning of this section. A general feature of this analysis, which might have occurred as a difficulty on first sight, the diversity of decay channels in the classification of the di- $\tau$  system, allows for such cross-calibrations, not only across event categories, but also across decay channels and helps to increase the robustness of the analysis.

Apart from the six inclusive decay channels an independent analysis had been performed based on the exclusive VH production mode in several multi-lepton final states with very low background expectation. But this analysis will not be further discussed, as it added less than 3% to the over all sensitivity of the combined analysis in the  $H \to \tau\tau$  decay channel. In Fig. 4.24 (left), all selected events in all event categories in the  $H \to \tau\tau$  analysis are shown, ordered by their values of S/(S+B). The black points with error bars correspond to the data, while the colored stacked histograms correspond to the expected number of background events split by event

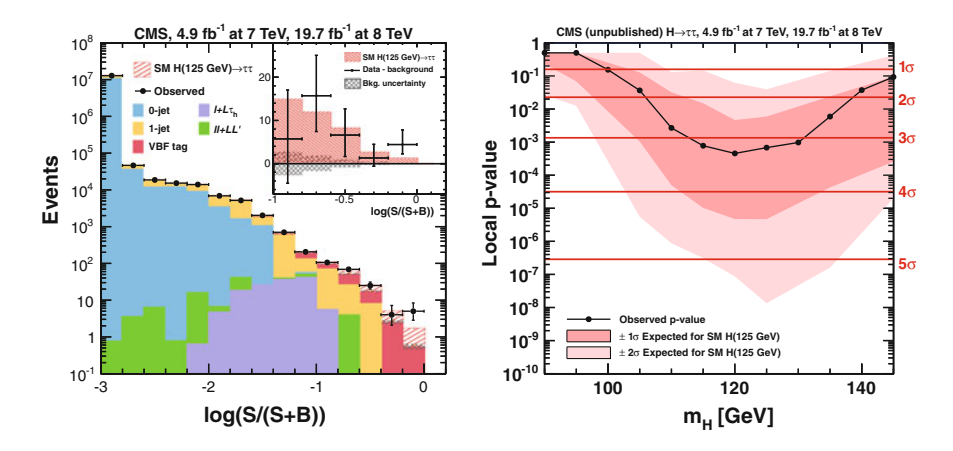


Fig. 4.24 (*Left*) Combination of all selected events in all event categories in the  $H \to \tau\tau$  analysis ordered by S/(S+B) and (right) the p-value for the combination of all sub-decay channels [30]. In the figure on the *left* the *black points* with error bars correspond to the data. The filled histograms indicate the distribution of the expected background events across the different event categories. In the figure on the *right* the *black points* correspond to the observed p-value at each tested value of  $m_H$ . The *dark* and *pale red band* correspond to the  $1\sigma$  and  $2\sigma$  uncertainty for the expected p-value in the presence of a SM Higgs boson with  $m_H = 125\,\text{GeV}$ 

categories. The red hatched histogram corresponds to the expectation for a SM Higgs boson with  $m_H = 125$  GeV. In the inlet the data are shown after subtracting the expected number of background events. The figure illustrates that those events with the largest value of S/(S+B) are located in the one and two jet event categories (the latter being labeled as "VBF tag"). In Fig. 4.24 (right) the local p-value is shown for the combination of all events in all event categories (including the exclusive VH analysis). The black points correspond to the observed p-value evaluated at each tested value of  $m_H$  on the x-axis, the dark and pale red band correspond to the 68% and 95% CL uncertainties of the expected p-value for the (s+b)-hypothesis with  $m_H = 125$  GeV.

The data reveal an evidence for a signal with  $>3\sigma$  in a mass range between 115 and 130 GeV, with a minimum at  $\approx$ 120 GeV. For  $m_H = 125$  GeV the observed (expected) significance is  $3.2\sigma$  (3.7 $\sigma$ ), corresponding to a most probable value of  $\hat{\mu} = 0.78 \pm 0.27$ . In the full mass range, between 90 and 145 GeV, in which this analysis is sensitive, the observation is well compatible with the expectation for a SM Higgs boson signal with  $m_H = 125 \,\text{GeV}$  within the 68 % CL. The analysis in the  $H \to \tau \tau$  decay channel has the peculiarity that the signal cannot be distinguished from the signal in the  $H \to WW$  decay channel. This was especially the case in the  $e\mu$  final state and in the exclusive VH analysis. In all other sub-decay channels of the analysis the contribution from  $H \to WW$  events was checked to be negligible. To assure that the analysis result resembles the coupling to fermions and not a combination of fermions and W bosons, the expected signal for  $H \to WW$  events in the  $e\mu$  decay channel and in the exclusive VH analysis had been treated as an additional background, assuming the production cross section and branching fraction as expected by the SM. Figure 4.24 (right) thus explicitly shows the evidence for the coupling of the Higgs boson to  $\tau$ -leptons and hence to fermions. Including the  $H \to WW$  contribution to the signal and assuming the relative signal fractions as in the SM results in an observed (expected) significance of  $3.9\sigma$  (3.9 $\sigma$ ), corresponding to a most probable value of  $\hat{\mu} = 0.91 \pm 0.27$ , for  $m_H = 125 \, \text{GeV}$ .

Already shortly after the time of the discovery the analysis had been "re-blinded" and the data re-analyzed with an improved definition of  $E_T^{\rm miss}$ , which is based on a multivariate regression approach. This approach led to a significant improvement of the  $E_T^{\rm miss}$  resolution and at the same time to a much reduced dependency on pileup. Also the independent analysis in the VH production mode had been added. Later on the rejection of background from  $t\bar{t}$  events in the  $e\mu$  decay channel had been revised and the event categorization substantially increased, from originally three event categories, only based on the jet multiplicity in the event to the event categories as discussed above. These extensions lead to an increase of the sensitivity of the analysis in the  $H\to \tau\tau$  decay channel of  $\mathcal{O}(40\,\%)$  in addition to the increased dataset, which was a necessary prerequisite to make the observation of the evidence possible.

#### **Muons and Electrons**

As discussed above with the number of events collected during the *LHC* run-1 data taking period there is no realistic chance to observe a signal from the SM Higgs boson

in the  $H \to \mu\mu$  and even less in the  $H \to ee$  decay channel. The branching fraction of  $H \to \mu\mu$  is 0.000221 and thus  $\approx$ 290 times smaller than the branching fraction to  $\tau$ -leptons, resulting in an expected number of signal events before reconstruction and selection of  $\approx$ 100 on the 8 TeV dataset. While this number is comparable to the  $H \to ZZ$  decay channel these events are buried under an overwhelming background of  $Z \to \mu\mu$  events. Despite of the hopeless situation in the context of the SM, the search has been conducted to exclude the presence of an anomalously high coupling in both decay channels [44]. Both decay channels correspond to high resolution channels with large background, implying a search strategy similar to the  $H \to \gamma\gamma$  decay channel.

For the analyses events with two isolated muons (electrons) were selected. The muons were required to have a transverse momentum of  $p_T > 25 (15) \,\text{GeV}$  for the (sub-)leading muon, where the higher threshold on the  $p_T$  of the leading muon was chosen to guarantee a high efficiency of the online selection. The  $p_T$  of the (sub-) leading electron was required to be larger 17 (8) GeV, with the same reasoning. For a SM Higgs boson with  $m_H = 125 \,\text{GeV}$  the resolution of  $m_{\mu\mu}$  was found to be between 3.8 and 5.9 GeV in the full width half maximum, depending on the angular orientation of the muons, which translates into a Gaussian resolution between 1.6 and 2.5 GeV. The resolution of  $m_{ee}$  was found to be between 4.0 and 7.2 GeV in the full width half maximum, corresponding to a Gaussian resolution of 1.7 and 3.1 GeV. To improve the sensitivity of the di-muon analysis, also here the selected events where categorized into a two-jet and an inclusive 0/1-jet event category, representing the topology of the  $gg \to H$  and  $qq \to H$  production modes. The two-jet event category was further split into a tight vector boson fusion, a tight gluon fusion and a loose gluon fusion event category. The 0/1-jet event category was further divided into a tight and loose sub-category. Each of these sub-categories were then further split according to the angular orientation of each muon distinguishing between the barrel region ( $|\eta| < 0.8$ ), a barrel endcap transition region (0.8 <  $|\eta| < 1.6$ ) and the endcap region  $(1.6 < |\eta|)$  of the outer track detectors of the muon system. This resulted in a classification of the events in 15 exclusive event categories for the 7 and 8 TeV dataset each.

In the di-electron analysis the events were divided into four event categories according to a tight and loose two-jet event category and an inclusive 0/1-jet event category split into a sub-category with both electrons in the ECAL barrel ( $|\eta| < 1.44$ ) and a complementary event sub-category. The di-electron analysis had only been performed on the 8 TeV dataset.

For the statistical inference in both decay channels the invariant mass distributions,  $m_{\mu\mu}$  and  $m_{ee}$ , were used in the mass range between 110 and 160 GeV to search for a narrow resonance on top of a continuous background. The signal was modeled by a double Gaussian distribution representing the experimental resolution in the different regions of the detector. The background was modeled by the sum of a *Breit-Wigner* function for the contribution from non-resonant  $Z \to \ell\ell$  events and a  $1/m_{\ell\ell}^2$  term for

the contribution from non-resonant diphoton radiation, multiplied by an exponential function to describe the kinematic constraints from the parton distribution functions:

$$f(m_{\ell\ell}) = e^{\lambda \cdot m_{\ell\ell}} \left( C_1 \cdot \frac{\beta}{(m_{\ell\ell} - m_Z)^2 + \Gamma^2/4} + C_2 \cdot \frac{1 - \beta}{m_{\ell\ell}^2} \right)$$

where  $C_1$  and  $C_2$  were pre-determined normalization parameters,  $\lambda$  and  $\beta$  were free parameters of the model and  $m_Z$  and  $\Gamma$  were determined prior to the fit used for the signal extraction from a fit to the reconstructed  $m_{\ell\ell}$  distribution in a mass range between 88 and 94 GeV. This function had been checked to describe the background distribution well also in the presence of other backgrounds than the ones motivated above, e.g. like  $t\bar{t}$  events. The  $m_{\mu\mu}$  distribution in the range between 110 and 160 GeV in the inclusive 0/1-jet, tight event category with both muons in the barrel region (labeled as "0,1-jet Tight BB") and for the two-jet VBF, tight event category, for the 8 TeV dataset are shown in Fig. 4.25. The black points with error bars correspond to the data. The blue line with the bright blue band corresponds to the result and the 68 % CL uncertainty of the maximum likelihood fit of the b-hypothesis. The signal for a SM Higgs boson with  $m_H = 125$  GeV, enhanced by a factor of  $\times$  20 is shown by a red line for comparison. In the lower panels of the figures the data points are shown after subtracting the expectation for the b-hypothesis and dividing by the fit uncertainty.

In the absence of a signal 95 % CL upper limits have been set on the cross section times branching fraction ( $\sigma \times BR$ ), based on the test statistic as defined in Eq. (4.1) in the mass range between 120 and 150 GeV. For the 8 TeV dataset the expected and observed limit on  $\sigma \times BR$  for the di-muon and for the di-electron channel are

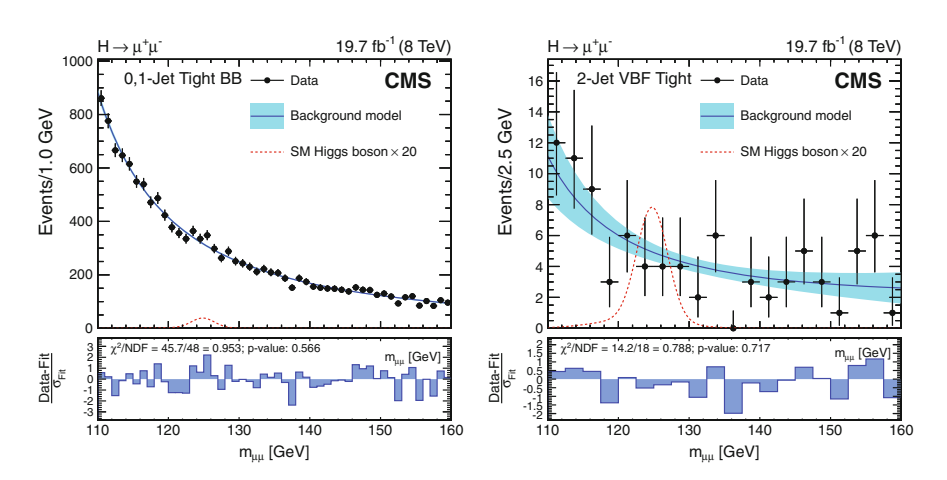


Fig. 4.25 Invariant mass of the di-muon system,  $m_{\mu\mu}$ , (left) in the inclusive 0/1-jet, tight event category with both muons in the barrel region of the detector and (right) in the two-jet VBF, tight event category, each for the 8 TeV dataset [44]

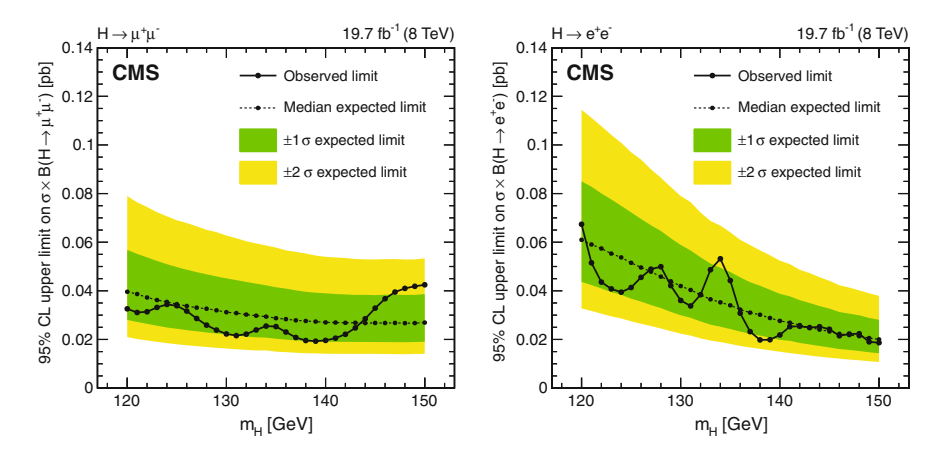


Fig. 4.26 95% CL upper limits on the production cross section times branching fraction,  $\sigma \times BR$ , as determined on the 8 TeV dataset and as a function of the tested Higgs boson mass,  $m_H$  (*left*) in the di-muon and (*right*) in the di-electron channel [44]

shown in Fig. 4.26. No significant deviation is observed from the expectation for the *b*-hypothesis in accordance with the expectation from the SM. The limits are roughly of similar size for the muon and the electron analysis due to the comparable resolutions and selection efficiencies in both decay channels. For  $m_H = 125\,\text{GeV}$  the observed (expected) limit on  $\sigma \times BR$  in the di-muon channel is 0.084 (0.062) pb on the 7 TeV dataset and 0.033 (0.034) pb on the 8 TeV dataset. Combining both datasets under the assumption of the production cross section for the SM Higgs boson with  $m_H = 125\,\text{GeV}$  leads to an observed 95% CL upper limit of  $BR(H \to \mu\mu) \le 0.0016$ , corresponding to an observed (expected) limit 7.4 (6.5) times larger than the expected branching fraction by the SM.

The observed (expected) 95% CL upper limit on  $\sigma \times BR$  for  $m_H = 125\,\text{GeV}$  in the di-electron channel is 0.041 (0.052) pb on the 8 TeV dataset. Assuming the production cross section for the SM Higgs boson with  $m_H = 125\,\text{GeV}$  leads to an observed 95% CL upper limit of  $BR(H \to ee) \leq 0.0019$ , corresponding to an observed limit  $\approx 3.7 \times 10^5$  times larger than the expected branching fraction by the SM.

# 4.4.2 The Coupling to Quarks

#### **Light Flavor and** *b***-Quarks**

The inevitable difficulty, when studying the coupling of the Higgs boson to quarks lies in their color charge, which disguises them as jets of colorless particles in the detector. The first challenge is to identify, the quark (or gluon) of the hard scattering

process that initiated the jet, and to infer its kinematics from the jet energy and direction. This is usually only possible on a statistical basis. Another main problem, when searching for Higgs boson decays into quarks is to distinguish them from the overwhelmingly large background from events with normal *QCD* induced jets, which occur with a nearly indistinguishable signature and exceed the rate of the events of interest by many orders of magnitude. The high rate of *QCD* multijet processes poses the additional problem of getting the interesting events written to tape during the time of data taking, which can be done only with a limited band width as discussed in Sect. 4.1.2.

When studying the decay of the SM Higgs boson into quarks, the lightest quarks u, d and s drop out form consideration right away, due to their low mass and therefore small coupling. The same is true for the c-quark, which might not be completely out of scope, but still is too light and too difficult to be separated from the overwhelming background. The only quark, for which the decay is energetically allowed for a SM Higgs boson mass of  $m_H = 125 \,\text{GeV}$  and for which the identification and reconstruction is possible is the b-quark. For  $m_H = 125 \,\mathrm{GeV}$  the  $H \to b\bar{b}$  decay channel provides the largest branching fraction, with 56 %, due to the high mass of  $m_b = 4.18(3)$  GeV, resulting in an expected number of  $\approx 250\,000$  SM Higgs boson events in this decay channel before reconstruction and selection, on the 8 TeV dataset. To distinguish these events from ordinary QCD multijet production and to cope with the enormous rate of this background during the online event selection, the analysis in this decay channel is focused on Higgs boson production in association with vector bosons. In the decay channels of the W or Z boson into electrons, muons or neutrinos this production mode provides event signatures, which are clean enough to be isolated from other events. At the same time they rare enough to be written to tape with an acceptable rate. This trade has to be made at a cost of losing 95 % of the expected 250 000 SM Higgs boson events, produced during the collisions, resulting in a number of potentially  $\approx$ 12 000 events in the recorded dataset.

In the final analysis six decay channels were considered:  $W(\tau\nu)H$ ,  $W(\mu\nu)H$ ,  $W(e\nu)H$ , Z(ee)H,  $Z(\mu\mu)H$ ,  $Z(\nu\nu)H$ , always with the subsequent  $H\to b\bar{b}$  decay, indicating the final state of the vector boson in braces [31]. As in the other decay channels that have been discussed in the previous sections the decay channels with electrons or muons in the final state profit from the clear signature of the isolated leptons in the detector. The  $Z\to\nu\nu$  decay channel, relies on the measurement of  $E_T^{\rm miss}$ , which is much more difficult to control. In return it brings a significant gain in statistics, due to its branching fraction, which is 50% larger than the sum of the  $Z\to ee$  and the  $Z\to\mu\mu$  decay channel. The  $W(\tau\nu)$  decay channel in this section only refers to hadronically decaying  $\tau$ -leptons that have been discussed in Sect. 4.4.1. The  $\tau\to\mu\nu_\tau\nu_\mu$  and  $\tau\to e\nu_\tau\nu_e$  decays had been subsumed in the corresponding  $W(\mu\nu)$  or  $W(e\nu)$  final state for the further analysis. To increase the purity of reconstructed  $\tau_h$ -leptons, only those decay channels with exactly one one-prong were considered.

Due to the choice of the specific production mode the dominant backgrounds in the event selection did not primarily arise from QCD multijet production, but from the production of vector bosons in association with jets (V + jets),  $t\bar{t}$  production and

the production of diboson events (VV). Among those the WZ and ZZ production processes, with a subsequent  $Z \to b\bar{b}$  decay are especially hard to distinguish from the expected SM Higgs boson signal. On the other hand a reliable prediction of this background can be used to benchmark the analysis and to crosscheck its validity even when the analysis is still "blind" in the signal region.

For those events which fulfilled the final event selection, in each of the decay channels, the efficiency to write the events to tape had been found to be well above 90% with the lowest efficiency of 88% for  $Z \rightarrow \nu\nu$  events with  $100 < E_T^{\rm miss} < 130\,{\rm GeV}$ . The final reconstruction efficiency ranged between 87–91% for isolated high  $p_T$  muons and 81–98% for isolated high  $p_T$  electrons. The reconstruction efficiency of  $\tau$ -leptons corresponded to 50% with a mis-identification rate of 1%. Particle jets originating from the hadronization of b-quarks were identified based on the combined information of the impact parameters of the associated tracks, the presence of secondary vertices and the shape of the jet, featuring the longer lifetime of B-hadrons and the higher mass of the b-quark when compared to jets initiated from light quarks, c-quarks or high  $p_T$  gluons [45]. Several working points with different expected purities for the jet being initiated by a b-quark were used throughout the analysis with efficiencies for identifying jets initiated by b-, c-, light quarks or gluons ranging between 50–75%, 5–25% and 0.15–3%.

In the decay channels containing W bosons, the boson was identified by the isolated lepton and the  $E_T^{\rm miss}$  in the direction of the lepton. The thresholds on the lepton  $p_T$  were required to be 20, 30, 40 GeV for muons, electrons and  $\tau$ -leptons, respectively. The  $E_T^{\rm miss}$  was required to be larger than 45 GeV in the  $W(\mu\nu)$  and  $W(e\nu)$  case and larger than 80 GeV in the more challenging  $W(\tau\nu)$  case.  $Z\to\ell\ell$  events were identified by two isolated leptons of same flavor and opposite charge. The transverse momentum of the leptons was required to be  $p_T(\ell)>20$  GeV each, and the invariant dilepton mass to be within  $75< m_{\ell\ell}<105$  GeV. In the  $Z\to\nu\nu$  decay channel events were primarily selected based on  $E_T^{\rm miss}$ . To increase the sensitivity of the analysis all selected events were categorized according to the transverse momentum of the reconstructed vector boson into maximally three boost categories, as summarized in Table 4.4, where the  $p_T$  was reconstructed from the transverse momentum of the vectorial sum of the momenta of the two isolated leptons, in the  $Z\to\ell\ell$  cases and from  $E_T^{\rm miss}$  and the transverse momentum of the isolated lepton in the  $W\to\ell\nu$  cases.

The reconstruction of the  $H \to b\bar{b}$  decay was performed by considering all jets in the event with  $|\eta(j)| < 2.5$  and above a minimum  $p_T(j)$  threshold (depending on the boost category and the decay channel). Of those jets the pair was chosen that led to the highest value of the transverse momentum calculated from the vectorial sum of the individual jet momenta,  $p_T(jj)$ , if both jets had a high probability to originate from a b-quark. After the full event selection the resolution of the invariant dijet mass,  $m_{jj} \equiv m_H^{\rm rec}$ , was found to be  $\approx 10$  %, depending on the  $p_T$  of the reconstructed Higgs boson candidate. This resolution could be improved by another  $\approx 15$  % with the help of a dedicated multivariate energy regression method. For the further analysis a requirement of  $m_{jj} < 250\,{\rm GeV}$  on the dijet invariant mass was applied for all decay

	Boost categories				
	Low	Medium	High		
$W(\tau \nu)$	_	_	$120\mathrm{GeV} < p_T(V)$		
$W(\mu\nu)$	$100 < p_T(V) < 130 \mathrm{GeV}$	$130 < p_T(V) < 180 \mathrm{GeV}$	$180\mathrm{GeV} < p_T(V)$		
$W(e\nu)$	$100 < p_T(V) < 130 \mathrm{GeV}$	$130 < p_T(V) < 180 \mathrm{GeV}$	$180\mathrm{GeV} < p_T(V)$		
$Z(\mu\mu)$	$50 < p_T(V) < 100 \text{GeV}$	_	$100\mathrm{GeV} < p_T(V)$		
Z(ee)	$50 < p_T(V) < 100 \text{GeV}$	_	$100\mathrm{GeV} < p_T(V)$		
$Z(\nu\nu)$	$100 < E_T^{\text{miss}} < 130 \text{GeV}$	$130 < E_T^{\rm miss} < 170{\rm GeV}$	$170\mathrm{GeV} < E_T^{\mathrm{miss}}$		
up to thre	sive decay channels in the pro e event categories depending of son resulted in 14 exclusive ev	on the transverse momentum			

**Table 4.4** Main event categorization used in the search for the SM Higgs boson in the  $H \to b\bar{b}$ decay channel

channels and in all event categories. In the low boost event category in the  $Z \to \ell\ell$ decay channels in addition the invariant dijet mass was required to be  $40 \,\mathrm{GeV} < m_{ii}$ .

In the final analysis step all selected events in all decay channels and boost categories were further categorized according to a set of BDT classifiers, exploiting various differences in event kinematics and topology between the VH signal events and all individual background processes. Input variables to these BDT classifiers were the invariant mass of the dijet system, the transverse momenta of the selected jets, the probability for these jets to originate from a b-quark, according to the value of the b-quark discriminator, several angles of the jets, distances in angular space between the jets and the number of additional jets in the event. From these input variables three individual BDT classifiers were trained to separate the signal from the three most important backgrounds of  $t\bar{t}$ , V + jets and VV events. All events were passed through the first BDT classifier to separate the signal from  $t\bar{t}$  events. Those events, which failed the selection based on this BDT were classified as enriched by this background process. Those events that passed the selection were successively passed on to the BDT classifiers to separate the signal from the V + jets and VVevents. Events, which failed the selection based on these BDTs were classified as enriched in these background processes accordingly. Those events that passed all three BDT selections were classified as enriched in VH signal events. In this way four event classes were formed in addition to the separation in decay channels and boost categories. These four event classes were then individually passed on to a final BDT classifier, which was optimized to discriminate the VH signal from all backgrounds. This further event categorization had been found to increase the sensitivity of the analysis by 5-10%, relative to the single BDT discrimination. It has not been applied in the  $Z \to \ell\ell$  channels, were no such improvement was observed nor in the  $W \to \tau \nu$  channel, where the number of simulated events was too small to allow for a separate training of more than one BDT. This further separation effectively increased the number of event categories on the dataset of 2012 from 14 to 41.

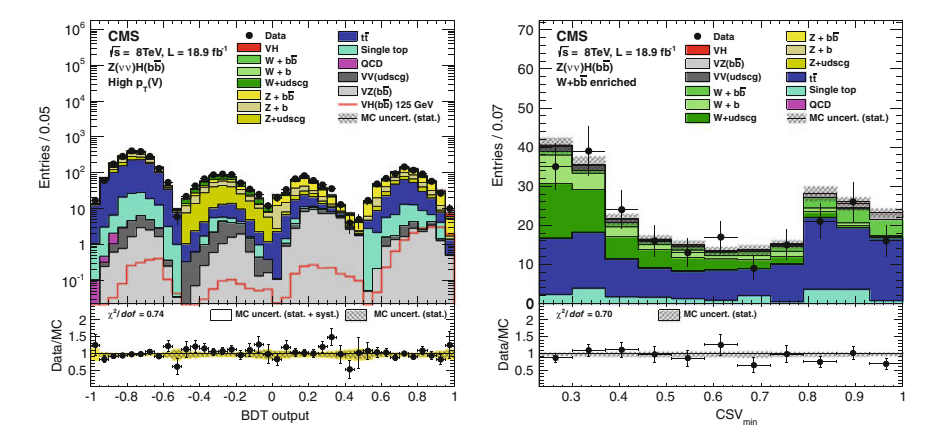


**Fig. 4.27** (Right) Output of the multivariate discriminator (labeled as "BDT output") in the  $Z \to \nu \nu$  decay channel and the high  $p_T(V)$  event category as defined in Table 4.4 and (left) output of the probability for a reconstructed jet to originate from the hadronization of a b-quark (labeled as "CSV<sub>min</sub>"), in a control region which has been defined to test the normalization of the background from W boson production in association with one or two b-quarks, in the same decay channel [31]. In both cases the template distributions for the individual background processes have been fitted to the data, within their uncertainties

A typical shape of the final BDT classifier output, for the  $Z \to \nu \nu$  high  $p_T(V)$ event category in the 8TeV dataset is shown in Fig. 4.27 (left), where the classification into the  $t\bar{t}$  enriched, V + jets enriched, VV enriched and signal enriched sub-categories has been visualized in one final discriminant by rescaling and shifting the value of the output discriminant of the final BDT classifier accordingly. The subset of  $t\bar{t}$  enriched events is visible in the most to the left part of the distribution, followed by the V + jets enriched and the VV enriched subset of events to the right. The VH signal enriched subset of events is shown in the most to the right part of the distribution. The black points with error bars correspond to the data. The expectation from the simulation, has been split into the most important background processes and is shown by filled histograms in different colors. Via the color coding a transition in the expected event composition can be seen from blue (i.e.  $t\bar{t}$ ), via yellow and green (i.e. V + jets) to gray (i.e. VV) according to the event sub-categorization. The VHsignal is shown as an additional red histogram on top of all expected background events and for better visibility once again as a red open line in addition to the stacked histograms. In the lower panel of the figure the ratio of data over the expected number of events by the simulation is shown, which demonstrates the good understanding of the data across all sub-categories. The yellow band centered around one in the lower panel corresponds to the systematic uncertainty that has been assigned for the final signal extraction and further inference.

The normalization of each of the background processes shown in the Fig. 4.27 (left) has been crosschecked and if necessary corrected by scale factors according to the findings in several dedicated sideband regions, in which each corresponding

background had been enriched. For this purpose the simulated event samples for the production of vector bosons in association with jets had been split in samples with jets originating from b-quarks and samples with jets originating from light quarks. The scale factors had then been determined for each event category by template fits to the b-quark identification discriminant of the jets identified to be initiated by b-quarks with the second highest score, indicated by  $CSV_{min}$ . A typical distribution of this discriminant in the  $W+b(\bar{b})$ -quark enriched control region in the  $Z\to\nu\nu$  decay channel is shown in Fig. 4.27 (right). The black points with error bars correspond to the data and the filled histograms in different colors to the expected number of events from different background processes. As can be seen from the expected event composition, events with W bosons and one or two b-quark induced jets are indeed enriched in this control region. It can also be seen that the data points in this quantity are well reproduced by the expectation from the simulated events, demonstrating the good understanding of the data.

In Fig. 4.27 (left) a clear ordering of bins by S/B is visible with the bin with the largest value of S/B on the right side of the distribution. A histogram, where all bins from all channels and event categories have been filled according to their expected value of  $\log(S/B)$  is shown in Fig. 4.28 (left). For this figure all backgrounds have been combined into one histogram, shown in pale gray. The most sensitive bin in this distribution is shown on the right (with  $S/B \approx 1$ ). The statistical inference led to a signal scale factor of  $\hat{\mu} = 1.0 \pm 0.5$  and an observed (expected) significance for  $m_H = 125\,\text{GeV}$  of  $2.1\sigma$  (2.1 $\sigma$ ).

By the time of the publication the  $gg \to ZH$  contribution to the ZH signal processes, which became available at NLO accuracy and as a function of  $p_T(Z)$  only afterwards [46–49], had not yet been taken into account in the statistical inference.

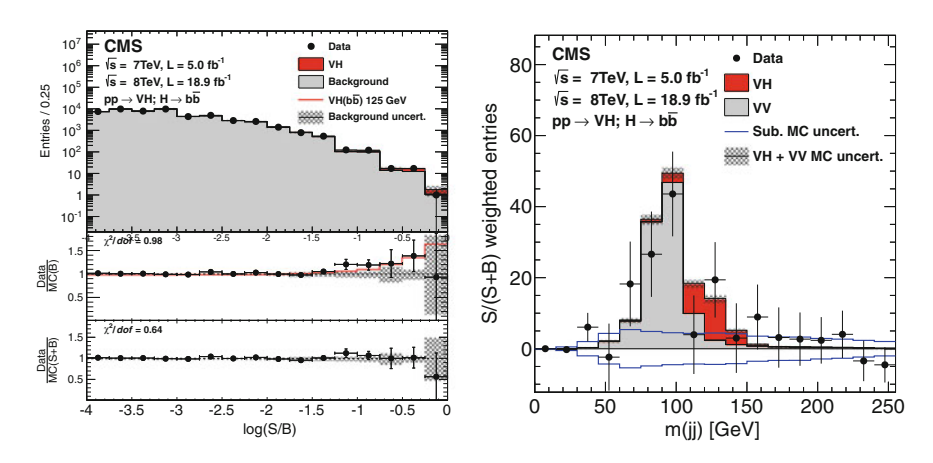


**Fig. 4.28** (*Left*) Distribution of  $\log(S/B)$  for the events in all event (sub-)categories and decay channels and (*right*) the invariant dijet mass,  $m_{jj}$ , for the events summed over all event categories (without further splitting in sub-categories) and decay channels, where all expected backgrounds apart from diboson production have been subtracted [31]

In the  $Z(\nu\nu)H$  and  $Z(\ell\ell)H$  channels, the addition of this process led to an increase of the expected signal yields between 10% for  $p_T(Z) \approx 150\,\mathrm{GeV}$  and 30% for  $p_T(Z) > 150\,\mathrm{GeV}$ . When combined with the unchanged WH channels, the overall expected sensitivity for VH production in the  $H\to b\bar{b}$  decay channel of the SM Higgs boson increased by about 20% leading to an observed (expected) significance of  $2.1\sigma$  ( $2.5\sigma$ ) for  $m_H=125\,\mathrm{GeV}$  corresponding to a most probable value of  $\hat{\mu}=0.84\pm0.44$ . Despite all the analysis effort the significance of the excess is still small, corresponding to a p-value of  $\approx 0.02$ . This resembles the difficulty to extract the signal, which compared to the bosonic decay channels is expected to be sizable, from a much larger, nearly overwhelming background of events, with a comparable signature. As a function of  $m_H$  the highest significance can be found for a value of  $m_H \approx 125\,\mathrm{GeV}$ , while this minimum in the range of  $110 < m_H < 135\,\mathrm{GeV}$ , where this decay channel is sensitive, is very shallow. This corresponds to the resolution of  $\delta m_{bb}/m_{bb} \approx 10\%$ .

The BDT based approach has been validated using WZ and ZZ events, with the subsequent  $Z \to bb$  decay as signal process, instead of VH production, as discussed at the beginning of this section. For this validation the VH signal as expected for a SM Higgs boson with  $m_H = 125 \,\text{GeV}$  had been treated as an additional background. Within this validation procedure the signal for diboson production with the subsequent  $Z \to b\bar{b}$  decay, could be established with a significance of  $7\sigma$  and with a signal strength scale factor of  $\hat{\mu}_{VV} = 1.19 \pm 0.28_{0.23}^{0.28}$ , confirming the potential of the analysis to establish a discovery and at the same time confirming the consistent determination of the scale factors for vector boson production in association with bquark induced jets, from the control regions. As a crosscheck an alternative analysis had been performed, which was only based on the invariant mass of the selected dijet system,  $m_{bb}$ . In Fig. 4.28 (right), the distribution of  $m_{bb}$  is shown summed over the events in all channels and event categories (without sub-categorization), and weighted by the S/(S+B) value determined in each event category. From this distribution all expected background processes but diboson production have been subtracted. The data are consistent with a signal from diboson production with the subsequent  $Z \to bb$  decay and a normalization as determined in the main analysis with a small additional excess consistent with the signal of a SM Higgs boson with  $m_H = 125 \,\mathrm{GeV}$ , which is indicated by the red histogram in the figure. For the VHsignal a scale factor consistent with the main analysis was found corresponding to a significance of  $1.1\sigma$  for a SM Higgs boson signal with  $m_H = 125 \,\text{GeV}$ . This crosscheck demonstrates the gain obtained by the much more complex main analysis based on the multivariate discriminator and the increased number of event categories.

Compared to the analysis as published by the time of the discovery, the  $W(\tau\nu)H$  decay channel had been added, the main event categorization had been extended and the event sub-categorization in the  $W(\ell\nu)H$  and  $Z(\nu\nu)H$  decay channel had been introduced as described in the text.

#### **Top Quarks**

Since for  $m_H \lesssim 350 \,\text{GeV}$  the decay into *top* quark pairs is energetically not allowed the *top* quark is out of scope, when discussing decay channels. Assuming the SM

the coupling to the top quark is indirectly constraint from its dominant contribution to the gluon fusion production mode  $(gg \rightarrow H)$  and its contribution to the decay into photons  $(H \rightarrow \gamma \gamma)$ , which both would lead to significant deviations from the predicted event yields if the coupling to the top quark were very different from the expectation of the SM. A model independent estimate of the tree-level coupling of the Higgs boson to the top quark can be obtained via the production mode, in association with top quark pairs  $(t\bar{t}H)$ , as shown in Fig. 4.8 (lower right), which can be inclusively analyzed in all decay channels. From Table 4.1 (left) it is obvious that this production mode, which contributes to less than 1% to the total production cross section for  $m_H = 125$  GeV, according to the expectation by the SM, will be difficult to access within the statistical precision of the LHC run-1 dataset of the years 2011 and 2012.

Nonetheless the search has been conducted with the CMS experiment with a publication based on all main decay channels that have been discussed before [50]. Since the emphasize in this analysis was on a high efficiency and a pure selection of the production mode the analysis started off from the selection of the typical topology for top quark pair production in addition to a Higgs boson. Since the top quark nearly exclusively decays into b-quarks via the emission of a real W boson, top quark pair production is characterized by the presence of two b-quark induced jets and the decay products of the W bosons in the final state: (i) when both W bosons decay into quarks the decay is classified as "all hadronic", with six jets in the detector, of which two originate from a b-quark; (ii) the channel, where one of the W bosons decays leptonically is referred to as "lepton plus jets" decay channel, with an isolated high  $p_T$  lepton, moderate  $E_T^{\text{miss}}$  and four jets, of which two originate from a b-quark; (iii) the decay channel where both W bosons decay leptonically is referred to as "dilepton" channel, with two isolated high  $p_T$  leptons, high  $E_T^{\text{miss}}$ and two jets originating from a b-quark. All three of these signatures had been used in the analysis. The selection of the decay channel of the Higgs boson candidate on the other hand had been chosen to be very loose and, with the exception of the diphoton final state not too channel specific. Instead the events had been grouped into three main categories according to generic inclusive decays of the Higgs boson candidate into hadrons, leptons or photons. These main event categories are expected to have a different population of specific decay channels as lined out in Table 4.5. The  $H \to \gamma \gamma$  event category forms the only exception of this inclusive treatment of the decay channels due to its distinct signature and the high resolution of  $m_{\gamma\gamma}$ , in this decay channel, which has also been used for signal extraction as will be discussed below.

Each main event category had been split into further sub-categories according to the decay channel of the  $t\bar{t}$  system and the Higgs boson candidate. The  $H\to$  hadrons sub-categories were then further split according to the number of reconstructed jets and the number of jets identified as originating from a b-quark, resulting in seven final event classes in the  $H\to$  hadrons ( $\ell$  + jet) sub-category, three event classes in the  $\ell$  hadrons ( $\ell$  + jet) sub-category and six event classes in the  $\ell$  hadrons (hadronic  $\ell$ ) sub-category on the 8 TeV dataset. The  $\ell$  hadrons ( $\ell$  + jet) sub-category was further split into an  $\ell$  hadron and  $\ell$  class according to the flavor of the

	association with a top quark pair (trii)								
		$H \rightarrow \text{hadrons}$			$H \rightarrow \gamma \gamma$		$H \rightarrow \text{leptons}$		
		$\ell$ + jets	2\ell	Hadronic $\tau$	Leptonic	Hadronic	$\ell^{\pm}\ell^{\pm}$	$3\ell$	4ℓ
	H decay	bb		$\tau \tau / W W$	$\gamma\gamma$		$\tau \tau / WW$ $ZZ$		ZZ
1	$t\bar{t}$ decay	$\ell \nu j j$	$\ell \nu \ell \nu$	$\ell \nu j j$	$\ell \nu \ell \nu / j j$	jjjj	$\ell \nu j j$		$\ell \nu \ell \nu$

**Table 4.5** Event categorization for the inclusive analysis in the Higgs boson production mode in association with a *top* quark pair  $(t\bar{t}H)$ 

The inclusive main categories are indicated in the first, the sub-categories in the second line. The third and fourth line indicate the decay channels of the Higgs boson and of the  $t\bar{t}$  pair that are expected to contribute to each corresponding event (sub-)category. In the  $H\to$  hadrons event category fully hadronic  $\tau\tau/WW$  decays are subsumed, the  $H\to$  leptons event category is supposed to contain all (semi-)leptonic  $\tau\tau/WW$  decays. Each sub-category was further split into another set of classes resulting in 23 event classes on the 8 TeV dataset

leptons in the decay. The full characterization of the selected events thus spanned over 23 final event classes on the 8 TeV dataset. Finally, all event classes based on the 8 TeV dataset had been combined with one further event category based on the 7 TeV dataset in the  $H \to \gamma \gamma$  category and with the search for the SM Higgs boson in the  $t\bar{t}H$  production mode in the  $H \to b\bar{b}$  and  $H \to \tau \tau$  decay channels based on the 7 TeV dataset as published in [51].

The  $H\to \tau\tau$  and the  $H\to WW$  decay channels are the most difficult to separate from each other. These decay channels are mostly located in the  $H\to$  hadrons (hadronic  $\tau$ ) and  $H\to$  leptons  $(\ell^\pm\ell^\pm)$  and  $(3\ell)$  event categories: the  $H\to$  hadrons (hadronic  $\tau$ ) event sub-category is expected to be equally populated by Higgs boson events in the  $H\to \tau\tau$  decay channel, where both  $\tau$ -leptons decay hadronically, and Higgs boson events in the  $H\to WW$  decay channel, in the subsequent  $W\to \tau\nu$  decay, where the  $\tau$ -lepton decays into hadrons. The  $H\to$  leptons  $\ell^\pm\ell^\pm$  and  $3\ell$  sub-categories are expected to be populated by Higgs boson events in the decay channels, where at least one  $\tau$ -lepton or W boson ( $\ell^\pm\ell^\pm$ ), or both  $\tau$ -leptons or W bosons ( $\ell^\pm\ell^\pm$ ) decay leptonically, in each of these cases in the  $\ell^\pm\ell^\pm$  decay channel of the  $\ell^\pm\ell^\pm$  system. The dominant background contribution mostly originates from  $\ell^\pm\ell^\pm$  production in association with additional jets originating from light flavor,  $\ell^\pm\ell^\pm$ 0 or  $\ell^\pm\ell^\pm$ 1 pairs in association with vector bosons.

In the  $H \to \gamma \gamma$  sub-categories,  $m_{\gamma \gamma}$  had been used to extract the signal on top of the background. In these categories, care had to be taken to separate the actual  $t\bar{t}H$  signal from Higgs boson events originating from other production modes, which contribute to the same peak in  $m_{\gamma \gamma}$ . In the  $H \to$  hadrons and the  $H \to$  leptons decay channels the separation between signal and backgrounds was achieved by training multivariate BDT discriminators in each category, usually based on  $\mathcal{O}(10-15)$  discriminating variables, resembling the kinematics of the process, the probabilities of the reconstructed jets to originate from a b-quark and the specific topology of the events. These discriminators were trained with simulated  $t\bar{t}H$  events with  $m_H = 125\,\text{GeV}$  as signal and simulated  $t\bar{t}$  events in association with additional jets as background. The simulation had been checked to represent the shape and correlations of the input variables as observed in data using various dedicated control

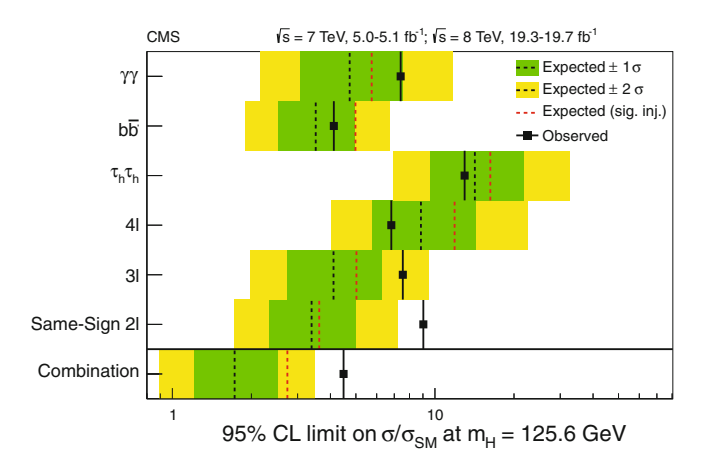


Fig. 4.29 Observed and expected 95 % CL upper limits for the production of the SM Higgs boson in association with a *top* quark pair  $(t\bar{t}H)$  [50]. The limit is shown split by the main sub-categories as discussed in the text and given in Table 4.5 and in the combination of all event categories (*bottom line*). The  $H \to \text{hadrons}$  ( $\ell + \text{jet}$ ) and  $(2\ell)$  sub-categories have been combined into one category labeled by " $b\bar{b}$ ", the  $H \to \text{hadrons}$  (hadronic  $\tau$ ) event category is labeled by " $\tau_h \tau_h$ " in the figure

regions and correction factors had been derived and applied to improve the simulation where necessary. For this purpose the background simulation had been split in the individual contributions from  $t\bar{t}$  production in association with additional jets originating from light flavor, c- and b-quarks, to be able to address the different levels of uncertainty associated to each of these background production channels individually. In the  $H \to \text{leptons}\ (4\ell)$  category the jet multiplicity, N(jet) was used to extract the signal due to the limited number of simulated events, which did not allow to train a dedicated BDT for signal extraction. In this sub-category only one event, with three additional jets, had been found after the final selection.

For the statistical inference, 95% CL limits were set using the test statistic as given in Eq. (4.1). Input distributions to this analysis were the distributions of the BDT discriminants or N(jet) in the  $H \to \text{hadrons}$  and  $H \to \text{leptons}$  sub-categories and  $m_{\gamma\gamma}$  in the  $H \to \gamma\gamma$  sub-categories. The resulting limit is shown in Fig. 4.29, where the limits are shown split by event sub-categories and in the combination of all events, in the different rows. The black points correspond to the observed limits, while the black dashed lines with the dark green and bright yellow bands correspond to the median and the 68 and 95% quantiles of the expected exclusion limits based on the b-hypothesis. The red dashed line indicates the median of the expected limits in the presence of a SM Higgs boson with  $m_H = 125\,\text{GeV}$ . In the figure, the  $H \to \text{hadrons}$  ( $\ell + \text{jet}$ ) and ( $2\ell$ ) sub-categories have been combined into one event sub-category labeled by " $b\bar{b}$ ", the  $H \to \text{hadrons}$  (hadronic  $\tau$ ) sub-category has been labeled by " $\tau_h \tau_h$ ".

For the combination of all event classes the observed (expected) limit is  $4.5 \times \sigma_{\text{SM}}$  (1.7 ×  $\sigma_{\text{SM}}$ ). The expected limit in the presence of a SM Higgs boson with  $m_H =$ 

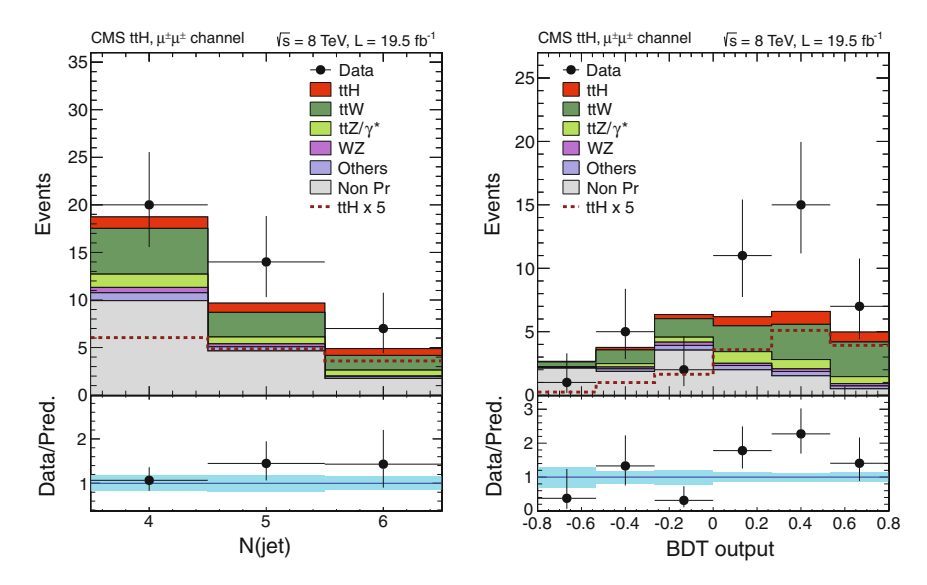


Fig. 4.30 (*Left*) jet multiplicity, N(jet), and (*right*) BDT output in the  $H \to \text{leptons } \mu^{\pm}\mu^{\pm}$  event category, which is driving the excess of the observed over the expected limit in the statistical inference in the inclusive search for  $t\bar{t}H$  production [50]

125 GeV is  $2.7 \times \sigma_{SM}$ . The expected limit based on the b-hypothesis leads to the conclusion that the sensitivity to observe the SM Higgs boson in the  $t\bar{t}H$  production mode has not been reached, yet. The high observed limit with respect to the expected limit (based on the b-hypothesis) corresponds to an excess of  $3.4\sigma$  (equivalent to a p-value of 0.04 %) for an expected significance of 1.2 $\sigma$ . With respect to the expected limit in the presence of a SM Higgs boson at  $m_H = 125 \,\mathrm{GeV}$  it corresponds to an upward fluctuation of  $2.1\sigma$  (equivalent to a p-value of 2.0%). The observed limit corresponds to a signal strength value of  $\hat{\mu} = 2.8 \pm ^{1.0}_{0.9}$ . This excess is driven by the  $H \to \text{leptons } (\ell^{\pm}\ell^{\pm}) \text{ and } (3\ell) \text{ sub-categories with the largest excess over the } b$ hypothesis in the  $H \to \text{leptons} (\mu^{\pm} \mu^{\pm})$  event class. The jet multiplicity, N(jet) and the output of the BDT discriminant as used for the statistical inference in this event class are shown in Fig. 4.30. The black points with the error bars correspond to the data. The filled histograms in different colors to the expectation from all expected backgrounds and the  $t\bar{t}H$  signal. Also shown is the  $t\bar{t}H$  signal  $\times 5$  as an extra red dashed histogram, to allow shape comparisons. In the lower parts of the figures the ratio of the data points over the expected event yields is shown, where the bright cyan colored band around 1 corresponds to the systematic uncertainty of the background expectation. A slight broad excess is visible across N(jet), which appears more localized in the signal region in the BDT distribution. The figure also shows, that this excess is based on only a hand full of events. While the excess is driven in the same charge  $\mu\mu$  event class in fact it builds up across more event classes, also in the (3 $\ell$ ) and  $(\gamma\gamma)$  sub-categories as visible from Fig. 4.29. The compatibility of the  $H\to$  leptons  $(\mu^{\pm}\mu^{\pm})$   $(\hat{\mu} = 8.5 \pm \frac{3.3}{2.7}), (e^{\pm}e^{\pm})$   $(\hat{\mu} = 2.7 \pm \frac{4.6}{4.1}), (e^{\pm}\mu^{\pm})$   $(\hat{\mu} = 1.8 \pm \frac{2.5}{2.3}), (3\ell)$  and  $(4\ell)$ 

event sub-classes was found to be 16%. The compatibility of the results in the six independent event classes shown in Fig. 4.29 was found to be 29%. Several tests had been made to assure that the excess is not due to a mis-measurement or mistake in the analysis. According to these tests the excess is still well compatible with a statistical fluctuation. The increased datasets of the upcoming data taking periods of the *LHC* will shed more light on this question.

## 4.4.3 Conclusions on the Coupling to Fermions

The observed significances, in each of the three fermionic couplings, which are accessible at the LHC are summarized in Table 4.6. The results of the ATLAS collaboration are given in the upper part of the table and the results of the CMS collaboration in the lower part. All significances are given for  $m_H = 125 \,\mathrm{GeV}$ , while their sensitivity to the exact value of  $m_H$  is much lower than in the case of the bosonic decay channels. For the  $H \to b\bar{b}$  decay channel in the case of both collaborations the values are given including the  $gg \rightarrow ZH$  contribution to the ZH production mode as discussed for the CMS analysis in Sect. 4.4.2. The expected significance, as a measure of the sensitivity of each analysis to establish the signal is also given in braces. The significances given for 10 fb<sup>-1</sup> correspond to the values that had been published, based on the dataset collected by the time of the discovery announcement, on 4 July 2012. By the time of the discovery there was no dedicated analysis, yet, for a direct test of the tree-level Yukawa coupling to top quarks via Higgs boson production in association with top quark pairs  $(t\bar{t}H)$  from neither of the experiments. Also the Higgs boson discovery announcement by the ATLAS collaboration had only been based on the bosonic decay channels, which is why no results for the coupling to fermions from the ATLAS collaboration are available from that time. In the analysis of the  $H \to \tau \tau$  decay channel of the CMS collaboration no excess had been

**Table 4.6** Significance and most probable value of the signal strength parameter  $\mu$ , for the decay channels into fermions, as published by the *ATLAS* and *CMS* collaboration, based on the dataset of  $10\,\mathrm{fb}^{-1}$ , that had been collected by the time of the discovery announcement at 4 July 2012, and based on the final dataset corresponding to  $25\,\mathrm{fb}^{-1}$ 

		$10{\rm fb}^{-1}$		$25  {\rm fb}^{-1}$	$25  \text{fb}^{-1}$	
			Significance $(\sigma)$		Significance $(\sigma)$	
ATLAS	$H \to \tau \tau$	_		4.5(3.4)	[52]	$1.43 \pm 0.40$
	$H  o b ar{b}$	_		1.4(2.6)	[53]	$0.52 \pm 0.40$
	$t\bar{t}H(\gamma\gamma)$	_		_	[54]	$1.30 \pm 2.20$
CMS	$H \to \tau \tau$	-(1.4)	[25]	3.2(3.7)	[30]	$0.78 \pm 0.27$
	$H  o b ar{b}$	0.7(1.9)	[25]	2.1(2.5)	[31]	$0.84 \pm 0.44$
	$t\bar{t}H$	_		3.4(1.2)	[50]	$2.80 \pm 0.95$

The values in braces correspond to the expected significance, indicating the sensitivity of the corresponding analyses to establish the signal. All values are given for a SM Higgs boson with  $m_H=125\,\mathrm{GeV}$ 

observed, for an expected significance of  $1.4\sigma$  in the presence of a SM Higgs boson with  $m_H = 125$  GeV, which is why this number had also not been reported. In spring 2013 the  $H \to \tau\tau$  channel was the first single decay channel into fermions, in which the evidence of the direct coupling of the Higgs boson to fermions could be established with a significance of  $>3\sigma$ . This was one of the main results and major achievements of the *LHC* experiments in the year after the discovery.

The significances and values of  $\hat{\mu}$  given for 25 fb<sup>-1</sup> correspond to the final analyses on the full *LHC* run-1 dataset of the years 2011 and 2012. For the *CMS* collaboration these results correspond to the analyses as discussed in the previous sections. In addition to the values given in the table 95 % CL upper limits had been set of  $BR(H \to \mu\mu) \leq 0.0016$  and  $BR(H \to ee) \leq 0.0019$ . Since the branching fraction of the Higgs boson to  $\tau$ -leptons has been found to be consistent with the expectation of the SM, corresponding to  $BR(H \to \tau\tau) = 0.0637$  ( $\approx$ 40 times larger than the limit, that has been set on  $BR(H \to \mu\mu)$ ) this is the first manifest evidence that the coupling of the Higgs boson to leptons, in contrast to the gauge couplings is not universal across the lepton flavor generations.

Determining the coupling to quarks still remained challenging mostly due to the difficulty to separate the signal from the overwhelming background of QCD multijet production and the production of top quark pairs in association with additional jets. In the Higgs boson production mode in association with top quark pairs an analysis which was inclusive in all decay channels reached a sensitivity to exclude the signal in this production mode up to a cross section of 1.7  $\times \sigma_{SM}$ , or alternatively to establish it with a significance of  $1.2\sigma$ , assuming the couplings to the other fermions and bosons as predicted by the SM. Indeed an excess of signal events had been observed, which formed in event classes with more than one lepton. This excess corresponds to a significance of  $3.4\sigma$  over the b-hypothesis and  $2.1\sigma$  over the (s+b)hypothesis for a SM Higgs boson with  $m_H = 125$  GeV, corresponding to a p-value of 2% for the (s + b)-hypothesis. An analysis searching for the production of Higgs bosons in association with top quark pairs has also been published by the ATLAS collaboration, but this analysis only covers the  $H \to \gamma \gamma$  decay channel and therefore is less sensitive. This analysis has obtained a value of  $\hat{\mu} = 1.3 \pm 2.2$  and an observed (expected) 95 % CL upper limit of  $6.7 \times \sigma_{SM}$  (4.9 ×  $\sigma_{SM}$ ). The corresponding values of the CMS result restricted to the  $H \to \gamma \gamma$  event classes is  $\hat{\mu} = 2.7 \pm 2.2$  with an observed (expected) 95 % CL upper limit of  $7.4 \times \sigma_{SM}$  (4.7 ×  $\sigma_{SM}$ ) (corresponding to the first row of Fig. 4.29).

All reported values of  $\hat{\mu}$ , in the fermionic decay channels, are compatible with each other and with the expectation from the SM within their uncertainties with a value  $\chi^2_{\text{ATLAS}}/ndf = 2.5/3$ , corresponding to a  $\chi^2$  probability of 36%, for the results obtained by the *ATLAS* collaboration and  $\chi^2_{\text{CMS}}/ndf = 4.39/3$ , corresponding to a  $\chi^2$  probability of 23% for the results obtained by the *CMS* collaboration. For all reported values across both experiments the compatibility with the SM is  $\chi^2_{\text{LHC}}/ndf = 6.89/6$ , corresponding to a  $\chi^2$  probability of 28%. Ignoring all correlations across uncertainties the weighted mean of the individual values of  $\hat{\mu}$  results in a value of  $\langle \hat{\mu} \rangle_{\text{ATLAS}} = 0.96 \pm 0.28$  for the results obtained by the *ATLAS* collaboration and  $\langle \hat{\mu} \rangle_{\text{CMS}} = 0.91 \pm 0.22$  for the results obtained by the *CMS* collaboration.

The weighted mean across both experiments results in a value of  $\langle \hat{\mu} \rangle_{LHC} = 0.93 \pm 0.18$ . The comparison with the uncertainties in the bosonic decay channels illustrates how much more challenging the analyses in the fermionic decay channels are due to the more challenging signal and background separation.

The weighted mean of the individual  $\hat{\mu}$  values for all bosonic and all fermionic decay channel is  $\langle \hat{\mu} \rangle_{\rm ALAS} = 1.12 \pm 0.13$  for the results obtained by the *ALTAS* collaboration,  $\langle \hat{\mu} \rangle_{\rm CMS} = 0.95 \pm 0.12$  for the results obtained by the *CMS* collaboration and  $\langle \hat{\mu} \rangle_{\rm LHC} = 1.03 \pm 0.09$  when combining the results of both experiments. A more detailed analysis of the signal strengths obtained from the combination of all decay channels of the *CMS* analyses taking all correlations into account will be given in Chap. 5. The comparison of the weighted mean with this result indicates the importance of a correct treatment of all correlated uncertainties in the likelihood analyses.

The exciting LHC data taking period of the years 2011 and 2012 concluded with the clear discovery of a new particle in the bosonic decay channels and a convincing evidence of the coupling of the new particle to fermions driven by the analysis in the  $H \to \tau \tau$  decay channel. In the combination with the results from the  $H \to bb$  decay channel of the CMS collaboration this evidence has been reported in the Nature Physics Journal [55]. The physics results of this timespan of the SM Higgs boson search were a tremendous success of all participants in the areas of the accelerator, experiments and theory. The tree-level Yukawa coupling to the top quark was furthermore probed in the  $t\bar{t}H$  production mode. The preceding discussion has shown that the analysis of the fermionic decay channels of the Higgs boson is more challenging than it is the case for the bosonic decay channels. The full exploration of the fermionic decay channels has still been left to the upcoming data taking periods from 2015 on. The evidence of the new particle in all analyzed production modes and nearly all decay channels already now allowed for an impressive first check of the properties of the new particle, based on the LHC run-1 dataset, which gives an impression of how much information will be extracted from the increased datasets in the upcoming data taking periods. The first checks already allowed to conclude that the observed particle is not only a boson, but a Higgs boson. All what is known about its properties will be discussed in the following chapter.

#### References

- 1. H1 and ZEUS Collaboration, Combined measurement and QCD analysis of the inclusive  $e^{+/-}p$  scattering cross sections at HERA. JHEP **1001**, 109 (2010). arXiv:0911.0884
- J.C. Collins, D.E. Soper, G.F. Sterman, Factorization of hard processes in QCD. Adv. Ser. Direct. High Energy Phys. 5, 1–91 (1988). arXiv:hep-ph/0409313
- ATLAS Collaboration, The ATLAS experiment at the CERN large hadron collider. JINST 3, S08003 (2008)
- 4. CMS Collaboration, The CMS experiment at the CERN LHC. JINST 3, S08004 (2008)
- CMS Collaboration, Particle-flow event reconstruction in CMS and performance for Jets, Taus, and MET. Technical report CMS-PAS-PFT-09-001, CERN, Geneva, April 2009

References 149

 CMS Collaboration, Commissioning of the particle-flow reconstruction in minimum-bias and jet events from pp collisions at 7 TeV. Technical report CMS-PAS-PFT-10-002, CERN, Geneva (2010)

- 7. CMS, Performance of CMS muon reconstruction in pp collision events at  $\sqrt{s}=7$  TeV. JINST 7, P10002 (2012). arXiv:1206.4071
- S. Baffioni, C. Charlot, F. Ferri et al., Electron reconstruction in CMS. Eur. Phys. J. C 49, 1099–1116 (2007)
- W. Adam, R. Fruhwirth, A. Strandlie et al., Reconstruction of electrons with the gaussian sum filter in the CMS tracker at LHC. eConf. C0303241, TULT009 (2003). arXiv:physics/0306087
- 10. G.P. Salam, Towards jetography. Eur. Phys. J. C 67, 637–686 (2010). arXiv:0906.1833
- CMS, Determination of jet energy calibration and transverse momentum resolution in CMS. JINST 6, P11002 (2011). arXiv:1107.4277
- CMS Collaboration, https://twiki.cern.ch/twiki/pub/CMSPublic/PhysicsResultsCombined/ SigmaNew\_v3.pdf
- CMS Collaboration, https://twiki.cern.ch/twiki/pub/CMSPublic/PhysicsResultsCombined/ SigmaR v5.pdf
- 14. CMS Collaboration, Measurements of inclusive W and Z cross sections in pp collisions at  $\sqrt{s} = 7$  TeV. JHEP **1101**, 080 (2011), arXiv:1012.2466
- 15. CMS Collaboration, First measurement of the cross section for top-quark pair production in proton-proton collisions at  $\sqrt{s} = 7$  TeV. Phys. Lett. B **695**, 424–443 (2011). arXiv:1010.5994
- 16. CMS Collaboration, Measurement of the *t*-channel single top quark production cross section in pp collisions at  $\sqrt{s} = 7$  TeV. Phys. Rev. Lett. **107**, 091802 (2011). arXiv:1106.3052
- LHC Higgs Cross Section Working Group, S. Dittmaier, C. Mariotti et al., Handbook of LHC Higgs Cross Sections: 1. Inclusive Observables. CERN-2011-002 (CERN, Geneva, 2011). arXiv:1101.0593
- 18. A. Denner, S. Heinemeyer, I. Puljak et al., Standard model Higgs-boson branching ratios with uncertainties. Eur. Phys. J. C 71, 1753 (2011). arXiv:1107.5909
- LHC Higgs Cross Section Working Group, S. Dittmaier, C. Mariotti et al., Handbook of LHC Higgs Cross Sections: 2. Differential Distributions. CERN-2012-002 (CERN, Geneva, 2012). arXiv:1201.3084
- LHC Higgs Cross Section Working Group, Handbook of LHC Higgs Cross Sections: 3. Higgs Properties. arXiv:1307.1347
- 21. ATLAS Collaboration, Combined search for the standard model Higgs boson in pp collisions at  $\sqrt{s} = 7$  TeV with the ATLAS detector. Phys. Rev. D **86**, 032003 (2012). arXiv:1207.0319
- 22. CMS Collaboration, Combined results of searches for the standard model Higgs boson in pp collisions at  $\sqrt{s} = 7$  TeV. Phys. Lett. B **710**, 26–48 (2012). arXiv:1202.1488
- G. Cowan, K. Cranmer, E. Gross et al., Asymptotic formulae for likelihood-based tests of new physics. Eur. Phys. J. C 71, 1554 (2011). arXiv:1007.1727
- 24. ATLAS Collaboration, Observation of a new particle in the search for the standard model Higgs boson with the ATLAS detector at the LHC. Phys. Lett. B 716, 1–29 (2012). arXiv:1207.7214
- 25. CMS Collaboration, Observation of a new boson at a Mass of 125 GeV with the CMS experiment at the LHC. Phys. Lett. B **716**, 30–61 (2012). arXiv:1207.7235
- 26. CMS Collaboration, Observation of a New Boson with mass near 125 GeV in pp collisions at  $\sqrt{s} = 7$  and 8 TeV. JHEP **06**, 081 (2013). arXiv:1303.4571
- CMS Collaboration, Observation of the diphoton decay of the Higgs boson and measurement of its properties. Eur. Phys. J. C 74(10), 3076 (2014). arXiv:1407.0558
- CMS Collaboration, Measurement of the properties of a Higgs boson in the four-lepton final state. Phys. Rev. D 89, 092007 (2014). arXiv:1312.5353
- 29. CMS Collaboration, Measurement of Higgs boson production and properties in the WW decay channel with leptonic final states. JHEP **1401**, 096 (2014). arXiv:1312.1129
- 30. CMS Collaboration, Evidence for the 125 GeV Higgs boson decaying to a pair of  $\tau$  leptons. JHEP **1405**, 104 (2014). arXiv:1401.5041
- 31. CMS Collaboration, Search for the standard model Higgs boson produced in association with a *W* or a *Z* Boson and decaying to bottom quarks. Phys. Rev. D **89**, 012003 (2014). arXiv:1310.3687

- 32. L. Rokach, O. Maimon, *Data Mining with Decision Trees: Theory and Applications* (World Scientific Publishing Company Inc., New York, 2008)
- J.R. Quinlan, Induction of Decision Trees. Machine Learning (Kluwer Academic Publishers, Boston, 1986)
- 34. L. Breiman et al., *Classification and Regression Trees* (Wadsworth & Brooks/Cole Advanced Books & Softwar, Monterey, 1984)
- ATLAS Collaboration, Measurement of Higgs boson production in the diphoton decay channel in pp collisions at center-of-mass energies of 7 and 8 TeV with the ATLAS detector. Phys. Rev. D 90(11), 112015 (2014). arXiv:1408.7084
- ATLAS Collaboration, Measurements of Higgs boson production and couplings in the fourlepton channel in pp Collisions at center-of-mass energies of 7 and 8 TeV with the ATLAS detector, Phys. Rev. D91, 012006 (2015). arXiv:1408.5191
- 37. ATLAS Collaboration, Observation and measurement of Higgs boson decays to WW\* with the ATLAS detector. Submitted to Phys. Rev. D (2014). arXiv:1412.2641
- 38. Particle Data Group, Review of particle physics. Chin. Phys. C38, 090001 (2014). doi:10. 1088/1674-1137/38/9/090001
- 39. CMS, Performance of  $\tau$ -lepton reconstruction and identification in CMS. JINST 7, P01001 (2012). arXiv:1109.6034
- 40. R.K. Ellis, I. Hinchliffe, M. Soldate et al., Higgs decay to  $\tau^+\tau^-$ : a possible signature of intermediate mass Higgs Bosons at the SSC. Nucl. Phys. **B297**, 221 (1988)
- 41. A. Elagin, P. Murat, A. Pranko et al., A new mass reconstruction technique for resonances decaying to Di-τ. Nucl. Instrum. Methods **A654**, 481–489 (2011), arXiv:1012.4686
- N. Davidson, G. Nanava, T. Przedzinski et al., Universal interface of TAUOLA technical and physics documentation. Comput. Phys. Commun. 183, 821–843 (2012). arXiv:1002.0543
- 43. B. Bullock, K. Hagiwara, A.D. Martin, Tau polarization and its correlations as a probe of new physics. Nucl. Phys. **B395**, 499–533 (1993)
- 44. CMS Collaboration, Search for a standard model-like Higgs boson in the  $\mu^+\mu^-$  and  $e^+e^-$  decay channels at the LHC. Submitted to Phys. Lett. B (2014), arXiv:1410.6679
- 45. CMS, Identification of *b*-quark jets with the CMS experiment. JINST **8**, P04013 (2013). arXiv:1211.4462
- L. Altenkamp, S. Dittmaier, R.V. Harlander et al., Gluon-induced Higgs-Strahlung at nextto-leading order QCD. JHEP 1302, 078 (2013). arXiv:1211.5015
- C. Englert, M. McCullough, M. Spannowsky, Gluon-initiated associated production boosts Higgs physics. Phys. Rev. D89(1), 013013 (2014). arXiv:1310.4828
- 48. G. Luisoni, P. Nason, C. Oleari et al., HW<sup>±</sup>/HZ + 0 and 1 jet at NLO with the POWHEG BOX interfaced to GoSam and their merging within MiNLO. JHEP 1310, 083 (2013). arXiv:1306.2542
- G. Ferrera, M. Grazzini, F. Tramontano, Associated ZH production at hadron colliders: the fully differential NNLO QCD calculation. Phys. Lett. B740, 51–55 (2014). arXiv:1407.4747
- 50. CMS Collaboration, Search for the associated production of the Higgs boson with a top-quark pair. JHEP **1409**, 087 (2014). arXiv:1408.1682
- 51. CMS Collaboration, Search for the standard model Higgs boson produced in association with a top-quark pair in *pp* collisions at the LHC. JHEP **1305**, 145 (2013). arXiv:1303.0763
- 52. ATLAS Collaboration, Evidence for the Higgs-boson Yukawa coupling to  $\tau$  leptons with the ATLAS detector. Submitted to JHEP (2015). arXiv:1501.04943
- 53. ATLAS Collaboration, Search for the  $b\bar{b}$  decay of the standard model Higgs boson in associated (W/Z)H production with the ATLAS detector. JHEP **1501**, 069 (2015). arxiv:1409.6212
- 54. ATLAS Collaboration, Search for  $H \to \gamma \gamma$  produced in association with top quarks and constraints on the Yukawa coupling between the top quark and the Higgs boson using data taken at 7 TeV and 8 TeV with the ATLAS detector. Phys. Lett. **B740**, 222–242 (2015). arXiv:1409.3122
- CMS Collaboration, Evidence for the direct decay of the 125 GeV Higgs boson to fermions. Nat. Phys. 10 (2014). arXiv:1401.6527

# **Chapter 5 Properties of the New Particle**

The observations in the main SM Higgs boson decay channels as discussed in Chap. 4 have lead to the following conclusions: (i) the observation in all three bosonic decay channels is consistent with a single particle resonance; (ii) the two bosonic high mass resolution decay channels  $H \to \gamma \gamma$  and  $H \to ZZ$ , pin this mass to a value of  $m_H \approx 125 \, \text{GeV}$ ; (iii) there is an evidence that this new particle couples to fermions, with a coupling strength to b-quarks and  $\tau$ -leptons as expected for a SM Higgs boson with the given mass; (iv) this coupling is non/universal across the lepton generations.

These findings corroborate the discovery of a unique new particle, with properties as expected for a Higgs boson. These properties have been inferred from several comprehensive analyses of the single observations: since a particle with half-integer spin can not decay into two particles with integer spin the bosonic nature of the new particle was already evident from the fact that the discovery had been made in the bosonic decay channels; the mass of the new particle could be measured with an accuracy of a few hundred MeV in the combination of the  $H \to \gamma \gamma$  and  $H \to ZZ$  decay channel; also the decay width and the CP properties of the new particle could be constrained to an unexpected level of accuracy in the further analysis of the few events in the  $H \to ZZ$  decay channel; finally the coupling strength that could be inferred for top quarks, b-quarks,  $\tau$ -leptons, muons, W bosons and Z bosons indicates that the coupling of the new particle increases linearly with the mass of the fermions,  $m_f$ , and quadratically with the mass of the heavy vector bosons,  $m_V$ , that the new particle couples to, as expected for a Higgs boson. These analyses will be discussed in the following sections.

# 5.1 Mass and Decay Width of the New Particle

# 5.1.1 Canonical Estimate of the Mass and Decay Width

In the  $H \to \gamma \gamma$  decay channel the mass of the observed particle is obtained from the distribution of  $m_{\gamma\gamma}$  in all event categories that have been described in Sect. 4.3.1

performing a scan of the likelihood function in a mass range between 123.6 and 125.8 GeV and using the same signal model as for the extraction of the signal strength,  $\mu$ , consisting of several Gaussian distributions with different widths on top of a continuous background distribution [1]. To obtain an unbiased estimate of m<sub>H</sub>, which does not rely on information about the expected signal strength as a function  $m_H$ , or on the expected coupling structure of the new particle, two additional parameters,  $\mu_{VBF,VH}$  and  $\mu_{aaH,t\bar{t}H}$  had been added to the statistical model, allowing those signal processes that involve the coupling to vector bosons or fermions to float independently in the fit. The most probable value of  $m_H$  was found to be  $\hat{m}_H = 124.70 \pm 0.31$  (stat)  $\pm 0.15$  (syst) GeV, where the purely statistical component of the uncertainty had been determined from a likelihood model where the nuisance parameters of all systematic uncertainties had been set to their most probable values and the uncertainties had been removed from the likelihood function. This estimate reveals a mass measurement with an uncertainty of  $\approx 2.5\%$ , which is still dominated by the statistical component. The limit of precision of this measurement given by the systematic uncertainties is at  $\approx 1.2$  %. The systematic uncertainties represent the limited knowledge of residual differences in the energy response for electrons and photons in the ECAL, which appear since the energy response of the ECAL had been validated with  $Z \rightarrow ee$  events; the limited knowledge of the linearity of the photon energy scale; and the residual uncertainties on the calibration of the energy scale and resolution. The most probable values of the two individual signal strength parameters came out to be  $\hat{\mu}_{VBF,VH} = 1.15 \pm ^{0.63}_{0.58}$  and  $\hat{\mu}_{ggH,t\bar{t}H} = 1.13 \pm ^{0.37}_{0.31}$ . When combining both parameters into a single parameter  $\mu$  in the statistical model, this parameter takes the value  $\hat{\mu} = 1.14 \pm \frac{0.26}{0.23}$ , as reported in Sect. 4.3.1 while the value of  $\hat{m}_H$  varies by less than  $1\sigma$  of the estimated uncertainty. The likelihood function for different values of  $m_H$ , as used with two independent parameters  $\hat{\mu}_{VBF,VH}$  and  $\hat{\mu}_{aqH,t\bar{t}H}$  is shown by the blue line in Fig. 5.1 (left) (labeled as " $H \to \gamma \gamma$  tagged").

From the lineshape of the  $m_{\gamma\gamma}$  distributions apart from the exact mass also an estimate on the decay width can be obtained by replacing the Gaussian functions in the signal model by an analytic convolution of a Gaussian function with a common *Breit-Wigner* distribution in each case. In a scan of this likelihood function also the value of  $m_H$  had been left as a free parameter. The likelihood scan had been found to be consistent with  $\Gamma_H=0$  resulting in an observed (expected) 95% CL upper limit of  $\Gamma_H<2.4$  (3.1) GeV, still by a factor of 600 larger than the decay width of 4.04 MeV as expected in the SM.

Also from the  $H \to ZZ$  decay channel the mass of the observed particle is obtained from a dedicated scan of the likelihood function, using all events in all event categories that have been described in Sect. 4.3.2 [3]. For this purpose the factor in the likelihood function of Eq. (4.4) that depends on  $p_T^{4\ell}|m_{4\ell}$  or  $\mathcal{D}_{\rm jet}|m_{4\ell}$  had been replaced by an estimate of the  $m_{4\ell}$  resolution,  $\mathcal{D}_m$ , which can been obtained on a per-event basis from the resolution of each of the leptons. This resolution estimate had been crosschecked with  $Z \to \ell \ell$  events and residual correction factors  $\mathcal{O}(10\%)$ 

had been derived and applied. The likelihood function as used for the measurement of the mass thus took the form

$$\mathcal{L}_{3D}^{\mu} \equiv \mathcal{P}(m_{4\ell}|m_H, \Gamma_H, \mathcal{D}_m) \cdot \mathcal{P}(\mathcal{D}_{\text{bkg}}^{\text{kin}}|m_{4\ell}) \cdot \mathcal{P}(\mathcal{D}_m|m_{4\ell})$$

As in the case of the  $H\to\gamma\gamma$  decay channels the signal strength,  $\mu$ , had been left as a free parameter to remove the dependency of the expected cross section of SM Higgs boson production on  $m_H$ . The scan led to a most probable value of  $\hat{m}_H=125.6\pm^{0.5}_{0.4}$  (stat)  $\pm 0.1$  (syst) GeV, for a value of the signal strength of  $\hat{\mu}=0.93\pm^{0.26}_{0.23}$  (stat)  $\pm^{0.13}_{0.09}$  (syst), where the split in the statistical and systematic part of the uncertainty had been obtained in the same way, as for the  $H\to\gamma\gamma$  decay channel. The systematic uncertainties of the measurement of  $m_H$  in the  $H\to ZZ$  decay channel are dominated by the residual uncertainty of the energy momentum scale of the leptons. As a crosscheck of the method a similar likelihood scan had been applied in the range of the Z boson mass, which lies close to the signal region, obtaining a value of  $\hat{m}_Z=91.1\pm0.1$  GeV, where the uncertainty corresponds to the combined statistical and systematic uncertainty. The result of this scan was found to be well compatible with the world average of the Z boson mass of 91.1876 $\pm$ 0.0021 GeV [4] justifying the method.

The likelihood scan of the  $4\mu$ ,  $2e2\mu$  and 4e final states combined, is shown by the black line in Fig. 5.1 (right). Also shown is the same likelihood scan, setting all nuisances parameters to their best fit values and ignoring the systematic uncertainties, indicated by the dashed black line, which demonstrates that also this measurement is still dominated by the statistical uncertainty. The scan of the same likelihood function

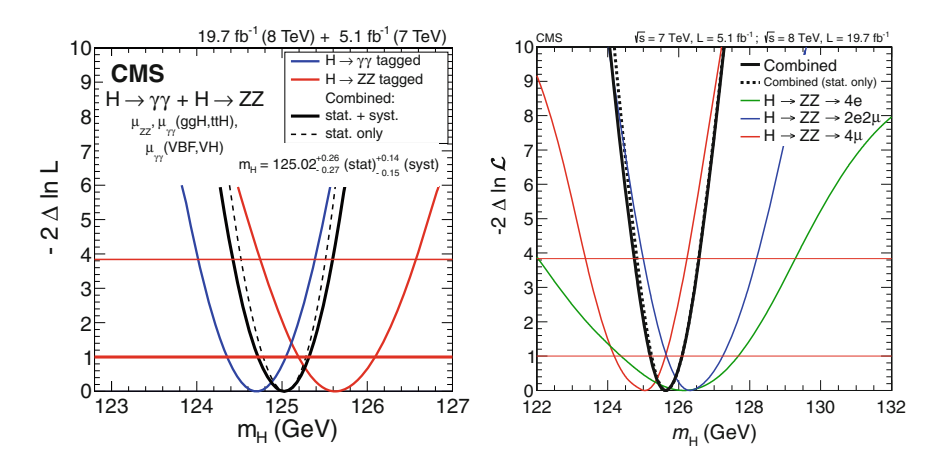


Fig. 5.1 Scans of the likelihood function,  $-2\Delta \ln \mathcal{L}$ , for the measurement of the mass of the new particle at  $m_H \approx 125\,\text{GeV}$ . (*Left*) Likelihood functions from the  $H \to \gamma\gamma$  and  $H \to ZZ$  decay channel and from the statistical combination of both [2] and (*right*) the split of the likelihood function for the mass estimate in the  $H \to ZZ$  decay channel into the  $4\mu$ ,  $2\mu 2e$  and 4e sub-decay channels [3]

for each of the  $H \to ZZ$  final states individually is indicated by the red, blue and green line corresponding to the  $4\mu$ ,  $2e2\mu$  and 4e final state. The obtained values are

$$\hat{m}_{H}^{4\mu} = 125.1 \pm _{0.9}^{0.6} \text{ GeV}$$
 $\hat{m}_{H}^{2e2\mu} = 126.3 \pm _{0.7}^{0.9} \text{ GeV}$ 
 $\hat{m}_{H}^{4e} = 126.2 \pm _{1.8}^{1.5} \text{ GeV}$ 

in each sub-decay channel, where the uncertainties correspond to the combined statistical and systematic uncertainties. Good compatibility within the uncertainties is observed between each of the values of  $\hat{m}_H^X$ . A scan of the likelihood function versus the decay width,  $\Gamma_H$ , leaving the signal strength,  $\mu$  and the mass,  $m_H$ , as additional free parameters led to results that were compatible with  $\Gamma_H=0$  with an observed (expected) 95% CL upper limit of  $\Gamma_H<3.4$  (2.8) GeV, again three orders of magnitude larger than the expected decay width for the SM Higgs boson at  $m_H=125\,\text{GeV}$ .

Naively adding statistical and systematic uncertainties of the two measurements quadratically, thus treating all systematic uncertainties as uncorrelated shows that the two results are compatible with each other within  $1.6\sigma$ . The same result can be obtained from a combined likelihood analysis, using the difference  $m_H^{\gamma\gamma}-m_H^{4\ell}$ as parameter of interest and taking all correlations between the two measurements fully into account. This demonstrates the validity of the assumption that these two measurements are uncorrelated. It is supported by the fact that both measurements are still dominated by the statistical uncertainty. An obvious source of correlation between  $m_H^{\gamma\gamma}$  and  $m_H^{4\ell}$  comes to mind in the  $H\to ZZ\to 4e$  and  $2e2\mu$  final states via the residual uncertainty of the calibration of the ECAL. The weighted mean of the two mass measurements leads to a combined value, as obtained by the CMS experiment of  $m_H = 125.02 \pm 0.27$  GeV. The scan of the combined likelihood function of the measurements from both decay channels, taking all correlations properly into account is shown by the black line in Fig. 5.1 (left) [2]. Also shown are the likelihood functions, as obtained from each individual decay channel, indicated by the red and the blue line. As for the measurements in each individual decay channel before, the signal strength parameters,  $\mu_{ggH,t\bar{t}H}^{\gamma\gamma}$ ,  $\mu_{VBF,VH}^{\gamma\gamma}$  and  $\mu_{ZZ}$  had been added as free parameters to the fit to remove the dependency of the SM Higgs boson production cross section from the measurement. The result of this combined measurement is

$$\hat{m}_H = 125.03 \pm 0.27 \text{ (stat) } \pm 0.14 \text{ (syst) GeV}$$
 (CMS experiment) (5.1)

in good agreement with the result of the weighted mean, with a slightly larger combined systematic and statistical uncertainty of  $\pm 0.3\,\text{GeV}$ . The comparison of the result as obtained from the combined likelihood analysis with the weighted mean of the measurements in the individual decay channels, as obtained by the *CMS* collaboration helps to assess the use and limits of combining individual results without the proper knowledge of all correlations between the individual measurements in this case.

A measurement of  $m_H$  has also been published by the ATLAS collaboration, from a combined likelihood analysis of the  $H \to \gamma \gamma$  and  $H \to ZZ$  decay channels [5]. The values of  $\hat{m}_H$  as obtained in each individual decay channel are  $\hat{m}_H = 125.98 \pm 0.42$  (stat)  $\pm 0.28$  (syst) GeV in the  $H \to \gamma \gamma$  decay channel and  $\hat{m}_H = 124.51 \pm 0.52$  (stat)  $\pm 0.06$  (syst) GeV in the  $H \to ZZ$  decay channel. A similar analysis had been performed as in the case of the CMS experiment to check the compatibility of these two measurements and they have been found to be compatible with each other within  $2\sigma$ . The slight tension that appears between the two measurements has been discussed in [5] and potential sources might point to residual limitations in the understanding of the photon energy scale in the ATLAS detector. The result of the combined likelihood analysis is found to be

$$\hat{m}_H = 125.36 \pm 0.37 \text{ (stat) } \pm 0.18 \text{ (syst) GeV}$$
 (ATLAS experiment) (5.2)

The combined measurements of both experiments are well compatible with each other within their uncertainties. The weighted mean of both measurements leads to a value of  $\hat{m}_H = 125.10 \pm 0.18$  GeV, where the combined statistical and systematic uncertainties of each measurement have been used for the mean and the corresponding uncertainty. A summary of the individual and combined results as obtained by each collaboration is given in Table 5.1. This result a posteriori justifies the assumption of  $m_H = 125$  GeV that had been made in the discussion of the expected Higgs boson production cross section for the (s+b)-hypotheses in Chap. 4.

# 5.1.2 Decay Width Estimate from the Off-Shell Cross Section

As shown for the individual decay channels for the *CMS* experiment obtaining a measurement of the Higgs boson decay width,  $\Gamma_H$ , just from a pure line shape analysis of an invariant mass distribution, even in the high mass resolution channels only allows to set upper bounds, which are by  $\approx$ 3 orders of magnitude larger than the expected decay width of the SM Higgs boson with  $m_H = 125$  GeV. For a long time

decay channels with the highest resolution on $m_H$ in both experiments							
ATLAS	$H \rightarrow \gamma \gamma$	$125.98 \pm 0.42 \text{ (stat)} \pm 0.28 \text{ (syst)}$	GeV	[5]			
	H  o ZZ	$124.51 \pm 0.52 \text{ (stat)} \pm 0.06 \text{ (syst)}$	GeV	[5]			
	Combined	$125.36 \pm 0.37 \text{ (stat)} \pm 0.18 \text{ (syst)}$	GeV	[5]			
CMS	$H \rightarrow \gamma \gamma$	$124.70 \pm 0.31 \text{ (stat) } \pm 0.15 \text{ (syst)}$	GeV	[1]			

**Table 5.1** Mass of the Higgs boson as obtained from measurements in the  $H \to \gamma \gamma$  and  $H \to ZZ$  decay channels with the highest resolution on  $m_H$  in both experiments

Also shown are the results of a combined likelihood analysis of both decay channels in the two experiments corresponding to the best measurement from each experiment. The results are based on the full *LHC* run-1 dataset of the data taking period of the years 2011 and 2012

 $125.60 \pm 0.45$  (stat)  $\pm 0.10$  (syst)

 $125.03 \pm 0.27$  (stat)  $\pm 0.14$  (syst)

GeV

GeV

[3]

[2]

 $H \rightarrow ZZ$ 

Combined

this had led to the opinion that a measurement of this quantity is beyond the scope of the *LHC*. But indeed much more information can be obtained from a study of more sensitive observables. One such observable is the ratio of off-shell production of Higgs bosons (far away from the invariant mass peak) with respect to the on-shell production, as proposed in [6] and picked up with a measurement in the  $H \to ZZ$  decay channel by the *CMS* collaboration [7].

In general the invariant mass distribution for the production of any particle follows the shape of a *Breit-Wigner* resonance curve

$$\frac{\mathrm{d}\sigma}{\mathrm{d}m^2} \propto \frac{1}{\left(q^2 - m^2\right)^2 + m^2 \Gamma^2} \xrightarrow{\Gamma \to 0} \frac{\pi}{m\Gamma} \delta\left(q^2 - m^2\right) \tag{5.3}$$

where m and  $\Gamma$  correspond to the mass and decay width of the particle and q to the momentum transfer in the scattering process. This term corresponds to the propagator term in the matrix element of the scattering process, squared. If the decay width of the particle,  $\Gamma$ , is small compared to the particle mass, as it is the case for the SM Higgs boson with  $\Gamma_H/m_H = \mathcal{O}(10^{-5})$  the *Breit-Wigner* term can be approximated by a delta distribution as indicated in the right part of Eq. (5.3). This is called the *narrow width approximation*. In the physics interpretation it implies that the particle is produced as a real physical particle that propagates for a certain time before it decays. The production and decay of the particle can be viewed as independent of each other and the rate to observe the particle in a certain final state can be composed of a simple product of a production cross section and a decay channel specific branching fraction as introduced in Sect. 4.2. The proposed estimate of  $\Gamma_H$  starts from the full *Breit-Wigner* term in the  $H \to ZZ \to 4\ell$  decay channel

$$\frac{\mathrm{d}\sigma(gg \to ZZ \to 4\ell)}{\mathrm{d}m_{4\ell}^2} \propto \frac{\kappa_g^2 \kappa_Z^2}{\left(m_{4\ell}^2 - m_H^2\right)^2 + m_H^2 \Gamma_H^2} \tag{5.4}$$

where  $q = m_{4\ell}$  while  $\kappa_g$  and  $\kappa_Z$  correspond to the (effective) coupling strength of the Higgs boson to the gluon and the Z boson (as will be discussed in more detail in Sect. 5.3.3). Making use of the zero width approximation close to the resonant peak leads to a cross section dependency of the form

$$\frac{\mathrm{d}\sigma(gg \to ZZ \to 4\ell)}{\mathrm{d}m_{4\ell}^2} \bigg|_{\text{on-shell}} \propto \frac{\kappa_g^2 \kappa_Z^2}{m_H \Gamma_H} \bigg|_{m_{4\ell} \approx m_H}$$
(5.5)

while far off the peak the dependency turns into

$$\frac{\mathrm{d}\sigma(gg \to ZZ \to 4\ell)}{\mathrm{d}m_{4\ell}^2} \bigg|_{\text{off-shell}} \propto \frac{\kappa_g^2 \kappa_Z^2}{m_{4\ell}^4} \bigg|_{m_{4\ell} \gg m_{4\ell}} \tag{5.6}$$

and from the ratio of the two cross sections information can be inferred of  $\Gamma_H$ . The obvious problem of this ansatz is that the off-shell cross section is strongly suppressed by  $m_{\Lambda \ell}^{-4}$  and that especially for such a narrow resonance as for the SM Higgs boson the naively expected cross section, multiples of  $\Gamma_H$  away from the peak position should be literally zero and thus without any chance to be experimentally observable. On closer inspection two peculiarities of the SM Higgs boson with  $m_H \approx 125\,\mathrm{GeV}$ resurrect this ansatz: (i) with  $m_H \approx 125 \,\text{GeV}$ , the Higgs boson has a mass very close to the kinematic edge, where the decay into Z and W bosons opens up; (ii) the coupling of the Higgs boson proportional to the mass and even to the mass squared in the case of the massive vector bosons leads to a significant enhancement of the production cross section. These two effects imply that even in off-shell regions as far apart from the resonant mass as  $m_{4\ell} \approx 200 \, \text{GeV}$  the effect of the off-shell production of SM Higgs bosons on the over all  $qq \to ZZ \to 4\ell$  production cross section can still be  $\mathcal{O}(8\%)$  [8, 9]. Quantum mechanically the production of four isolated high  $p_T$ leptons from two gluons in the initial state  $(qq \rightarrow 4\ell)$  is a superposition of several processes, which are indistinguishable by their final state. These processes include e.g.: the production via an intermediate  $Z\gamma^*$  pair  $(gg \to Z\gamma^* \to 4\ell)$ ; the production via two intermediate Z bosons in the subsequent decay channel  $(gg \to ZZ^* \to 4\ell)$ ; as well as the (resonant) production via an intermediate Higgs boson state ( $qq \rightarrow$  $H \to ZZ \to 4\ell$ ). Since these processes are indistinguishable by their final state the superposition leads to interference affects, which are obtained from the coherent addition on the amplitude level in contrast to an incoherent addition on the cross section level. An illustration of this effect is shown in Fig. 5.2.

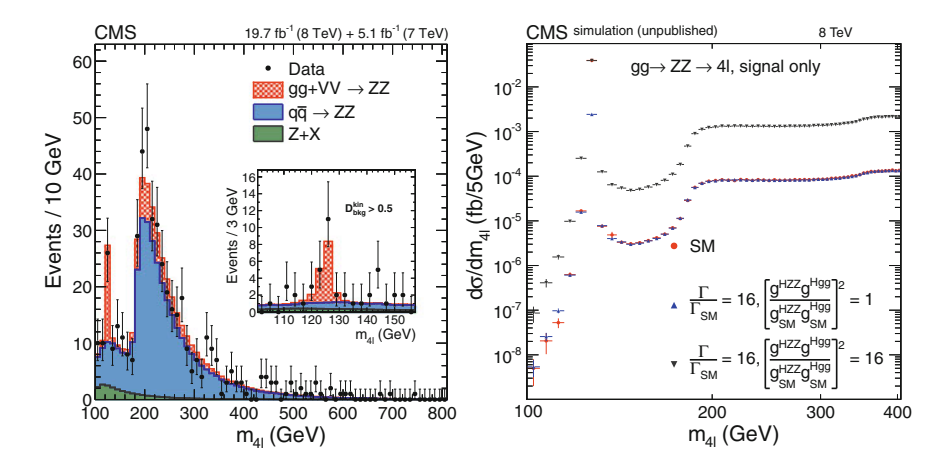


Fig. 5.2 Invariant four lepton mass distribution,  $m_{4\ell}$ , from the Higgs boson search in the  $H \to ZZ$  decay channel, as described in Sect. 4.3.2. On the *left*, the observed number of events from (non-) resonant  $gg \to ZZ \to 4\ell$  production is shown [3]. On the *right*, the expected effect of an increased value of  $\Gamma_H$  and increased (effective) couplings of the Higgs boson to gluons (labeled as  $g^{\text{Hgg}}$ ) or Z bosons (labeled as  $g^{\text{HZZ}}$ ) on the differential  $gg \to ZZ \to 4\ell$  production cross section are shown [7]

In Fig. 5.2 (left), the four lepton invariant mass,  $m_{4\ell}$ , is shown for the analysis in the  $H \to ZZ$  decay channels, as described in Sect. 4.3.2, in a mass range between  $100 < m_{4\ell} < 800 \,\text{GeV}$ . The black points with error bars correspond to the data, and the filled histograms to the expected number of events from the simulation, split into non-resonant  $q\bar{q} \to ZZ^*$  production (represented by the filled blue histogram) and the production via  $gg + VV \rightarrow ZZ$ , including resonant and non-resonant contributions (represented by the filled red histogram). In this notation the label "qq + VV" expresses the combination of gluon fusion and vector boson fusion diagrams in the initial state. The resonant contributions to the  $gg + VV \rightarrow ZZ$ process proceed via the creation of an intermediate Higgs boson (qq + VV) $H \to ZZ$ ). In the inlet figure, the low mass region with an additional requirement of  $\mathcal{D}_{bkg}^{kin} > 0.5$  is shown, as described in Sect. 4.3.2. Figure 5.2 (left) illustrates the clear peak at  $m_{4\ell} \approx 125 \, \text{GeV}$ , which is dominated by (intermediate) Higgs boson production and the still significant contribution of the  $qq + VV \rightarrow ZZ$  processes, even far off the mass peak of the Higgs boson. In Fig. 5.2 (right), the expected differential cross section for (non-)resonant  $gg \to ZZ$  production in the  $2e2\mu$  final state is shown, as expected in the SM (red points) and in two different modifications of the SM expectation: the blue up-pointing triangles correspond to the expectation where the couplings,  $\kappa_a$  and  $\kappa_Z$ , of the Higgs boson (labeled as  $g^{\text{Hgg}}$  and  $g^{\text{HZZ}}$  in the figure) have been set to the values as expected by the SM but the decay width,  $\Gamma_H$ , has been set to a value 16 times larger than expected for the SM; the green down-pointing triangles correspond to the expectation, where both the couplings squared and the decay width have been increased by a factor of 16. In the first case, the yield in the tail remains unchanged, reflecting the fact that  $\Gamma_H$  does not appear in Eq. (5.6), while the yield in the peak is reduced, as obvious from Eq. (5.5). This situation is already ruled out by the observation in the peak region. In the latter case, the appropriate scaling both of the couplings and the total width lead to the same yield in the peak, but to a significantly increased yield in the tail. This situation can not be excluded by an observation in the peak region only. It requires the additional measurement of the off-shell cross section.

It is clear that the sensitivity of such a measurement crucially relies on the theoretical understanding of the involved signal and background processes. For the analysis, all gluon fusion induced processes had been calculated at NNLO precision in  $\alpha_s$ , for the calculation of QCD radiative corrections, differential as a function of  $m_{ZZ}$ , including interference effects. Vector boson fusion induced processes had been calculated at NNLO precision in  $\alpha_s$  and NLO precision in  $\alpha$  for electroweak corrections. The leading background from  $qq \rightarrow ZZ$  production, especially in the off-shell analysis, had been calculated to NLO accuracy in  $\alpha_s$ .

For the measurement in the on-shell region, which had been defined by  $105.6 < m_{4\ell} < 140.6 \,\text{GeV}$ , the analysis had been performed, as described in Sect. 4.3.2, using the three dimensional likelihood discriminant as given in Eq. (4.4). In the offshell region, which had been defined by  $m_{4\ell} > 220 \,\text{GeV}$ , the signal extraction had

been performed using a two dimensional likelihood function based on  $m_{4\ell}$  and an additional discriminating likelihood function

$$\mathcal{D}_{gg} = \frac{\mathcal{P}_{\text{tot}}^{gg}}{\mathcal{P}_{\text{tot}}^{gg} + \mathcal{P}_{\text{bkg}}^{q\bar{q}}} = \left[1 + \frac{\mathcal{P}_{\text{bkg}}^{q\bar{q}}}{a \cdot \mathcal{P}_{\text{sig}}^{gg} + \sqrt{a} \cdot \mathcal{P}_{\text{int}}^{gg} + \mathcal{P}_{\text{bkg}}^{gg}}\right]^{-1}$$

exploiting the kinematic differences between the  $gg \to 4\ell$  and  $qq \to 4\ell$  processes, where  $\mathcal{P}_i^{gg}(q\bar{q})$  corresponds to the probability density for a  $gg \to 4\ell$  ( $qq \to 4\ell$ ) event to obtain a kinematic configuration in  $m_{Z_1}, m_{Z_2}, \bar{\Omega}$ , as observed in data, and the total contribution  $\mathcal{P}_{tot}^{gg}$  had been split into the individual components of Higgs boson signal (sig),  $gg \to ZZ \to 4\ell$  background (bkg) and the corresponding interference term (int). For this discriminant, the off-shell Higgs boson signal had been enhanced by a factor of a=10, roughly corresponding to the sensitivity of the measurement. In addition, the analysis had been extended by the decay channel into  $2\ell 2\nu$ , where one Z boson decays into a pair of neutrinos, using the transverse mass above a value of  $m_T > 180\,\text{GeV}$  as discriminating variable, to enhance the statistical power of the analysis. For the statistical inference a model of type

$$\mathcal{P}_{\text{tot}}^{\text{on-shell}}(\vec{x}) = \mu_{gg} \cdot \left(\mathcal{P}_{\text{sig}}^{gg}(\vec{x}) + \mathcal{P}_{\text{sig}}^{t\bar{t}H}(\vec{x})\right) + \mu_{\text{VBF}} \cdot \left(\mathcal{P}_{\text{sig}}^{\text{VBF}}(\vec{x}) + \mathcal{P}_{\text{sig}}^{VH}(\vec{x})\right) + \mathcal{P}_{\text{bkg}}^{gg} + \mathcal{P}_{\text{bkg}}^{g\bar{q}} + \dots$$

$$\mathcal{P}_{\text{tot}}^{\text{off-shell}}(\vec{x}) = \left(\mu_{gg} \cdot \frac{\Gamma_{H}}{\Gamma_{\text{SM}}} \cdot \mathcal{P}_{\text{sig}}^{gg}(\vec{x}) + \sqrt{\mu_{gg} \cdot \frac{\Gamma_{H}}{\Gamma_{\text{SM}}}} \cdot \mathcal{P}_{\text{int}}^{gg}(\vec{x}) + \mathcal{P}_{\text{bkg}}^{gg}\right)$$

$$+ \left(\mu_{\text{VBF}} \cdot \frac{\Gamma_{H}}{\Gamma_{\text{SM}}} \cdot \mathcal{P}_{\text{sig}}^{\text{VBF}}(\vec{x}) + \sqrt{\mu_{\text{VBF}} \cdot \frac{\Gamma_{H}}{\Gamma_{\text{SM}}}} \cdot \mathcal{P}_{\text{int}}^{\text{VBF}}(\vec{x}) + \mathcal{P}_{\text{bkg}}^{\text{VBF}}\right)$$

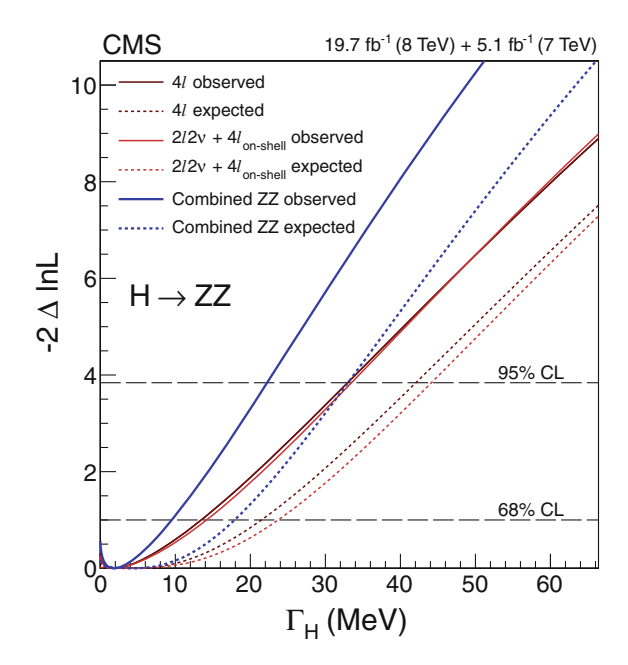
$$+ \mathcal{P}_{\text{bkg}}^{q\bar{q}}(\vec{x}) + \dots$$

$$(5.7)$$

had been exploited, where the  $\mathcal{P}_i^j$  correspond to the probability density functions as discussed above. In this model, the minor contributions for SM Higgs boson production in association with vector bosons (VH) and  $t\bar{t}$  pairs  $(t\bar{t}H)$  had been added for the on-shell signal. The variables  $\mu_{gg}$  and  $\mu_{VBF}$  correspond to the signal strength for Higgs boson production in gluon fusion (and  $t\bar{t}H$ ) and vector boson fusion (and VH) and  $\Gamma_{SM}$  corresponds to the decay width of the Higgs boson as predicted by the SM. In the signal extraction, the parameters  $\mu_{ggH}$  and  $\mu_{VBF}$  had been added as free parameters when estimating the decay width,  $\Gamma_H$ , via a scan of the likelihood function.

The scan of the likelihood function is shown in Fig. 5.3 where the solid dark and bright red curves correspond to the observed scan of the likelihood function taking only the  $4\ell$  or only the  $2\ell 2\nu$  analysis in the off-shell region into account and the solid blue curve corresponds to the observed scan of the likelihood function taking

Fig. 5.3 Scan of the likelihood function as defined in Eq. (5.7) to obtain the best estimate of the measured decay width,  $\hat{\Gamma}_H$ , from a combined measurement of the on- and off-shell cross section for Higgs boson production as described in the text [7]



both analyses in the off-shell region into account. The dashed curves correspond to the distributions as expected for the SM. The figure demonstrates that both off-shell analyses contribute with equal sensitivity and lead to comparable results when considered individually. The individual best estimates for  $\Gamma_H$  are  $\hat{\Gamma}_H^{4\ell}=1.9\pm_{1.9}^{11.7} {
m MeV}$ for the  $4\ell$  off-shell analysis and  $\hat{\Gamma}_H^{2\ell 2\nu} = 1.8 \pm ^{12.4}_{1.8}$  MeV for the  $2\ell 2\nu$  off-shell analysis. Combining both off-shell analyses leads to a value of  $\hat{\Gamma}_H = 1.8 \pm \frac{7.7}{1.8} \text{MeV}$ , well compatible with the expectation of the SM, where in each case the given uncertainties correspond to the 68 % CL intervals of the likelihood scan. This result translates into an observed (expected) 95% CL upper bound on the decay width of the observed Higgs boson of 22 (33) MeV, corresponding to an observed (expected) upper limit of 5.4 (8.0) times the expected SM value. The statistical compatibility of this measurement with the expectation from the SM corresponds to a p-value of 24 %. This measurement is a good example of how the sensitivity of a naive line shape analysis could be improved by several orders of magnitude by a different ansatz. In this ansatz the coupling strengths and the total decay width of the Higgs boson are measured from data at the same time. But the method still relies on the assumption that the coupling strengths do not change as a function of the involved energy scale,  $m_{ZZ}$ , when going from  $m_{ZZ} \approx 125 \, \text{GeV}$  to  $m_{ZZ} \gtrsim 220 \, \text{GeV}$ , an assumption which is violated if new physics effects influence the couplings at the level of higher-order corrections. This would be the case for most extensions of the SM, which are being discussed at the moment. In this sense, it is the most conservative interpretation of the obtained upper limit to understand it as an additional consistency check under the SM assumption.

### 5.2 Spin and CP Symmetry

## 5.2.1 Groundwork for Spin and CP Analyses

As discussed in Sect. 4.3.4 from the observation in the three bosonic decay channels the bosonic nature of the new particle became evident. Furthermore, the discovery in the  $H \to \gamma \gamma$  decay channel implied that the new particle should not be of spin 1 since the direct decay of a spin-1 particle into two photons is forbidden by the *Landau-Yang* theorem [10, 11].

In the SM the Higgs boson is characterized by the quantum numbers of the vacuum: it has spin 0 and the CP eigenstate +1. CP is a discrete symmetry operation, composed of the charge conjugation operator, C, and the parity operator, P. For a quantum system C corresponds to a switch of a particle into its anti-particle, P corresponds to the switch of the spacial coordinates from x to -x. By construction C and P are projection operators, with the eigenvalues  $\pm 1$ , similar to the projection operators, defined in Eq. (2.18). The eigenvalue +1 is often referred to as CP-even, the eigenvalue of -1 as CP-odd Both, C and P are conserved symmetries under electromagnetic or strong interactions, but the weak interaction maximally violates the P symmetry, by the fact that the W boson only couples to left-handed fermions and right-handed anti-fermions. The fact the W boson couples with the same strength to left-handed fermions and to right-handed anti-fermions led to the assumption that the combination of C and P, CP, could be a conserved quantity in strong and electroweak interactions. Nowadays it is clear that also the CP symmetry is violated in weak interactions in the SM, while this violation has been observed to be very small.

Neither the C nor the P eigenvalue of a quantum system are directly observable. They have to be inferred from a careful analysis of the angular momentum configuration of the whole quantum system, usually described by a spacial wave function,  $\psi(t, \mathbf{x})$  and a spin wave function  $\chi(\vec{s_i})$ , where the  $\vec{s_i}$  correspond to the spins of all particles in the system. In the analysis of the angular momentum  $\psi(t, \mathbf{x})$  is usually decomposed in orbital wave functions  $Y_i^m(\theta, \varphi)$ , which have the symmetry behavior

$$P(Y_l^m(\theta,\varphi)) = (-1)^l \cdot Y_l^m(\theta,\varphi)$$

where l corresponds to the orbital angular momentum and m to the z-component of the orbital angular momentum along a pre-defined quantization axis. The parity eigenvalue of the complete system is then determined by the product of the orbital angular momentum and the intrinsic parity of all involved particles in the system.

The main decay channel for an angular momentum analysis with the current limited number of events is again the  $H \to ZZ \to 4\ell$  decay channel, which has the advantage that all kinematic information, which is necessary for the inference is

<sup>&</sup>lt;sup>1</sup>Note that also the coupling of the Z boson to left- and right-handed particles is different (though not maximally P violating) as shown in Eq. (2.28).

preserved and hardly distorted by the experimental resolution. The intrinsic parity of the four lepton system in the final state can be obtained from the product of the individual leptons<sup>2</sup> (+1 for fermions and -1 for anti-fermions) leading to a parity *eigenvalue* of the final state of

$$P(4\ell) = (-1)^{\ell} (-1)^{2} (+1)^{2} = (-1)^{\ell}$$
(5.8)

The parity of the system thus depends on the presence of additional orbital angular momentum in the system, which further on depends on the initial spin of the decaying particle and the combined spin of all decay products. According to the quantum theorem of angular momenta the spins of the ZZ diboson system can take the following values:

$$\begin{split} |2,\pm 2\rangle &= |1,\pm 1\rangle \otimes |1,\pm 1\rangle \\ |2,\pm 1\rangle &= \sqrt{\frac{1}{2}}|1,\ 0\rangle \otimes |1,\pm 1\rangle + \sqrt{\frac{1}{2}}|1,\pm 1\rangle \otimes |1,\ 0\rangle \\ |2,\ 0\rangle &= \sqrt{\frac{1}{6}}|1,\ 1\rangle \otimes |1,-1\rangle + \sqrt{\frac{2}{3}}|1,\ 0\rangle \otimes |1,\ 0\rangle + \sqrt{\frac{1}{6}}|1,-1\rangle \otimes |1,\ 1\rangle \\ |1,\pm 1\rangle &= \sqrt{\frac{1}{2}}|1,\pm 1\rangle \otimes |1,\ 0\rangle - \sqrt{\frac{1}{2}}|1,\ 0\rangle \otimes |1,\pm 1\rangle \\ |1,\ 0\rangle &= \sqrt{\frac{1}{2}}|1,\ 1\rangle \otimes |1,-1\rangle - \sqrt{\frac{1}{2}}|1,-1\rangle \otimes |1,\ 1\rangle \\ |0,\ 0\rangle &= \sqrt{\frac{1}{3}}|1,\ 1\rangle \otimes |1,-1\rangle - \sqrt{\frac{1}{3}}|1,\ 0\rangle \otimes |1,\ 0\rangle + \sqrt{\frac{1}{3}}|1,-1\rangle \otimes |1,\ 1\rangle \end{split}$$

using the bracket notation,  $|s, s_z\rangle$ , where the bracket on the left side of the equations represents s and  $s_z$  of the combined system, while the direct products on the right side of the equations correspond to the spins of the individual spin-1 objects. The two spin-1 objects can either couple to a combined spin-2 (upper three lines), spin-1 (middle two lines) or spin-0 (lower line) object, equivalent to a parity even spin hypothesis for the resonance, if no additional orbital angular momentum is involved. When combining the spin-1 configurations with an orbital angular momentum of l=1, e.g. a hypothesis for a parity odd spin-0 resonance can be constructed. The discussion in this section will be concentrated on the spin-0 hypotheses for the following reasons: (i) the test of the spin-1 hypotheses in the  $H \rightarrow ZZ$  decay channel can be viewed as an independent crosscheck of the statement obtained from the Landau-Yang theorem. The object observed in the  $H \rightarrow ZZ$  decay channel might not be the same object as observed in the  $H \rightarrow \gamma\gamma$  decay channel, or the Landau-Yang theorem might be

 $<sup>^2</sup>$ Note that the particles of importance are the leptons in the physical final state and not the intermediate Z bosons. The Z bosons do not even have a well defined intrinsic parity due to their parity violating nature.

violated. But this crosscheck is more of academic nature; (ii) if the new particle were a spin-2 particle its spin structure would be by far more complicated. The tests that have been made could give hints, but would require much more detailed studies with more data. The consequences can not be discussed in the scope of this book; (iii) of all spin hypotheses the  $J^P=0^-$  hypothesis is the most interesting alternative to the SM, since all extensions of the Higgs boson sector by an additional Higgs doublet,  $\tilde{\phi}$ , as mentioned in Sect. 2.4.2 would lead to the presence of an additional Higgs boson with spin 0 and CP=-1.

An example of a  $J^P = 0^+$  spin-parity configuration is shown in Fig. 5.4 (left). In this notation J corresponds to the combined angular momentum of the system and P to the parity eigenvalue. The solid arrows correspond to the momenta of the Z bosons in the restframe of the decaying resonance. The dashed arrows to the momenta of the leptons in the restframe of the subsequent decay of the Z bosons. The open arrows correspond to the spin of the corresponding decay products. In the restframe of the resonance the two Z bosons emerge from the decay in a back to back configuration. Their spins compensate each other to form a spin-0 system. There is no additional orbital angular momentum, which is the reason, why the parity of the system is  $(-1)^l\big|_{l=0}=+1$ . Also in the restframe of each of the subsequent decays of the Z bosons the corresponding leptons emerge from the decay in a back to back configuration. Due to the helicity of the leptons the  $\ell^+$  preferentially moves in the direction of the Z boson spin, and the  $\ell^-$  in the opposite direction. In Fig. 5.4 (right) an example for a  $J^P = 0^-$  spin-parity configuration is shown. In this case the spins of the Z boson add up to a combined spin of 1, which is completed to a spin-0 system by one additional unit of orbital angular momentum. The parity of the system is  $(-1)^l|_{l=1} = -1$ . The influence of the spin configurations of the Z bosons on the angles between the two  $Z \to \ell^+ \ell^-$  decay planes becomes obvious from the two figures.

When analyzing the *C* eigenvalue of the decay system the effect in  $\psi(t, \mathbf{x})$  as well as the effect on  $\chi(\vec{s}_i)$  have to be taken into account. As can be seen from Fig. 5.4 a transition of all particles into anti-particles can be achieved by the application of the *P* operator and a permutation of the spin-1 objects in the discussion



**Fig. 5.4** Two examples of a spin configuration (left) for a  $J^P=0^+$  and (right) for a  $J^P=0^-$  particle in the  $H\to ZZ\to 4\ell$  decay channel. On the left the two spins of the Z bosons combine to a system with spin 0. On the right the spins of the Z bosons combine to a residual spin 1, which is completed to a spin-0 system by one additional unit of orbital angular momentum, l=1. This leads to the eigenvalue of P=-1. Note that the shown spin configurations are only examples of the spin configurations given in Eq. (5.9) and that the composed spin-0 object in each case is described by a superposition of more than one spin configuration

of the spin configuration of the combined system in Eq. (5.9). The spin-0 and spin-2 configurations of Eq. (5.9) are symmetric under permutations of the spin components on the right side of the equations, while the spin-1 configurations are anti-symmetric. So the  $J^P=0^+$  configuration, without additional orbital angular momentum, also has a C eigenvalue of +1 and consequently a CP eigenvalue of +1. The  $J^P=0^-$  configuration, with additional orbital angular momentum of l=1, acquires one factor of -1 from the application of the P operator and one additional factor of -1 from the permutation of the spin-1 objects in the spin configuration. The resulting eigenvalue of C is +1 and the eigenvalue of C P is -1. In both cases the eigenvalues of P and C P are the same.

### 5.2.2 Estimate of Spin and CP in the $H \rightarrow ZZ$ Decay Channel

For the data analysis the same event selection had been used as described in Sect. 4.3.2. In addition the events of interest had been required to lie in the restricted mass range of  $106 < m_{4\ell} < 141\,\text{GeV}$ . After this selection 50 events remain in the final event sample, based on all events of the *LHC* run-1 data taking period, of which  $\approx 50\,\%$  are expected to be due to the Higgs boson signal. These event numbers are too small for a reliable measurement. Therefore the events had been used for a statistical test of different spin-parity hypotheses. For these tests not the three dimensional likelihood function  $\mathcal{L}_{3D}^{\mu}$ , as defined in Eq. (4.4), but a two dimensional likelihood function  $\mathcal{L}_{2D}^{JP}(\mathcal{D}_{\text{bkg}}, \mathcal{D}_{JP})$  was used. The kinematic discriminants forming the arguments of this likelihood function had been defined as:

$$\mathcal{D}_{bkg} = \left[ 1 + \frac{\mathcal{P}_{bkg}^{kin}(m_{Z_1}, m_{Z_2}, \vec{\Omega}|m_{4\ell}) \cdot \mathcal{P}_{bkg}(m_{4\ell})}{\mathcal{P}_{0+}^{kin}(m_{Z_1}, m_{Z_2}, \vec{\Omega}|m_{4\ell}) \cdot \mathcal{P}_{0+}(m_{4\ell})} \right]^{-1}$$

$$\mathcal{D}_{JP} = \left[ 1 + \frac{\mathcal{P}_{JP}^{kin}(m_{Z_1}, m_{Z_2}, \vec{\Omega}|m_{4\ell})}{\mathcal{P}_{0+}^{kin}(m_{Z_1}, m_{Z_2}, \vec{\Omega}|m_{4\ell})} \right]^{-1}$$
(5.10)

where, as discussed in Sect. 4.3.2,  $\mathcal{P}_{bkg}^{(kin)}$ ,  $\mathcal{P}_{J^P}^{kin}$  and  $\mathcal{P}_{0^+}^{kin}$  correspond to the probability density functions to find an event in the configuration given by  $m_{Z_1}$ ,  $m_{Z_2}$ ,  $\vec{\Omega}$  and  $m_{4\ell}$  in the case of the  $qq \to ZZ$  background hypothesis or the Higgs boson signal hypothesis, either in the  $0^+$  spin-parity configuration, as predicted by the SM, or in the configuration of an alternative  $J^P$  spin-parity hypothesis. All probability density functions had been obtained from LO matrix element calculations. The difference between  $\mathcal{D}_{bkg}$ , as defined in Eq. (5.10) and  $\mathcal{D}_{bkg}^{kin}$ , as defined in Eq. (4.3) is that in  $\mathcal{D}_{bkg}$  the information on  $m_{4\ell}$  has been implicitly encoded, which is not the case for  $\mathcal{D}_{bkg}$ .

In the case of spin-0 hypotheses (which will be mainly discussed in this context), by nature, there are no correlations with the spin configuration of the initial partons in the production. This is not the case for the spin-1 and spin-2 hypotheses, which

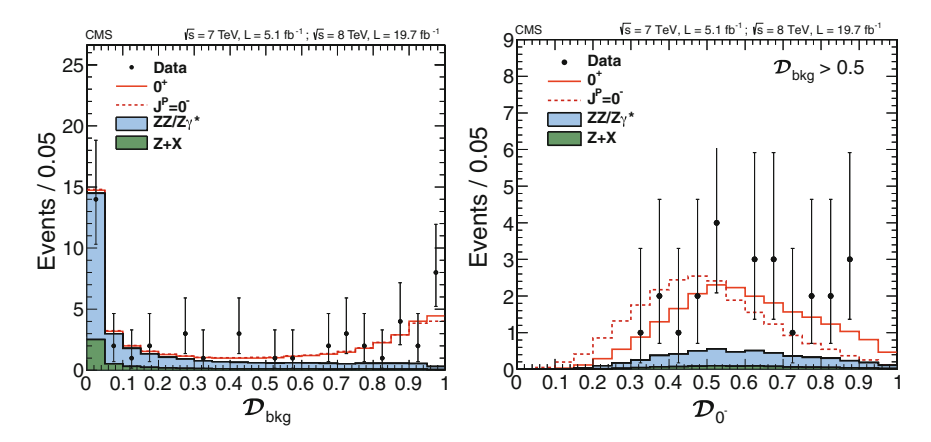


Fig. 5.5 Probability density functions (left)  $\mathcal{D}_{\text{bkg}}$  and (right)  $\mathcal{D}_{0^-}$ , that have been used for the spinparity analysis in the  $H \to ZZ \to 4\ell$  decay channel for testing the SM hypothesis,  $0^+$  against the  $J^P = 0^-$  hypothesis [3]. For  $\mathcal{D}_{0^-}$  an additional requirement  $\mathcal{D}_{\text{bkg}} > 0.5$  has been applied to remove those events, which are anyhow very likely to originate from  $qq \to ZZ$  background. For the statistical inference the full two dimensional likelihood function  $\mathcal{L}_{2D}^{0}(\mathcal{D}_{\text{bkg}}, \mathcal{D}_{0^-}))$  was used

is the reason that for the analyses of these hypotheses the variables related to the production mode, namely  $d\Phi_1$  and  $d\cos\theta^*$  had been integrated out in all relevant probability density functions in Eq. (5.10).

In Fig. 5.5 the kinematic discriminants  $\mathcal{D}_{bkg}$  and  $\mathcal{D}_{0^-}$  are shown, that had been used for the test of the SM hypothesis,  $0^+$ , against the  $J^P = 0^-$  hypothesis. The black points with the error bars correspond to the data, the green and blue filled histograms to the expected contribution of non-Higgs boson background processes and the red lines to the signal contribution as expected for a Higgs boson with  $m_H = 125.6 \,\mathrm{GeV}$ . In both figures a solid and a dashed red line is shown. The solid red line corresponds to the  $0^+$  hypothesis, as expected by the SM, while the dashed red line corresponds to the alternative 0<sup>-</sup> hypothesis. For the statistical inference the full two dimensional likelihood function,  $\mathcal{L}_{2D}^{0^-}(\mathcal{D}_{bkg},\mathcal{D}_{0^-})$  had been used. For easier presentation the distributions in the figure are shown only in one dimension,  $\mathcal{D}_{bkg}$ (left) and  $\mathcal{D}_{0-}$  (right), where the events have been integrated along the corresponding other dimension. In addition to enhance the visibility of the distinction of the two alternative hypotheses in  $\mathcal{D}_{0^-}$  for Fig. 5.5 (right) a further selection had been applied of  $\mathcal{D}_{bkg} > 0.5$ , to remove those events, which anyhow are very likely to originate from  $qq \rightarrow ZZ$  background. The similarity of the curves corresponding to the  $0^-$  and the  $0^+$  hypothesis in  $\mathcal{D}_{bkg}$ , demonstrate that the choice of the actual spin hypothesis for  $\mathcal{D}_{bkg}$  is not of large importance, which is also true for all other spinparity hypothesis tests.

The final test statistic for the spin-parity hypothesis tests had been defined as

$$q = -2\ln Q; \qquad Q = \frac{\mathcal{L}_{2D}^{J^P}}{\mathcal{L}_{2D}^{0^+}}$$

With this definition events, which are more compatible with the  $0^-$  hypothesis lead to negative values of q, while events, which are more compatible with the  $0^+$  hypothesis lead to positive values of q. For the data a single value of q is obtained. To determine the expected value and the probability density distribution for obtaining a given value of q for the  $0^+$  or the  $0^-$  hypothesis q is evaluated based on a huge number of pseudo experiments under the assumption of each corresponding hypothesis. In Fig. 5.6 (top) the obtained probability density functions and the observed value of q are shown for

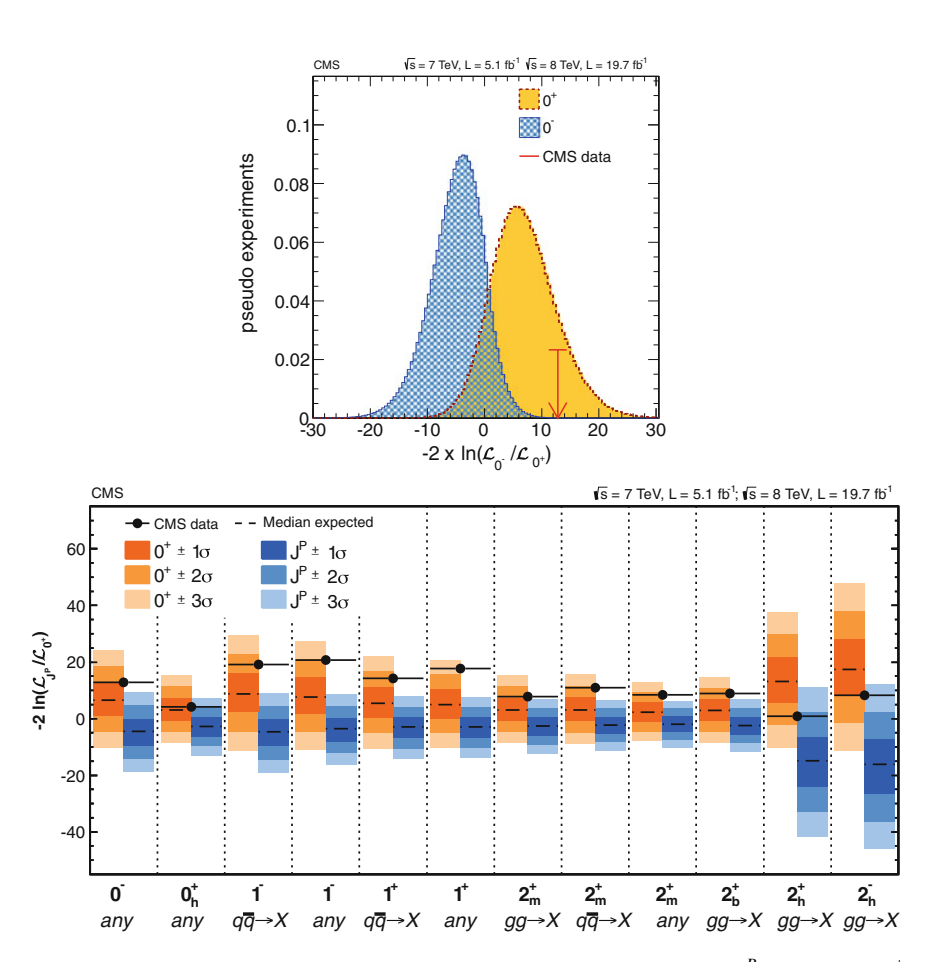


Fig. 5.6 Hypothesis tests for several alternative spin-parity configurations,  $J^P$ , against the  $0^+$  hypothesis as expected by the SM [3]. On the *top* the observed test statistic (*red arrow*) and the probability density functions for the  $0^-$  (*blue histogram*) and the  $0^+$  (*yellow histogram*) hypothesis are shown. On the *bottom* the observed test statistics and the double sided  $1\sigma$ ,  $2\sigma$  and  $3\sigma$  quantiles for each corresponding hypothesis are shown as *orange* (*blue*) shaded bands for the SM (alternative) hypothesis. The different hypotheses are listed on the *x*-axis of the figure. The  $0^-$  hypothesis test that has been discussed in detail in the text is given in the first bin of this summary plot. The exact models and their notation are described in the text and in more detail in [12, 13]

the example of the  $J^P = 0^-$  test. The red arrow corresponds to the observed value in the data, the blue filled histogram to the probability density function for the 0<sup>-</sup> hypothesis and the filled yellow histogram to the probability density function of the 0<sup>+</sup> hypothesis. As can be seen from the figure the two spin-parity hypotheses do still have a significant overlap, for the given statistics of the measurement, which becomes clear also from Fig. 5.5 (right). With more events the separation between these two hypotheses will become stronger. But it can also be seen that the observed value of q already now is significantly more favored by the 0<sup>+</sup> hypothesis, as given for the SM, than for the  $0^-$  hypothesis. This is supported by the fact that even for the assumption of the  $0^+$  hypothesis the observed value of q lies at the right side of the expected median, which might be considered a lucky or unlucky fluctuation depending on the personal flavor of the reader. With more data the observed value of q would lie at a different value, which should not be too far away from the value that it has now, and the probability density functions would become more peaky, thus allowing a better separation of the two hypotheses. For completeness it should be mentioned that Fig. 5.6 (top), while representing different hypotheses, in its statistical meaning and technical making can be directly compared to the probability density functions as determined for the hypothesis tests for the very first Higgs boson searches at LEP, as shown in Fig. 3.6.

In Fig. 5.6 (bottom) a compilation of several hypothesis test that have been performed in this way is shown. On the y-axis the corresponding value of q = $-2\ln(\mathcal{L}_{IP}/\mathcal{L}_{0+})$  is given. On the x-axis the different hypotheses  $J^{P}$ , that have been tested against the 0<sup>+</sup> hypothesis are listed. The exact models and their notation are described in [12, 13]. The black points correspond to the observed values of q and the differently shaded bands in blue and orange to the  $1\sigma$ ,  $2\sigma$  and  $3\sigma$  contours of the double sided 68, 95 and 99 quantiles of the probability density functions of the corresponding  $J^P$  (blue) and  $0^+$  (orange) hypothesis. The dashed lines correspond to the expected median of each probability density function. The 0<sup>-</sup> hypothesis test, which has been discussed in more detail above is shown in the first bin of the distribution. In the second bin the test of a  $0_h^+$  hypothesis with distortions from higher dimension operators in the Lagrangian density function is shown, the next four columns correspond to different tests of 1<sup>±</sup> hypotheses with different assumptions on the production mode and the last columns correspond to several spin-2 hypothesis tests with different assumptions on the production mode. In all hypothesis tests the 0<sup>+</sup> hypothesis as advocated by the SM is favored. Based on a  $CL_s$  criterion according to

$$CL_s = \frac{\mathcal{P}(q \ge q_{\text{obs}}|J^p + \text{bkg})}{\mathcal{P}(q \ge q_{\text{obs}}|0^+ + \text{bkg})} < \alpha$$

a quantitative CL for the exclusion of the tested  $J^P$  hypothesis could be obtained, where in analogy to the signal search a maximum likelihood fit had been applied prior to the limit estimate to determine the most probable values for all nuisance parameters in the statistical model for the given hypothesis. To remove the dependency of the hypotheses on the expected value of the signal strength,  $\mu$ , this parameter had been

treated as an additional free parameter in the minimization of the corresponding likelihood function. According to this  $CL_s$  criterion the  $0^-$  hypothesis could be excluded at 99.9 % CL corresponding to a deviation of  $3.6\sigma$  from the expected median. The deviation from the expected median for the  $0^-$  hypothesis in the presence of the  $0^+$  hypothesis was expected to be  $2.4\sigma$  for the most probable value,  $\hat{\mu} =$  $0.93 \pm 0.27$  as given in Table 4.2 and  $2.7\sigma$  for a fixed value of  $\mu = 1$  in the statistical treatment. Note that there is a weakening effect on the significance of the deviation from the  $CL_s$  value when compared to the plain deviation from the expected median from the  $0^-$  hypothesis as shown in Fig. 5.6 (top). The fact that the deviation from the expected median for the  $0^-$  hypothesis in the presence of the  $0^+$  hypothesis is weaker than the observed deviation resembles the fact that the observed value of q lies even beyond the expected median of the  $0^+$  hypothesis. The deviation from the  $0^+$ hypothesis has been quantified in a similar way to be  $-0.9\sigma$  for  $\mu = 1.3$  As obvious from Fig. 5.6 (bottom) all but the  $0^+$  hypothesis in these tests are disfavored, with the largest exclusion for the spin-1 hypotheses and the weakest exclusions for the various spin-2 and the  $0_h^+$ -hypothesis. In summary these observations strengthen the assumption that the observed particle has the spin-parity  $0^+$ , as expected by the SM.

It should be mentioned though that these tests are still limited in several ways: in the first place hypothesis tests do not replace unbiased measurements. They give only binary information on the proposed hypotheses, within confidence intervals. They also imply the correctness of one of the two hypotheses. The  $CL_s$  method is one way to deal with the fact that the pure mathematical concept of a hypothesis test might lead to misleading and unintuitive results in the case of low statistics, which is even more true if none of the two hypotheses is correct (i.e. compatible with the data). Beyond this limitation the hypothesis tests in this special decay channel are subject to a bunch of further specific limitations: (i) the spin-1 hypotheses are already excluded from the Landau-Yang theorem as discussed in the beginning of this section. The findings do however support the assumption that the resonance discovered in the  $H \to \gamma \gamma$ decay channel and the resonance discovered in the  $H \to ZZ$  decay channel are the same; (ii) spin-2 configurations are so complex that the models, that have been tested can only light a small sector of this rich phenomenology; (iii) finally also the test of the 0<sup>-</sup> hypothesis is limited by the fact that in any serious extension of the SM, that is being discussed at the moment a coupling of a CP-odd Higgs boson to vector bosons is suppressed at tree level. So the test does not tell anything about the presence of a CP-odd Higgs boson or a CP-odd admixture to the discovered Higgs boson. This admixture could well be there. But the  $H \rightarrow ZZ$  decay channel would be blind for it due to a loop suppressed coupling. The observation of a CP-odd coupling of the Higgs boson, would in the reverse conclusion correspond to an anomalously high coupling. These limitations culminate in the resume that while observing a positive hypothesis test for anything else but the  $0^+$  hypothesis in this decay channel would have been a sensation, the non-observation was indeed not much of a surprise.

<sup>&</sup>lt;sup>3</sup>Note that this is also the result of the naive subtraction of the observed significance from the expected significance in the presence of the  $0^+$  hypothesis for  $\mu=1$ .

Spin-parity analyses are one of the obvious sectors of Higgs physics that will profit from the increased number of events in the upcoming data taking periods from 2015 on: (i) the hypothesis tests in the  $H \to ZZ$  decay channel will be replaced by unbiased, conclusive measurements; (ii) similar analyses in the  $H \to \gamma\gamma$  and  $H \to WW$  decay channel will become more interesting. These analyses have already been made on the existing dataset, but they have not been discussed in this context, since they are by far less sensitive, when compared to the  $H \to ZZ$  decay channel; (iii) finally the potential of spin-parity analyses in the  $H \to \tau\tau$  decay channel will open up, where a CP-odd and a CP-even coupling are expected to enter on an equal footing at tree level, giving a much higher theoretical potential in the search for CP-odd Higgs bosons or CP-odd admixtures to the couplings of the observed Higgs boson.

### **5.3 Coupling Structure**

#### 5.3.1 Prerequisite Studies

Up to this point the new particle has been shown to lead to an observable signal (with a significance of more than  $3-5\sigma$ ) in three bosonic and one fermionic decay channel. It has been shown to be a boson that is compatible with the signature of a CP-even spin-0 particle and unlike a gauge boson, to have a non universal coupling to fermions. To conclude on the Higgs boson search all analyses of the CMS collaboration that have been discussed in Chap. 4 had been combined to determine the coupling structure of the new boson, comprising all event (sub-)categories in the (i)  $H \to \gamma \gamma$  [1]; (ii)  $H \rightarrow ZZ$  [3]; (iii)  $H \rightarrow WW$  [14]; (iv)  $H \rightarrow \tau\tau$  [15]; (v)  $H \rightarrow \mu\mu$  [16] and; (vi)  $H \rightarrow b\bar{b}$  [17] decay channels and; (vii) the inclusive search for the SM Higgs boson signal in the  $t\bar{t}H$  production mode [18]. This combination included  $\approx 230$ event (sub-)categories and 1784 nuisance parameters in the maximum likelihood fit to allow profiling of systematic uncertainties, some of which, like the uncertainty on the integrated luminosity of the 7 and 8 TeV dataset or the theoretical uncertainties of SM Higgs boson production have been treated as 100% correlated across different decay channels or event categories [2]. Written in human readable form the model for the statistical analysis filled a plain table of 145 MB. The binary compilation that had been created from these inputs reached a size of 16MB. A maximum likelihood fit with a single signal strength modifier,  $\mu$ , assuming the SM relations between different production modes and decay channels led to a value of

$$\hat{\mu} = 1.03 \pm 0.09 \text{ (stat.) } \pm 0.10 \text{ (syst.)}$$
 (5.11)

where the first component in the uncertainties corresponds to the statistical uncertainty and the second component to the combined systematic uncertainties of the estimate. To obtain this value the Higgs boson signal had been evaluated at the

most probable value of  $m_H$  given by Eq.(5.1). A split of the analyzed dataset in up to 16 event (sub-)categories resembling different production modes and decay channels did not reveal any significant tension across these (or less) event (sub-)categories. The  $\chi^2$ /ndf of the spread of the values of  $\hat{\mu}_i$ , obtained in each of the event (sub-)categories individually, in the case of the split into 16 event (sub-)categories resulted in a value of 10.5/16, corresponding to a *p*-value of 84 %.

Three important conclusions can already be drawn from these studies: (i) the coupling structure of the observed boson in each decay channel and production mode, as obtained from the data is consistent with the expected signal strength contributions in presence of the SM Higgs boson; (ii) not only the relative signal strength contributions across all event (sub-)categories, but also the overall magnitude of the signal strength of the observed boson is consistent with the expectation of the SM within the reachable experimental accuracy; (iii) on the currently available dataset the experimental accuracy to test the consistency of the observations with the expectations of the SM is  $\mathcal{O}(10\,\%)$  for the statistical and of the same order for the systematic uncertainty. Combining all data and using maximal input of the SM on the expected coupling structure leads to the maximal statistical power to test the SM assumption on the overall normalization of the signal. Further separation and adding more degrees of freedom in the statistical model will only lead to reduced statistical power of the analysis.

An important prerequisite to the analysis of the coupling structure of the new particle is the assumption that the observed signal is due to only one single and not a superposition of more than one particle. The possibility that the signal might be composed of more particles, which could be split in mass up to a difference of 2.5–4 GeV had been tested in a dedicated line shape analysis in the  $H \to \gamma \gamma$  decay channel [1]. The single particle hypothesis is further supported by the studies of the spin of the new particle in the  $H \to ZZ$  decay channel [3], which are consistent with the requirement that the new boson could not be of spin 1, as inferred from the observation in the  $H \to \gamma \gamma$  decay channel [10, 11]. A third crosscheck along this line is the consistency of the upper limits of the decay width,  $\Gamma_H$ , with the expectation of the SM in both, the  $H \to \gamma \gamma$  and the  $H \to ZZ$  decay channel. Even though this is only a weak consistency check of the SM it implies that there is no indication of more than one particle giving rise to the observed signal within the experimental resolution of the analyses. What these checks can not exclude is the presence of more particles, which are degenerate in mass. To be able also to address this question the signal strengths split by the four considered production modes,  $qq \to H$ ,  $qq \to H$ , VH,  $t\bar{t}H$  and the five considered decay channels,  $H \to \gamma\gamma$ ,  $H \to ZZ$ ,  $H \to WW$ ,  $H \to b\bar{b}, H \to \tau\tau$  had been analyzed using a likelihood ratio

$$q_{\lambda} = -2 \ln \left( \frac{\mathcal{L}(\text{data}|_{\text{single part}})}{\mathcal{L}(\text{data}|_{\text{saturated}})} \right)$$

where the likelihood function  $\mathcal{L}(\text{data}|_{\text{single part}})$  allows for eight free signal strength parameters: one parameter,  $\mu_i$  ( $i = \gamma \gamma$ , ZZ, WW,  $b\bar{b}$ ,  $\tau \tau$ ) for each decay channel

and one parameter,  $\lambda_i$  ( $j = qq \rightarrow H, VH, t\bar{t}H$ ) for each production mode (where the modifier for gluon fusion has been absorbed into the  $\mu_i$  parameters) with the requirement that the  $\lambda_i$  should be the same across all decay channels, i, and the  $\mu_i$  the same across all production modes, j. This model gives enough degrees of freedom in the maximum likelihood fit to relief the dependency on the SM, while it still corresponds to a single particle hypothesis. In the presence of more than one particle that would couple differently in at least one production mode or decay channel the correlation across production mode or decay channel does not hold anymore. To account for this additional degree of freedom, for the likelihood function  $\mathcal{L}(\text{data}|_{\text{saturated}})$  the correlation across production modes (or decay channels) had been removed by adding  $5 \times 4 = 20$  independent signal strength parameters for each individual combination of production mode and decay channel. In statistics such a model is called saturated. It implies that in the maximum likelihood fit each signal strength parameter will take the best possible value in each pair of production mode and decay channel. In the likelihood ratio,  $q_{\lambda}$ ,  $\mathcal{L}(\text{data}|_{\text{saturated}})$  will thus gauge  $\mathcal{L}(\text{data}|_{\text{single part}})$  to the largest reachable value.

The test statistic of a likelihood ratio with a saturated model like  $q_{\lambda}$ , is a generalization of the classical minimal  $\chi^2$  test for a given test hypothesis  $H_0$ . This can be understood assuming that the parameters of interest in both likelihood functions are normal distributed. In this case the likelihood ratio takes the form

$$\mathcal{L}(\text{data}|_{H_0}) = \prod_{i} \frac{1}{\sqrt{2\pi\sigma_i}} e^{-(d_i - \lambda_i)^2/2\sigma_i}$$

$$\mathcal{L}(\text{data}|_{\text{saturated}}) = \prod_{i} \frac{1}{\sqrt{2\pi\sigma_i}}$$

$$q_{\lambda} = -2\ln\left(\frac{\mathcal{L}(\text{data}|_{H_0})}{\mathcal{L}(\text{data}|_{\text{saturated}})}\right) = \sum_{i} \frac{(d_i - \lambda_i)^2}{\sigma_i}$$

where the  $d_i$  correspond to the (measured) values in data with uncertainty  $\sigma_i$  and the  $\lambda_i$  to the parameters of interest for i measurements. For  $\mathcal{L}(\text{data}|_{\text{saturated}})$  the maximum likelihood fit has enough degrees of freedom so that each  $\lambda_i$  will match each value of  $d_i$ . This is why the exponential in this likelihood function is zero and only the normalization factor  $1/\sqrt{2\pi\sigma_i}$  remains.

For the test of the single particle hypothesis based on  $q_{\lambda}$  the observed value of  $q_{\lambda}$  has been compared to the expectation for the SM, which has been used as a proxy for a single particle model, based on a large number of toy experiments. The p-value to observe values of  $q_{\lambda} \geq q_{\lambda}^{\text{obs}}$  has been found to be  $\approx 8\,\%$  corresponding to a deviation from the expectation for a single particle hypothesis of  $1.4\sigma$ . On close inspection a small tension was observed in the two jet event category in the  $H \to ZZ$  decay channel, which in itself is only of limited statistical sensitivity. In this event category the data prefer a large contribution due to the VH and a very small contribution due to the  $qq \to H$  production mode. Removing the contributions of the  $H \to ZZ$  decay channel from the likelihood model results in a p-value of 33 % corresponding

to a deviation from the expectation of  $0.5\sigma$ . Based on these tests the single particle hypothesis is well justified within the experimental resolution of the analyses.

#### 5.3.2 Statistical Model

Only very few of the analyzed event (sub-)categories are so pure that information on a single production mode or decay channel could be directly inferred from the estimated signal strength parameter,  $\mu_i$  in that category. Also in single decay channels the statistical power to analyze certain production modes is still very limited. The analysis of the coupling structure of the new boson therefore has been performed as a compatibility check of the individual observations in each event (sub-)category with the best available predictions of the SM, which have been provided by theory with an accuracy as given in Sect. 4.2.1. In this ansatz the following well justified assumptions have been made: (i) the signal originates from a single particle; (ii) the model does not take into account that kinematic distributions, which have been used for signal extraction in the individual event (sub-)categories might have been affected by potential deviation from the SM expectation. In this sense the model implicitly relies on the assumption of the new particle to be CP-even and of spin 0; (iii) the width of the new particle is assumed to be narrow enough so that the narrow width approximation, as discussed in Eq. (5.3) can be applied. The latter assumption implies that the signal rate for a given production mode and decay channel factorizes into two independent parts for the production and the decay of the new particle

$$(\sigma \cdot BR)(i \to H \to f) = \frac{\sigma_i \cdot \Gamma_f}{\Gamma_H}$$
 (5.12)

where the cross section,  $\sigma_i$  for a given production mode, i, and the partial decay width,  $\Gamma_f$ , for a decay into a given final state f have to be determined by calculation and the total decay width,  $\Gamma_H$ , is obtained from the sum of the partial decay widths over all energetically accessible final states,  $\sum_{f} \Gamma_{f}$ ,  $(f = \gamma \gamma, Z \gamma, Z Z, W W, b \bar{b}, c \bar{c}, g g,$  $s\bar{s}, \tau\tau, \mu\mu$ ). In this sum the light quark contributions and the electron are neglected due to their low mass and thus very small coupling strength. Deviations from these predictions have been parametrized as effective coupling strength parameters in form of multipliers  $\kappa_f$ , at the amplitude level, which are trivial for all direct (tree-level) couplings, like f = W, Z for the coupling to W or Z bosons, or  $f = t, b, \tau, \mu$  for the coupling to  $\tau$ -leptons, muons, b- or top quarks. The coupling to the c- and s-quark, which (at least in the available dataset) are not directly accessible at the LHC are usually coupled to  $\kappa_t$  and  $\kappa_b$ . For couplings, which occur via loops or which are summed across several amplitudes in the SM, like in the case of the production via gluon fusion or the  $H \to \gamma \gamma$  decay two options have been followed: (i) in an effective approach no attempt has been made to resolve these couplings and they have been modified by a single parameter  $\kappa_q$  or  $\kappa_\gamma$  as in the case of the tree-level couplings; (ii) in a more SM like approach the loop structure has been resolved taking all relevant contributions and their interference terms at the amplitude level into account [19]. In (ii) the resolved processes are the production via gluon fusion  $(gg \to H)$ , the production via vector boson fusion  $(qq \to H)$ , the decay into gluons  $(H \to gg)$ , the decay into photons  $(H \to \gamma\gamma)$  and the decay into a photon and a Z boson  $(H \to Z\gamma)$ . The decay into gluons is not observable at the LHC, but it is included in the calculation of the total decay width,  $\Gamma_H$ , since it has a sizable contribution there.

At 8 TeV the contributions of W and Z boson fusion are shared with a fraction of  $\approx \frac{3}{4}$  (W boson fusion) to  $\approx \frac{1}{4}$  (Z boson fusion). Interference terms have been estimated to be less than 0.1 % of the total cross section. For gluon fusion the contributions from the b- and the top quark have been taken into account. The loop is largely dominated by the top quark contribution, the contribution from the b-quark at the cross section level being  $\approx 1\%$ . The effect of tb-interference terms, summed over all contributing leading and higher-order amplitudes, on the other hand has been found to be  $\mathcal{O}(-7\%)$ , larger that the contributions of the single b-quark amplitude (and destructive as indicated by the minus sign). For the partial decay width into gluons the b-quark contribution is again  $\mathcal{O}(1\%)$  and the destructive tb-terms are found to be  $\mathcal{O}(-12\%)$ . For the decay into photons the contributions from the W boson and from the top quark are dominant. The decay via the top quark loop contributes at  $\mathcal{O}(7\%)$  to the decay width, the sum of all tW-interference terms is again destructive and  $\mathcal{O}(-64\%)$ . All contributions via b- or  $\tau$ -loops have been found to be below 1 % of the partial decay width and are not further discussed in this section, though they have been used in the statistical model. A summary of all dominant contributions to resolved cross sections or partial decay widths is given in Table 5.2.

Depending on the question in consideration and to increase the statistical power of the analysis for some tests the coupling strength parameters for individual particles have been grouped into common parameters, resulting in a correlated movement in

Table 3.2 Structure of resolved processes in the SM [17]						
$\sigma(gg \to H)$	tt	bb	tb			
19.27 pb	1.06	0.01	-0.07			
$\sigma(qq \to H)$	WW	ZZ	ZW			
1.578 pb	0.74	0.26	<0.001			
$\Gamma_{gg}$	tt	bb	tb			
$8.55 \cdot 10^{-2} \times \Gamma_H$	1.11	0.01	-0.12			
$\Gamma_{\gamma\gamma}$	WW	tt	Wt			
$2.29 \cdot 10^{-3} \times \Gamma_H$	1.56	0.07	-0.64			
$\Gamma_{Z\gamma}$	WW	tt	Wt			
$1.55 \cdot 10^{-3} \times \Gamma_H$	1.12	0.003	-0.12			

**Table 5.2** Structure of resolved processes in the SM [19]

In the upper part of the table the fractions of individual contributions to the resolved production cross sections, in the lower part of the table the dominant contributions to the resolved loop induced couplings are given in form of relative fractions to the summed cross section or summed partial decay width. The second and third row correspond to the contributions of single particle amplitudes of the two dominant contributions and the third row to the interference term

the maximum likelihood fit. Examples for such a grouping are  $\kappa_V$  ("V" for vector boson), correlating the coupling to the W and Z boson and  $\kappa_f$  ("f" for fermion), correlating all couplings to fermions. The largest simplification of this kind is obtained from combining all coupling strength parameters into one single parameter  $\kappa$ . This leads to the relation  $\mu = \kappa^2$  between  $\kappa$  and the signal strength parameter  $\mu$  of Eq. (5.11). The coupling strength parameters, are defined such that for  $\kappa_j = 1, \ \forall j$  the prediction of the SM is retained to best knowledge. The model will not have predictive power beyond testing the SM though, since in the case of significant deviations in one or more parameters  $\kappa_j$  the higher-order corrections that rely on the SM assumption are not strictly valid any more. In addition, since the  $\kappa_j$  do not only appear in the numerator but also as part of  $\Gamma_H$  in the denominator an absolute measurement of the couplings is not possible.

### 5.3.3 Test of the Coupling Structure

The main model to test the coupling structure of the new boson contains six parameters of interest in form of a coupling strength parameter  $\kappa_j$  for each tree-level coupling that could be addressed by the analyses described in Chap. 4 ( $j = W, Z, t, b, \tau$  and  $\mu$ ). All couplings via loops that have been described above have been resolved according to the expectation by the SM. The result of the maximum likelihood fit is shown in Fig. 5.7. The black points correspond to the central values, the red and blue error bars to the 68 and 95% CL intervals, including statistical and

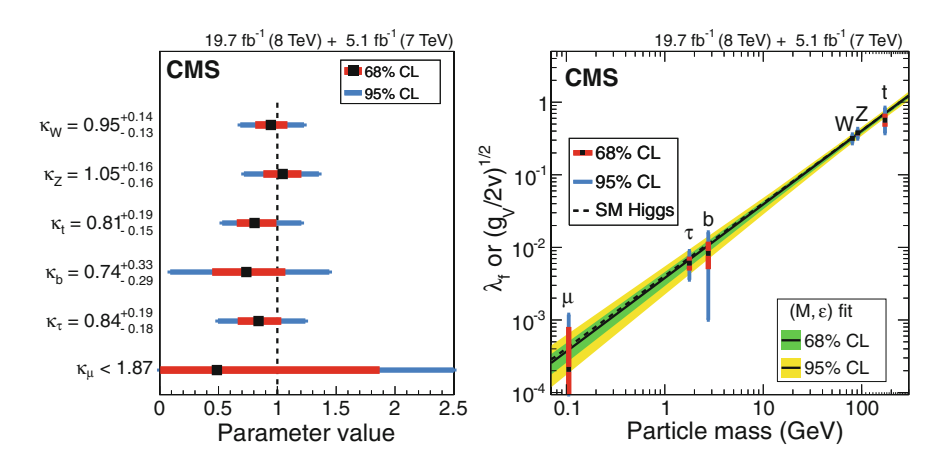


Fig. 5.7 Coupling structure as obtained from a maximum likelihood fit to the data described in Chap. 4, with  $\kappa_j$ , j=W, Z, t, b,  $\tau$ ,  $\mu$  as free parameters of interest [2]. The figure on the *left* indicates, that all values  $\kappa_j$  are consistent with 1 within the 68 % CL uncertainty of the fit and thus with the expectation of the SM. The figure on the *right* illustrates how well the coupling structure of a Higgs boson is exhibited by the couplings obtained from the fit

systematic uncertainties, as obtained from the maximum likelihood fit. The dashed line corresponds to the expectation for the SM. All couplings are found to be compatible with the expectation by the SM, within their 68 % CL uncertainty, thus confirming that the new boson has a coupling structure, as expected for a Higgs boson that is an excitation of a field for which the  $SU(2)_L$  symmetry is spontaneously broken in the quantum vacuum. For this to be the case the coupling has to be proportional to the mass of the heavy gauge bosons squared and linearly proportional to the mass of the fermions. To give more emphasize to this finding the observed values for the couplings to fermions and vector bosons have been transformed motivated by Eq. (2.50) to have the same linear dependence on the mass of the corresponding fermion or vector boson in case that the new particle exhibits the coupling structure of a Higgs boson:

$$\begin{split} |f_{H\to ff}^{\text{obs}}| &= \kappa_f \cdot |f_{H\to ff}^{\text{SM}}| = \kappa_f \cdot \frac{m_f}{\text{v}} \quad f = \mu, \tau, b, t \\ \sqrt{\frac{|f_{H\to VV}^{\text{obs}}|}{2\text{v}}} &= \sqrt{\kappa_V} \cdot \sqrt{\frac{|f_{H\to VV}^{\text{SM}}|}{2\text{v}}} = \sqrt{\kappa_V} \cdot \frac{m_V}{\text{v}} \quad V = W, Z \end{split}$$

The behavior of these transformed couplings as a function of the fermion or vector boson mass is shown in Fig. 5.7 (right). In the figure the dashed line corresponds to the expectation of the SM. Also shown by a continuous line with dark green and bright yellow uncertainty bands is the result of the fit of a model where each coupling strength parameter had been modified to be  $\kappa_f = v \cdot \frac{m_f^{\epsilon}}{M^{\epsilon+1}}$  for fermions and  $\kappa_V = v \cdot \frac{m_V^{2\epsilon}}{M^{2\epsilon+1}}$  for vector bosons to account for a bending and a shift of the linear dependency. In this phenomenological model the SM expectation is retained from the value pair  $(M, \epsilon) = (v, 0)$ . The obtained most probable values have been found to be  $M = 245 \pm 15 \,\text{GeV}$  and  $\epsilon = 0.01 \pm \frac{0.041}{0.036}$ . In summary the coupling structure of the new particle is confirmed to be Higgs boson-like within the  $10-20\,\%$  accuracy of the analysis, with the weakest constraint on  $\kappa_\mu$  and  $\kappa_b$ . The central values for  $\kappa_j$  and the corresponding confidence intervals are given in the upper part of Table 5.3.

While the coupling to the mass squared in the case of vector bosons is an essential ingredient to the coupling structure of the Higgs boson, to retain the  $SU(2)_L$  symmetry of the SM, the coupling proportional to the mass in the case of fermions resembles the special choice of a Yukawa coupling of the fermions to the Higgs doublet field,  $\phi$ . The coupling structure to fermions is thus theoretically less stringent than the coupling structure to vector bosons. Furthermore in the SM the couplings to W and Z bosons are protected to be of similar magnitude and not affected by large radiative corrections by an additional global custodial symmetry as discussed in Sect. 2.4.1. These and other properties of the observed Higgs boson have been tested with the help of simplified models within the  $\kappa$  framework to increase the statistical power of the analysis. The couplings via loops have been resolved according to the expectation by the SM where appropriate.

To test the assumption of *custodial* symmetry a simplified model had been exploited consisting of one coupling strength parameter,  $\kappa_f$ , common to all fermi-

Coupling str	ucture of the ne	w boson				
	$-2\sigma$	$-1\sigma$	Central value	$+1\sigma$	$+2\sigma$	
$\kappa_Z$	0.72	0.89	1.05	1.21	1.35	
$\kappa_W$	0.68	0.82	0.95	1.09	1.23	
$\kappa_t$	0.68	0.66	0.81	1.21	1.35	
$\kappa_b$	0.09	0.45	0.74	1.07	1.44	
$\kappa_{ au}$	0.50	0.66	0.84	1.03	1.24	
$\kappa_{\mu}$	0.00	0.00	0.49	1.87	2.77	
$\lambda_{WZ}$	0.70	0.79	0.91	1.05	1.22	
$\lambda_{du}$	0.66	0.82	1.01	1.20	1.43	
$\lambda_{\ell q}$	0.61	0.81	1.02	1.24	1.49	
$\kappa_V$	0.88	0.94	1.01	1.08	1.15	
$\kappa_f$	0.64	0.75	0.89	1.02	1.16	
$\kappa_g$	0.69	0.79	0.89	0.99	1.10	
$\kappa_{\gamma}$	0.89	1.02	1.15	1.28	1.42	
$BR_{\mathrm{BSM}}$	0.00	0.00	0.00 (0.00)	0.13 (0.39)	0.32 (0.52)	
B Riny	0.00	0.00	0.03 (0.17)	0.18 (0.34)	0.32 (0.49)	

**Table 5.3** Central values, 68 and 95 % CL intervals of several parameters that have been used to test the coupling structure of the observed Higgs boson [2]

In the upper part of the table the coupling strength parameters  $\kappa_j$  used in the maximum likelihood fit for the determination of the overall coupling structure of the observed Higgs boson are given. The values correspond to the points shown in Fig. 5.7. In the middle part of the table the values  $\lambda_j$  to further investigate the bosonic and fermionic part of the coupling structure are listed. In the lower part of the table the results of the coupling analysis split by vector bosons and fermions and the results of the search for effects of physics beyond the SM in the loop induced couplings and in potential decays of the observed Higgs boson into invisible particles are summarized. The values in braces correspond to the central values and confidence intervals if the requirements on  $\kappa_j$  are weakened to reduce the model dependency as described in the text

ons, one coupling strength parameter,  $\kappa_Z$  for the coupling to the Z boson and the ratio  $\lambda_{WZ}=\kappa_W/\kappa_Z$  for the coupling of the W boson relative to the coupling of the Z boson as parameter of interest. In the maximum likelihood fit  $\kappa_f$  and  $\kappa_Z$  had been left as free parameters. The obtained value of  $\lambda_{WZ}$  has been found to be  $\lambda_{WZ}=0.91\pm^{0.14}_{0.12}$ , where the given uncertainties include the statistical and systematic component. The result is consistent with the expectation of *custodial* symmetry. In an alternative approach the fit had been applied only to the  $gg\to H$  dominated event (sub-)categories in the  $H\to ZZ$  and  $H\to WW$  decay channels. Assuming that the production mechanism of the observed Higgs boson is the same in both decay channels this choice minimizes residual dependencies on the SM. The result of the maximum likelihood fit has been found to be  $\lambda_{WZ}=0.94\pm^{0.22}_{0.18}$  consistent with the more inclusive analysis.

In the SM the Higgs boson only couples to down-type fermions. The *Yukawa* coupling to up-type fermions is achieved by the coupling of the charge conjugate,  $\phi_c$  of the Higgs boson field. In the most popular extension of the SM, *supersymme*-

try [20–23] this is not possible, since the Higgs boson and its charge conjugate have to match into a larger multiplet structure. Supersymmetry therefore strictly requires that a second  $SU(2)_L$  doublet exists, giving rise to more than one physical Higgs boson. This in general implies deviations of the couplings to up and down-type fermions with respect to the expectation by the SM. More general two Higgs doublet models (2HDM) [24] may also allow for different couplings to leptons and quarks with respect to the expectation by the SM. To further investigate the coupling structure of the observed Higgs boson in the fermion sector two further simplified models had been exploited consisting of one coupling strength parameter,  $\kappa_V$ , for the coupling to vector bosons and (i) one coupling strength parameter,  $\kappa_u$  for up-type fermions and the ratio  $\lambda_{du} = \kappa_d / \kappa_u$  for the coupling of down-type relative to up-type fermions as parameter of interest and; (ii) one coupling strength parameter,  $\kappa_q$  for the coupling to quarks and the ratio  $\lambda_{\ell q} = \kappa_{\ell}/\kappa_q$  for the coupling to leptons relative to quarks as parameter of interest. The obtained value of  $\lambda_{du}$  has been found to be  $\lambda_{du} = 1.01 \pm 0.20$ . The obtained value of  $\lambda_{\ell q}$  has been found to be  $\lambda_{\ell q} = 1.02 \pm 0.21$ , where the given uncertainties include the statistical and the systematic component in each case. Both results are consistent with the expectation of the SM. For these tests not only the central value is of interest, but also the uncertainties, since deviations e.g. in ranges of the still allowed parameter space of supersymmetric models are expected to be  $\mathcal{O}(3\%)$  and thus still below the statistical sensitivity of the current analysis. A summary of the tests of the coupling structure in the bosonic and fermionic Higgs sector is given in the middle part of Table 5.3.

To test the coupling structure to fermions with respect to vector bosons the coupling strength parameters  $\kappa_f$  have been comprised into a single parameter,  $\kappa_V$  for the coupling to the W and the Z boson and a single parameter  $\kappa_f$  for the coupling to fermions. In Table 5.4 it is indicated how  $\kappa_V$  and  $\kappa_f$  explicitly enter in the statistical model for each production mode and decay channel. Since  $\kappa_V$  and  $\kappa_f$  enter quadratically on the level of cross sections and partial decay widths, they imply a sign ambiguity, which is only resolved by the interference term in the loop induced  $H \to \gamma \gamma$  coupling, where both coupling strength parameters enter linearly. A negative sign of  $\kappa_f$  with respect to  $\kappa_V$  would turn the destructive into a constructive interference and thus enhance the signal in the  $H \to \gamma \gamma$  decay channel with respect to the other decay channels.

**Table 5.4** Representation of each production mode and decay channel by the coupling strength parameters  $\kappa_V$  and  $\kappa_f$ 

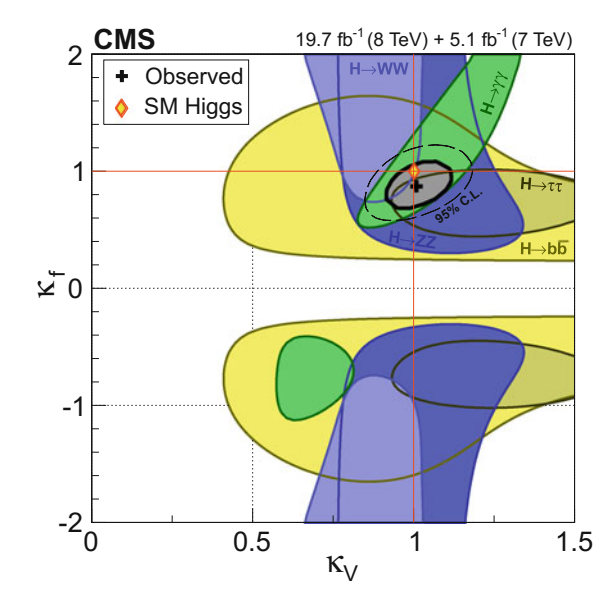
	$H \rightarrow VV$	$H \rightarrow ff$	$H \to \gamma \gamma$
$VH, qq \rightarrow H$	$\kappa_V^2 \kappa_V^2$	$\kappa_f^2 \kappa_V^2$	$\kappa_V^2 (1.56\kappa_V^2 - 0.64\kappa_V \kappa_f + 0.07\kappa_f^2)$
$t\bar{t}H, gg \to H$	$\kappa_f^2 \kappa_V^2$	$\kappa_f^2 \kappa_f^2$	$\kappa_f^2 (1.56\kappa_V^2 - 0.64\kappa_V \kappa_f + 0.07\kappa_f^2)$

The last column corresponds to the resolved  $H \to \gamma \gamma$  coupling according to [19], where the relative weights for  $\kappa_V^2$ ,  $\kappa_f^2$  and the interference term,  $\kappa_V \kappa_f$  are given. A common normalization factor corresponding to the parametrization of  $\Gamma_H$  has been omitted in the table

This option had been heavily discussed in the timespan shortly after the discovery, when the signal in the  $H \to \gamma \gamma$  decay channel was indeed by a factor of two larger than expected by the SM, while still well compatible within statistical uncertainties. During these times a relative minus sign between  $\kappa_V$  and  $\kappa_f$  could indeed not be excluded in the analysis of the coupling structure of the observed particle. The obtained values of  $\kappa_V$  and  $\kappa_f$  on the final dataset have been found to be  $\kappa_V = 1.01 \pm \frac{0.07}{0.07}$  and  $\kappa_f = 0.89 \pm \frac{0.14}{0.13}$ , where the given uncertainties include the statistical and systematic component. These results are consistent with the expectation of the SM. In Fig. 5.8, a graphical representation of the fit result is shown. The black cross and the solid and dashed black contours correspond to the most probable value and the 68 and 95 % CL contours of the parameter estimate using all event (sub-) categories in all decay channels. The colored contours correspond to the 68 % CL contours as determined from each decay channel individually. The yellow diamond corresponds to the value pair  $(\kappa_V, \kappa_f) = (1, 1)$  as expected by the SM. The split in individual decay channels illustrates the ambiguity in the sign of  $\kappa_f$  relative to  $\kappa_V$ in all but the  $H \to \gamma \gamma$  decay channel. From the combined fit a relative minus sign between  $\kappa_V$  and  $\kappa_f$  can be excluded at 95 % CL.

The coupling analysis could also be used to search for the effects of new physics in deviations of the loop induced couplings to gluons and photons from the expectation as by the SM. To further investigate this option a simplified model had been introduced where all tree-level couplings had been set to one, corresponding to the expectation of the SM and the effective couplings  $\kappa_g$  and  $\kappa_\gamma$  had been introduced as parameters of interest. In Fig. 5.9 (right) the result of the two dimensional parameter estimate is shown with  $\kappa_\gamma$  given on the x-axis and  $\kappa_g$  on the y-axis, where in the para-

Fig. 5.8 Coupling structure of the observed Higgs boson represented by the coupling to vector bosons,  $\kappa_V$ , and fermions,  $\kappa_f$  [2]. The black cross and the black solid and dashed contours correspond to the most probable value and the 68 and 95 % CL contours of the parameter estimate. The colored contours correspond to the 68 % CL contours as determined from each decay channel individually. The yellow diamond corresponds to the value pair  $(\kappa_V, \kappa_f) = (1, 1)$  as expected by the SM



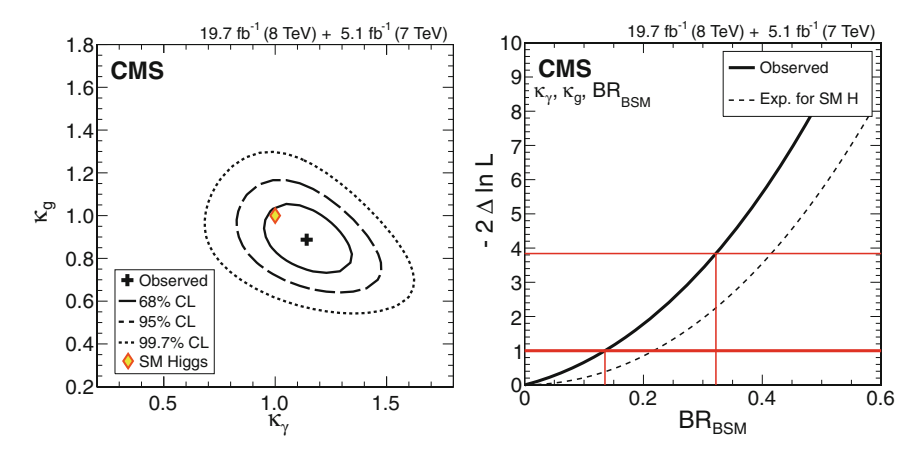


Fig. 5.9 Tests of the coupling structure of the observed Higgs boson to search for indirect indications of physics beyond the SM (*left*) in the loop induced couplings to the photon ( $\kappa_{\gamma}$ ) and the gluon ( $\kappa_{g}$ ) and (*right*) expressed in form of a limit on the branching fraction of the Higgs boson decay into non-observed particles,  $BR_{\rm BSM}$  [2]

meter estimate the additional requirement had been applied in the statistical model that the branching fraction into additional non-detected particles be zero. The black cross and the solid, dashed and dotted black contours correspond to the most probable value and the 68, 95 and 99 % CL contours of the parameter estimate. The yellow diamond corresponds to the parameter pair  $(\kappa_{\gamma}, \kappa_{q}) = (1, 1)$  as expected by the SM. The results of the parameter estimate are  $\kappa_{\gamma} = 1.15 \pm ^{0.13}_{0.13}$  and  $\kappa_{g} = 0.89 \pm ^{0.10}_{0.10}$ , where the given uncertainties include the statistical and systematic component. The result on  $\kappa_{\gamma}$  is clearly driven by the slightly larger observed event yield than expected in the  $H \to \gamma \gamma$  decay channel. The result on  $\kappa_q$  is driven by an over all slightly lower observed event yield than expected by the SM across all decay channels. This test could also be turned into an estimate on the branching fraction into non-observed Higgs boson decays, originating from physics beyond the SM. For this purpose the statistical model had been extended by an additional parameter BR<sub>BSM</sub> to account for such additional contributions to the total decay width and  $\kappa_{\gamma}$  and  $\kappa_{q}$  had been left as free parameters in the maximum likelihood fit. In Fig. 5.9 (left) a scan of the likelihood function for different values of  $BR_{BSM}$  between 0 and 0.6 is shown. The solid black line corresponds to the difference  $-2\Delta \ln \mathcal{L}$  of the likelihood function from the global minimum, as obtained from the data. The dashed black line corresponds to the expectation by the SM. The observed value of  $BR_{BSM}$  is 0 and thus compatible with the expectation by the SM. The 68% and 95% CL intervals for  $BR_{\rm BSM}$  are found to be 0.13 and 0.32. The observed limit is pushed to be more stringent due to the observed lower value of  $\kappa_q$ , which contributes stronger to  $\Gamma_H$  than  $\kappa_{\gamma}$ .

This estimate has been extended by a dedicated search for Higgs boson decays into invisible particles performed in the  $Z(\ell\ell)H(\text{inv})$ ,  $Z(b\bar{b})H(\text{inv})$  and  $qq \to H(\text{inv})$  production modes [25], assuming the production cross section and acceptance as

expected for the SM. From this dedicated search a direct observed (expected) 95 % CL upper limit on the branching fraction for Higgs boson decays into invisible particles of  $BR(H \to \text{inv}) < 0.58$  (0.44) could be obtained. The combination of this direct search with the coupling analysis, when adding the requirement that all contributions to  $\Gamma_H$  in the coupling analysis be due to the decay into invisible particles and not due to a decay into particles, which have just not been detected, leads to a value of  $BR_{\text{inv}} = 0.03 \pm_{0.03}^{0.15}$ . While the observed 95 % CL upper limit (by chance) remains at the same value of 0.32 the gain from the combination in sensitivity becomes obvious when comparing the expected 95 % CL limit, which reduces from 0.42 to 0.28.

Since the requirement of all tree-level couplings to be one is very strong the limits on  $BR_{\rm BSM}$  and  $BR_{\rm inv}$  represent the strongest statements that CMS can make on the subject with the current analysis and on the current dataset. There is a way to weaken the assumptions that have been made by leaving the parameters  $\kappa_j$ ,  $j=\gamma,g,b,t$  and  $\tau$  free with the only requirement that  $\kappa_V \leq 1$ , which is met in most extensions of the SM that are being discussed nowadays. With these weakened assumptions the 95 % CL upper limits cited above take the values  $BR_{\rm BSM} \leq 0.58$  and  $BR_{\rm inv} \leq 0.49$ , which means that to our best knowledge  $\approx 50\,\%$  of the branching fraction of the observed particle could still be unexplored! These values indicate how much freedom is still left in the analysis of the dataset for physics beyond the SM and how much there is still to gain in statistical power from the upcoming data taking periods from 2015 on. A summary of the results of the analysis of the coupling structure split by the coupling to vector bosons and fermions and in scope of the search for physics effects beyond the SM is given in the lower part of Table 5.3.

## References

- CMS Collaboration, Observation of the diphoton decay of the Higgs boson and measurement of its properties, Eur. Phys. J. C74(10), 3076 (2014). arXiv:1407.0558
- C.M.S. Collaboration, Precise determination of the mass of the Higgs boson and tests of compatibility of its couplings with the standard model predictions using proton collisions at 7 and 8 TeV, submitted to Eur. Phys, J. C (2014). arXiv:1412.8662
- 3. C.M.S. Collaboration, Measurement of the properties of a Higgs boson in the four-lepton final state. Phys. Rev. **D89**, 092007 (2014). arXiv:1312.5353
- Particle Data Group, Chin. Phys. Review of particle physics. C38, 090001 (2014). doi:10.1088/ 1674-1137/38/9/090001
- 5. ATLAS Collaboration, Measurement of the Higgs boson mass from the  $H\to\gamma\gamma$  and  $H\to ZZ^*\to 4\ell$  channels with the ATLAS detector using 25 fb<sup>-1</sup> of pp collision data, Phys. Rev. **D90**, 052004 (2014). arXiv:1406.3827
- F. Caola, K. Melnikov, Constraining the Higgs boson Width with ZZ production at the LHC. Phys. Rev. D88, 054024 (2013). arXiv:1307.4935
- C.M.S. Collaboration, Constraints on the Higgs boson width from off-shell production and decay to Z-boson Pairs. Phys. Lett. B736, 64 (2014). arXiv:1405.3455
- 8. N. Kauer, G. Passarino, Inadequacy of zero-width approximation for a light Higgs boson signal. JHEP 1208, 116 (2012). arXiv:1206.4803
- N. Kauer, Inadequacy of zero-width approximation for a light Higgs boson signal. Mod. Phys. Lett. A28, 1330015 (2013). arXiv:1305.2092

References 181

 L. Landau, On the angular momentum of a two-photon system. Dokl. Akad. Nauk Ser. Fiz. 60, 207–209 (1948)

- 11. C.-N. Yang, Selection rules for the dematerialization of a particle into two photons. Phys. Rev. 77, 242–245 (1950)
- 12. Y. Gao, A.V. Gritsan, Z. Guo et al., Spin determination of single-produced resonances at hadron colliders. Phys. Rev. **D81**, 075022 (2010). arXiv:1001.3396
- 13. S. Bolognesi, Y. Gao, A.V. Gritsan et al., On the spin and parity of a single-produced resonance at the LHC. Phys. Rev. **D86**, 095031 (2012). arXiv:1208.4018
- C.M.S. Collaboration, Measurement of Higgs boson production and properties in the WW decay channel with leptonic final states. JHEP 1401, 096 (2014). arXiv:1312.1129
- 15. C.M.S. Collaboration, Evidence for the 125 GeV Higgs boson decaying to a pair of  $\tau$  leptons. JHEP **1405**, 104 (2014). arXiv:1401.5041
- 16. CMS Collaboration, Search for a standard model-like Higgs boson in the  $\mu^+\mu^-$  and  $e^+e^-$  decay channels at the LHC. Submitted to Phys. Lett. B (2014). arXiv:1410.6679
- 17. C.M.S. Collaboration, Search for the standard model Higgs boson produced in association with a *W* or a *Z* boson and decaying to bottom quarks. Phys. Rev. **D89**, 012003 (2014). arXiv:1310.3687
- C.M.S. Collaboration, Search for the associated production of the Higgs boson with a top-quark pair. JHEP 1409, 087 (2014). arXiv:1408.1682
- LHC Higgs Cross Section Working Group, Handbook of LHC Higgs cross sections: 3. Higgs properties, arXiv:1307.1347
- 20. Y. Golfand, E. Likhtman, Extension of the algebra of poincare group generators and violation of P invariance. JETP Lett. **13**, 323–326 (1971)
- J. Wess, B. Zumino, Supergauge transformations in four-dimensions. Nucl. Phys. B70, 39–50 (1974)
- 22. P. Fayet, Supergauge invariant extension of the Higgs mechanism and a model for the electron and its neutrino. Nucl. Phys. **B90**, 104–124 (1975)
- P. Fayet, Spontaneously broken supersymmetric theories of weak, electromagnetic and strong interactions. Phys. Lett. B69, 489 (1977)
- 24. G. Branco, P. Ferreira, L. Lavoura et al., Theory and phenomenology of two-Higgs-doublet models. Phys. Rep. **516**, 1–102 (2012). arXiv:1106.0034
- CMS Collaboration, Search for invisible decays of Higgs bosons in the vector boson fusion and associated ZH production modes, Eur. Phys. J. C74(8), 2980 (2014). arXiv:1404.1344

## Chapter 6 Conclusions

With the analysis of the coupling structure of the observed particle the search for the SM Higgs boson concluded for the CMS collaboration with the complete and exhaustive analysis of the full *LHC* run-1 dataset of the years 2011 and 2012. The final lap of this hunt had started with the commissioning of the LHC and the experiments in 2010 and the establishment of all known SM processes with tremendous reliability and precision. The hot phase started in 2011 with the first limits based on the searches in the main SM Higgs boson decay channels,  $H \to \gamma \gamma$ ,  $H \to ZZ$ ,  $H \to WW$ ,  $H \to \tau \tau$  and  $H \to b\bar{b}$ , in a range of  $100 < m_H < 1000$  GeV. These days were characterized by a vibrant atmosphere of tension and excitement at CERN, which reached its first and highest peak on 4 July 2012 with the announcement of the discovery of a new particle in both large scale main purpose experiments at the LHC, ATLAS and CMS, in the combination of the bosonic decay channels at ATLAS and all main decay channels at CMS. This discovery was based on roughly half of the dataset that has been collected across the whole timespan of the years 2011 and 2012. It was driven by the bosonic decay channels, while the two main fermionic decay channels,  $H \to \tau \tau$  and  $H \to b\bar{b}$ , were just around the corner to reach the sensitivity for observing the new particle. The discovery was followed by the evidence that the new particle indeed couples to fermions end of 2013 and a complete analysis of its spin, CP properties and coupling structure, as far as possible with the available dataset.

These analyses tracked unprecedented features of the new particle: it is a boson which very likely is of spin 0 with a CP eigenvalue of +1. It has a non-universal coupling structure across the fermion flavor generations. These features, which could be confirmed within the experimental resolution of the existing analyses demonstrated the compatibility of the new particle with being the Higgs boson of the SM, as postulated roughly 50 years ago. The mass of the new particle could be determined with a precision of  $\mathcal{O}(2\,\%)$  in the combination of the  $H\to\gamma\gamma$  and  $H\to ZZ$  decay channels. The presence of a SM like Higgs boson with a mass of  $m_H>130$  GeV could be excluded in the  $H\to WW$  decay channel at more than 95 % CL over the whole mass range up to 1 TeV. Other  $J^P$  hypotheses than  $0^+$  could be excluded in a series of hypothesis tests in the  $H\to ZZ$  decay channel at more than 95% CL. Finally the compatibility of the coupling structure of the new particle with the expectation for

184 6 Conclusions

the SM Higgs boson could be confirmed with a precision between 10-20% across all couplings, which are accessible at the *LHC*. It is this coupling structure, which proofs the new particle to be a Higgs boson.

This discovery confirms a highly non-trivial aspect in the structure of the SM: the aspect of spontaneous  $SU(2)_L$  symmetry breaking, which had led to the introduction of a complete new "hidden" sector spanned by the  $SU(2)_L$  doublet field  $\phi$  which has a dedicated coupling structure to gauge bosons and fermions. The discovery of a particle, which is compatible with the predictions of the SM constitutes a fantastic success of the theory. The discovered new particle represents an entirely new type with a new and unique set of properties. The fact that both large multipurpose experiments at the *LHC*, *ATLAS* and *CMS* independently made the discovery with compatible results and in accordance concerning signal strength, mass and properties of the new particle gives strong confidence in the discovery. It is reinforced by the fact that both experiments had been build with independent and partially complementary design choices as outlined Sect. 4.1.2.

The LHC stopped operation end of 2012 to enter a phase of maintenance and upgrade of the accelerator and the experiments. This shutdown formed the endpoint of the *LHC* run-1 data taking period with a dataset of 25 fb<sup>-1</sup> collected at each of the two main experiments at center-of-mass energies of 7 and 8 TeV. This concluded the search for the SM Higgs boson, as the most exciting time in the lives of many junior and senior scientists. The search was a great success, which many senior scientists would not have dared to dream of. This book has been written with the scope to describe the final results of this enterprise in its main aspects. To be concise I have restricted myself to the most important established results. In this course I have left out a few more comprehensive studies of the properties of the new particle, if they were still limited in their conclusions due to the small size of the available dataset. This choice was made not to dilute the main message of the document. Among those studies a detailed analysis of the tensor structure of the  $H \to VV$  decay [1] under the assumption of anomalously high couplings to vector bosons and a search for the SM Higgs boson in the rare  $H \to \gamma Z$  decay channel [2] should at least be mentioned. With the same reasoning I have only very briefly touched the search for the decay of the Higgs boson into invisible particles [3], which is not a SM Higgs boson search in the actual sense and left out all searches for Higgs bosons in the context of models beyond the SM. The most important of these searches is the search for neutral Higgs bosons in the context of the minimal supersymmetric SM (MSSM) in the di- $\tau$  final state [4]. The reasoning here is that these searches did not lead to a discovery, but only to limits on the parameter space of the considered models. While the analyses are very interesting and would easily fill another chapter of this book they will hopefully be superseded as soon as the new data arrive.

In the previous chapters I have also tried to indicate the questions that remained unanswered and the work that still lies ahead in the investigation of the Higgs sector of the SM. The upcoming data taking period from 2015 on has the technical scope to collect 300 fb<sup>-1</sup> of proton proton collisions with a center-of-mass energy of 13 TeV. The number of collected events will be 15 times larger than the number of events collected at 8 TeV center-of-mass energy in 2012 and the production cross section will

6 Conclusions 185

be enhanced by a factor of  $\approx 2.25$  due to the increased parton luminosity at the higher center-of-mass energy. Ignoring reconstruction and selection inefficiencies this will lead to an expected number of 33 000 SM Higgs boson events in the  $H \to \gamma \gamma$  decay channel, 1500 events in the  $H \to ZZ$  decay channel, 150 000 events in the  $H \to WW$  decay channel, 1 million events(!) in the  $H \to \tau \tau$  decay channel, 3000 events in the  $H \to \mu \mu$  decay channel and 400 000 events in the  $H \to b\bar{b}$  decay channel. The expected numbers of SM Higgs boson events broken down by production mode and decay channel are summarized in Table 6.1.

This amount of data will open the next era of SM Higgs boson physics: the era of precision measurements. It will bring the final proof of the coupling of the new particle to fermions; the signal in the  $H \to \mu\mu$  decay channel will be established; the number of events will be sufficient fully to explore all production modes in nearly all main decay channels. This will lift the analysis of the coupling structure to a precision of better than  $\mathcal{O}(5\%)$  on most of the couplings. The most difficult to control will still be the coupling to b-quarks. If the Higgs boson behaves as expected by the SM the rare decay channel into  $\gamma Z$  will be established. Deviations of the properties of the discovered Higgs boson in the context of popular models beyond the SM, like supersymmetry or more general 2HDM are expected still to be small compared to this level of precision. So a distinction of the SM from such theories based only on the analysis of the coupling structure of the discovered Higgs boson will still be difficult unless the deviations will be larger than expected. But all of these models predict a rich phenomenology in the Higgs sector with a large number of additional Higgs bosons. Searches for these Higgs bosons as mentioned above will gain more and more importance and might easily lead to the next great discovery at the LHC. A prime channel to search for these Higgs bosons is the  $H \to \tau\tau$  decay channel: all of these models predict an enhanced coupling of the additional Higgs bosons to

**Table 6.1** Rough estimates for expected event numbers ignoring reconstruction and selection inefficiencies and broken down by decay channel and production mode

Decay	$\sqrt{s} =$	$\sqrt{s} = 13 \text{ TeV}, 300 \text{ fb}^{-1}$						
Channel	8 TeV, 20 fb <sup>-1</sup>							
	inclusive	inclusive	$gg \rightarrow H$	$qq \rightarrow H$	WH	ZH	$t\bar{t}H$	
$\gamma\gamma$	1000	33 000	30 000	2300	1000	700	300	
ZZ	50	1500	1300	100	50	30	15	
WW	5000	150 000	130 000	10 000	4500	3000	1500	
$b\bar{b}$	12 000	400 000	350 000	30 000	12 000	10 000	40 000	
au au	30 000	1000000	900 000	70 000	30 000	20 000	10 000	
μμ	100	3000	2500	200	90	60	30	

The second column corresponds to the numbers for 8 TeV and  $20~{\rm fb^{-1}}$ , as given at the beginning of each corresponding section of Chap. 4. The following columns correspond to the expected event numbers for 13 TeV and  $300~{\rm fb^{-1}}$ , for all decay channels, inclusive and broken down by production modes

186 6 Conclusions

down-type fermions; the  $H \to \tau \tau$  decay channel at the same time is the cleanest and most promising fermionic decay channel.

The new data will also bring high precision measurements of the tensor structure of the coupling of the new boson to Z bosons, that have partially been laid out already in [1]. It will lead to a first unambiguous measurement of the spin and CP of the new boson. As discussed in Sect. 5.2.2 what can not be addressed that easily in the  $H \to ZZ$  decay channel is the question of CP-odd admixtures to the Higgs boson couplings, since in extensions of the SM, which are currently under discussion, CP-odd admixtures to the couplings to vector bosons are suppressed at leading order. A prime candidate for such searches will again be the  $H \to \tau\tau$  decay channel, where CP-even and CP-odd contributions to the Higgs boson coupling should appear on the same footing. The concrete analyses turn out to be experimentally challenging however. They will require an excellent understanding of the detector and a large amount of data.

In summary the SM has proven to be one of the most powerful theories that has ever been developed to decipher the code of nature from first principles. It has demonstrated, over many decades, how a plethora of phenomena of particle physics can be described and understood in terms of a handful of intuitive assumptions and symmetry principles. Nearly all of these phenomena are experimentally difficult to detect and non-trivial to understand. In consequence they have no correspondence in our daily life experience and are far apart from our daily life intuition. This makes it even more remarkable that the SM does such a good job in understanding these realms. The discovery of a Higgs boson 50 years after its postulation leads particle physicists to the assumption that the laws of nature can be understood even better and with less parameters, which due to their phenomenological nature can not provide further insights into the underlying rules and mechanics of nature. E.g. the Higgs mechanism uncovers the masses of elementary particles, which are just parameters in any other theory, as couplings to an omnipresent new field with non-vanishing vacuum expectation value. It thus gives a complete new view on these parameters. On the other hand the question, why the masses of the individual elementary particles are so different still remains unanswered.

The *LHC* at *CERN* has been a great and unique place in the world, where mankind could experience and celebrate its great understanding and control over the laws of nature. As a single machine it has confirmed the last decades of particle physics from the discovery of the  $J/\psi$  1975 [5, 6] up to the discovery of the top quark [7, 8] 1995. It has helped completing the SM as a self-consistent theory in the years from 2011 till 2015. It has brought new insights in the way nature works. The discovery has opened a new door in the house of physics, with new rooms to explore: after the strong, electroweak and the top sector, the Higgs sector will open up for precise mensuration. Near term goals are defined, questions to answer have been posed. It is not presumptuous to believe that upcoming periods with more data at higher energies will lead to more glorious times, which will drive us into the unknown and most likely the unexpected. I will conclude with these prospects.

## References

 CMS Collaboration, Constraints on the spin-parity and anomalous HVV couplings of the Higgs boson in proton collisions at 7 and 8 TeV, submitted to Phys. Rev. D.,89 (2014) arXiv:1411.3441

- 2. C.M.S. Collaboration, Search for a higgs boson decaying into a z and a photon in pp collisions at  $\sqrt{s} = 7$  and 8 TeV. Phys. Lett. **B726**, 587–609 (2013). arXiv:1307.5515
- 3. CMS Collaboration, Search for invisible decays of Higgs bosons in the vector boson fusion and associated ZH production modes. Eur. Phys. J. C74(8), 2980 (2014). arXiv:1404.1344
- 4. C.M.S. Collaboration, Search for neutral MSSM Higgs bosons decaying to a pair of  $\tau$  leptons in pp collisions. JHEP **1410**, 160 (2014). arXiv:1408.3316
- 5. J. Aubert, U. Becker, P. Biggs et al., Discovery of the new particle. J. Nucl. Phys. B89(1) (1975)
- 6. SLAC-SP-017 Collaboration, Discovery of a narrow resonance in  $e^+e^-$  annihilation. Phys. Rev. Lett. **33** 1406–1408 (1974)
- 7. CDF Collaboration, Observation of top quark production in  $\bar{p}p$  collisions. Phys. Rev. Lett. **74**, 2626–2631. (1995) arXiv:hep-ex/9503002
- 8. D0 Collaboration, Search for high mass top quark production in  $p\bar{p}$  collisions at  $\sqrt{s}=1.8$  TeV. Phys. Rev. Lett. **74**, 2422–2426. (1995) arXiv:hep-ex/9411001